



**The Predictability and Representation of South
Asian Monsoon Low-Pressure Systems in
Reanalyses and Subseasonal-to-Seasonal
Prediction Models**

Akshay Sameer Deoras

A thesis submitted in fulfilment of the requirements for the degree of
Doctor of Philosophy

PhD Atmosphere, Oceans and Climate

Department of Meteorology

School of Mathematical, Physical and Computational Sciences

May 2022
University of Reading

DECLARATION

I confirm that this is my own work and the use of all material from other sources has been properly and fully acknowledged.

Akshay Sameer Deoras

Abstract

Monsoon low-pressure systems (LPSs) are synoptic-scale systems that form during boreal summer, mainly over the head of the Bay of Bengal (BoB). However, regional varieties can also form over the Arabian Sea and near Sri Lanka. Despite their ability to cause catastrophic floods in the Indian subcontinent, there has been insufficient exploration of their predictability and prediction skill. This thesis examines LPS prediction and structure as well as large-scale controls on their frequency in Subseasonal-to-Seasonal (S2S) prediction models. Using a feature-tracking algorithm, we identify LPSs in eleven S2S models during a common reforecast period of June–September 1999–2010, verifying the results against ERA-Interim (ERA-I) and MERRA-2 reanalyses. Moreover, we examine characteristics of LPS regional varieties using ERA-I.

The S2S models simulate tracks and structure of LPSs reasonably well; however, all models underestimate their frequency, and BoM, CMA and HMCR models have large biases in their simulation. The subseasonal probabilistic frequency predictions by BoM, CMA, CNRM and ECMWF models are the most accurate.

Among regional varieties, Arabian Sea LPSs are least frequent. Short-lived BoB LPSs are most frequent and bring the most precipitation to eastern India. We then examine the modulation of LPSs on different time scales: the tropical intraseasonal oscillation modulates genesis of all varieties, and La Niña and negative Indian Ocean Dipole enhance genesis of Sri Lankan LPSs. Most S2S models correctly simulate enhanced LPS frequency when the active phase of the Madden-Julian Oscillation is over the Indian Ocean and Maritime Continent. Large-scale conditions, such as the position of the tropical easterly jet and mid-tropospheric relative humidity, play a role in determining whether BoB LPSs continue their propagation across north-central India.

These results provide a framework for understanding LPS predictability, envisaging improved disaster preparedness in the Indian subcontinent.

ACKNOWLEDGEMENTS

I would like to thank my supervisors Dr Andrew G. Turner and Dr Kieran M. R. Hunt for their invaluable advice and constant support throughout my PhD. I would also like to thank my Monitoring Committee members Dr Kevin I. Hodges and Dr Peter M. Inness for their guidance and feedback during the course of my PhD. A special thanks to my examiners Dr Frédéric Vitart and Dr Kevin Hodges for examining my thesis and giving valuable suggestions, which helped in improving the quality of my thesis.

1	Introduction	1
1.1	Background	1
1.1.1	The Indian summer monsoon	1
1.1.2	Indian monsoon low-pressure systems	3
1.1.3	Variability of LPSs	7
1.1.4	The Subseasonal-to-Seasonal time scale	9
1.2	Aims of the thesis	10
1.3	Thesis structure	13
2	Data and Methods	15
2.1	Data overview	15
2.1.1	The Subseasonal-to-Seasonal prediction project database	15
2.1.2	ERA-Interim reanalysis	20
2.1.3	MERRA-2 reanalysis	20
2.1.4	GPM IMERG	21
2.1.5	Tropical Rainfall Measuring Mission	22

2.1.6	LPS catalogue	23
2.1.7	Observed SST dataset	23
2.1.8	Computing the ENSO and IOD indices	25
2.2	Tracking and post-tracking processes	26
2.2.1	Tracking algorithm	26
2.2.2	Temperature-pressure filtering	29
2.2.3	Matching methodology	30

3 Comparison of the Prediction of Indian Monsoon Low Pressure Systems by Subseasonal-to-Seasonal Prediction Models 34

3.1	Introduction	34
3.2	Data and methodology	37
3.2.1	The S2S database	37
3.2.2	Observed datasets	37
3.3	Climatology of LPSs	37
3.3.1	Seasonal numbers	38
3.3.2	Intensity distribution	38
3.3.3	Track density	40
3.3.4	Genesis and lysis	43
3.4	The skill of LPS prediction	43
3.4.1	Relative skill of ensemble members	44
3.4.2	Spatial distribution of position errors	48
3.4.3	Control and ensemble mean error	49
3.4.4	Ensemble spread-error relationship	51
3.5	Evaluation of subseasonal probabilistic predictions	53
3.5.1	Brier Score and Brier Skill Score	54
3.5.2	Sensitivity of the BSS to the ensemble size	56

3.6	Precipitation errors	57
3.7	Discussion and conclusions	61
4	The structure of strong Indian monsoon low-pressure systems in Subseasonal-to-Seasonal prediction models	66
4.1	Introduction	66
4.2	Data and methods	68
4.2.1	Various datasets	68
4.2.2	Root mean square error	68
4.3	Simulation of the lower-tropospheric South Asian monsoon circulation . . .	69
4.4	Precipitation	72
4.4.1	Precipitation biases	72
4.4.2	Precipitation contribution	75
4.5	Horizontal structure of SLPS	79
4.5.1	Precipitation and wind	80
4.5.2	MSLP and relative vorticity	83
4.6	Vertical structure	84
4.6.1	Relative vorticity	84
4.6.2	Temperature	86
4.6.3	Moist static energy	90
4.7	Variability	91
4.7.1	Evolution over forecast lead time	92
4.7.2	Evolution over LPS lifespan	94
4.8	Conclusions	97
5	The four regional varieties of South Asian monsoon low-pressure systems	101
5.1	Introduction	101

5.2	Data and methods	104
5.2.1	LPS catalogue	104
5.2.2	ERA-Interim and TRMM	104
5.2.3	BSISO, MISO and MJO indices	105
5.2.4	ENSO and IOD indices	106
5.2.5	Significance testing	106
5.3	Track statistics	106
5.3.1	Frequency and track characteristics	106
5.3.2	Track density	108
5.4	Vertical structure of temperature and moisture	110
5.5	Precipitation contribution	112
5.6	Modulation of LPS activity by the ISO	113
5.7	Modulation of Sri Lankan LPSs by ENSO and IOD	119
5.8	Discussion and conclusions	122
6	Large-scale controls on Indian monsoon low-pressure systems	128
6.1	Introduction	128
6.2	Data and methods	131
6.2.1	The S2S, ERA-I, TRMM and LPS datasets	131
6.2.2	Identifying downstream LPSs in ERA-I	132
6.2.3	IMD Cyclone e-Atlas	132
6.2.4	MJO index	134
6.2.5	ENSO and IOD indices	134
6.2.6	Significance testing	134
6.3	Relationship between the MDGI and SLPS frequency	134
6.3.1	Genesis potential of SLPSs in S2S models	135

6.3.2	Time-varying relationship between the MDGI and observed SLPS frequency	138
6.4	Intraseasonal and interannual variability of SLPSs	143
6.4.1	Madden-Julian Oscillation	143
6.4.2	El Niño Southern Oscillation	145
6.4.3	Indian Ocean Dipole	147
6.4.4	Interannual variability of SLPSs over a long time period	148
6.5	Relationship between large-scale atmospheric fields and frequency of BoB LPS varieties	151
6.5.1	MDGI components	151
6.5.2	Monsoon trough	153
6.5.3	Zonal vertical shear and winds	154
6.6	Characteristics of downstream LPSs	157
6.6.1	Frequency and track characteristics	158
6.6.2	Steering of low-pressure systems in different clusters	160
6.6.3	Evolution over lifespan	162
6.6.4	Precipitation contribution	165
6.7	Conclusions	165
7	Conclusions	170
7.1	Summary of major results	170
7.2	Limitations	176
7.3	Future work	177
7.4	Applications	180
	Bibliography	183

1.1 Background

1.1.1 The Indian summer monsoon

The Indian summer monsoon is an important part of the Asian summer monsoon, and is responsible for producing more than 75% of the annual precipitation over India (Parthasarathy and Mooley, 1978). Over a billion people in India depend on the monsoon rainfall, which is important for agriculture, ground water recharge, hydroelectric power generation, industry and basic human needs. The summer monsoon season lasts from June to September, and most rainfall in this period occurs over the Western Ghats mountains on the west coast, the Himalayan foothills, parts of eastern and central India, and the coast of Myanmar (Figure 1.1). At a very basic level, the monsoon is considered to be a giant land-sea breeze—a mechanism first suggested by Halley (1686), and then modified by Hadley (1735) to incorporate the Coriolis effect. The seasonal cycle of solar heating warms land regions of southern and southeastern Asia faster than the adjoining oceans, which is due to differences in heat capacity between water and land. This results in the formation of a

pressure gradient across the Indian subcontinent and Indian Ocean, which then induces a cross-equatorial surface flow towards the land and a return flow aloft. The presence of the Himalayas and Tibetan Plateau imposes elevated heating and the topography prevents the intrusion of cold and dry extra-tropical air into the warm and moist air of the monsoon, both of which are important for the establishment, maintenance and variability of the Asian/Indian summer monsoon (e.g., Blanford 1884; Flohn 1957; Yanai et al. 1992; Boos and Kuang 2010; Rajagopalan and Molnar 2013). Thus, if the land-ocean contrast in a particular summer monsoon season is stronger than normal, rainfall over India should increase in that season. However, Kothawale and Kumar (2002) found positive and negative land surface temperature anomalies during droughts and excess monsoon years between 1971 and 2000, respectively. This suggests that a stronger monsoon will be associated with a stronger land–ocean contrast, only if the sea surface temperature anomaly of the Indian Ocean is negative and its magnitude is larger than that of the land surface temperature anomaly (Gadgil, 2018). Gadgil (2018) also showed that a weaker than normal land-ocean contrast was always associated with above average monsoon rainfall during 1950–2014. Thus, spatio-temporal variations of summer monsoon rainfall over India are not always consistent with the theory of land-ocean contrast (Gadgil, 2018).

An alternative theory considers the monsoon as a manifestation of the seasonal migration of the equatorial trough or the Intertropical Convergence Zone (ITCZ), which is in response to the seasonal variation in the solar radiation (Blanford, 1886; Riehl, 1954; Charney, 1969). The ITCZ swings dramatically between average latitudes of 20°N in boreal summer and 8°S in boreal winter, causing seasonal variations in rainfall over South Asia (Gadgil, 2003; Schneider et al., 2014). Sikka and Gadgil (1980) found that there is a series of northward propagation of cloud bands from the equatorial Indian Ocean onto the Indian region (i.e., to the north of 15°N) during the summer monsoon season. Their analysis suggested the presence of two ITCZs—a continental one over the Indian region and an oceanic one in the equatorial belt. Whilst the continental ITCZ is present on

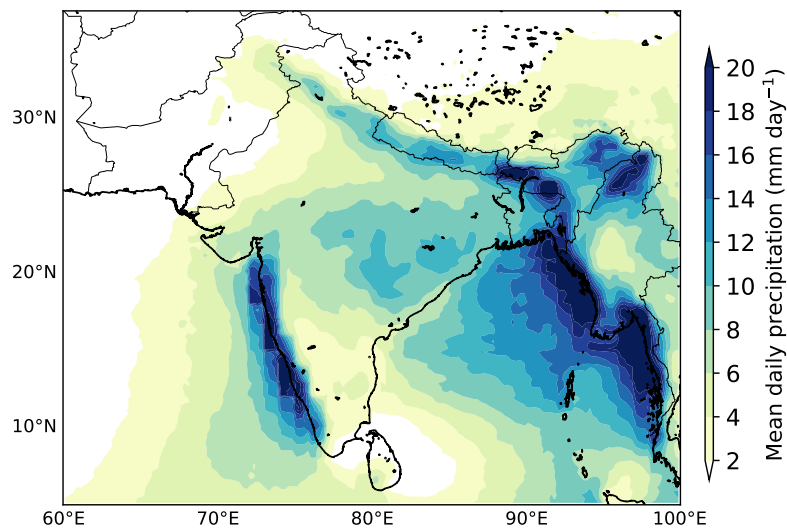


Figure 1.1: Mean daily precipitation (mm day^{-1}) during June–September 1998–2018, calculated using the TRMM 3B42 v7 dataset.

most days of the summer monsoon season, the oceanic one appears intermittently. Thus, the variability of summer monsoon rainfall over India is associated with the space-time variation of the continental ITCZ.

1.1.2 Indian monsoon low-pressure systems

The Indian subcontinent is affected by synoptic-scale cyclonic vortices each summer monsoon season, which have a lifespan of 3–5 days (Daggupati and Sikka, 1977; Godbole, 1977). These vortices, which are known as monsoon low-pressure systems (LPSs), most frequently develop over the head of the Bay of Bengal (BoB) and nearby coastal regions, propagate west-northwestward over India (Figure 1.2), and produce abundant precipitation along their tracks (e.g., Mooley 1973; Godbole 1977).

According to the India Meteorological Department (IMD), LPSs featuring two closed isobars in surface pressure at 2 hPa intervals over land, or those featuring 3-minute maximum sustained surface wind speeds of $8.5\text{--}13.5 \text{ m s}^{-1}$ over sea are referred to as monsoon depressions (MDs), whereas systems weaker than this are referred to as monsoon

low-pressure areas. A full classification is provided in Table 1.1. Typically, around 14 LPSs form each summer and half of them intensify into strong LPSs such as MDs (Boos et al., 2015). Typically, LPSs do not intensify into tropical cyclones over the north Indian Ocean during the summer monsoon season as substantial vertical wind shear, which is created by the low-level monsoon westerlies and the upper-level tropical easterly jet (Figure 1.3), inhibits this intensification (Riehl and Shafer, 1944; DeMaria, 1996). In fact, there are only 11 tropical cyclones over the BoB in the IMD Cyclone eAtlas database (<http://14.139.191.203/Login.aspx>) that had their genesis during the June–September season in the 1979–2020 period, as opposed to 124 MDs.

Category	Ocean	Land
Low-pressure area	$U < 17$	$\epsilon = 1$
Depression	$17 < U < 27$	$\epsilon = 2$
Deep depression	$28 < U < 33$	$\epsilon = 3, 4$
Cyclonic storm	$34 < U < 47$	$\epsilon > 4$
Severe cyclonic storm	$48 < U < 63$	$\epsilon > 4$
Very severe cyclonic storm	$64 < U < 119$	$\epsilon > 4$
Super cyclonic storm	$U \geq 120$	$\epsilon > 4$

Table 1.1: The official classification of low-pressure systems, as outlined by the glossary published by the IMD (<https://www.imdpune.gov.in/Weather/Reports/glossary.pdf>). U denotes the 3-minute maximum sustained surface wind speed (knots) and ϵ denotes the number of closed isobars within a radius of 3° from the centre of systems when they are over land. 1 knot = 0.51 m s^{-1} .

LPSs produce around half of the summer monsoon rainfall over India (Hunt and Fletcher, 2019). Since their peak composite precipitation rates are about 50 mm day^{-1} (Yoon and Chen, 2005), high-impact flood events due to these weather systems are frequent over the Indian subcontinent during the summer monsoon season. Over the last decade,

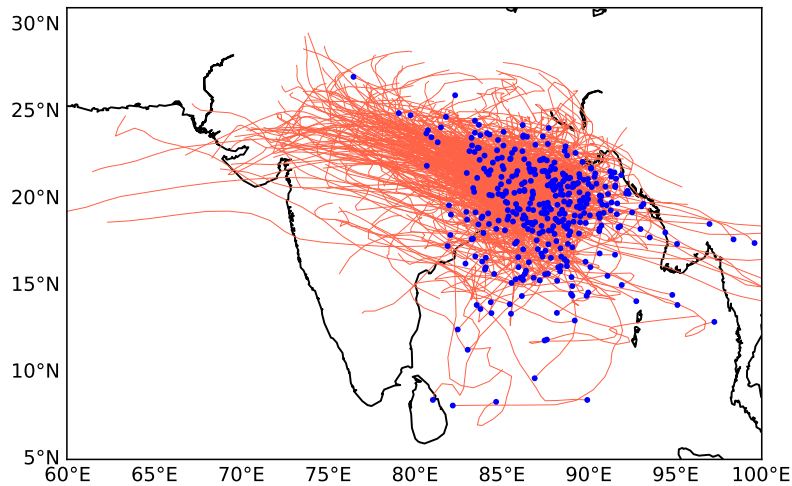


Figure 1.2: Tracks of 364 monsoon low-pressure systems (LPSs) that had their genesis over the Bay of Bengal and nearby regions during June–September 1979–2018. These LPSs were identified in ERA-I by Hunt and Fletcher (2019). LPS tracks are smoothed using a 1-D Gaussian filter with a smoothing radius of ~ 70 km. Blue dots show genesis locations of each LPS.

LPSs have triggered at least three catastrophic floods in India: Uttarakhand (16–18 June 2013), Gujarat and Rajasthan (23–25 July 2017), and Kerala (August 2018), affecting millions of people and causing unprecedented damage to property (Ray et al., 2019; Hunt and Menon, 2020). LPSs have triggered 82% of extreme precipitation events over central India during 1979–2012 (Thomas et al., 2021). Furthermore, they are of particular concern in the Himalayan region, since they can interact with extratropical systems (i.e., western disturbances), causing extreme precipitation events such as the 2013 Uttarakhand floods (Kotal et al., 2014; Hunt et al., 2021b). Despite their important role for water supply and triggering catastrophic floods in the subcontinent, the predictability and prediction skill of LPSs remain less explored than other phenomena such as tropical cyclones. Skilful predictions of LPSs at long lead times, such as the subseasonal-to-seasonal time scale (to be discussed in Section 1.1.4), could benefit stakeholders (e.g., farmers, disaster management organisations and governments) by giving them more time for preparedness and planning.

The occurrence of LPSs was reported as early as the late-nineteenth century by Eliot

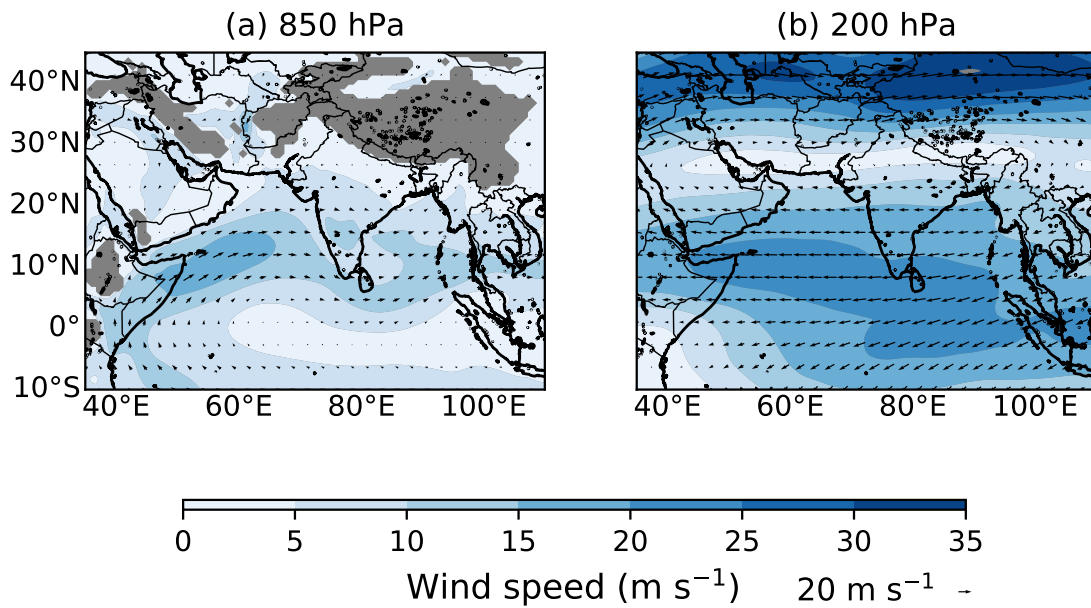


Figure 1.3: The climatology of 850 hPa and 200 hPa winds in ERA-Interim reanalysis dataset during June–September 1979–2018. Grey areas in (a) indicate where the mean surface pressure is less than 850 hPa.

(1884), who found that LPSs regularly form during July and August, they are weaker than tropical cyclones, and most of them dissipate without reaching northwestern parts of India. In the 20th century, many studies analysed synoptic features of MDs. Mulky and Banerji (1960) analysed circulation features of a composite of 22 MDs that occurred during 1954–1958. They found that MDs tilt towards the southwest, a feature previously reported by Pisharoty and Asnani (1957), and later reconfirmed by Mooley (1973) in a larger composite of MDs occurring during 1891–1960. Using meteorological charts and radiosonde data, Krishnamurti et al. (1975, 1976), Godbole (1977) and Sarker and Chowdhury (1988) analysed more composite MD fields such as temperature and relative vorticity. They found that MDs have a cold (warm) core in the lower (upper) troposphere, with the most intense relative vorticity, winds, moisture, cloud cover and precipitation occurring in the southwestern quadrant of the composite MD. Hunt et al. (2016a) performed a composite analysis of 106 MDs that occurred between 1979 and 2014. Apart from confirming the pre-

viously known features of MDs, they found that MDs occurring during active phases of the monsoon are more intense than those during break phases. Some studies have suggested that MDs grow due to baroclinic instability (e.g., Mishra and Salvekar 1980). However, this mechanism requires these weather systems to tilt upshear with height (Cohen and Boos, 2016) instead of the observed downshear tilt (e.g., Hunt et al. 2016a). Diaz and Boos (2019) concluded that barotropic instability coupled to convection in the monsoon flow due to a meridional shear in the low-level winds favours the growth of MDs.

Whilst MDs forming over the BoB have been extensively studied, LPSs forming over other regions of South Asia such as the Arabian Sea and Sri Lanka remain excluded. Hunt and Fletcher (2019) identified four regional varieties of South Asian LPSs by applying a feature-tracking algorithm to ERA-Interim reanalysis and then partitioning LPS tracks into four clusters. These four LPS varieties, whose mean tracks are shown in Figure 1.4, are: short-lived BoB LPSs, long-lived BoB LPSs, Arabian and Sri Lankan LPSs. They examined the precipitation contribution of these four LPS varieties to the summer monsoon precipitation. Whilst BoB-short LPSs produced most precipitation over India, BoB-long LPSs, Arabian and Sri Lankan were important for precipitation over northwest India, Pakistan and Sri Lanka respectively. However, characteristics of these four LPS varieties and the potential for their predictability remain unknown, the results of which could open a new avenue for research on LPSs, ultimately benefitting stakeholders.

1.1.3 Variability of LPSs

LPS frequency is modulated by modes of tropical intraseasonal variability. Krishnamurthy and Ajayamohan (2010) analysed LPSs during all phases of the two intraseasonal modes, which were first obtained by Krishnamurthy and Shukla (2007, 2008). These intraseasonal modes are related to the Boreal Summer Intraseasonal Oscillation (BSISO). Whilst the eastward-propagating Madden-Julian Oscillation (MJO) is the dominant signal of the tropical intraseasonal oscillation (ISO) in boreal winter (e.g., Zhang 2005), the BSISO

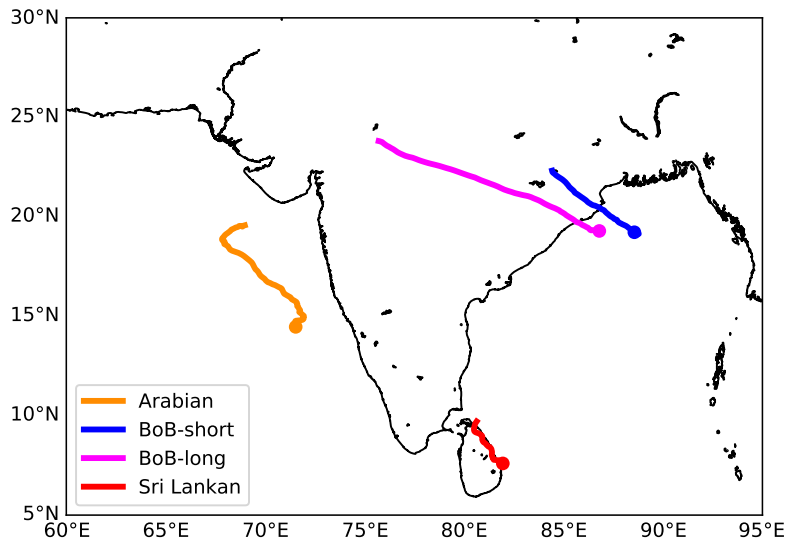


Figure 1.4: The mean tracks of the four regional varieties of South Asian monsoon low-pressure systems that had their genesis during June–September 1979–2018. These LPS varieties were identified in ERA-I by Hunt and Fletcher (2019), and their data has been used to plot this figure.

prevails in boreal summer (Wang and Xie, 1997; Kikuchi et al., 2012). Compared to the MJO, convective anomalies associated with the BSISO show an additional northward/northeastward propagation over the Indian summer monsoon region (e.g., Yasunari 1979) and northward/northwestward propagation over the Western North Pacific and East Asian regions (e.g., Murakami 1984). Krishnamurthy and Ajayamohan (2010) concluded that both the location and area covered by LPSs are tied to the propagation of convective anomalies of these intraseasonal modes—LPS tracks occur further south over the subcontinent when convective anomalies are located over the equatorial Indian Ocean, and further north when the convective anomalies are located over India and the northwestern Pacific Ocean. Haertel and Boos (2017) found that LPS frequency is not significantly affected by the amplitude of the MJO. With increasing MJO amplitude, there is a slight decrease in the number of monsoon low-pressure areas, but roughly the same number of MDs and deep depressions form. However, LPS frequency is modulated by MJO phase, with phases

4–6 (where convection is favoured over the eastern Indian Ocean and the western Pacific Ocean) supporting the genesis of LPSs in general.

In addition to intraseasonal time scales, LPS frequency is suggested to feature variations on interannual time scales. Hunt et al. (2016a) and Singh et al. (2002) found that more MDs form during El Niño years than La Niña years. Vishnu et al. (2020a), who analysed LPSs in six datasets, found that ENSO has greater control over the frequency of low-pressure areas than MDs during La Niña and negative phase of the Indian Ocean Dipole (IOD). Thus, there is no consensus about the exact role of ENSO and IOD in modulating LPS frequency. Moreover, there is a gap in our understanding of the mechanisms by which these large-scale modes might exert controls on LPS frequency.

The aspect of mechanisms controlling the frequency of BoB LPSs gains importance since LPS genesis over the BoB appears to feature two modes—these systems can form either *in situ* or spin up from the vortical remnants of westward-propagating tropical disturbances from the South China Sea or western Pacific Ocean. The latter are commonly known as *downstream LPSs* since they propagate in the direction of the tropical easterly jet (e.g., Krishnamurti et al. 1977; Saha et al. 1981). Such systems can regenerate over the BoB due to favourable conditions such as warm sea surface temperature and cyclonic vorticity provided by the monsoon trough (Krishnamurti et al., 1977; Sikka, 1978). Given that their genesis location is far from India, these systems can provide a larger window of opportunity for preparedness in India than that provided by LPSs forming over the BoB. However, characteristics of downstream LPSs remain less explored than for BoB MDs.

More detailed background discussions are included in relevant later chapters.

1.1.4 The Subseasonal-to-Seasonal time scale

The subseasonal-to-seasonal (S2S) timescale, which is defined as the time scale between two weeks and two months (e.g., Vitart and Robertson 2018), bridges the gap between

medium-range and seasonal predictions. The S2S time scale has recently gained a lot of attention due to the ongoing S2S prediction project (Vitart et al., 2012). An important outcome of this project was the creation of the S2S dataset that contains reforecasts and near real-time forecasts from eleven international prediction centres (Vitart et al., 2017).

The S2S time scale was long thought to be a “predictability desert” (Vitart et al., 2012). It is considered too long for much of the memory of atmospheric initial conditions to persist, and too short for variations in the surface boundary conditions (e.g., sea surface temperature) to play an important role (Robertson et al., 2020). Figure 1.5 shows a comparison between the forecast skill and potential sources of predictability for forecasts/outlooks based on different forecast range. The forecast skill for short to medium-range weather forecasts depends on atmospheric initial conditions, whereas that for monthly or seasonal outlooks depends on initial conditions of the coupled land-ocean system (e.g., sea surface temperature). At the S2S forecast lead times, mean-state biases in models can become substantial as models drift towards their own climatologies. This can affect the overall forecast performance. Charney and Shukla (1981) have shown that the interannual variability in tropics is determined by changes in the boundary forcing at the Earth’s surface such as sea surface temperature, albedo and soil moisture. Although not fully understood, recent studies (e.g., Vitart et al. 2015) have suggested that the predictability at the S2S time scale comes from the following multiple sources: soil moisture, sea ice, snow cover, oceanic conditions, stratosphere-troposphere interaction, tropical-extratropical teleconnections, and large-scale circulation patterns such as the MJO and ENSO.

1.2 Aims of the thesis

Given that LPSs have triggered many catastrophic floods across the Indian subcontinent, a thorough understanding of the predictability and prediction skill of these weather systems on the S2S time scale is important for disaster preparedness and long-term planning.

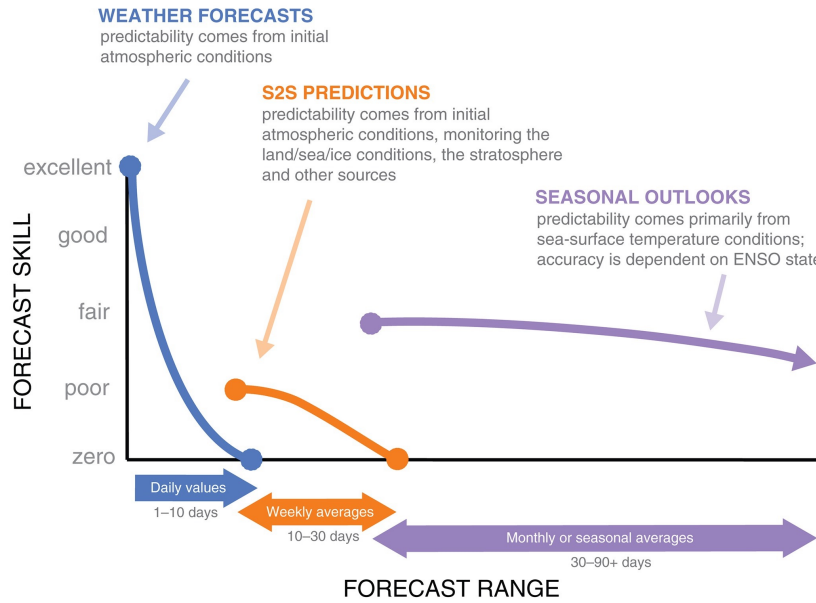


Figure 1.5: Fig. 1a from White et al. (2017) showing an estimate of the forecast skill and potential sources of predictability as a function of forecast lead time.

This is particularly important for improving reservoir operations in India since the presence of LPSs has forced dam operators to suddenly release dam water to prevent dam overflow, thereby worsening floods such as the 2018 Kerala flood (Lal et al., 2020). First of all, we must identify a suitable dataset for our investigation. Many LPS datasets are available, such as Hurley and Boos (2015), Vishnu et al. (2020a) and Hunt (2021), which contain track details of LPSs identified in various reanalysis datasets. But to understand the prediction skill of LPSs, we must also track them in reforecasts (e.g., the S2S dataset), which are retrospective weather forecasts generated using a fixed numerical model (Hamill et al., 2006). Reforecasts can help model developers to diagnose biases in models when developing updated versions. Furthermore, meteorologists and researchers can use analysis of reforecasts to apply statistical corrections to forecasts, which can also benefit the development of forecasting products for weather-dependent stakeholders (e.g., farmers).

Successful tracking and identification of LPSs in a reforecast dataset such as the S2S dataset will open the opportunity to understand the skill of LPS predictions, which is

the first aim of this thesis. First of all, how well do models predict the frequency and intensity of LPSs? This is an important question since these factors affect precipitation forecasts of LPSs. We will also examine the simulation of LPS tracks, including genesis and lysis of these weather systems. This will then open up questions about how forecast lead time affects the evolution of position and intensity errors of LPSs and at what lead times these forecasts are no longer useful. We can then determine if S2S forecasts of LPSs suffer from underdispersion, in which the ensemble spread is smaller than the error in the ensemble mean. Ideally, the ensemble spread should be able to cover all possible forecast outcomes and predict the forecast error (Leutbecher and Palmer, 2008; Hopson, 2014). However, ensemble prediction systems tend to display underdispersion since not all sources of forecast uncertainties related to initial conditions and model errors are simulated (Buizza and Leutbecher, 2015).

The analyses of LPS predictions will partly motivate us to explore the simulation of LPS structure since this may offer insights into position and intensity errors of LPSs as well as the overall efficacy of S2S models. This is the second aim of this thesis. For example, do models featuring large LPS position errors also feature large biases in the simulation of the LPS structure? We will expand our analysis by investigating the simulation of precipitation due to LPSs and their precipitation contribution to the summer mean precipitation. This analysis will be important for identifying models simulating large biases; if such models are operationalised, it could adversely affect the management of water resources and disaster preparedness in the Indian subcontinent. We will then analyse the evolution of LPS structure with LPS lifespan, and as a function of forecast lead time of S2S models in order to understand how errors develop. This analysis could help the modelling community in improving the representation of various LPS processes in models.

Given that we will then have the required framework to analyse track characteristics and structure of LPSs, we can explore the four regional varieties of South Asian LPSs. This is the third aim of this thesis, which will help in identifying if there are important

differences between these LPS varieties. We can also explore their precipitation contribution to the summer monsoon rainfall as well as the modulation of their genesis by the ISO.

We can then focus on understanding what large-scale conditions control the frequency of LPSs, which is the fourth aim of this thesis. This will help in understanding how large-scale modes of climate variability at intraseasonal (e.g., MJO) and interannual (e.g., ENSO and IOD) time scales influence LPS behaviour by modifying the background state. We can also explore characteristics of downstream LPSs such as their frequency and track characteristics, steering mechanism, evolution of their structure over lifespan and precipitation contribution to the summer monsoon rainfall.

In summary, we will address the following four key questions in this thesis:

1. How skilful are S2S models at predicting LPSs?
2. How well do S2S models simulate the structure of LPSs?
3. What are the differences between the four regional varieties of South Asian LPSs?
4. What large-scale conditions control the frequency of LPSs on the S2S time scale?

1.3 Thesis structure

This thesis is presented as a collection of four working chapters, which were completed during the course of the degree; of these four chapters, three are papers and a summary of their status is given in Table 1.2. These papers are presented in the thesis as close as possible to the form in which they were published. The respective introduction, data and methodology, and conclusions sections of each paper have been altered so as to reduce repetition and build effective connections between chapters of the thesis.

Title	Journal	Submission	Acceptance	Citation
Comparison of the Prediction of Indian Monsoon Low Pressure Systems by Subseasonal-to-Seasonal Prediction Models	<i>WAF</i>	22-05-2020	16-02-2021	Deoras et al. (2021a)
The four regional varieties of South Asian monsoon low-pressure systems and their modulation by tropical intraseasonal variability	<i>Weather</i>	15-12-2020	08-04-2021	Deoras et al. (2021b)
The structure of strong Indian monsoon low-pressure systems in Subseasonal-to-Seasonal prediction models	<i>QJRMS</i>	02-08-2021	26-04-2022	Deoras et al. (2022)

Table 1.2: A summary of the published papers forming contributions to this thesis, ordered by submission date.

In Chapter 2, we will describe various datasets that are used throughout this thesis. We will also describe the feature-tracking algorithm, tracking and post processing, which are used to identify LPSs in the S2S dataset. In Chapter 3 (Deoras et al., 2021a), we will explore various aspects related to predictions of LPSs (i.e., first key question), such as their position and intensity errors, spread-skill relationship, and the evolution of precipitation errors. We will then investigate in detail the simulation of LPS structure (i.e., second key question) in Chapter 4 (Deoras et al., 2022). Partially motivated by the analyses presented in these two chapters, we will explore characteristics of the four regional LPS varieties (i.e., third key question) in Chapter 5 (Deoras et al., 2021b). We will investigate the role of large-scale controls in modulating LPS frequency (i.e., fourth key question) in Chapter 6, before summarising the main findings of this thesis and discussing the avenues for future work in Chapter 7.

Opening remarks

In this short chapter, a broad overview of datasets and methodology, which are used throughout the thesis, is presented. This would prevent a repetition of their description in the later chapters. However, the methodology that is unique to a chapter is retained therein.

2.1 Data overview

2.1.1 The Subseasonal-to-Seasonal prediction project database

As discussed in Section 1.2, a reforecast dataset is an important requirement for the proposed study. Many datasets are available that contain reforecasts from a single model such as the Global Ensemble Forecast System (GEFS; Hamill et al. 2013) or multiple models such as the THORPEX Interactive Grand Global Ensemble (TIGGE; Richardson 2005) and Subseasonal-to-Seasonal (S2S) prediction project (Vitart et al., 2017). For our analysis, it is more beneficial to use a reforecast database containing multiple models than

a single model since an intercomparison of different models is possible in such a case. This could help meteorologists, researchers and flood forecasters in selecting the most skilful model for developing forecast products for stakeholders. Furthermore, a multimodel mean could be computed, which could be used as a benchmark for various comparisons. We did not consider the TIGGE database since it had forecast data from not more than 8 models at the time when our analysis commenced in October 2018. Moreover, models in that database have a maximum forecast lead time of 16 days, which would prevent analysis of LPSs at the S2S time scale.

The S2S prediction project was launched in November 2013 as a joint project between the World Climate Research Programme and World Weather Research Programme (Vitart et al., 2017). Its primary objective is to improve the forecast skill and understanding of the sources of predictability at the S2S time scale, with a special emphasis on high-impact weather events. An important outcome of this project is the development of the S2S database, which can be downloaded from: <https://apps.ecmwf.int/datasets/data/s2s-realtime-instantaneous-accum-ecmf/>. The S2S database consists of near real-time forecasts (with a lag of three weeks) and reforecasts from the following eleven¹ global centres:

- The Bureau of Meteorology, Australia (BoM)
- The China Meteorological Administration (CMA)
- The Météo-France/Centre National de Recherche Meteorologiques (CNRM)
- The Environment and Climate Change Canada (ECCC)
- The European Centre for Medium-Range Weather Forecasts (ECMWF)
- The Hydrometeorological Centre of Russia (HMCR)

¹A new model from the Institute of Atmospheric Physics, Chinese Academy of Sciences was added to the S2S database on 12th September 2021, which was more than two years after we commenced our analysis. Hence, we have not considered this model in any of our analysis.

- The Institute of Atmospheric Sciences and Climate of the National Research Council (ISAC-CNR)
- The Japan Meteorological Agency (JMA)
- The Korea Meteorological Administration (KMA)
- The National Centers for Environmental Prediction (NCEP)
- The Met Office (UKMO)

Tables 2.1 and 2.2 show details related to the configuration of S2S reforecasts. Each reforecast comprises of a control reforecast and a number of perturbed reforecasts that produce ensemble members. Most models feature a coupled ocean component, whereas CNRM, ECCC, ECMWF, KMA, NCEP and UKMO feature a coupled sea-ice component. All S2S reforecasts are archived on a $1.5^\circ \times 1.5^\circ$ grid, except for BoM reforecasts that are archived on a $2.5^\circ \times 2.5^\circ$ grid. All reforecasts are archived at a daily resolution. Some models (e.g., ECMWF) are run in a burst mode² on a subweekly basis, whereas those having a small ensemble size (e.g., NCEP) are run daily. The database has two types of reforecasts: fixed and on-the-fly. For fixed reforecasts, the model version used to produce forecasts is “frozen” for a number of years and reforecasts are then produced once in the lifetime of that model. However, the model version changes frequently, and reforecasts are produced accordingly in on-the-fly configurations. For the analysis, the following model version dates are considered: 31 January 2017 for the JMA model, 8 June 2017 for the ISAC-CNR model and 1 May 2014 for the CMA model. These model versions attempt to advance upon the previous model versions in terms of factors such as ensemble size. For models featuring on-the-fly configuration such as HMCR, ECCC, KMA, ECMWF and UKMO, model versions used in the year 2019 have been considered for maintaining homogeneity.

²In a burst mode, all ensemble members of a model are initialised with conditions on the same start date, but from perturbed initial states. This is intended to sample the uncertainty in observations.

Model	Rfc length (days)	Atmospheric model resolution	Ocean model resolution	Rfc size	Rfc frequency	Intensity threshold
BoM ^c	62	$\sim 2^\circ \times 2^\circ$, L17	$2^\circ \times 0.5^\circ$, L25	33 (3×11)	Six per month	6.16
CMA ^c	60	$\sim 1^\circ \times 1^\circ$, L40	$0.33^\circ \times 1^\circ$, L40	4	Daily	4.97
ECCC	32	$0.45^\circ \times 0.45^\circ$, L40	-	4	Weekly	3.99
ECMWF ^c	46	Tco639: days 0-15 Tco319: after day 15 L91	$1^\circ \times 1^\circ$, L42	11	Two per week	4.16
HMCR	61	$1.1^\circ \times 1.4^\circ$, L28	-	10	Weekly	2.97
ISAC-CNR	32	$0.75^\circ \times 0.56^\circ$, L54	-	5	Every five days	4.43
JMA	33	$\sim 0.5^\circ \times 0.5^\circ$, L100	-	5	Three per month	3.92
KMA ^c	60	$0.83^\circ \times 0.56^\circ$, L85	$0.25^\circ \times 0.25^\circ$, L75	3	Four per month	4.31
CNRM ^c	61	$\sim 0.7^\circ \times 0.7^\circ$, L91	$1^\circ \times 1^\circ$	15	Four per month	3.80
NCEP ^c	44	$\sim 1^\circ \times 1^\circ$, L64	$0.5^\circ \times 0.25^\circ$, L40	4	Daily	4.17
UKMO ^c	60	$\sim 0.5^\circ \times 0.8^\circ$, L85	0.25° , L75	7	Four per month	4.35
ERA-Interim	-	$\sim 0.7^\circ \times 0.7^\circ$, L60	-	-	-	3.97
MERRA-2	-	$\sim 0.63^\circ \times 0.5^\circ$, L72	-	-	-	5.11

Table 2.1: Configuration of reforecasts (Rfc) in the eleven S2S models, ERA-Interim and MERRA-2 reanalysis datasets that are considered in this thesis. The intensity threshold column shows the minimum vorticity (10^{-5} s^{-1}) of strong LPSs (see Section 3.3.3 for details of how this threshold is determined). The relative vorticity is taken from the centre of LPSs at 850 hPa. The coupled atmosphere-ocean S2S models are indicated using a superscript “c” in the column containing model names. The details of ERA-Interim and MERRA-2 reanalysis datasets are also shown, which are used for forecast verification.

For tracking and post-tracking processes (to be discussed in Section 2.2), mean sea-level pressure, u and v winds at 850 hPa and temperature at 925 hPa are used. These variables are instantaneous, once per day (0000 UTC). In addition, total precipitation is used to investigate the simulation of precipitation by S2S models. These variables are accumulated four times per day for all S2S models, except for the BoM model in which they are accumulated once per day. For analysing vertical structure of LPSs in Chapter 4, we use all available pressure levels in the archive, which are: 1000 hPa, 925 hPa, 850

hPa, 700 hPa, 500 hPa, 300 hPa, 200 hPa and 100 hPa.

The S2S models have different reforecast periods, but 1999–2010 is common to all models. As a result, the reforecast period between 1 June and 30 September 1999–2010 is considered.

Model	Data assimilation	Ensemble perturbation
BoM	Nudging from 4D-Var reanalysis	Coupled bred vectors
CMA	3D-Var (oceanic analysis) Nudging (atmospheric analysis)	Adding LAF perturbations to control analysis
ECCC	Mean of EnKF	Mean of EnKF
ECMWF	4D-Var	Singular vectors + adding EDA perturbations to control analysis
HMCR	3D-Var	Breeding perturbations added to control analysis
ISAC-CNR	Direct interpolation of GEFS-NCEP global analyses	Mixed lagged-ensemble technique
JMA	4D-Var	Local Ensemble Transform Kalman Filter + singular vectors
KMA	4D-Var	Stochastic Kinetic Energy Backscatter Scheme, version 2
CNRM	4D-Var	None (in-run perturbations only)
NCEP	Climate Forecast System Reanalysis	Add a small perturbation at each cycle
UKMO	4D-Var	Lagged initialisation

Table 2.2: Summary of data assimilation and ensemble generation methods used in S2S reforecasts. Abbreviations: 4D-Var, 4D variational data assimilation; 3D-Var, 3D variational data assimilation; LAF, lagged average forecasting; EnKF, ensemble Kalman filter; EDA, ensemble data assimilation; GEFS, Global Ensemble Forecasting System.

The S2S database has been used in many studies to understand the predictability of tropical cyclones (e.g., Lee et al. 2020), heat waves (e.g., Ardilouze et al. 2017), and extratropical cyclones (e.g., Zheng et al. 2019). However, one limitation of this database is that the common reforecast period is limited to only 12 years, which prevents model intercomparison over a long period of time. Furthermore, not all atmospheric fields are

available in the database (e.g., vertical velocity), which limits the scope of analysis.

2.1.2 ERA-Interim reanalysis

Atmospheric reanalyses are popular meteorological datasets that are used for analysing past atmospheric conditions. A reanalysis system combines observations from various sources (e.g., satellites, radiosondes and ships) with past short-range weather forecasts using an unchanging data assimilation system for producing a gridded global dataset of several atmospheric variables, which is spatially consistent and has a temporal span of several decades. Thus, atmospheric reanalysis datasets can fill gaps in the historical observational record. Many atmospheric reanalysis datasets are available, including for example: the NCEP’s Climate Forecast System Reanalysis (CFSR; Saha et al. 2010), the Japanese 25-year reanalysis data (JRA-25; Onogi et al. 2005, 2007) and the ECMWF Reanalysis Interim (hereafter ERA-I; Dee et al. 2011). We select ERA-I as the primary dataset for verifying our results since the LPS catalogue (to be discussed in Section 2.1.6) is derived from it.

ERA-I has a horizontal resolution of $\sim 0.7^\circ \times 0.7^\circ$ and a temporal resolution of 6 hours. It can be downloaded from: <https://apps.ecmwf.int/datasets/data/interim-full-daily/>. It covers the period between January 1979 and August 2019, and is available at 37 output pressure levels between 1000 hPa and 0.1 hPa. Observations in ERA-I are assimilated using 4-dimensional variational analysis (4D-Var) with a 12-hour analysis window at 0000 UTC and 1200 UTC. ERA-I is produced using the ECMWF IFS (Cy31r2 version) as the atmospheric model. Further details of atmospheric fields and output pressure levels used in various analyses are provided in the respective chapters.

2.1.3 MERRA-2 reanalysis

An additional reanalysis dataset for forecast verification is essential to account for the observational uncertainty. Furthermore, since the S2S database contains reforecasts from

the ECMWF model, there is a possibility that the verification of the results against ERA-I alone might confer an advantage to this model. Of the available reanalysis datasets, we select the Modern-Era Retrospective analysis for Research and Applications, Version 2 (MERRA-2) dataset (Gelaro et al., 2017) since its spatial resolution of $0.625^\circ \times 0.5^\circ$ (longitude \times latitude) is closest to ERA-I. It can be downloaded from: <https://disc.gsfc.nasa.gov/datasets?project=MERRA-2>. It is available from January 1980 at a temporal resolution of 3 hours. It has 42 output pressure levels between 1000 hPa and 0.1 hPa. Unlike in ERA-I, observations in MERRA-2 are assimilated using a 3-dimensional variational (3D-Var) data assimilation system with a 6-hourly update cycle. It is produced using the Goddard Earth Observing System (GEOS) atmospheric model (Rienecker et al., 2008; Molod et al., 2015).

2.1.4 GPM IMERG

The Global Precipitation Measurement (GPM) Integrated Multi-satellitE Retrievals for GPM (IMERG) is a merged precipitation product that provides precipitation estimates on a $0.1^\circ \times 0.1^\circ$ grid globally every half-hour (Huffman et al., 2015). It can be downloaded from: <https://gpm.nasa.gov/data-access/downloads/gpm>. It combines inter-calibrated observations from satellites in the GPM constellation. It is available from June 2000 in three runs: early, late and final (Tan et al., 2019). We use the final runs of IMERG V06 to investigate precipitation errors in S2S models in Chapter 3, and precipitation contribution of LPSs to summer monsoon rainfall as well as the horizontal structure of precipitation of LPSs tracked in ERA-I and MERRA-2 reanalysis datasets in Chapter 4. The performance of the IMERG V06 precipitation product has not been evaluated so far for the Indian monsoon; however, its previous versions have been intercompared (Wang et al., 2018) and compared with other datasets such as the TRMM Multi-satellite Precipitation Analysis (TMPA) and IMD gauge-based dataset (Liu, 2016; Prakash et al., 2016, 2018) for the 2014 summer season. IMERG shows notable improvements over TMPA in capturing

heavy rainfall over India during the summer season and represents mean-monsoon rainfall more realistically. It must be noted that IMERG has difficulty in detecting rainfall over southeast and northeast India and underestimates the frequency of heavy rainfall over parts of northeast India, which might be due to a sharp gradient in rainfall due to the orography and multi-scale interaction of monsoon systems (Prakash et al., 2018). For analyses in Chapters 3 and 4, IMERG data has been regridded to $1^\circ \times 1^\circ$ to make a fairer comparison with the coarser S2S dataset.

2.1.5 Tropical Rainfall Measuring Mission

Launched in November 1997, the Tropical Rainfall Measuring Mission (TRMM) was a joint mission between the National Aeronautics and Space Administration (NASA) and the Japan Aerospace Exploration Agency (JAXA). The TRMM satellite carried the following instruments: Visible Infrared Radiometer, TRMM Microwave Imager, Precipitation Radar, Cloud and Earth Radiant Energy Sensor, and Lightning Imaging Sensor. Many precipitation retrieval algorithms, such as the TMPA, have been developed using observations from TRMM sensors. The TMPA algorithm combines observations recorded by ground rainfall gauges and satellite-based infrared and microwave sensors. The TRMM 3B42 version 7 product is computed using the TMPA algorithm, and it can be downloaded from: <https://mirador.gsfc.nasa.gov/>. It has a spatial resolution of $0.25^\circ \times 0.25^\circ$ and a temporal resolution of three hours. The data is available between 1998 and 2019 in a latitude band between 50°S and 50°N . Prakash et al. (2015) intercompared many high-resolution precipitation datasets with the gridded rainfall dataset maintained by the IMD. They found that whilst all precipitation datasets, including TRMM 3B42 v7, underestimated the summer monsoon rainfall over India, the underestimation was comparatively smaller in TRMM 3B42 v7 than in others. It outperformed other datasets as well as its predecessor (i.e, TRMM 3B42 version 6) due to the incorporation of additional satellite observations, improved rain gauge analyses and updated algorithms (Prakash et al., 2016).

It must be noted that we have considered GPM IMERG as the observed precipitation dataset for most precipitation analysis in this thesis. However, TRMM 3B42 version 7 is considered in Chapters 5 and 6 to calculate the precipitation contribution of LPSs to summer monsoon rainfall. We did not consider GPM IMERG for this analysis since we followed the precipitation dataset used by Hunt and Fletcher (2019) in order to compare the results. We bilinearly interpolate precipitation in our analyses in Sections 3.6 and 4.4 since the precipitation data is daily and its spatial resolution makes it reasonably smooth for bilinear interpolation.

2.1.6 LPS catalogue

We use an LPS catalogue (Hunt, 2021) for verifying the results in Chapters 3, 4 and 6, and investigating further properties of LPSs in Chapters 5 and 6. In this catalogue, LPSs, which include monsoon low-pressure areas, depressions and deep depressions, are tracked in ERA-I by applying a feature-tracking algorithm (Hunt et al., 2016a, 2018b) on truncated 850 hPa relative vorticity. We retain those LPSs that had their genesis during June–September 1979–2018, since ERA-I data for September 2019 is not available.

2.1.7 Observed SST dataset

We use the National Oceanic and Atmospheric Administration Extended Reconstructed Sea Surface Temperature V5 (ERSST v5; Huang et al. 2017) dataset as the observed SST dataset for computing ENSO and IOD indices, which are used in Chapters 5 and 6. It contains monthly data from January 1854 at a spatial resolution of $2^\circ \times 2^\circ$. It was downloaded from: <https://psl.noaa.gov/data/gridded/data.noaa.ersst.v5.html>. The SST in this dataset is reconstructed using observations from ships, buoys and Argo floats. To account for the observational uncertainty, we compare the ERSSTv5 dataset with the Met Office Hadley Centre Sea Ice and Sea Surface Temperature data set (HadISST; Rayner et al. 2003). It contains monthly data from January 1870 at a spatial

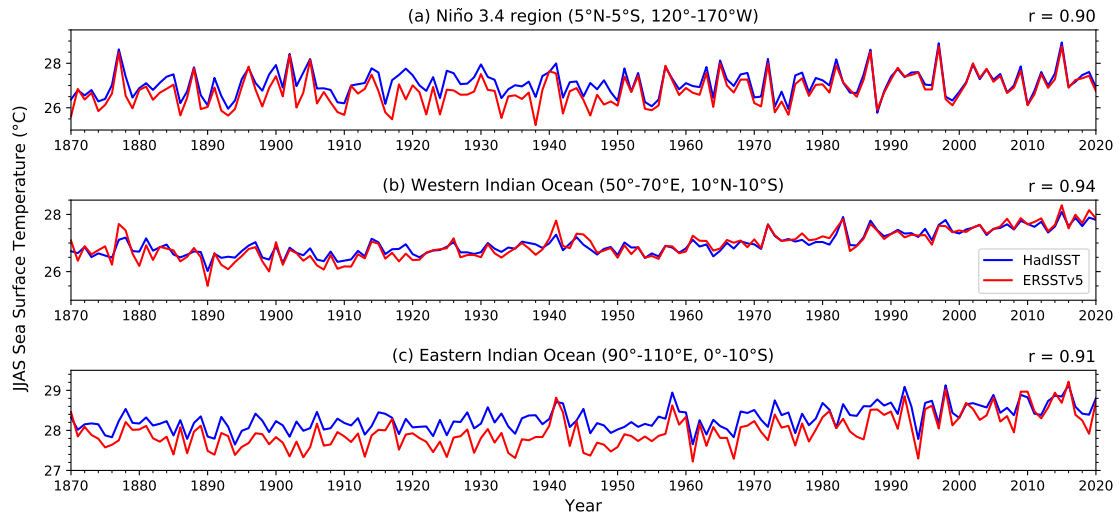


Figure 2.1: Time series showing sea surface temperature (SST) in (a) the Niño 3.4 region, (b) western, and (c) eastern Indian Ocean regions in the NOAA Extended Reconstructed Sea Surface Temperature version 5 (ERSSTv5; red) and the Met Office Hadley Centre Sea Ice and Sea Surface Temperature data set (HadISST; blue) datasets during June–September 1870–2020. The Pearson correlation coefficient between the two time series is also shown in each subfigure.

resolution of $1^\circ \times 1^\circ$. It was downloaded from: <https://www.metoffice.gov.uk/hadobs/hadisst/data/download.html>. It differs from ERSSTv5 since it uses both *in situ* and satellite observations (from the 1980s). Furthermore, the source data for the HadISST dataset includes additional *in situ* observations from the Met Office that are not present in ERSSTv5.

We now compare the mean SST during June–September (JJAS) in the Niño 3.4 region (5°N – 5°S , 120°W – 170°W), western (10°N – 10°S , 50°E – 70°E) and eastern Indian Ocean (0° – 10°S , 90°E – 110°E). Figure 2.1 shows a time series of the SST during JJAS 1870–2020. The two datasets are highly positively correlated for all three regions, with the highest correlation (Pearson correlation coefficient of 0.94) over the western Indian Ocean region. In contrast, the correlation is weaker over the eastern Indian Ocean region, which is more prominent during the pre-satellite era than during the satellite era.

2.1.8 Computing the ENSO and IOD indices

There is an increasing linear trend in SST in the Niño 3.4 region, eastern and western Indian Ocean since around 1950, which is statistically significant at the 95% confidence level (Figure 2.2). The warming trend over the western and eastern Indian Ocean has accelerated since the 1950s (e.g., Ihara et al. 2008). In fact, the western Indian Ocean is warming at a rate faster than any other regions of tropical oceans due to a combination of greenhouse warming, asymmetry in the ENSO teleconnection and more frequent El Niño events during recent decades (Roxy et al., 2014). As a result of this warming trend, El Niño and La Niña events that are defined using a single fixed climatology (e.g., 1971–2000) incorporate longer-term secular or decadal trends, and thus do not reflect true interannual ENSO variability (L’Heureux et al., 2013). Furthermore, the linear trend in the SST in the Niño 3.4 region does not persist across the entire time series shown in Figure 2.2a. Therefore, this warming trend needs to be removed carefully before computing indices. We consider multiple centred 30-year base periods for constructing the SST climatology; this technique is followed by the NOAA Climate Prediction Centre (e.g., Huang et al. 2016) for defining ENSO events. The SST anomalies are calculated for successive 5-year periods. For example, we consider 1936–1965 as the base period for computing SST anomalies during 1950–1955. Similarly, we consider 1941–1970 as the base period for computing SST anomalies during 1956–1960. It must be noted that for years between 2006 and 2021, we use 1991–2010 as the base period since the 1996–2025 climatology does not exist. We follow the same approach for calculating climatologies for the Dipole Mode Index (DMI; Saji et al. 1999). The DMI is the difference between SST anomalies in the tropical western (10°N – 10°S , 50°E – 70°E) and tropical eastern (0° – 10°S , 90°E – 110°E) equatorial Indian Ocean regions. Figure 2.3 shows a comparison of time series of the SST anomaly in the Niño 3.4 region and DMI during June–September 1886–2020. The two indices are highly positively correlated in both SST datasets, with a stronger positive correlation for

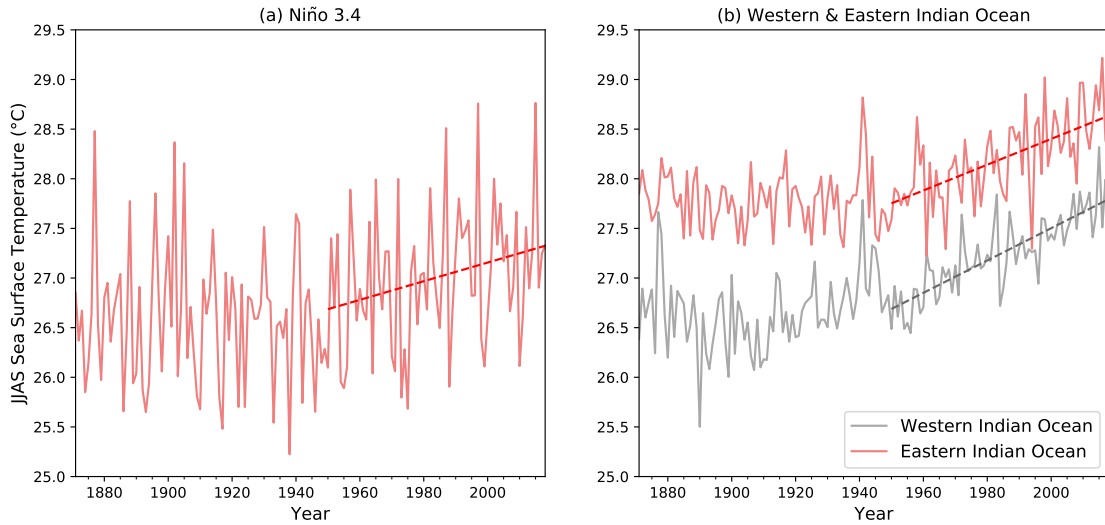


Figure 2.2: Time series of sea surface temperature in (a) Niño 3.4 region and (b) western and eastern Indian Ocean regions during June–September 1870–2020. Dashed red and grey lines show trendlines from 1950 onwards. The SST is derived from the ERSSTv5 dataset.

the Niño 3.4 region and overall better agreement between the two SST datasets after around 1950.

2.2 Tracking and post-tracking processes

In this section, we will discuss the process of identifying LPSs in S2S models and matching them with LPSs identified in ERA-I and MERRA-2 reanalysis datasets.

2.2.1 Tracking algorithm

The identification and tracking of LPSs in all ensemble members of the eleven S2S models have been carried out by applying a feature-tracking algorithm (Hunt et al., 2016a, 2018b) on 850 hPa relative vorticity. It was originally designed to identify LPSs in ERA-I as specified in the IMD classification criteria (see Section 1.1.2). However, we cannot follow the IMD classification criteria since the surface wind field is not available in all S2S models.

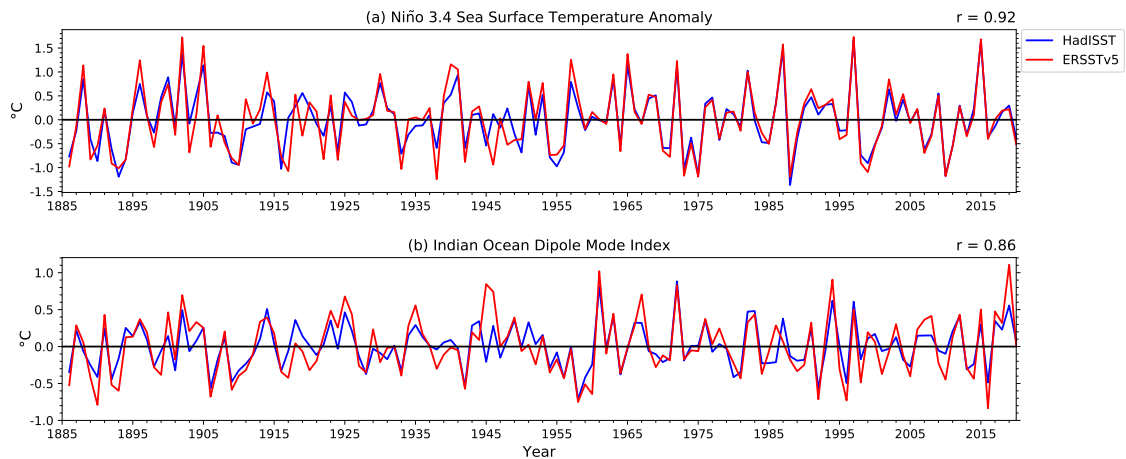


Figure 2.3: Time series showing (a) Niño 3.4 sea surface temperature (SST) anomaly and (b) Indian Ocean Dipole Mode index (DMI) in the ERSSTv5 (red) and HadISST (blue) datasets during June–September 1886–2020. The Pearson correlation coefficient between the two time series is also shown in each subfigure.

We therefore solely focus on using relative vorticity for tracking LPSs. The choice of using vorticity instead of mean sea-level pressure for tracking is justified since the former is less sensitive to the background flow, low-pressure systems are identified at an earlier stage of development and mean sea-level pressure may be sensitive to the interpolation technique and representation of orography in the model (Hoskins and Hodges, 2002). Moreover, production of good quality statistics is possible when vorticity is used since more features are identified (Froude, 2010).

Figure 2.4 shows a schematic of the feature-tracking algorithm. It computes relative vorticity from 24-hourly u and v winds on the 850 hPa level in all ensemble members of the eleven S2S models. In order to filter out small-scale vorticity features that are prevalent near orography, the spectral resolution is truncated at T63 (~ 200 km at the Equator) and all local maxima are located within a radius of 1000 km in the domain 0° – 40° N, 40° E– 120° E. This radius was determined empirically by running the tracking algorithm over several case study dates, following which the combination giving the highest fidelity was selected (Hunt, 2017). For each such local maximum, local positive non-zero values

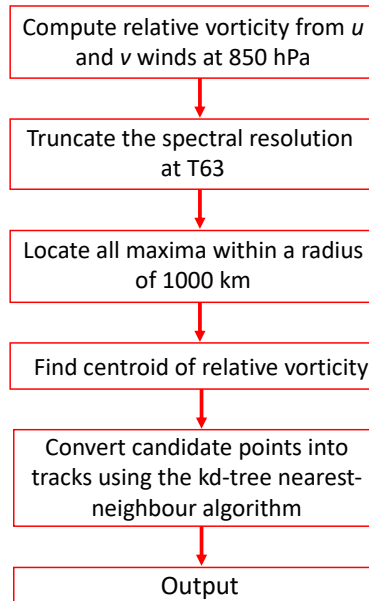


Figure 2.4: A schematic of the feature-tracking algorithm that is used to identify monsoon low-pressure systems.

of relative vorticity are associated and integrated to find the centroid of relative vorticity. For each such point, the nearest neighbour is located and attached using the kd-tree nearest-neighbour algorithm (Yianilos, 1993).

In the tracking algorithm, the minimum 850 hPa relative vorticity threshold was set to $1 \times 10^{-5} \text{ s}^{-1}$, which was useful in filtering out weaker eddies as suggested by (Hunt et al., 2016a). This filtering is essential since without the threshold, a large number of false positives are identified that commonly come from sources such as transient systems near the Himalayan foothills. The threshold value of $1 \times 10^{-5} \text{ s}^{-1}$ is much smaller than the typical peak relative vorticity attained by monsoon depressions and weak monsoon lows (Godbole, 1977; Hunt et al., 2016a). For further analysis, only those tracks that occurred between June and September 1999–2010 and lasted for more than 3 days have been retained. Such tracks are then subjected to a post-tracking filtering process, to be discussed in Sections 2.2.2 and 2.2.3. The feature-tracking algorithm was also applied to the MERRA-2 reanalysis dataset. During June–September 1999–2010, 290 and 281 LPSs

were identified in ERA-I and MERRA-2 reanalysis datasets, respectively. Tracking LPSs at a daily temporal resolution instead of a higher temporal resolution (e.g., 6-hourly) is a challenging task. This is because the process of linking candidate points to form an LPS track could be affected by the low temporal resolution of S2S models. This might result in linking of unrelated candidate points. However, LPSs propagate relatively slowly than other weather systems such as western disturbances, allowing their tracking at a daily temporal resolution.

2.2.2 Temperature-pressure filtering

The output of the feature-tracking algorithm needs to be filtered for further diagnostics since other features, such as tropical cyclones and heat lows, are tracked along with LPSs. In studies related to the tracking of tropical cyclones (TCs), the presence of a warm-core structure in various levels of the troposphere has been used as a criterion to segregate TCs from other tracked features (Camargo and Zebiak, 2002; Camargo, 2013; Camp et al., 2015). Since LPSs have a warm-over-cold core structure (see Section 1.1.2), we focus on track filtering on the basis of temperature anomalies at the 925 hPa level. In addition, the track filtering is done using mean sea-level pressure anomalies, which help in removing those track points featuring non-negative mean sea-level pressure anomalies. Both these anomalies are considered at the centre of the tracked system at each time step. The anomalies have been calculated by following a technique suggested by Vitart (2017), which is now described briefly. The climatologies of 925 hPa temperature and mean sea-level pressure have been constructed by averaging all reforecasts starting the same day and the same month, but excluding the actual year of reforecasts. For example, for a reforecast starting on 1 June 1999, the climatology will contain all reforecasts starting on 1 June 2000–2010. The forecast anomalies are then calculated by subtracting the climatologies from the ensemble member. The threshold value of 925 hPa temperature anomaly was obtained from sensitivity tests conducted for all tracks in all ensemble members of the

eleven S2S models. For illustration purposes, Figure 2.5 shows the result of the sensitivity test for all ensemble members of the BoM model. For each temperature anomaly (δ) in a range, a fraction is calculated (see Figure 2.5a for example), which represents a ratio between the number of track points with a temperature anomaly less than or equal to δ and the total number of track points. Following a similar technique by Hunt and Fletcher (2019), we then calculate the gradient of this fraction (see Figure 2.5b for example), and δ corresponding to the maximum gradient is selected as the threshold value. The maximum gradient is obtained at 0 K and 0.5 K, which is illustrated in Figure 2.5b as a shaded region. We select a threshold value of 0.5 K for all S2S models after noting that the results are not affected by this choice. Thus, an entire track is removed from the tracked dataset if all of its track points have central 925 hPa temperature anomaly greater than or equal to 0.5 K, or non-negative mean sea-level pressure anomaly at the centre. We will use this dataset for our analyses in Chapters 3, 4 and 6. We define strong LPSs (SLPSs) as LPSs whose minimum intensity (central 850 hPa relative vorticity) reaches at least the 75th percentile of the population of all tracked LPSs in the respective S2S model or reanalysis dataset. Since SLPSs have produced more catastrophic impacts in the Indian subcontinent than weaker LPSs such as low-pressure areas (e.g., Hunt and Menon 2020), we consider them for our analysis of S2S models in Chapters 3, 4 and 6.

2.2.3 Matching methodology

After successfully identifying LPSs in all S2S models, we are now interested in matching them with those in reanalysis datasets in order to determine errors in the intensity and position of LPSs in Chapter 3. We follow a technique of spatio-temporal matching in which two tracks are considered to match if they meet certain predefined spatial and temporal separation criteria. Froude et al. (2007a) investigated the sensitivity of track diagnostics to the choice of spatio-temporal matching parameters in the case of extratropical cyclones.

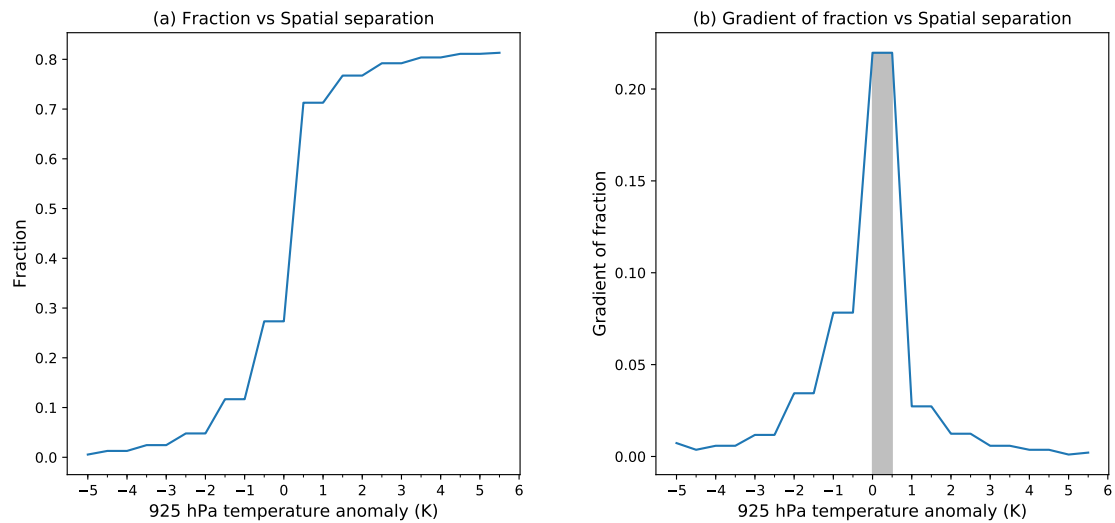


Figure 2.5: Result of the sensitivity test for determining the threshold value of 925 hPa temperature anomaly (K). For each temperature anomaly, the fraction represents a ratio between the number of track points featuring a temperature anomaly less than or equal to this value and the total number of track points. (a) shows the fraction vs 925 hPa temperature anomaly, whereas (b) shows the gradient of fraction vs 925 hPa temperature anomaly. The temperature anomaly is considered at the centre of each track point. Both results are for all ensemble members of the BoM model during June–September 1999–2010. Grey shading in (b) indicates the temperature threshold band of 0–0.5 K.

They found that the diagnostics produced from matched tracks are unaffected in spite of differences in the number of matched tracks that varied with different parametric values.

For our analysis, the threshold values of the spatial separation parameter were identified by sensitivity tests and the gradient technique (similar to the one discussed in Section 2.2.2) conducted for tracks in all ensemble members of the eleven S2S models. Using a technique similar to that employed by Froude et al. (2007b) and Froude (2010), we consider a track in an ensemble member of an S2S model to match with a track in a reanalysis dataset if the spatial separation between the first two data points (i.e., 48 hours) is less than a threshold value α . For illustration purposes, Figure 2.6 shows the result of the sensitivity test for all ensemble members of the UKMO model. The values of α are 600 km for the CNRM model, 200 km for the KMA model and 500 km for the remaining S2S

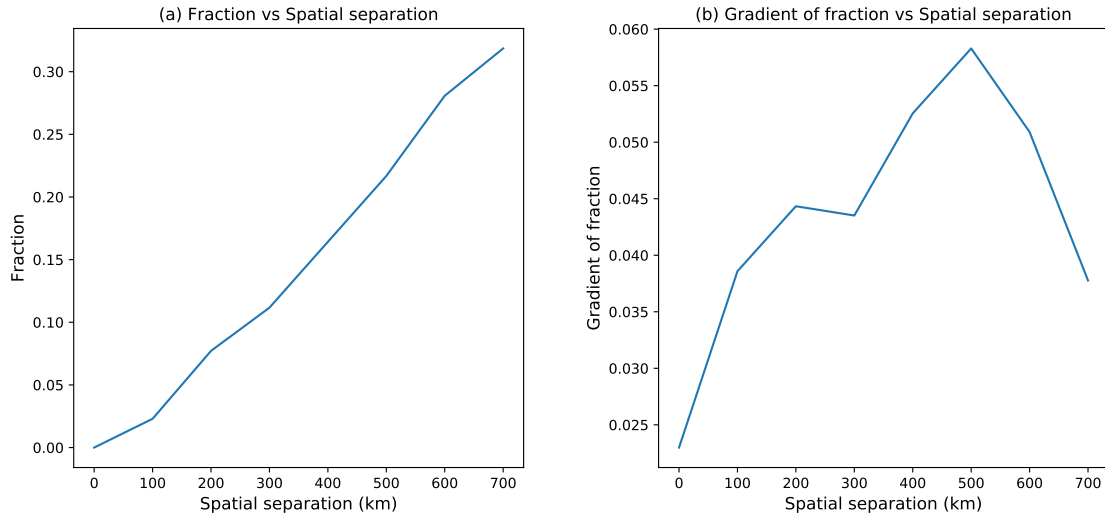


Figure 2.6: Result of the sensitivity test for the matching of LPSs identified in all ensemble members of the UKMO model and ERA-Interim. These LPSs occurred during June–September 1999–2010. The fraction represents a ratio of the number of matched tracks to the total of matched and unmatched tracks. (a) shows the fraction vs spatial separation (α ; km), whereas (b) shows the gradient of fraction vs spatial separation (α). Both results are for a fixed temporal separation of 2 days.

models (see Figure 2.6b for example). The spatial separation is considered for the first two data points instead of the entire track duration since a track in an ensemble member of an S2S model may begin very close to its corresponding track in a reanalysis dataset, but diverge with increasing forecast lead time. If multiple data points of different tracks in an ensemble member of an S2S model satisfy the spatial separation criterion for a track in a reanalysis dataset, the data point with the least temporal separation is chosen. Only those tracks that underwent genesis within the first three days of a reforecast or which existed already at initialisation, have been retained for the analysis of LPS position and intensity errors in Chapter 3. This additional constraint helps in eliminating matches that may have occurred due to chance rather than as a real prediction (Froude et al., 2007b; Hodges and Emerton, 2015). An outline of all steps followed in the post-tracking process is presented in Figure 2.7.

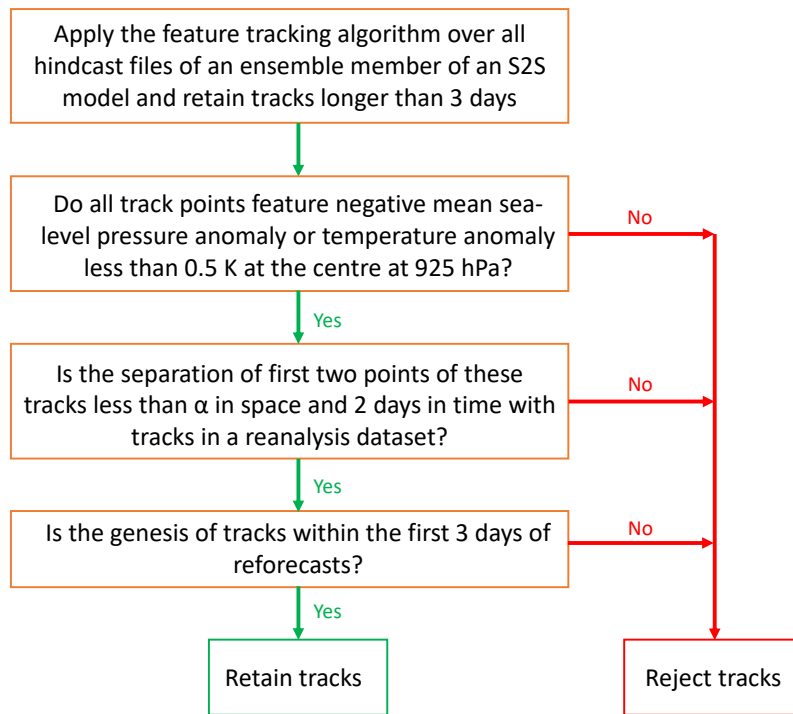


Figure 2.7: Flowchart outlining the steps followed in the matching of LPS tracks identified in an ensemble member of an S2S model with tracks in a reanalysis dataset. These steps are iterated for all ensemble members of the eleven S2S models. The threshold value α is determined for each model by a sensitivity test. This flowchart is adapted from Figure 1 of Deoras et al. (2021a).

CHAPTER 3

COMPARISON OF THE PREDICTION OF INDIAN MONSOON LOW PRESSURE SYSTEMS BY SUBSEASONAL-TO-SEASONAL PREDICTION MODELS

Opening remarks

This chapter was originally published as Deoras et al. (2021a). The published work has been modified for this chapter by modifying Figures 3.1, 3.3, 3.4 and 3.5 and their description in Sections 3.3.1, 3.3.3 and 3.3.4. Some additional analysis on the evaluation of subseasonal probabilistic predictions of genesis of LPSs has been included (Section 3.5). The text has also been modified from that published in the journal paper by adding appropriate cross references to elsewhere in the thesis.

3.1 Introduction

As discussed in Chapter 1, a thorough evaluation of predictions of LPSs is important for improving disaster preparedness and long-term planning in India. However, this has not been the main focus of previous studies that mainly investigated structural and dynamical

aspects of LPSs. Joseph et al. (2015) investigated the large-scale monsoon environment during the 2013 Uttarakhand floods in T126 (~ 100 km) and T382 (~ 38 km) model versions of the Climate Forecast System Version 2 (CFSv2) model. These two model versions could predict the occurrence of the rainfall event 10–12 days in advance, but the observed rainfall amount was underestimated by ~ 35 – 75% , with CFS T382 outperforming CFS T126. The forecasts of heavy precipitation events can improve if models correctly predict the position and intensity of LPSs, which play such an important role in monsoon precipitation.

Unlike for LPSs, many studies have evaluated predictions of tropical cyclones (TCs). Hodges et al. (2017) analysed TCs in six reanalysis datasets and inferred that low spatial resolutions of reanalyses are responsible for an underestimation of the intensity of TCs when compared to observations. Hodges and Emerton (2015) investigated the prediction of TCs in the Northern Hemisphere in the ECMWF ensemble and deterministic prediction systems during May–October 2008–12. They inferred that initial periods during forecasts had smaller error growth, and the location of TCs was more predictable than the intensity. They further inferred that ensemble forecasts are underdispersive—more for the intensity than the location. Murakami (2014) showed that the highest resolution reanalyses are not necessarily the best at simulating properties of TCs, thereby suggesting that the simulation of TCs in reanalyses is also dependent on the model formulation and/or data assimilation. Froude (2010) and Froude (2011) analysed the predictions of extratropical cyclones in both hemispheres in the TIGGE dataset and concluded that the ensemble mean error of individual models of the TIGGE dataset is less than the control and ensemble members of the respective models. The better performance of the ensemble mean than ensemble members is also seen in the prediction of TCs by the ECMWF ensemble and deterministic prediction systems (Hodges and Emerton, 2015). Lee et al. (2018a) studied the prediction of TCs in six S2S models and concluded that most of these models had skill at predicting TC genesis.

In contrast to TCs, LPSs spend a significant duration of their lifetime over land and

their propagation is confined mostly to the monsoon trough region (Godbole, 1977). Thus, the results of TC predictions might not be entirely relevant for LPSs, thereby highlighting the necessity of evaluating LPS predictions. In this chapter, we investigate the prediction of LPSs by the eleven S2S models. For most analyses, the prediction lead time is confined to 15 days, which is within the time scales of numerical weather prediction models. Hence, we carry out deterministic analyses of LPS predictions by considering metrics used for evaluating predictions of TCs and extratropical cyclones on similar time scales (e.g., Froude 2010; Hodges and Emerton 2015). We then evaluate subseasonal probabilistic predictions of genesis of LPSs, for which we consider forecast lead times of up to 32 days (i.e., the maximum common forecast lead time in all S2S models). Our objective is to understand the following aspects:

- How well do S2S models represent the frequency, intensity, tracks, genesis (initial track position) and lysis (final track position) of LPSs?
- How do LPS position and intensity errors evolve with forecast lead time in S2S models?
- How statistically reliable are S2S models at predicting LPSs?
- How accurate and skilful are subseasonal probabilistic predictions of genesis of LPSs and is there a dependence on the ensemble size?
- How do forecast lead time and the presence of LPSs influence the pattern of precipitation errors in S2S models?

3.2 Data and methodology

3.2.1 The S2S database

We outlined the S2S dataset in Section 2.1.1, and do not repeat the description here for brevity. We identify LPSs in all ensemble members of the eleven S2S models using a feature-tracking algorithm. The tracking and post-tracking processes are already described in Sections 2.2.1, 2.2.2 and 2.2.3, and we will not repeat their description here.

3.2.2 Observed datasets

We outlined ERA-I and MERRA-2 reanalysis datasets in Sections 2.1.2 and 2.1.3, respectively, and do not repeat the discussion here for brevity. For the purpose of verification, we use an LPS catalogue that is described in Section 2.1.6. In this catalogue, LPSs are identified in ERA-I. For identifying LPSs in MERRA-2, we apply the feature-tracking algorithm (see Section 2.2.1) to 850 hPa u and v winds. We also use a catalogue of LPSs (Vishnu et al., 2020b) identified in the ECMWF Reanalysis version 5 (ERA5; Hersbach et al. 2020) to intercompare some results in this chapter. In this catalogue, LPSs were identified using an automated Lagrangian pointwise feature tracker, TempestExtremes (Ullrich and Zarzycki, 2017); its full description is provided by Vishnu et al. (2020a). A full description of GPM IMERG is given in Section 2.1.4, and will not be repeated here. For the analysis in this chapter, IMERG data has been regridded to $1^\circ \times 1^\circ$ to make a fairer comparison with the coarser S2S dataset.

3.3 Climatology of LPSs

In this section, we present the verification results related to seasonal average numbers, intensity distribution, tracks, genesis and lysis density of LPSs.

3.3.1 Seasonal numbers

The seasonal average numbers of LPSs in all ensemble members of the eleven S2S models, MERRA-2, ERA5 and ERA-I during June–September 1999–2010 are shown in Figure 3.1 along with the multimodel mean (MMM), for forecast lead times of less than 15 days. We calculate the MMM in this thesis by assigning equal weight to each S2S model. The S2S models exhibit a prominent spread in the simulated frequency of LPSs, ranging from 9 (± 0.56) per season in the BoM model to 18 (± 1.20) in the NCEP model. Compared to 23.83 (± 3.26) and 23.42 (± 4.41) LPSs simulated per season by ERA-I and MERRA-2 respectively, all S2S models under-simulate the frequency, with only 14.81 (± 0.99) LPSs per season in the MMM. The range in brackets indicate one standard deviation about the seasonal average numbers of LPSs calculated across 1999–2010. The simulated LPS frequency by the MMM is almost similar to ERA-5 (15.42), and the ECCO, ECMWF, CMA, CNRM and NCEP models simulate a larger frequency of LPSs than ERA5. The low frequency of LPSs simulated by models such as BoM could be related to a weak and poorly defined monsoon trough, which provides cyclonic vorticity in the lower-troposphere to spin-up LPSs (Godbole, 1977). In addition, the frequency is also dependent on intraseasonal oscillations such as the BSISO (Kikuchi and Wang, 2010). However, this investigation is beyond the scope of this thesis.

3.3.2 Intensity distribution

The probability density of intensity (850 hPa relative vorticity) of LPSs in all ensemble members of the eleven S2S models, MMM, ERA-I and MERRA-2 is shown in Figure 3.2. The intensity is considered at the centre of each track at each lead time (up to 15 days) since the maximum relative vorticity is observed at the centre of LPSs in the lower troposphere (Godbole, 1977). Gaussian kernel density estimation, which is a non-parametric way to estimate the probability density function using Gaussian kernels (Scott,

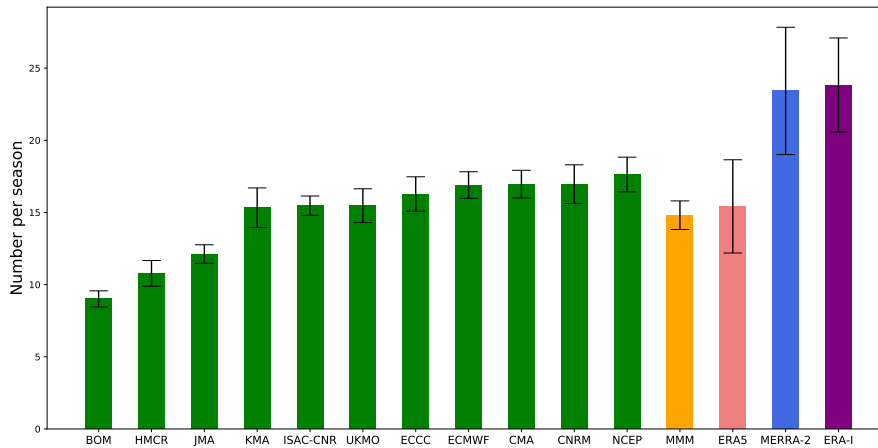


Figure 3.1: Seasonal average numbers of monsoon low-pressure systems in all ensemble members of the eleven S2S models (green), MERRA-2 (royal blue), ERA5 (light coral) and ERA-Interim (purple) over the period June–September 1999–2010. The multimodel mean (MMM) is also shown (orange). Error bars show ± 1 standard deviation about the mean and calculated across years. Model results are normalised with respect to ensemble size and reforecast frequency. Forecast lead times of 0–15 days are considered for each model.

2015), is also shown for comparison. Differences in the intensity distribution of LPSs can be found among different S2S models; however, in all these models and the MMM (Figure 3.2l), the highest probability density is observed for intensity in the range $2\text{--}3 \times 10^{-5} \text{ s}^{-1}$, which is in agreement with ERA-I (Figure 3.2m). This result was anticipated since not all LPSs intensify into stronger systems such as monsoon depressions. For all S2S models except the BoM model, the probability density of track points featuring intensity more than $3 \times 10^{-5} \text{ s}^{-1}$ decreases rapidly, which is also seen in ERA-I, but not in MERRA-2. The highest probability density in MERRA-2 is seen for the intensity in the range $3\text{--}4 \times 10^{-5} \text{ s}^{-1}$, following which there is a rapid decline in the probability density. For the BoM and CMA models (Figures 3.2a and 3.2e respectively), the probability density of track points featuring intensity greater than or equal to $6 \times 10^{-5} \text{ s}^{-1}$ is larger than ERA-I, but equal to MERRA-2 up to $8 \times 10^{-5} \text{ s}^{-1}$. It must be noted that unlike ERA-I, all S2S models and MERRA-2 have a noticeably smaller probability density of track points

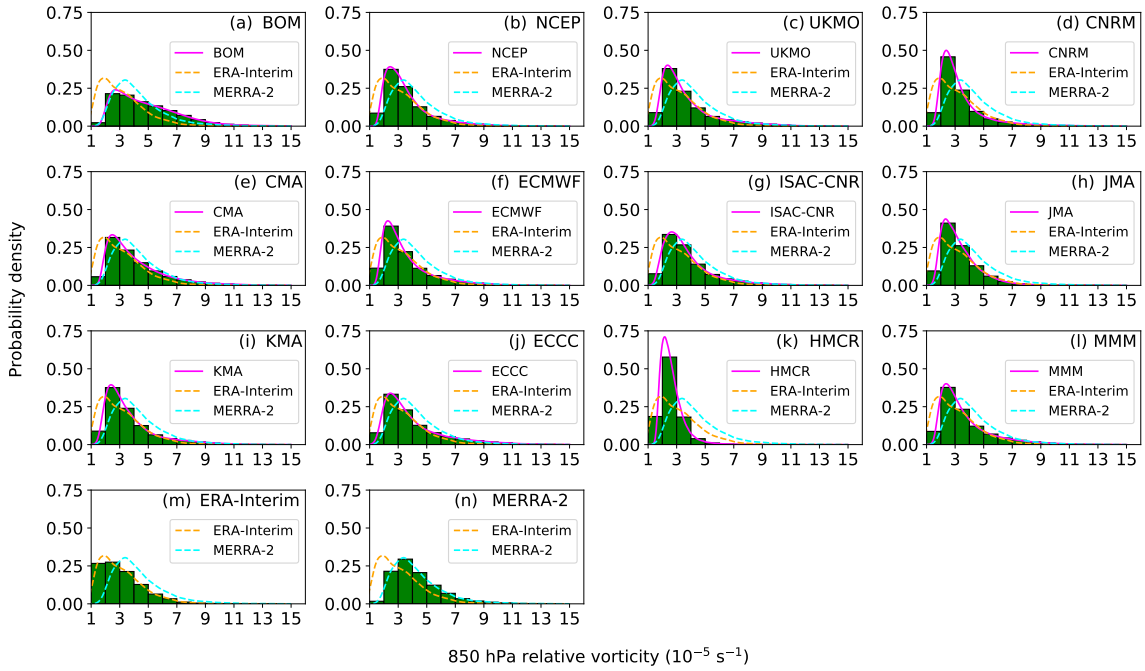


Figure 3.2: Normalised histograms (green) of 850 hPa relative vorticity of monsoon low-pressure systems calculated at each track point in all ensemble members of the eleven S2S models (a–k), ERA-Interim (m) and MERRA-2 (n) during June–September 1999–2010. The multimodel mean (MMM) is shown (l). Kernel density estimations using Gaussian kernels are also shown for respective individual models and MMM (solid magenta), ERA-Interim (dashed orange) and MERRA-2 (dashed cyan). Histograms are normalised with respect to ensemble size and reforecast frequency. Forecast lead times of 0–15 days are considered for each model.

featuring intensity in the range $1\text{--}2 \times 10^{-5} \text{ s}^{-1}$ than $2\text{--}3 \times 10^{-5} \text{ s}^{-1}$. This discrepancy is due to a greater genesis of weaker LPSs in ERA-I than in S2S models and MERRA-2. In addition, LPSs in ERA-I have shorter lifetime than in S2S models and MERRA-2.

3.3.3 Track density

As discussed in Section 2.2.2, among monsoon low-pressure areas and strong LPSs (SLPSs) such as monsoon depressions, the latter are known to have produced more catastrophic impacts in the Indian subcontinent than the former (e.g., Hunt and Menon 2020). Thus, it is essential to understand how S2S models represent transits of SLPSs and how they

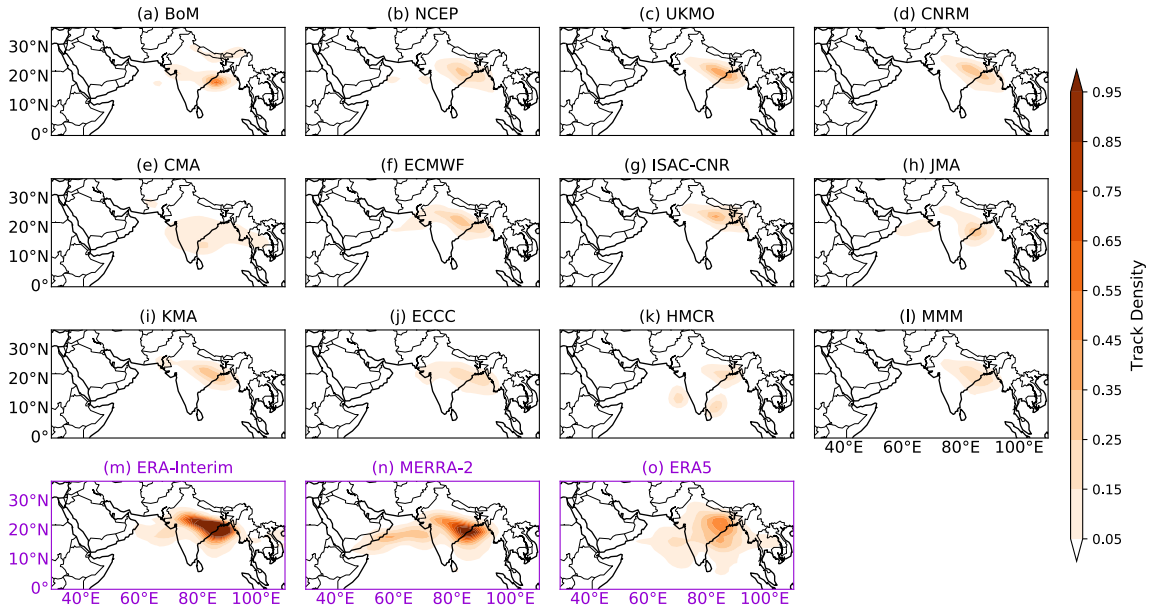


Figure 3.3: Track density of strong monsoon low-pressure systems (minimum intensity equal to the upper quartile in each model) tracked in all ensemble members of the eleven S2S models (a–k), ERA-Interim (m), MERRA-2 (n), and ERA5 (o) over the period June–September 1999–2010. Forecast lead times of 0–15 days are considered in S2S models. The track density is calculated using a kernel density estimation technique. The unit of track density is the number of SLPSs per $1.5^\circ \times 1.5^\circ$ for June–September 1999–2010. The multimodel mean (MMM) track density is also shown (l). Model results are normalised with respect to ensemble size and reforecast frequency.

differ from those in reanalyses. We define SLPSs as LPSs with minimum central 850 hPa relative vorticity greater than or equal to the third quartile of 850 hPa relative vorticity of all LPSs in an individual S2S model (or reanalysis). The threshold intensity values for S2S models, MERRA-2 and ERA-I were provided in Table 2.1. The track density of SLPSs is calculated by a kernel density estimation (KDE) technique (Bowman and Azzalini, 1999) and 2D Gaussian kernels are used. The KDE is a non-parametric method for constructing a smooth probability density estimate of an observed data, and it has been used to calculate the track density of tropical cyclones over the north Indian Ocean (e.g., Wahiduzzaman and Yeasmin 2020). The smoothing parameter is determined automatically using Scott’s rule for bandwidth selection. We first construct a smooth probability density estimate

for the centre of an LPS track at each time step. This process is iterated for all LPSs. We then multiply probability density estimates by the total number of LPSs to get the track density. The results are normalised with respect to ensemble size and reforecast frequency, similar to the methods used in Camp et al. (2015) and Lee et al. (2018a). All eleven S2S models are capable of simulating tracks of SLPSs over the head of the Bay of Bengal region and adjoining land area (Figures 3.3a–k), but their track density is smaller than in reanalyses, agreeing with the frequency result (Figure 3.1). The NCEP, UKMO, CNRM, ECMWF and KMA models perform better than other S2S models, and have their largest track density over the BoB, similar to ERA-I and MERRA-2. Tracks over these regions are also observed in the MMM (Figure 3.3l), which agrees with reanalyses. In the BoM (Figure 3.3a) and JMA (Figure 3.3h) models, SLPS tracks occur further south than in reanalyses, whereas in CMA, the track direction is westward as a result of easterly mid-tropospheric steering winds over the head Bay of Bengal region and central India (not shown). In the HMCR model, tracks over west-central India are not observed due to faster lysis (thus weaker intensity) of SLPSs and their low count. We find a greater number of SLPSs over the Arabian Sea in MERRA-2 than in other reanalyses as well as S2S models. In ERA5, the frequency of SLPSs propagating towards central India is smaller than in ERA-I and MERRA-2, and the track density over the BoB in MERRA-2 is smaller than in ERA-I.

We match ERA-I tracks with those in MERRA-2 using a spatiotemporal matching technique suggested by Hodges et al. (2003). A track in ERA-I matches with a track in MERRA-2 if the mean separation distance between them during the overlapping period is less than 4° (geodesic). Moreover, the temporal overlap criterion needs to be satisfied for at least 50% of the lifespan. We find that 57% of the total tracks in ERA-I match with those in MERRA-2. These differences in track densities between ERA-I and MERRA-2 could be due to factors such as differences in numerical weather prediction models, data assimilation schemes, and observations available for assimilation, as outlined in Sections

2.1.2 and 2.1.3. Thus, S2S models exhibit regional biases in simulating tracks of SLPSs, but the performance of the MMM is good in general.

3.3.4 Genesis and lysis

In this subsection, genesis and lysis locations of SLPSs are examined. Figures 3.4 and 3.5 show genesis and lysis densities of SLPSs, respectively, which have been calculated by following the same process discussed in the previous subsection. Most S2S models correctly represent the primary genesis region over the head of the Bay of Bengal and adjoining land area, which is also represented in the MMM (Figure 3.4). A secondary genesis region over the eastern Arabian Sea and the west coast of India is visible in some models such as ECCC, JMA and HMCR. As discussed in the previous subsection, there are more LPSs over the Arabian Sea in MERRA-2 than in ERA-I. ERA5 features smaller genesis density than ERA-I and MERRA-2.

In terms of lysis, most S2S models including the MMM (Figure 3.5) represent the primary lysis region over east India and the secondary lysis region over parts of western and central India. Similar to the track density and genesis density, all S2S models feature a smaller lysis density than ERA-I and MERRA-2. Thus, S2S models do a good job in general at simulating the primary genesis, primary lysis and secondary lysis regions.

3.4 The skill of LPS prediction

In this section, we discuss the relative skill of ensemble members, the spatial distribution of position errors, control and ensemble mean error, and the ensemble spread-error relationship.

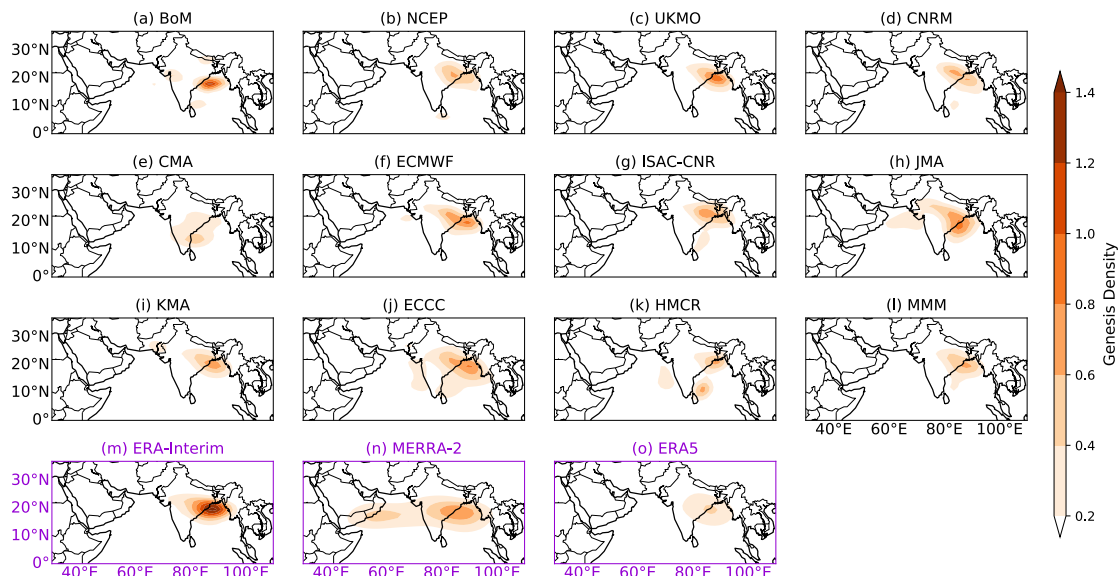


Figure 3.4: As in Fig. 3.3, but for genesis density. Note the different contour interval.

3.4.1 Relative skill of ensemble members

In this subsection, the relative skill of all ensemble members of the eleven S2S models at predicting the position and intensity of LPSs is examined. To calculate the position error, the geodesic separation distance between each pair of matched tracks at each lead time is considered during lead times of 0–15 days. The process of matching is already discussed in Section 2.2.3.

Figures 3.6a and 3.6d show the number of track points in S2S models that match with those in ERA-I and MERRA-2 respectively. These track points have been included in the statistics discussed in this subsection as well as Sections 3.4.3 and 3.4.4. The MMM is also shown. The results are normalised with respect to ensemble size and reforecast frequency. The number of data points decreases with an increase in lead time due to the lysis of LPSs. This decrease is rapid in many models after 4 days since only those LPSs, which had their genesis within the first 3 days of reforecasts or existed already at initialisation, have been considered (see Section 2.2.3).

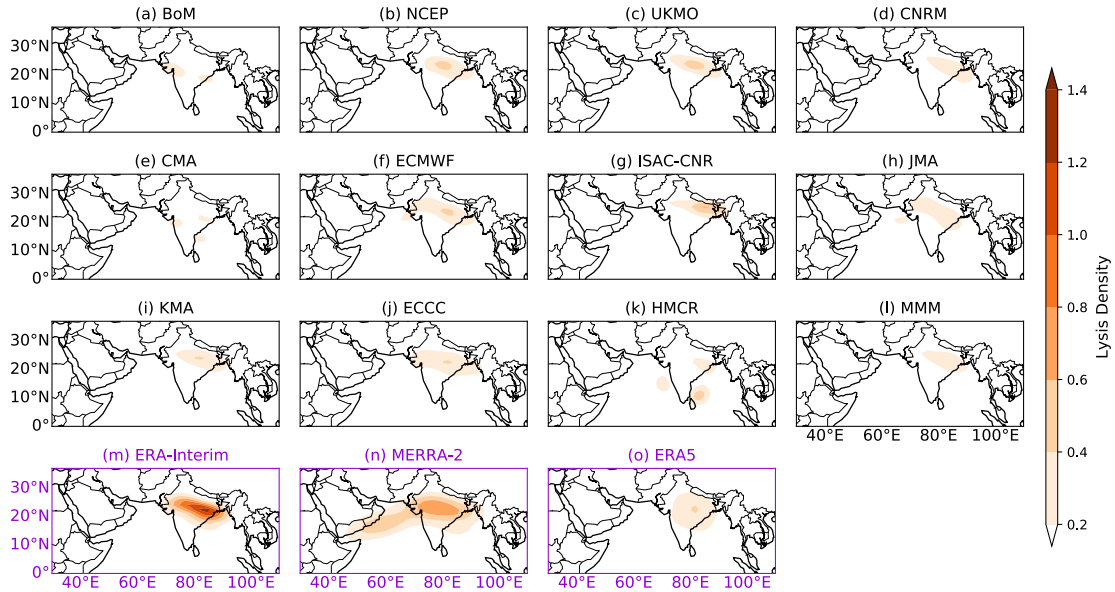


Figure 3.5: As in Fig. 3.3, but for lysis density. Note the different contour interval.

Figure 3.6b (3.6e) shows the position error of LPSs for all ensemble members of the eleven S2S models when matched with ERA-I (MERRA-2), whereas Figure 3.7 shows these position errors for each model separately when LPSs are matched with ERA-I. The position error increases with lead time in all models as well as the MMM, and this result is independent of the choice of the reanalysis dataset. In addition, there are differences in the skill of S2S models. When ERA-I is used for verification (Figure 3.6b), the CMA model has the lowest skill (the largest position error) for all lead times, whereas the ECCC, UKMO, JMA and KMA models have higher skill (smaller position error) than most S2S models. The CMA model has ~ 3 days less skill than among the best performing models such as UKMO. At 6 days, the position error in the CMA model is 1000 km, which becomes ~ 1600 km by 15 days lead time. The large position error in this model can be understood from the bias that leads to the westward propagation of LPSs (such as SLPSs in Figure 3.3e) instead of the observed west-northwest propagation in ERA-I (Figure 3.3m) and MERRA-2 (Figure 3.3n). The small position errors in the UKMO, JMA and KMA models and the large position error in the CMA model are also seen when

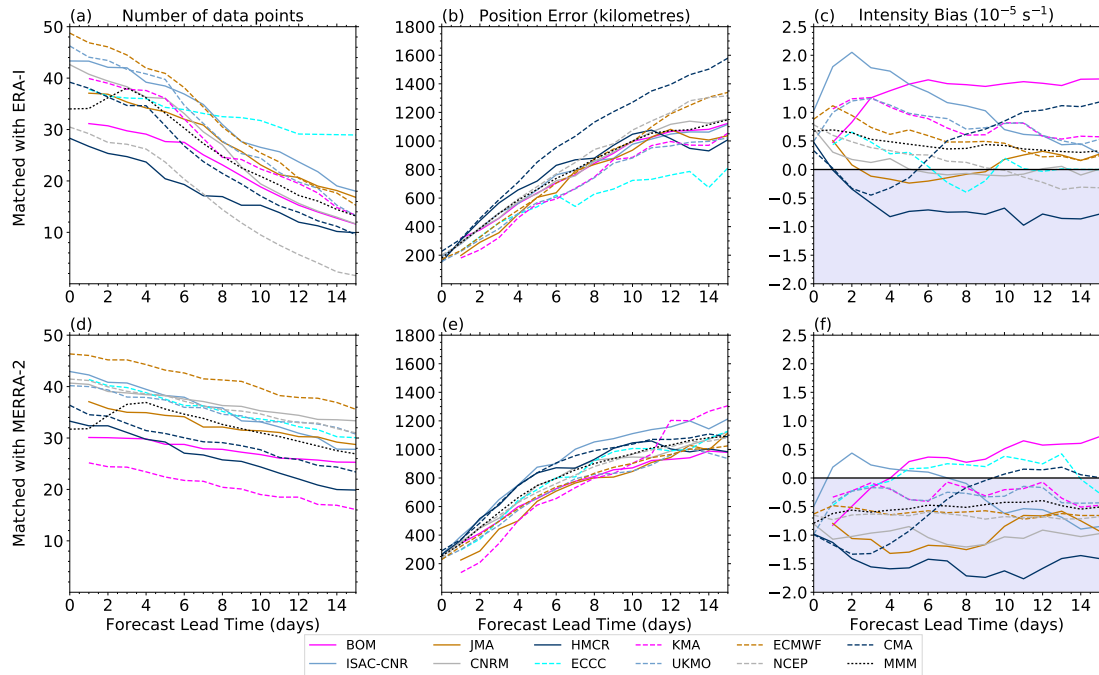


Figure 3.6: (a) The number of data points of tracks matched with ERA-I which are included in the statistics for Figures 3.6b, 3.6c, 3.10 and 3.11 as a function of forecast lead time (days). The results are normalised with respect to ensemble size and reforecast frequency. (b) Error in the position of monsoon low-pressure systems (kilometres) as a function of forecast lead time (days); (c) Bias in the intensity (10^{-5} s^{-1}) of monsoon low-pressure systems as a function of forecast lead time (days). The shaded region indicates negative bias in the intensity. These results are calculated for all ensemble members of the eleven S2S models. The multimodel mean is also shown in dotted black in each subplot. (d)–(f) show (a)–(c), but for tracks matched with MERRA-2. Output from step 0 is not available for the BoM, JMA, KMA and ECCC models in all subplots.

LPSs are matched with MERRA-2 (Figure 3.6e). However, the magnitude of the error in the CMA model is smaller as a result of a greater number of westward moving LPSs in MERRA-2 than in ERA-I. It must be noted that the range of the position error in the MMM is very similar in both verification results.

Figure 3.6c (3.6f) shows biases in the intensity of LPSs for all ensemble members of S2S models when matched with ERA-I (MERRA-2), whereas Figure 3.8 shows biases for each model separately when LPSs are matched with ERA-I. Similar to the position error, differences can be seen in the skill of S2S models; when LPSs are matched with ERA-I,

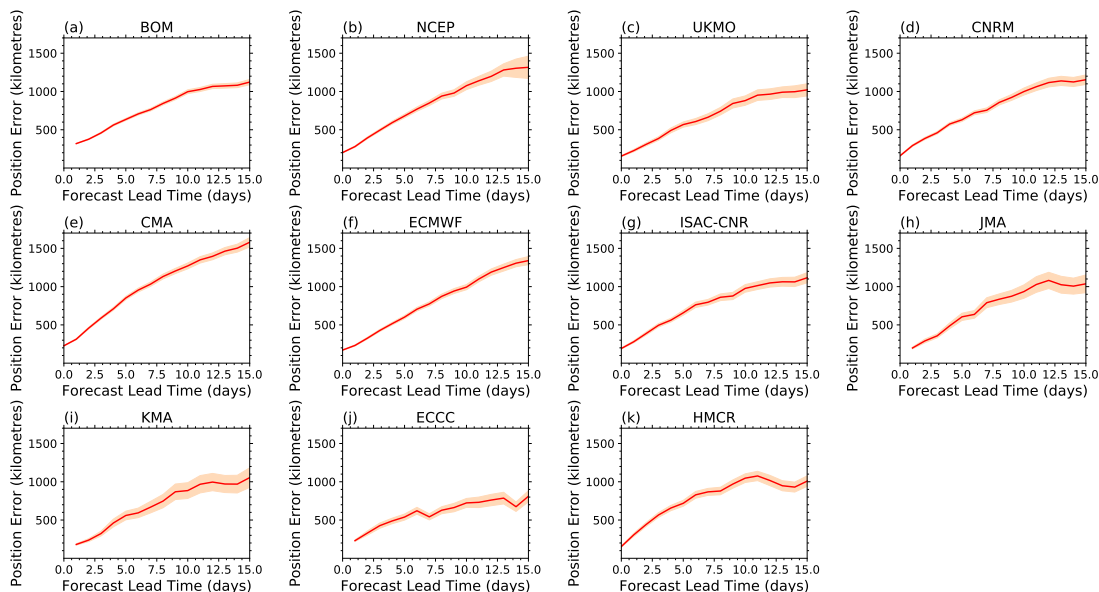


Figure 3.7: As in Fig. 3.6b, but position errors are shown separately for the eleven S2S models. The transparent shaded regions indicate the 95% confidence intervals for the mean position errors, which are computed from the standard errors. Output from step 0 is not available for the BoM, JMA, KMA, and ECCC models.

many models, including the MMM, overestimate the intensity of LPSs at all lead times, except for the HMCR model which underestimates the intensity beyond lead times of 1 day. The intensity bias is the smallest at most lead times for the JMA and CNRM models, whereas models such as BoM and HMCR exhibit the largest bias. A rapid increase in the bias can be observed in the HMCR, BoM and ISAC-CNR models at shorter lead times. However, when LPSs are matched with MERRA-2, most models including the MMM underestimate the intensity of LPSs at all lead times, except for models such as BoM and ISAC-CNR. This underestimation is a consequence of stronger LPSs in MERRA-2 than in ERA-I. It must be noted that the HMCR (BoM) model exhibits the largest negative (positive) intensity bias in both verification results and the overall pattern of biases among most models show consistency. These results suggest that using ERA-I for verification does not give an advantage to the ECMWF model since the latter does not exhibit the lowest position error and intensity bias when verified against both reanalysis

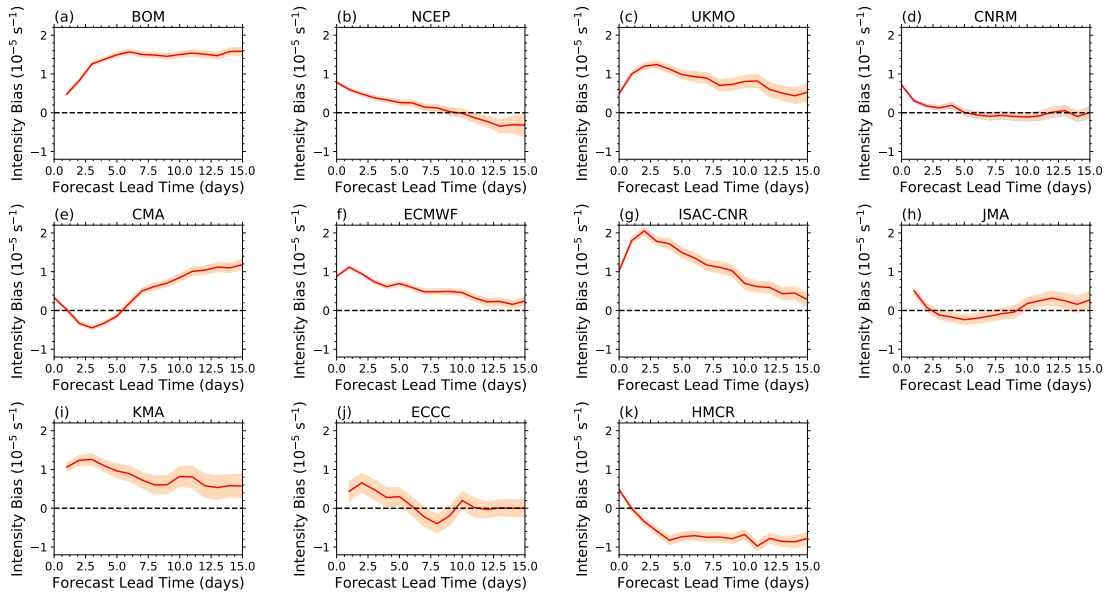


Figure 3.8: As in Fig. 3.6c, but intensity biases are shown separately for the eleven S2S models. The transparent shaded regions indicate the 95% confidence intervals for the mean intensity errors, which are computed from the standard errors. Output from step 0 is not available for the BoM, JMA, KMA, and ECCC models.

datasets. This contrasts with the findings of Froude (2010) and Froude (2011) in which verification of the results against ECMWF analysis was considered to be a reason for the best performance of the TIGGE-ECMWF model. The bias cannot be calculated for the position error since this error is positive.

3.4.2 Spatial distribution of position errors

In this subsection, we investigate how forecast lead time influences the spatial distribution of position errors of LPSs in the eleven S2S models. Figure 3.9 shows the difference in position errors of LPSs that match with those in ERA-I between lead times 0 to 3 days and 12 to 15 days in the eleven S2S models. The MMM is also shown (Figure 3.9l). The difference is calculated by subtracting position errors during 0 to 3-day lead times from 12 to 15-day lead times. The results confirm that position errors increase with forecast lead time over most of the domain in all S2S models, which is in agreement with Figure

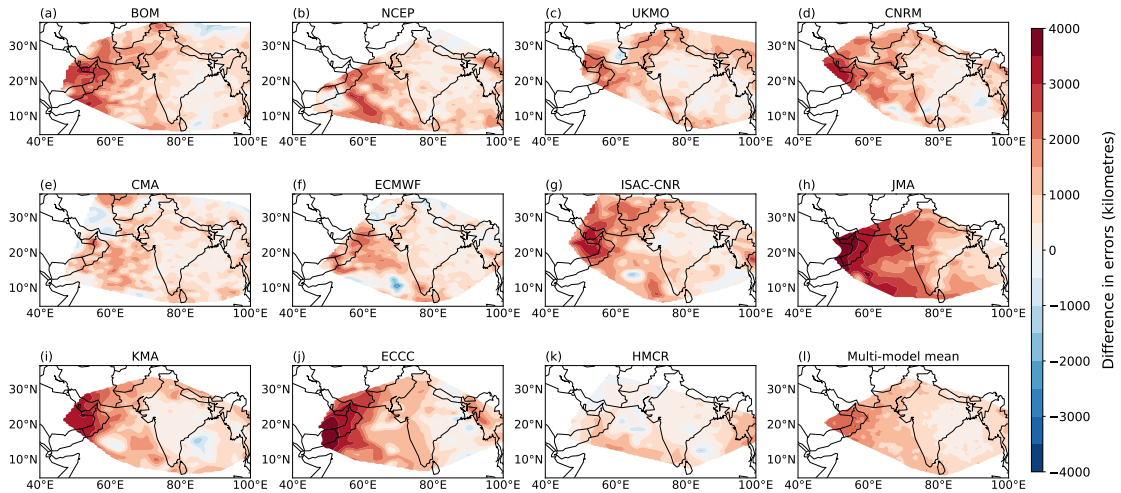


Figure 3.9: Difference in the position error (kilometres) of monsoon low-pressure systems between lead times 0 to 3 days and 12 to 15 days in the eleven S2S models (a–k). The difference is calculated by subtracting the position errors during 0 to 3 days lead times from 12 to 15 days lead times for tracks matched with ERA-I. The multimodel mean of the difference in the position error is also shown (l).

3.6b. The HMCR model (Figure 3.9k) outperforms the MMM (Figure 3.9l) for difference in the position error. In all models and the MMM, position errors are larger over the Arabian Sea than over the Bay of Bengal at lead times of more than 12 days. However, large position errors over the Arabian Sea are not seen when MERRA-2 is considered for verification (not shown). A greater number of LPSs, which have their genesis over the Arabian Sea, are tracked in MERRA-2 than in ERA-I. In addition, LPSs reaching the Arabian Sea from the Bay of Bengal have a longer lifespan (and thus persist to longer lead times) than those having their genesis over the Arabian Sea. These factors reduce the position error over the Arabian Sea in MERRA-2.

3.4.3 Control and ensemble mean error

An important advantage of an ensemble prediction system (EPS) is that an ensemble mean provides a superior forecast compared to a control since the process of averaging removes

the less predictable spatial scales (Leith, 1974; Toth and Kalnay, 1993, 1997; Hodges and Emerton, 2015). In this subsection, the skill of the ensemble mean at predicting the position and intensity of LPSs is compared with the control forecast for the eleven S2S models. The ensemble mean error for an EPS is calculated by first computing ensemble mean tracks of all LPSs in ensemble members that match LPSs in ERA-I. For an EPS, the number of ensemble members that have matching tracks and the length of such tracks in each ensemble member vary for different LPSs. In previous studies examining the prediction skill of EPSs, the tracks considered were those which were present in at least five ensemble members (Froude et al., 2007b; Froude, 2010, 2011). Since several S2S models have at most five ensemble members (see Table 2.1), we consider only those tracks in this diagnostic that are present in at least two ensemble members. For an LPS, the mean position error in an EPS is calculated as the mean geodesic separation distance between the ensemble mean track and its corresponding matched track in ERA-I at each lead time. This process is iterated for all LPSs in the eleven S2S models to obtain ensemble mean errors for all S2S models. It must be noted that for the BoM model, the mean of the control errors is considered since the EPS consists of three model versions and thus three control runs.

Figures 3.10 and 3.11 show ensemble mean error, control error and ensemble spread in LPS position and intensity, respectively, in all S2S models when LPSs are matched with those in ERA-I. Similar analyses are carried out using MERRA-2 (not shown). The ensemble spread will be discussed in the following subsection. For the position error, the ensemble mean provides an advantage over the control (i.e., the ensemble mean error is less than the control error) for most S2S models; however, it provides very little advantage in the KMA model (Figure 3.10i) at lead times greater than 10 days. These results are similar when MERRA-2 is used for verification—the ensemble mean in most models provides an advantage over the control run, but the difference between them is smaller than in ERA-I.

For the LPS intensity, the ensemble mean provides a little advantage over the control

run for some S2S models such as NCEP (Figure 3.11b), UKMO (Figure 3.11c), CMA (Figure 3.11e) and ECMWF (Figure 3.11f) when ERA-I is considered. It does not provide any distinct advantage for the JMA model (Figure 3.11h). However, the ensemble mean in most models provides greater advantage over the control run when MERRA-2 is considered for verification instead of ERA-I. Thus, the ensemble mean is more advantageous over the control forecast for the intensity of LPSs than their position when MERRA-2 is considered for verification. This result agrees with the findings of Froude (2010) and Froude (2011) for extratropical cyclones in the TIGGE dataset. It must be noted that the multimodel mean provides an advantage over the multimodel control for the position and intensity of LPSs when verified against ERA-I and MERRA-2.

3.4.4 Ensemble spread-error relationship

To ascertain the reliability of S2S models at predicting the position and intensity of LPSs, the ensemble-spread error relationship is investigated. For a statistically reliable EPS, the ensemble spread should be equal to the ensemble mean error (Froude, 2010). This means that the ensemble spread should be able to cover all possible forecast outcomes and predict the forecast error (Leutbecher and Palmer, 2008; Hopson, 2014). However, EPSs tend to display underdispersion since not all sources of forecast uncertainties related to initial conditions and model errors are simulated (Buizza et al., 2005).

In this chapter, the ensemble spread for an LPS in a S2S model is calculated as the mean geodesic separation distance between the ensemble mean track and corresponding ensemble member tracks at each lead time. The ensemble spread for all S2S models is then calculated by repeating the process for all matched LPSs in all S2S models. For the position of LPSs (Figure 3.10), the BoM (Figure 3.10a), NCEP (Figure 3.10b), UKMO (Figure 3.10c) and ECMWF (Figure 3.10f) models have the best ensemble spread-error relationship (i.e., the curves showing the ensemble spread and ensemble mean error are the closest to each other) when ERA-I is used for verification. The other S2S models

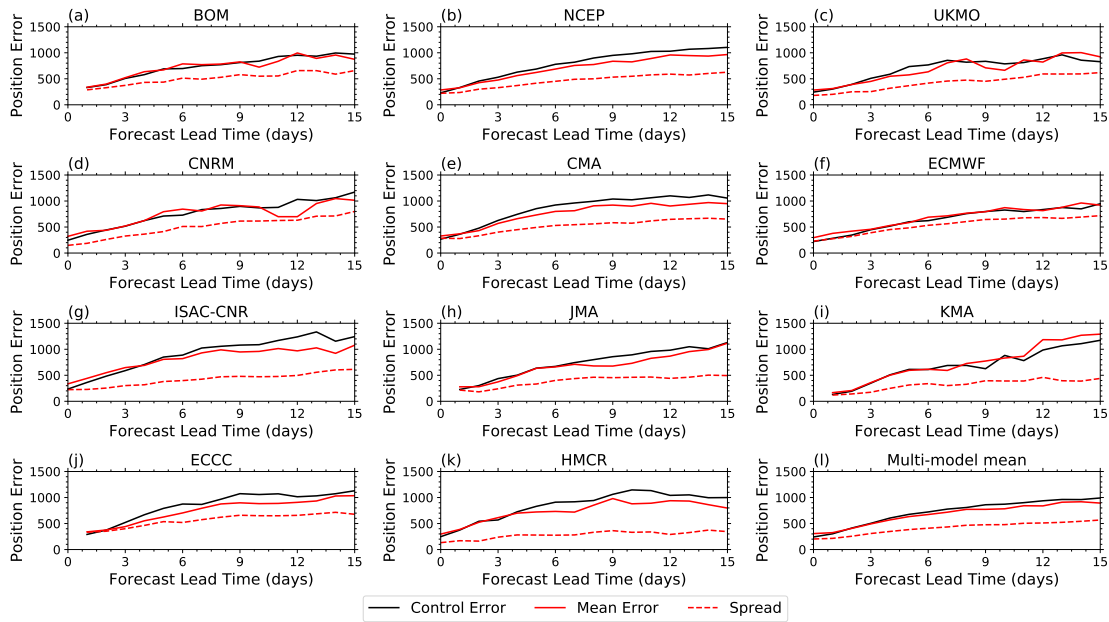


Figure 3.10: Ensemble mean error (solid red), control forecast error (solid black), and spread (dashed red) in the position of monsoon low-pressure systems in the eleven S2S models (a–k) and the multimodel mean (l). Errors and spread are calculated with respect to ERA-Interim. The unit of position error is kilometres. Output from step 0 is not available for the BoM, JMA, KMA and ECCC models.

are underdispersive to varying degrees, with the HMCR model having the worst ensemble spread-error relationship. When MERRA-2 is used for verification (not shown), the ECMWF model has the best ensemble spread-error relationship among all S2S models; this suggests that the result is not sensitive to the reanalysis dataset used for verification.

For the intensity of LPSs (Figure 3.11), there are larger differences between ensemble mean error and ensemble spread than the position of LPSs. The NCEP (Figure 3.11b), UKMO (Figure 3.11c) and ECMWF (Figure 3.11f) models have the best ensemble spread-error relationship, whereas the HMCR model (Figure 3.11k) has the worst. These results are consistent when verified against MERRA-2 (not shown). The ensemble spread depends on the number of ensemble members and the perturbation method. Despite having fewer ensemble members, many S2S models have better ensemble spread-error relationships

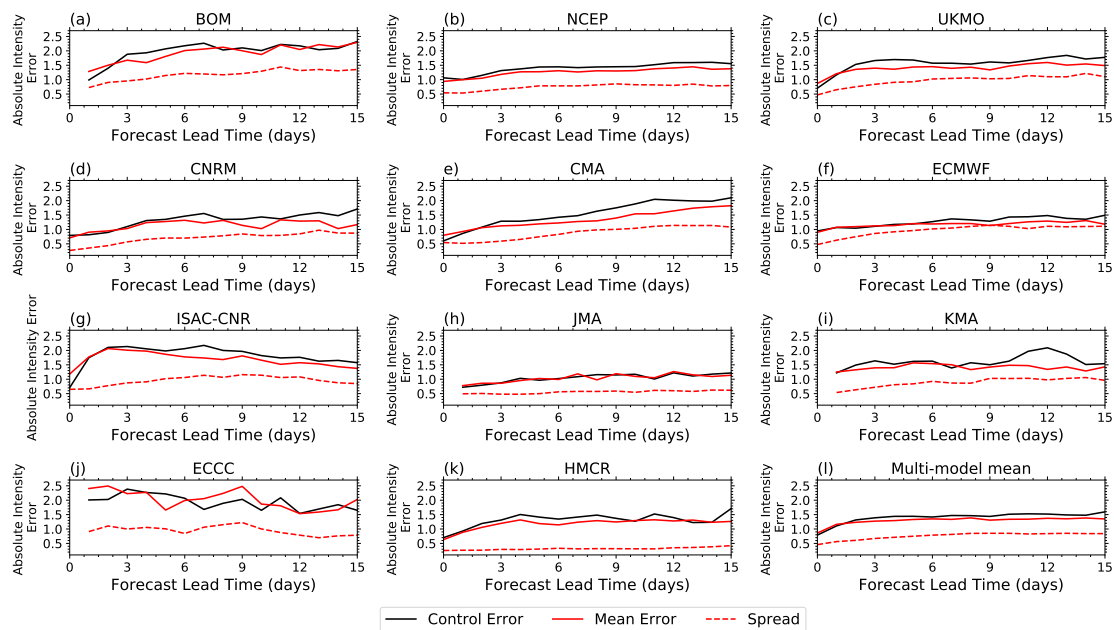


Figure 3.11: Ensemble mean error (solid red), control forecast error (solid black), and spread (dashed red) in the intensity of monsoon low-pressure systems in the eleven S2S models (a–k) and the multimodel mean (l). Errors and spread are calculated with respect to ERA-I. The unit of intensity error is 10^{-5} s^{-1} . Output from step 0 is not available for the BoM, JMA, KMA and ECCC models.

than the HMCR model. This suggests that the reason for the worse ensemble spread-error relationship in this model is perhaps the perturbation method. However, this analysis requires a sensitivity test with the model that is outside the scope of this thesis. Compared to the position of LPSs, models are more underdispersive for the intensity; this result is similar to that of extratropical cyclones in the TIGGE dataset (Froude, 2010, 2011).

3.5 Evaluation of subseasonal probabilistic predictions

We now evaluate subseasonal probabilistic predictions of SLPS genesis over the common forecast lead time of up to 32 days. As discussed in Section 1.2, skilful predictions of these weather systems at long lead times could benefit stakeholders by giving them more time for preparedness and planning. Furthermore, these results could help meteorologists in

developing products for the probabilistic forecasting of SLPS genesis using S2S models. We use the Brier Score (BS) and Brier Skill Score (BSS; Brier 1950) for this evaluation. These metrics have been used in previous studies to evaluate probabilistic predictions of TCs in S2S models (Lee et al., 2018a) and extratropical cyclones in various EPSs (e.g., Korfe and Colle 2018). We note that there is a range of probabilistic verification statistics to assess the skill, reliability and value of ensemble forecasts. However, carrying out a detailed evaluation of probabilistic predictions of SLPS genesis is beyond the scope of this thesis. Here, we consider the following forecast lead times in all ensemble members of the eleven S2S models: week 1 (1–7 days), week 2 (8–14 days), week 3 (15–21 days), week 4 (22–28 days) and week 5 (29–32 days). We then discuss the calibration of forecasts and sensitivity of the BSS to the ensemble size of S2S models.

3.5.1 Brier Score and Brier Skill Score

The BS and BSS are defined as:

$$BS = \frac{1}{N} \sum_{i=1}^N (p_i - o_i)^2 \quad (3.1)$$

where N is the total number of forecasts, o_i is the i^{th} observation, and p_i is the predicted probability of SLPS occurrence for the i^{th} forecast, which is defined as:

$$p_i = \frac{1}{M} \sum_{j=1}^M P_{ij} \quad (3.2)$$

where M is the number of ensembles, P_{ij} is the genesis prediction from the j^{th} ensemble member for the i^{th} forecast. Following Lee et al. (2018a), we set both P_{ij} and o_i as 0 for no genesis and 1 for one or more occurrences of SLPSs over 0° – 35° N, 50° E– 100° E during the forecast period. The BS_{ref} and BSS are defined as:

$$BS_{\text{ref}} = \frac{1}{N} \sum_{i=1}^N (\bar{o} - o_i)^2 \quad (3.3)$$

$$BSS = 1 - \frac{BS}{BS_{\text{ref}}} \quad (3.4)$$

where \bar{o} is the average actual outcome. The BS ranges between 0 and 1, with BS equal to zero representing perfect accuracy in a model; the BSS varies between $-\infty$ and 1, with a positive BSS suggesting that a model is more skilful than a climatological forecast. We find that the BS increases in most models at week 2 compared to week 1 (Figure 3.12a), whereas the BSS decreases (Figure 3.12b). This is due to the inclusion of pre-existing storms at the time of model initialisation. The models such as BoM, CMA, CNRM and ECMWF outperform individual models and feature a positive BSS during most weeks, whereas the HMCR model has the worst performance. The MMM is not more skilful than the climatology since its BSS is consistently negative during all weeks. We find similar results when MERRA-2 is used for verification (not shown), suggesting that these results are not biased towards ERA-I. Lee et al. (2018a) found negative BSS for forecasts of TCs over the north Indian Ocean in six S2S models (BoM, CMA, CNRM, ECMWF, JMA and NCEP) at weeks 2–5. We therefore conclude that the BoM, CMA, CNRM and ECMWF models have greater skill at the probabilistic prediction of SLPSs over the north Indian Ocean than they do for TCs.

We now calibrate S2S forecasts and determine if this process can improve the model skill, thereby making S2S models more useful for probabilistic forecasting of SLPS genesis. We follow a simple calibration technique suggested by Camp et al. (2018) in which we multiply forecast probabilities (p_i) by the ratio of the mean observed probability (\bar{o}) to the mean forecast probability (p) for each week. We then recompute the BSS for all S2S models. We find that the forecast calibration drastically improves the skill in all models

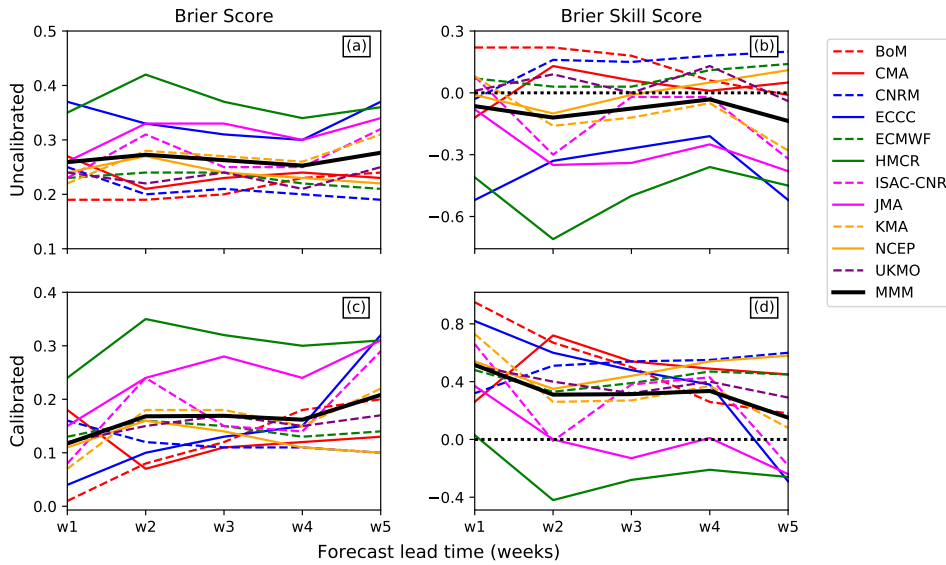


Figure 3.12: Brier score and Brier skill score for uncalibrated (a and b) and calibrated (c and d) probabilistic forecasts of weekly genesis of SLPs in all ensemble members of the eleven S2S models during June–September 1999–2010. These forecasts are verified against ERA-I. The multimodel mean (MMM) of S2S models is also shown.

(Figure 3.12d), with a BSS of ~ 0.9 in the BoM model during week 1. Almost all S2S models, including the MMM, attain positive BSS values for all weeks, except for the JMA and HMCR models.

We note that these forecasts can be calibrated using other techniques. For example, a cross-validated technique suggested by (Camp et al., 2018) could be used in which the aforementioned calibration is performed by excluding the forecast year. Other forecast calibration techniques, such as removing mean occurrence and mean genesis biases in S2S models (Lee et al., 2020), could also be explored; however, a detailed exploration of forecast calibration techniques is beyond the scope of this thesis.

3.5.2 Sensitivity of the BSS to the ensemble size

In this subsection, we investigate the impact of the ensemble size of S2S models on the skill of subseasonal probabilistic predictions. This investigation is important since S2S

models have a wide range of ensemble members: 3 in the KMA model to 33 in the BoM model. It is therefore important to determine if the BoM model has a greater prediction skill than others due to its ensemble size. For illustration, we consider week 2 forecasts since the BSS for many models drops at week 2 (see Figure 3.12b). For each model, we first calculate the BSS by reducing the number of ensemble members to 2; this threshold is due to the KMA model that has only 3 ensemble members. We then iterate this process by adding an ensemble member as per its order in the ensemble (i.e., we do not randomly select an ensemble member for each step).

Figure 3.13 shows the results for the BoM, CNRM, ECMWF, HMCR and UKMO models; meaningful comparisons are not possible for other models since they have at most 5 ensemble members. As expected, the BSS in these models decreases when the ensemble size is reduced. With 2 ensemble members, the HMCR model clearly has the worst skill, suggesting that its poor performance is not related to its small ensemble size. The forecast skill of all models starts improving as more ensemble members are added. The BSS of the BoM model starts reaching a saturation point when there are ~ 12 ensemble members, suggesting that a further increase in the number of ensemble members does not benefit the forecast skill. In comparison, other models reach respective saturation points with a smaller ensemble size, suggesting that their forecast strategy is probably more efficient than that of BoM, which agrees with the findings of Lee et al. (2018a).

3.6 Precipitation errors

In this section, we investigate how forecast lead time and the presence or absence of LPSs influence seasonal mean precipitation errors in the eleven S2S models. The S2S precipitation data has been regridded to $1^\circ \times 1^\circ$. The difference in daily precipitation is calculated by subtracting IMERG precipitation from S2S precipitation for forecast lead times of 12 to 15 days minus 0 to 3 days. This difference is calculated for three cases: all

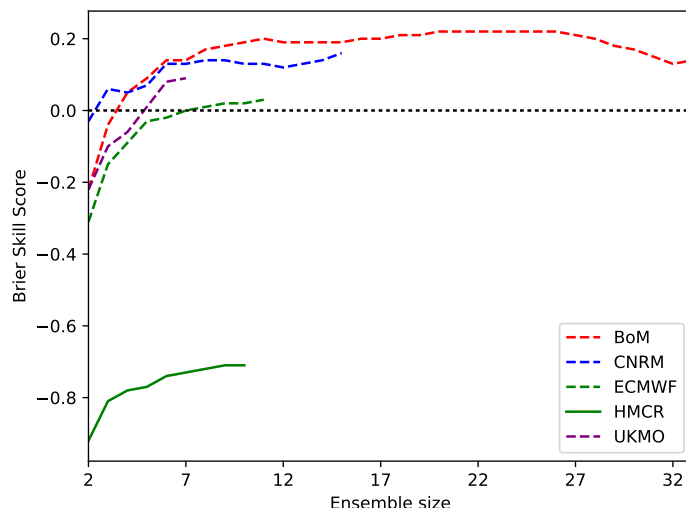


Figure 3.13: Brier skill score (BSS) for genesis of strong Indian monsoon low-pressure systems at week 2 (i.e., forecast lead times of 8–14 days) as a function of the ensemble size in the BoM, CNRM, ECMWF, HMCR and UKMO models. The BSS is calculated by verifying forecasts against ERA-I during June–September 1999–2010.

days in the time range, LPS days (when an LPS was present in the domain) and non-LPS days. The pattern correlation coefficient is also calculated to evaluate the strength of the relationship between LPS days and all days as well as non-LPS days and all days.

Figure 3.14 shows differences in daily precipitation in the JMA, ECCO, KMA and UKMO models. In the JMA (Figure 3.14a) and ECCO (Figure 3.14d) models, wet biases of 2–3 mm day⁻¹ are visible over most of the monsoon core zone, which increase to ~ 4 mm day⁻¹ over western India. However, a mostly dry bias is visible in the same regions in the KMA (Figure 3.14g) and UKMO (Figure 3.14j) models which has a peak value of ~ -3 mm day⁻¹. The precipitation differences for other S2S models are shown in Figures 3.15 and 3.16. Excluding the ISAC-CNR model, other models exhibit wet biases over most of the monsoon core zone; these biases are as large as ~ 20 mm day⁻¹ in the CMA model. Dry biases in the KMA and ISAC-CNR models could be due to moisture biases, but this cannot be investigated due to the unavailability of moisture-related parameters in the output data of these models. These results suggest that precipitation error over the

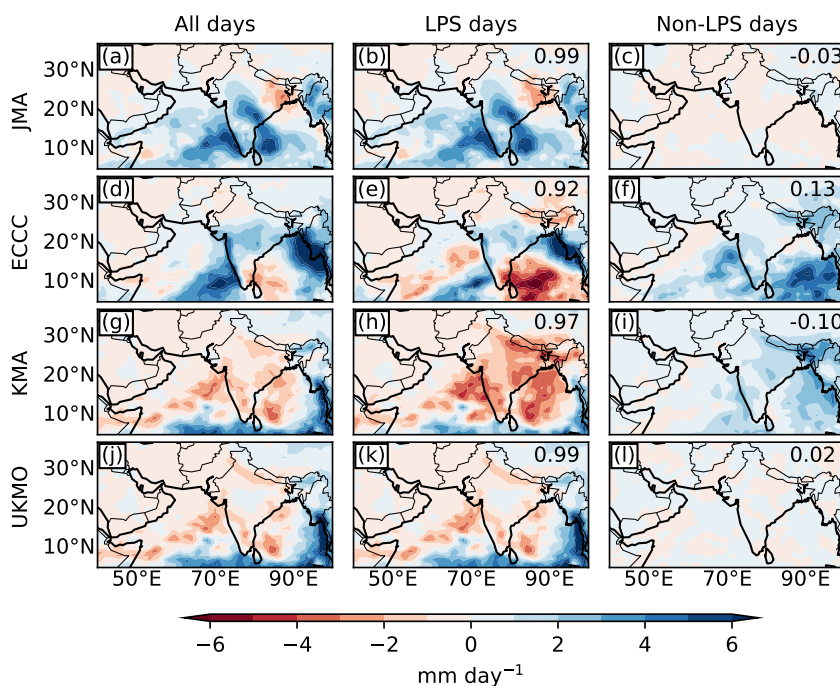


Figure 3.14: Difference in daily precipitation (mm day^{-1}) in the JMA (a–c), ECCC (d–f), KMA (g–i) and UKMO (j–l) models. For every model, the difference is calculated as model precipitation minus GPM IMERG precipitation for: all days (days 0 to 3 and 12 to 15) (left column), low-pressure system (LPS) days (middle), and non-LPS days (right column) in the same time range. Numbers indicate pattern correlation coefficient between LPS days and all days (middle) and non-LPS days and all days (right column).

monsoon core zone increases with forecast lead time in all the eleven S2S models except the KMA, UKMO and ISAC-CNR models. The multimodel mean of Coupled Model Intercomparison Project-5 (CMIP5) and CMIP3 models exhibit wet biases (dry biases) over eastern parts of the Arabian Sea (monsoon core zone) during the summer season (Sperber et al., 2013); similar wet (dry) biases are found in the JMA, ECCC and CMA (ISAC-CNR and KMA) models in our analysis.

The strong wet bias along the west coast of India in models such as CMA is due the intensification of an offshore trough (Francis and Gadgil, 2006) at 12 to 15 days lead times compared to 0 to 3 days. Over parts of the west coast, MSLP decreases by ~ 2 hPa and

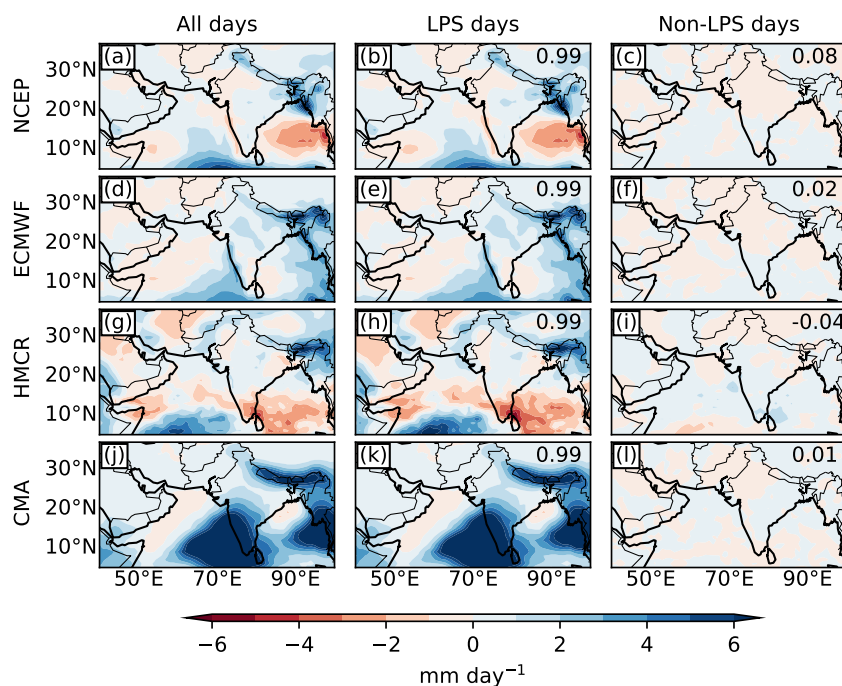


Figure 3.15: As in Fig. 3.14, but for the (a)–(c) NCEP, (d)–(f) ECMWF, (g)–(i) HMCR, and (j)–(l) CMA models.

specific humidity increases by $\sim 3 \times 10^{-3} \text{ kg kg}^{-1}$ at the 850 hPa level during 12 to 15 days lead times (not shown). In the UKMO model (not shown), specific humidity over the same region decreases during 12 to 15 days lead times, which causes the dry bias. The pattern correlation coefficient between LPS days and all days is 0.99 in most S2S models, suggesting that LPSs influence the pattern of precipitation errors in S2S models. Even in the ECCO and KMA models, the pattern of precipitation errors is the most similar between all days and LPS days instead of all days and non-LPS days. It must be noted that the precipitation difference for the eleven S2S models is similar even when matched LPSs are considered instead of unmatched LPSs (not shown).

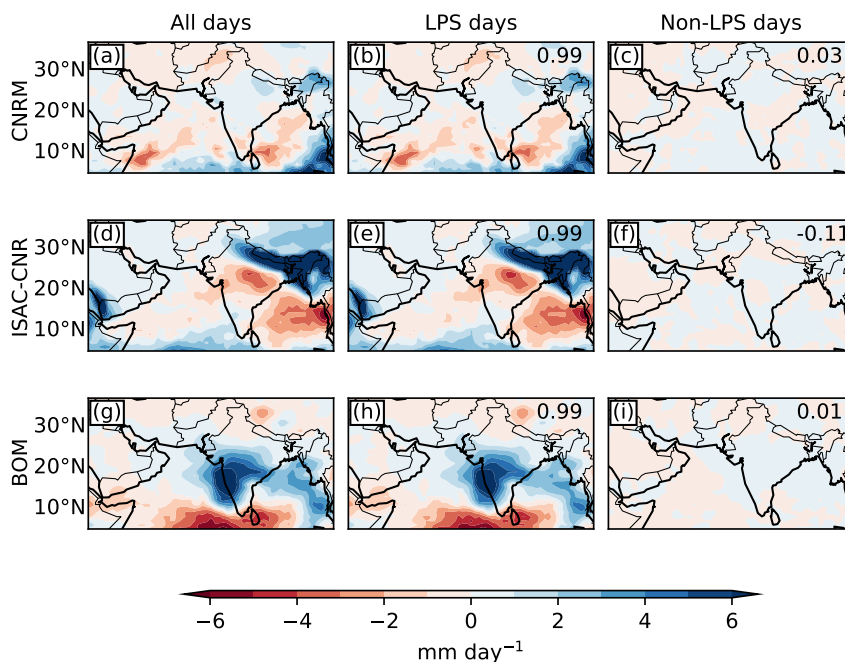


Figure 3.16: As in Fig. 3.14, but for (a)–(c) CNRM, (d)–(f) ISAC-CNR, and (g)–(i) BoM models.

3.7 Discussion and conclusions

In this chapter, we have analysed the prediction of Indian monsoon low-pressure systems (LPSs) by the eleven models of the Subseasonal-to-Seasonal (S2S) prediction project (Vitar et al., 2017). LPSs are a crucial component of the Indian monsoon since they produce substantial rainfall in the Indian subcontinent during the summer season. In spite of their important role for water supply and for triggering catastrophic flood events in the subcontinent, examining the potential for their predictability remains less explored than for other phenomena such as tropical cyclones. We used a feature-tracking algorithm to track LPSs in all ensemble members of the eleven S2S models during the common reforecast period of June–September 1999–2010. Tracks were then subjected to a post-tracking filtering process in which tropical cyclones and heat lows were eliminated. The retained

LPSs were compared with 290 and 281 LPSs identified in ERA-I and MERRA-2 datasets, respectively, for the purpose of verification. The results can be summarised as follows:

Representation of the frequency, intensity, tracks, genesis and lysis of LPSs

We found that the simulated seasonal frequency of LPSs in all S2S models was smaller than in ERA-I and MERRA-2, with the NCEP model having the largest frequency and the BoM model having the smallest frequency. While examining the probability density of the intensity of LPSs, we found that all S2S models had a modal 850 hPa relative vorticity in the range $1-2 \times 10^{-5} \text{ s}^{-1}$. In MERRA-2, the highest probability density was found for intensity in the range $3-4 \times 10^{-5} \text{ s}^{-1}$, which suggests that there are stronger LPSs in this reanalysis than in ERA-I and S2S models.

We defined strong LPSs (SLPSs) as systems featuring minimum intensity (850 hPa relative vorticity) greater than or equal to the third quartile intensity of all LPSs in an S2S model or reanalysis datasets and examined their track density, genesis and lysis given their role in triggering high-impact flood events in the Indian subcontinent. We found that all the eleven S2S models including the multimodel mean (MMM) represented transits of SLPSs over the head of the Bay of Bengal and adjoining land area; the NCEP, UKMO, CNRM, ECMWF and KMA models had the best performance, whereas the BoM, JMA and CMA models exhibited larger biases in their tracks. The observed west-northwest propagation of SLPSs was not simulated by the CMA model since the mid-tropospheric steering winds were easterly over the head of the Bay of Bengal region and central India. Tracks over west-central India were not simulated by the HMCR model due to faster lysis of SLPS and their low count. We also found that most S2S models as well as the multimodel mean correctly simulated the primary genesis region over the head of the Bay of Bengal and adjoining land area as well as the primary lysis region over east India. All the eleven S2S models had fewer genesis and lysis points than ERA-I and MERRA-2.

LPS position and intensity error

We investigated the position and intensity errors of LPSs; the CMA model had the largest position error, whereas the ECCO, UKMO, JMA and KMA models had smaller position errors than most S2S models when LPSs were verified against ERA-I. These models had similar performance when verified against MERRA-2, but a reduction in the position error in the CMA model was seen due to a greater number of westward moving LPSs in MERRA-2 than in ERA-I. We found that the range of the position error was similar in the multimodel mean when LPSs were verified against both reanalysis datasets. Many S2S models including the multimodel mean exhibited a positive bias in the intensity of LPSs at all lead times except the HMCR model when verified against ERA-I. However, most models including the multimodel mean underestimated the intensity when LPSs were verified against MERRA-2. In both cases, the bias was largest for the BoM and HMCR models and the overall pattern of biases among most models showed consistency. We found that position errors increased with forecast lead time over most of the domain in all S2S models when verified against ERA-I: the errors were larger over the Arabian Sea than the Bay of Bengal at lead times greater than 12 days. However, this was not seen when LPSs were verified against MERRA-2, suggesting that the presence of more LPSs over the Arabian Sea in MERRA-2 than in ERA-I reduced the position error.

The statistical reliability of S2S models at predicting LPSs

A good ensemble spread-error relationship is a desirable property of an ensemble prediction system (EPS) since it indicates the correct representation of all possible forecast outcomes as well as the ensemble mean error by the ensemble spread. We found that irrespective of the reanalysis used for verification, the ECMWF and UKMO models had the best ensemble spread-error relationship for the position and intensity of LPSs, whereas the HMCR model had the worst, possibly due to the perturbation method used in the model. We found that

most models were underdispersive for the position and intensity of LPSs—models were more underdispersive for the intensity than the position. These findings are similar to those for extratropical cyclones in the TIGGE dataset (Froude, 2010, 2011). Froude (2010, 2011) suspected that the best performance of the TIGGE-ECMWF model at predicting extratropical cyclones was due to a bias towards the ECMWF analysis used for verification in their studies. However, using ERA-I for verification did not give an advantage to the ECMWF model in our study.

The accuracy and skill of subseasonal probabilistic predictions

We used the Brier Score (BS) and Brier Skill Score (BSS) for evaluating subseasonal probabilistic predictions of SLPS genesis over a common forecast lead time of up to 32 days (i.e., the maximum common forecast lead time in all S2S models). We found that predictions by models such as BoM, CMA, CNRM and ECMWF were more skilful and accurate than others, whereas the HMCR model had the worst performance. The BoM, CMA, CNRM and ECMWF models had greater skill at predicting the occurrence of SLPS over the northern Indian Ocean than that of TCs. We found that a simple calibration technique boosted the BSS for all models, suggesting the possibility of using these models for forecasting the occurrence of SLPSs at the subseasonal time scale. We also examined the sensitivity of the BSS to the ensemble size of S2S models and found that the worst (best) performance of the HMCR (BoM) model was not related to its small (large) ensemble size.

The influence of forecast lead time and LPSs on the pattern of precipitation errors

We examined the role of forecast lead time and LPSs in influencing precipitation errors in S2S models. The growth of precipitation errors was considered by subtracting GPM IMERG precipitation from S2S precipitation for forecast lead times of 12 to 15 days minus 0 to 3 days. We found that S2S models, excluding the KMA, UKMO and ISAC-CNR

models, exhibited a wet bias over most of the monsoon core zone, thereby suggesting an increase in precipitation error with forecast lead time. Models such as CMA exhibited a strong wet bias (up to 20 mm day^{-1}) over the west coast of India, which was related to the intensification of an offshore trough. We also found that the presence of LPSs influenced the pattern of precipitation errors in all eleven models since there was a strong positive pattern correlation between precipitation errors on all days, and those during the presence of LPSs.

This study opens a new realm of exploring the predictability of LPSs on the time scales of numerical weather prediction models and the extended range and contributes to over a century of literature that has primarily looked at structural and dynamical aspects of LPSs. The results of this chapter are potentially useful to meteorologists and disaster management organisations. The most intense LPS related precipitation occurs within $\sim 1000 \text{ km}$ from the LPS centre. On several occasions, the presence of LPSs have forced dam operators to suddenly release dam water, thereby triggering dangerous floods such as the 2018 Kerala flood (Lal et al., 2020). Thus, an accurate prediction of an LPS track is crucial to issue flood warnings and skilful forecast of LPSs at longer lead times can help in improving flood forecasts and reservoir operations. Our study presents the first ever evaluation of the prediction of LPSs as well as their precipitation biases, which was a major gap in the literature. Hence, we expect our results to encourage researchers to carry out investigations on improving flood forecasting in India. Such results will ultimately benefit flood forecasters and dam operators in developing an advanced flood warning system.

Further work is required to carry out a comprehensive evaluation of deterministic as well as probabilistic predictions of genesis of LPSs at the subseasonal time scale. Moreover, the simulation of the structure of these weather systems by S2S models needs to be investigated since it can influence the prediction skill. We will analyse horizontal and vertical structures of these weather systems in the next chapter.

CHAPTER 4

THE STRUCTURE OF STRONG INDIAN MONSOON LOW-PRESSURE SYSTEMS IN SUBSEASONAL-TO-SEASONAL PREDICTION MODELS

Opening remarks

The published paper (Deoras et al., 2022) has been reproduced in this chapter. The text has been modified from that published in the journal paper by adding appropriate cross references to elsewhere in the thesis.

4.1 Introduction

As discussed in Chapter 1, LPSs have been investigated since the late-nineteenth century. Over this period, many of their features have been identified, such as a zonally asymmetric structure that tilts towards the southwest, the presence of a cold core in the lower troposphere and a warm core in the upper troposphere, and the occurrence of relative vorticity, winds, moisture, cloud cover and precipitation maxima in their absolute southwestern quadrant (e.g., Mulky and Banerji 1960; Krishnamurti et al. 1975, 1976; Godbole 1977;

Sarker and Chowdhury 1988). Whilst LPS studies in the last century were constrained by the lack of observations, especially over the Bay of Bengal (BoB), the availability of extensive satellite and reanalysis datasets in this century has facilitated the investigation of more properties of LPSs. Hurley and Boos (2015), who developed a global climatology of monsoon low-pressure systems, found that the thermal structure of monsoon depressions (MDs) over India is similar to those over the western Pacific and northern Australia. Hunt et al. (2016a) performed a composite analysis of 106 MDs that occurred between 1979–2014. Apart from confirming the previously known features of MDs, they found that MDs occurring during active phases of the monsoon are more intense than those during break phases.

Given the important role of LPSs during the summer monsoon season, it is necessary to understand the skill of LPS predictions, especially on an extended time scale of 15 days that is important for disaster preparedness and informing agricultural practice. As discussed in Chapter 2 (Deoras et al., 2021a), S2S models are able to simulate LPSs in general, but large biases are observed in the BoM, CMA and HMCR models. In fact, the multimodel mean track forecast error for LPSs at lead times of 4 days is approximately twice that of the IMD’s long-period average track error for tropical cyclones over the north Indian Ocean (Mishra et al., 2021). Therefore, it is important to improve the skill of LPS forecasts, for which it is essential to understand how S2S models simulate the structure and behaviour of LPSs. In this chapter, we focus on SLPSs due to their impacts on the Indian subcontinent during the summer monsoon season; our aim is to understand the following aspects:

- How well do S2S models simulate the lower-tropospheric monsoon circulation and summer mean precipitation?
- How well do S2S models simulate the structure of SLPSs?
- How do fields associated with LPSs evolve with forecast lead time and through LPS

lifetime in S2S models?

We present an outline of the data and methodology in Section 4.2. We look at the simulation of the lower-tropospheric South Asian monsoon circulation in Section 4.3, and precipitation biases as well as the precipitation contribution of LPSs in Section 4.4. We then investigate the storm-centred horizontal and vertical structures of LPSs in Sections 4.5 and 4.6, respectively, and evolution of fields in Section 4.7. Finally, we conclude in Section 4.8.

4.2 Data and methods

4.2.1 Various datasets

A full description of the S2S, ERA-I, MERRA-2 and GPM IMERG datasets is already given in Sections 2.1.1, 2.1.2, 2.1.3 and 2.1.4, respectively, and will not be repeated here. We compute anomalies against the summer mean climatology (June–September 1999–2010) in all S2S models and reanalysis datasets. We use an LPS catalogue that contains details of LPSs (monsoon depressions, deep depressions and low-pressure areas) tracked in all ensemble members of the eleven S2S models, ERA-I and MERRA-2 reanalysis datasets during June–September 1999–2010. This catalogue was used in Chapter 3. Details about the identification of LPSs are already provided in Sections 2.2.1, 2.2.2 and 2.2.3 and will not be repeated here.

4.2.2 Root mean square error

In order to compare the S2S results with ERA-I and MERRA-2, we calculate a root mean square error for different fields over the plotting domain. For vertical composites, the root mean square error value in a model output level is weighted by the density of air in that level. This will facilitate a comparison of our results with future studies that might consider vertical levels different from those here.

4.3 Simulation of the lower-tropospheric South Asian monsoon circulation

In this section, we first investigate the simulation of the mean state of the lower-tropospheric South Asian monsoon circulation (hereafter referred to as the monsoon circulation), and then investigate its simulation on SLPS days (i.e. when at least one SLPS was present in the domain). We consider forecast lead times of 0–15 days in all ensemble members of eleven S2S models. Jie et al. (2017) investigated biases in the simulation of the monsoon circulation in control forecasts of ten S2S models at forecast lead times of 10 days; however, their analysis was limited to the transition (25 May–25 June) and mature (25 June–25 July) phases of the Indian monsoon. We remain, therefore, without a complete understanding of the simulation of the monsoon circulation by S2S models at lead times of up to 15 days during the climatological period as well as on SLPS days.

Figure 4.1 shows the climatology of 850 hPa winds in the eleven S2S models at lead times of up to 15 days, ERA-I and MERRA-2 during June–September 1999–2010. The multimodel mean (MMM) of S2S models is also shown. Furthermore, the pattern correlation coefficient is also shown, which is the Pearson product-moment coefficient of linear correlation between two variables representing the same field at corresponding locations on two separate maps. In this thesis, the pattern correlation coefficient is computed by first flattening the 2D array of a field (e.g., wind magnitude in Figure 4.1) and then computing the Pearson product-moment coefficient between an S2S model and ERA-I. All S2S models and the MMM are able to simulate the main features of the monsoon circulation such as the cross-equatorial flow, Somali Jet and the position of the monsoon trough, and most models have a root mean square error consistent with the observational uncertainty. The monsoon trough, however, is located further to the south in the BoM model than in others. As a result, there are strong westerly winds over most of the Arabian Sea, southern India, and very weak northwesterly winds over north-central and northern parts of India.

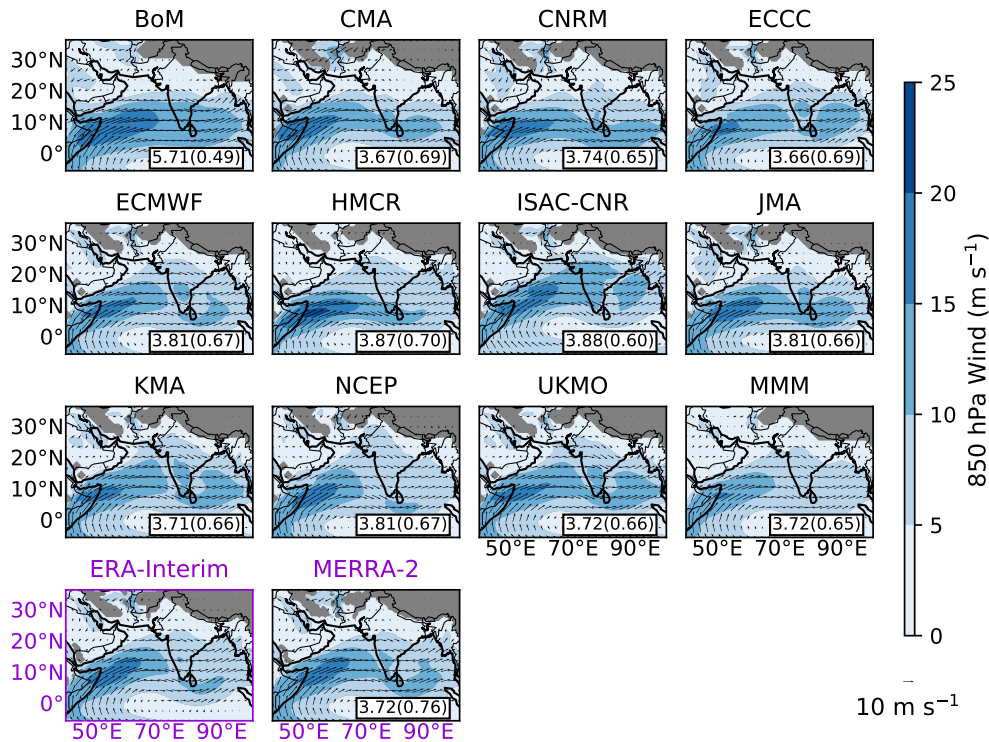


Figure 4.1: Coloured contours show the climatology of 850 hPa winds (m s^{-1}) in all ensemble members of eleven S2S models, ERA-Interim (ERA-I) and MERRA-2 reanalysis datasets during June–September 1999–2010. The multimodel mean (MMM) of S2S models is also shown. The climatology is considered for forecast lead times of 0–15 days in all S2S models and the MMM. Wind vectors in each subplot are regridded to match the coarsest spatial resolution of the BoM model, which is $2.5^\circ \times 2.5^\circ$. Numbers outside brackets in each subplot indicate the root mean square error in the wind speed (m s^{-1}) between the respective S2S models and ERA-I, whereas those in brackets indicate the pattern correlation coefficient between the respective S2S models and ERA-I. Grey areas indicate where the mean surface pressure is less than 850 hPa. The subplots of ERA-I and MERRA-2 are highlighted in dark violet to distinguish them from the S2S dataset.

The BoM model has the largest root mean square error in wind speed, and the spread of errors in S2S models is larger than the observational uncertainty (i.e. the root mean square error between MERRA-2 and ERA-I). We now turn to 850 hPa wind anomalies (Figure 4.2), which are computed by subtracting the summer mean climatology from 850 hPa winds on SLPS days. The summer mean climatology is computed for forecast lead times of 0–15 days in all ensemble members of each S2S model.

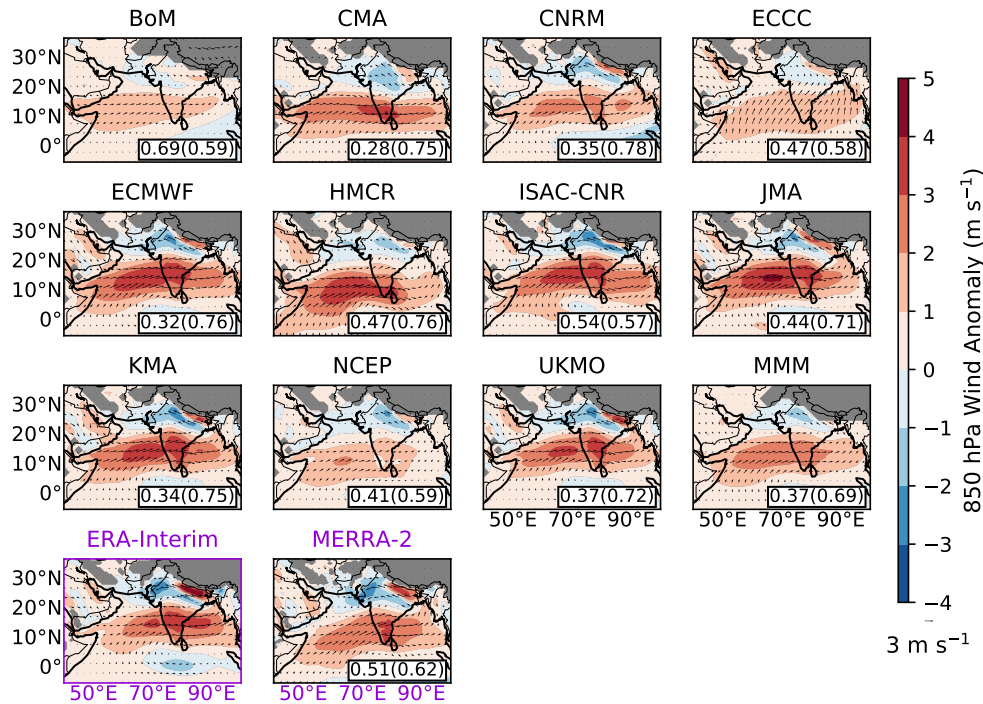


Figure 4.2: As Figure 4.1, but for wind anomaly on strong Indian monsoon low-pressure system days. Coloured contours show the wind anomaly, which is computed against the summer mean climatology for S2S models, the MMM, ERA-I and MERRA-2.

The cross-equatorial monsoon flow strengthens on SLPS days in all S2S models, the MMM, ERA-I and MERRA-2, evidenced by positive anomalies over the Arabian Sea, southern India and the BoB. This suggests that SLPSs influence the simulation of the monsoon circulation. The wind anomaly is smallest in the BoM and ECCC models. Furthermore, winds are inaccurately simulated by the ECCC model since there are anomalous south-westerly winds over the Arabian Sea at 15° N and anomalous southerly winds over the BoB at 10° N instead of westerlies. However, the root mean square error for most models is smaller than the observational uncertainty. As with the climatology, the root mean square error is largest in the BoM model with respect to ERA-I and smallest in the CMA model with respect to both ERA-I and MERRA-2.

In summary, S2S models and the MMM well simulate the monsoon circulation during

the climatological period and on SLPS days in general. Models such as CMA, ECMWF, KMA and UKMO have the best performance, whereas BoM and ECCO have prominent biases.

4.4 Precipitation

In this section, we investigate precipitation biases and the precipitation contribution of LPSs to the modelled summer mean precipitation. We carry out these analyses for forecast lead times of 0–15 days during June–September 2001–2010. These results could help stakeholders in many ways. The modelling community could thoroughly investigate reasons for precipitation biases, which would be useful for improving S2S precipitation forecasts in the future. Models featuring small biases in forecasts of precipitation as well as the precipitation contribution of LPSs can be used for developing better forecast products, thereby favouring better management of water resources. Since individual LPS events can cause significant floods in the Indian subcontinent, meteorologists and hydrologists can use such models for LPS forecasting, resulting in improved flood preparedness and agricultural decision making. Here we consider LPSs instead of SLPSs since weaker LPSs (e.g., low-pressure areas) still provide a significant precipitation contribution to the summer mean precipitation (Hunt and Fletcher, 2019).

4.4.1 Precipitation biases

Figure 4.3 shows precipitation biases for all ensemble members of the three best performing models: ECMWF, NCEP and UKMO. The result for the MMM is also shown in Figure 4.3, whereas the results for other models are shown in Figure 4.4. The biases are calculated for all days (i.e., climatology) and LPS days (i.e., when at least one LPS was present in the domain). Since the BoM model has the coarsest resolution ($2.5^\circ \times 2.5^\circ$), precipitation datasets of other S2S models and IMERG are regridded to this resolution. The biases are

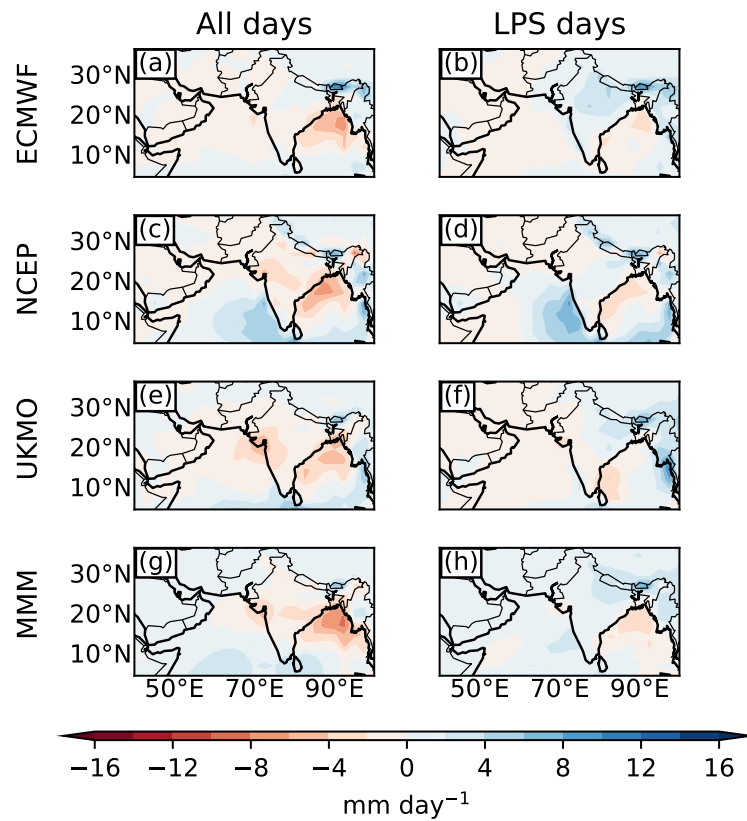


Figure 4.3: Precipitation bias (mm day^{-1}) in the ECMWF (a–b), NCEP (c–d), UKMO models (e–f), and the multimodel mean (MMM; g–h) of the eleven S2S models for forecast lead times of 0–15 days during June–September 2001–2010. For each model, the bias is calculated as the model precipitation minus GPM IMERG precipitation for: all days (left column) and LPS days (right column).

then calculated by subtracting IMERG precipitation from each model.

In all models, the patterns of precipitation biases on all days are similar to those on LPS days, suggesting that LPSs are among the important contributors to precipitation biases. In the BoM and CMA models, there are prominent dry biases over the monsoon core zone (Rajeevan et al., 2010), northeastern India, BoB and nearby coastal regions on all days and LPS days. Whilst the CNRM, HMCR, ISAC-CNR and NCEP models simulate weak dry biases over the monsoon core zone on all days, the ECCO and JMA models simulate weak wet biases. In contrast, the ISAC-CNR model simulates strong wet

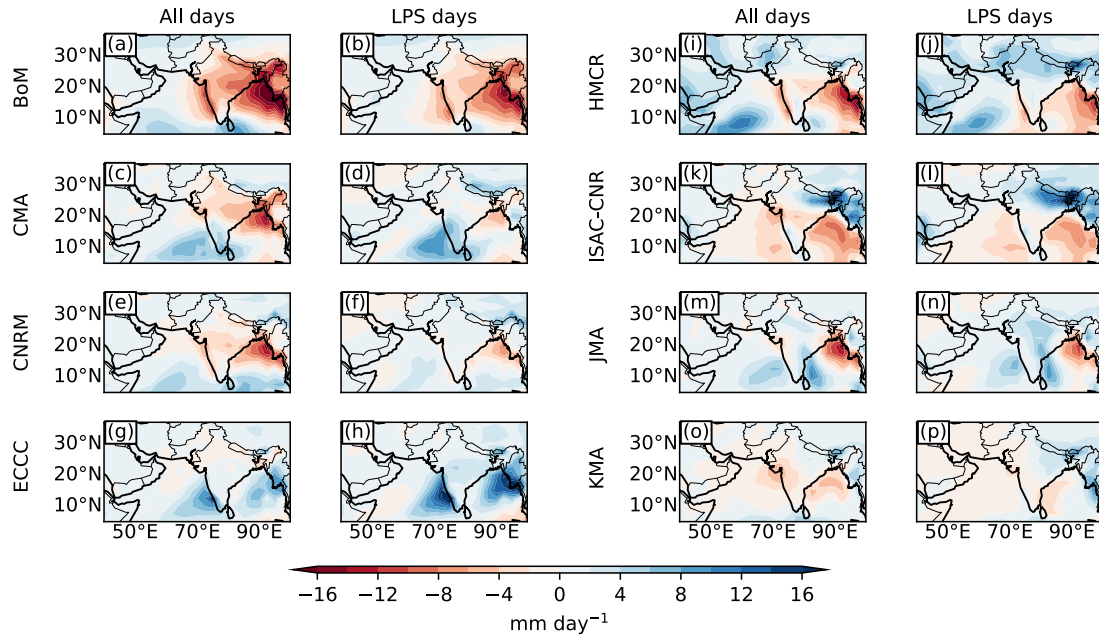


Figure 4.4: As Figure 4.3, but for the other eight S2S models.

biases along the Himalayan foothills and parts of eastern India on all days. In all models, LPSs reduce dry precipitation biases over the head of the BoB and the monsoon core zone, whereas in the ECCC model, they increase the wet bias. This is because LPSs usually inhabit these regions. The MMM features small dry biases over the BoB and small wet biases over India on all days. The pattern is reversed on LPS days.

The dry biases over the monsoon core zone, head of the BoB and nearby coastal regions are well known in the current general circulation models, including the multimodel mean of CMIP5 and CMIP3 models (e.g., Sperber et al. 2013; Praveen et al. 2015). Here, following Sperber et al. (2013) and Jie et al. (2017), we investigate how precipitation biases are associated with biases in the lower-tropospheric monsoon circulation. Figure 4.5 shows biases in 850 hPa winds on all days computed against ERA-Interim. These results are considered for forecast lead times of 0–15 days. The overall biases in the MMM are smaller than those in individual S2S models. The BoM, CMA and CNRM models have strong easterly or northeasterly anomalies over the head of the BoB and the monsoon core

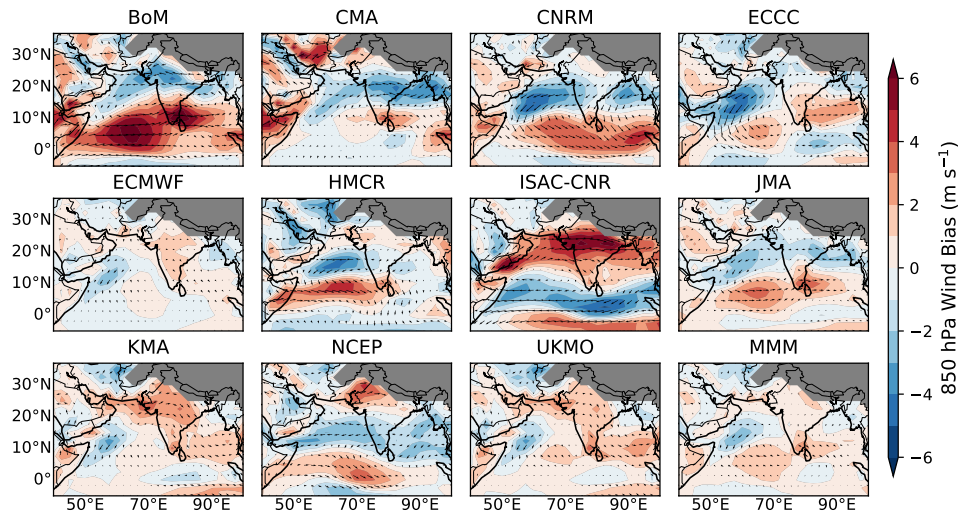


Figure 4.5: Bias in the climatology of 850 hPa winds during June–September 2001–2010. For each S2S model, the bias is calculated as the 850 hPa winds in the model minus those in ERA-Interim reanalysis. The bias is calculated for forecast lead times of 0–15 days in all S2S models. Wind vectors in each subplot are regridded to match the coarsest spatial resolution of the BoM model, which is $2.5^\circ \times 2.5^\circ$. The multimodel mean (MMM) of S2S models is also shown.

zone, suggesting that dry precipitation biases are associated with a weak monsoon flow. This is also seen in models such as JMA and NCEP, in which prominent dry biases over the Myanmar coast are associated with easterly wind anomalies. In contrast, a prominent wet bias over the monsoon trough region in the ECCC model and wet biases along the Himalayan foothills in the ISAC-CNR model are associated with strong westerly wind anomalies. These results agree with Jie et al. (2017) in general, who found similar wind biases at forecast lead times of 10 days in control runs of ten S2S models. We will explore the precipitation contribution of LPSs in the next subsection to better understand these results.

4.4.2 Precipitation contribution

Figure 4.6 shows the precipitation contribution of LPSs to the summer mean precipitation in all ensemble members as well as the MMM of eleven S2S models. The results for

LPSs tracked in ERA-I and MERRA-2, for which GPM IMERG precipitation is used, are also shown. We attribute precipitation to an LPS if it falls within 800 km of its centre, as initially suggested by Hunt and Fletcher (2019). The results agree with past studies (e.g., Hurley and Boos 2015; Hunt and Fletcher 2019) in general—LPSs in most models and the MMM have the largest precipitation contribution over parts of eastern and east-central India and adjoining parts of the BoB. However, the precipitation contribution over eastern India is smaller in all S2S models than in ERA-I. All S2S models underestimate the frequency of LPSs (Chapter 3; Deoras et al. 2021a). It is therefore important to delineate the roles of biases on LPS precipitation and LPS frequency in total LPS precipitation biases, for which we follow a linearised budget method. For each S2S model, we first approximate the total simulated precipitation (TP) as follows:

$$TP = P \times N \quad (4.1)$$

where P is the composite-mean LPS precipitation within 800 km of the LPS centre and N is the total number of LPSs. From the results of ERA-I, we then apply bias corrections to P and N :

$$TP_{bc} = (P + P_b) \times (N + N_b) \quad (4.2)$$

where TP_{bc} is the bias corrected total precipitation, P_b is the precipitation bias, and N_b is the LPS frequency bias. We then determine the bias in the total simulated precipitation (TP_b) by subtracting Equation 4.1 from Equation 4.2 and ignore the product term of P_b and N_b , which is small in magnitude since P_b and N_b are small (see Figures 3.1 and 4.9) and the product term is of second order in this linearisation equation:

$$TP_b = (P \times N_b) + (N \times P_b) \quad (4.3)$$

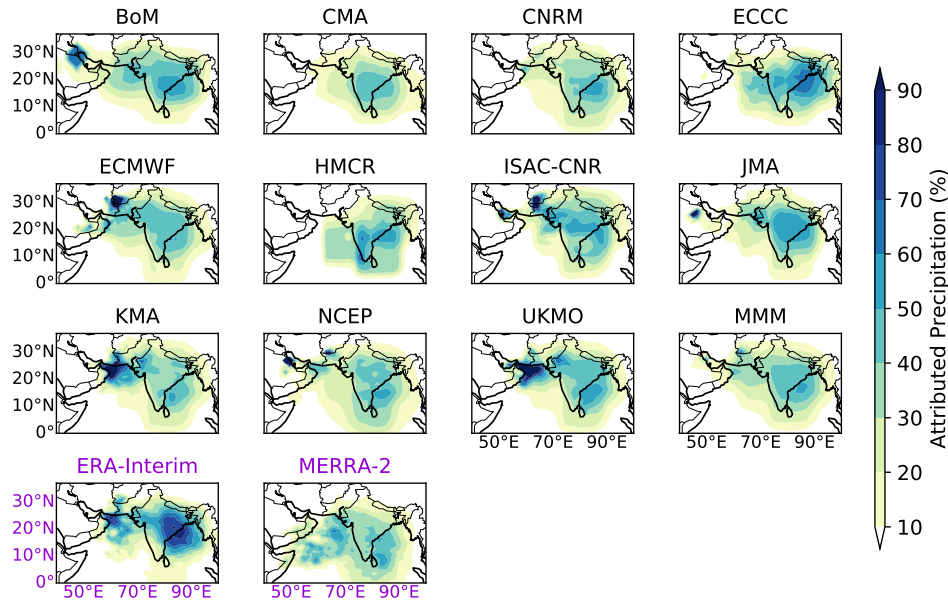


Figure 4.6: Percentage of seasonal (June–September 2001–2010) precipitation attributed to monsoon low-pressure systems tracked in all ensemble members of eleven S2S models for forecast lead times of 0–15 days, ERA-Interim and MERRA-2 reanalysis datasets. Precipitation is attributed to a low-pressure system if it falls within 800 km of its centre. The multimodel mean (MMM) of S2S models is also shown, which is computed by regridding the precipitation contribution in each S2S model to the coarsest spatial resolution of the BoM model ($2.5^\circ \times 2.5^\circ$). The GPM IMERG dataset is used for calculating the precipitation contribution of monsoon low-pressure systems tracked in ERA-Interim and MERRA-2 reanalysis datasets. The subplots of ERA-I and MERRA-2 are highlighted in dark violet to distinguish them from the S2S dataset.

We then estimate relative contributions of frequency and precipitation biases to the total precipitation bias from Equation 4.3. Compared to LPS frequency biases, LPS precipitation biases in most models have a greater relative contribution (0.6–0.8) to the total precipitation bias over eastern India (Figures 4.7 and 4.8). In contrast, biases in LPS frequency in the BoM, ECCC and JMA models contribute the most (relative contribution exceeding 0.8) to the total precipitation bias over eastern India.

The precipitation contribution depends on the propagation of LPSs over India. We find that biases in the simulation of LPS tracks (for example, see Figure 3.3 of Chapter 3) modulate their precipitation contribution. The precipitation contribution of LPSs in

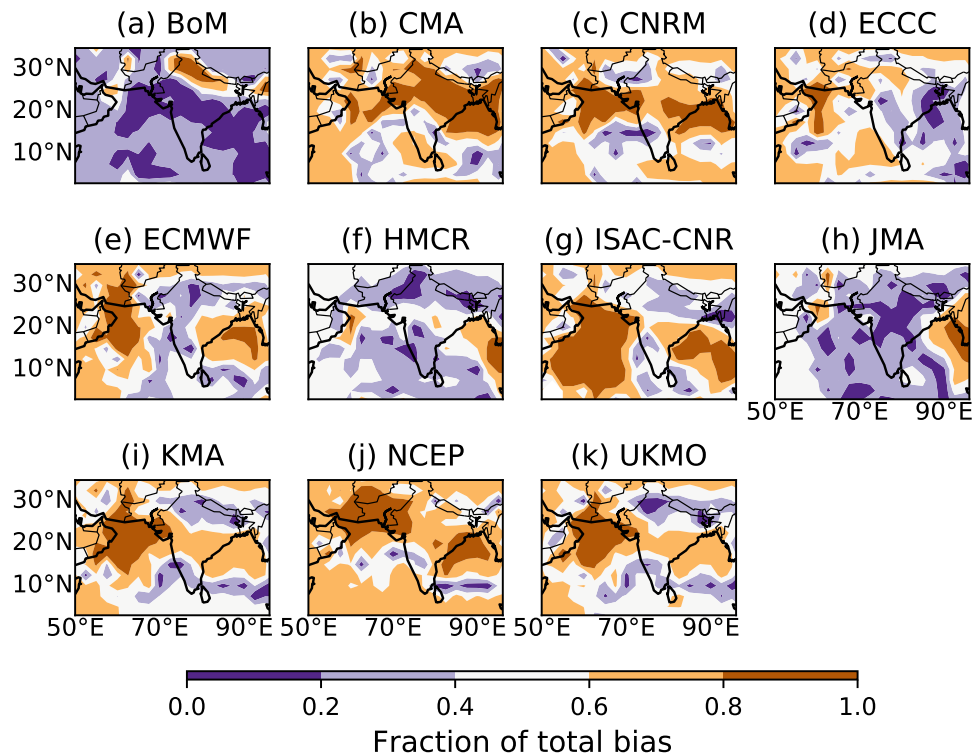


Figure 4.7: Relative contributions of precipitation biases of Indian monsoon low-pressure systems to total precipitation biases in the eleven S2S models during June–September 1999–2010. Forecast lead times of 0–15 days are considered in all S2S models.

models such as CMA and HMCR is the largest over south-central India since LPSs propagate further southward in these models than in others. In the ECMWF, ISAC-CNR, KMA and UKMO models, there is a large precipitation contribution over northern parts of the Arabian Sea as well as parts of Pakistan, Afghanistan and Iran, which is attributed to long-lived BoB LPSs and Arabian LPSs, as suggested by Deoras et al. (2021b). The climatological precipitation over these regions during the summer monsoon season is very small, which means that any passing LPS makes a proportionately large contribution to precipitation. The precipitation contribution over the Arabian Sea is larger in MERRA-2 than in ERA-I, which is due to a larger frequency of Arabian LPSs in the former (Chapter 3; Deoras et al. 2021a). Furthermore, the precipitation contribution of LPSs over eastern

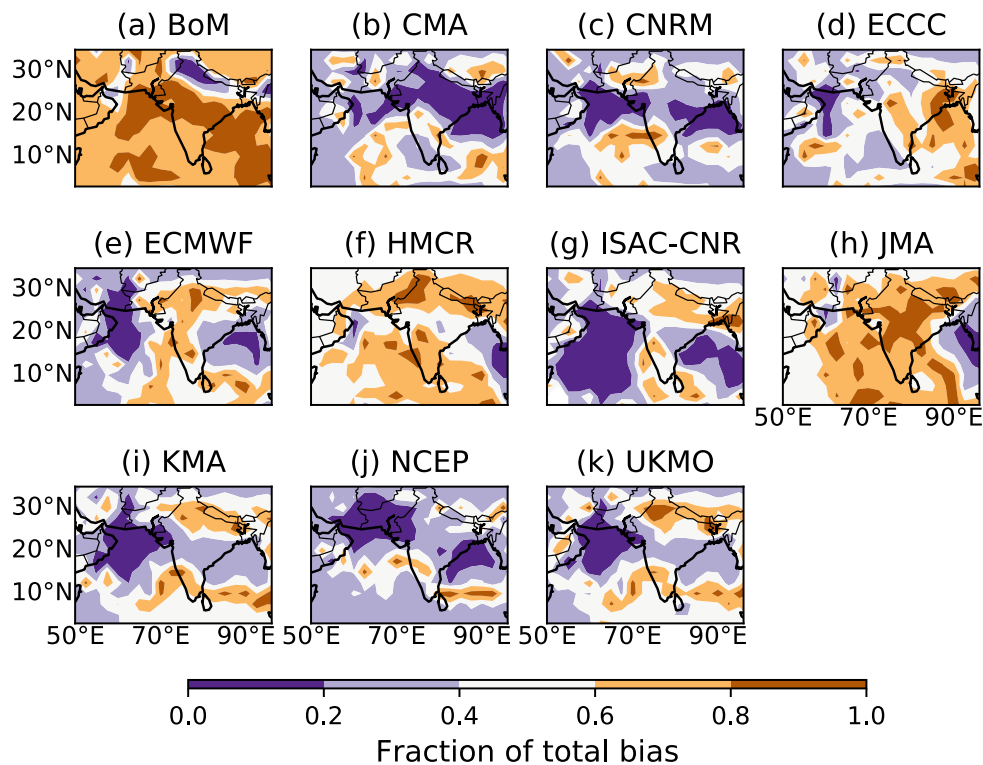


Figure 4.8: As in Fig 4.7, but for frequency biases.

parts of India is smaller in MERRA-2 than in ERA-I, which is attributed to a lower track density.

In conclusion, stakeholders could benefit from precipitation forecasts from the MMM since precipitation biases are small and the MMM simulates the precipitation contribution reasonably well. They could also benefit from precipitation forecasts of the ECCC, ECMWF, ISAC-CNR, JMA, UKMO models after applying suitable bias corrections.

4.5 Horizontal structure of SLPS

In this section, we discuss the horizontal structure of precipitation, 850 hPa wind, mean sea-level pressure and 850 hPa relative vorticity for composites of SLPSs. For compositing,

we centralise each SLPS at each time step to 0° relative latitude and 0° relative longitude. We have not rotated composites in this study. Hunt et al. (2016b) compared unrotated and rotated composites of storm-centred precipitation for MDs. They found that the location of maximum precipitation, which is not collocated with the LPS centre, is not affected by rotation, whereas its magnitude is reduced in the rotated composite. Other fields (e.g., relative vorticity) feature smaller variance than precipitation, and their maxima are collocated with the LPS centre.

4.5.1 Precipitation and wind

Figure 4.9 shows storm-centred precipitation for composites of SLPSs tracked in all ensemble members of the eleven S2S models, the MMM, ERA-I and MERRA-2 during June–September 2001–2010. Vectors showing storm-centred 850 hPa wind as an anomaly to the summer mean climatology are overlaid. The overall composite-mean precipitation produced by SLPSs in S2S models is in agreement with that produced by observed MDs, as investigated in past studies (e.g., Stano et al. 2002). Whilst all models underestimate the maximum precipitation (considered within 800 km of the composite centre), there is a prominent underestimation in the maximum and composite-mean precipitation in the HMCR model, which also poorly simulates the 850 hPa wind anomaly. Both mean and maximum precipitation are underestimated in the MMM. The BoM (CMA) model features the smallest (largest) root-mean-square error with respect to ERA-I. The error in S2S models is larger than the observational uncertainty in the composite-mean precipitation in reanalyses, which is calculated using the GPM IMERG dataset.

The region of maximum precipitation is located ~ 300 km from the centre. In the CNRM, ECMWF, JMA, NCEP and UKMO models, it is located to the southwest of the centre, which is in agreement with ERA-I, MERRA-2 and past studies (e.g., Godbole 1977; Yoon and Chen 2005; Hunt et al. 2016a). In contrast, it is located to the relative south of the centre in the BoM, CMA, ECCO, HMCR and ISAC-CNR models and the

MMM. The region of maximum precipitation is located to the west-southwest of the LPS

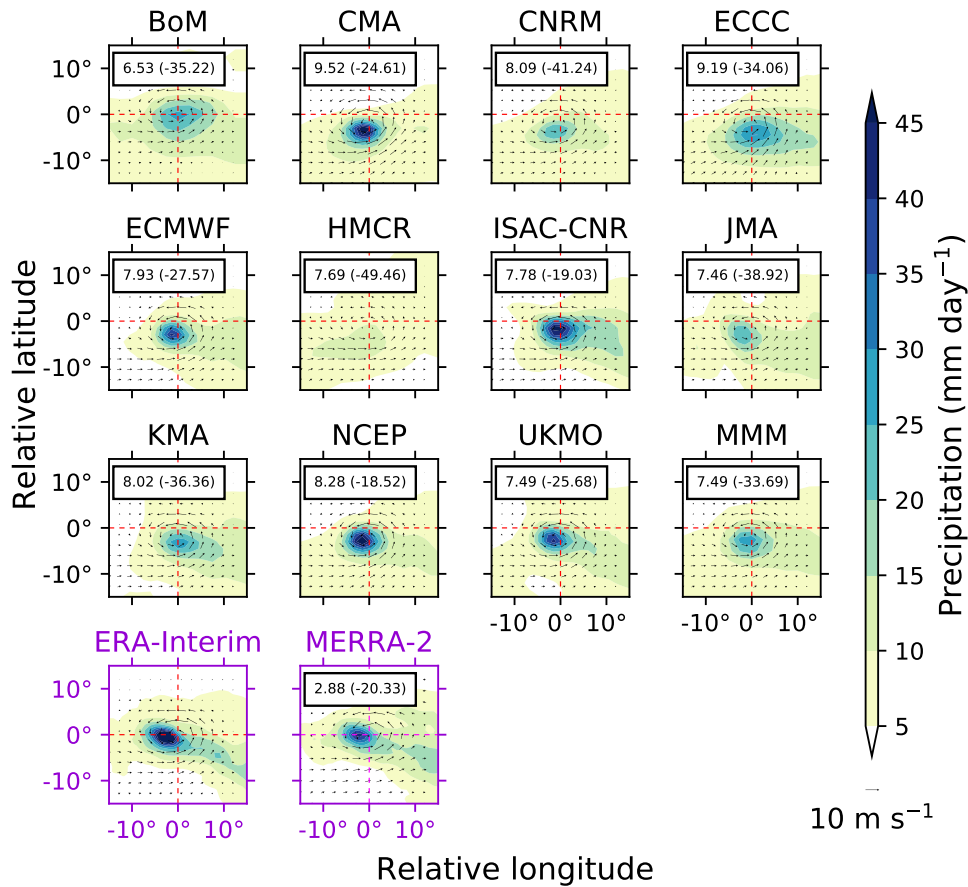


Figure 4.9: Storm-centred precipitation (mm day^{-1}) for composites of strong Indian monsoon low-pressure systems (SLPSs) tracked in all ensemble members of eleven S2S models, ERA-Interim (ERA-I) and MERRA-2 reanalysis datasets during June–September 2001–2010 (coloured contours). Wind vectors showing the 850 hPa wind speed as an anomaly to the summer mean climatology for the same period are overlaid. These results are considered for forecast lead times of 0–15 days. The multimodel mean (MMM) of S2S models is also shown. The GPM IMERG dataset is used for calculating precipitation for SLPSs tracked in ERA-I. Numbers indicate the root mean square error in the composite-mean precipitation (mm day^{-1}) between the respective S2S models and GPM IMERG for SLPSs in ERA-I, whereas numbers in brackets indicate the error (mm day^{-1}) in the maximum precipitation (within 800 km from the centre). For MERRA-2, numbers show the aforementioned errors between SLPSs in MERRA-2 and ERA-I.

centre, which is attributed to quasigeostrophic dynamical lifting (e.g., Sanders 1984; Boos et al. 2015) and horizontal moisture advection (e.g., Adames and Ming 2018), with adi-

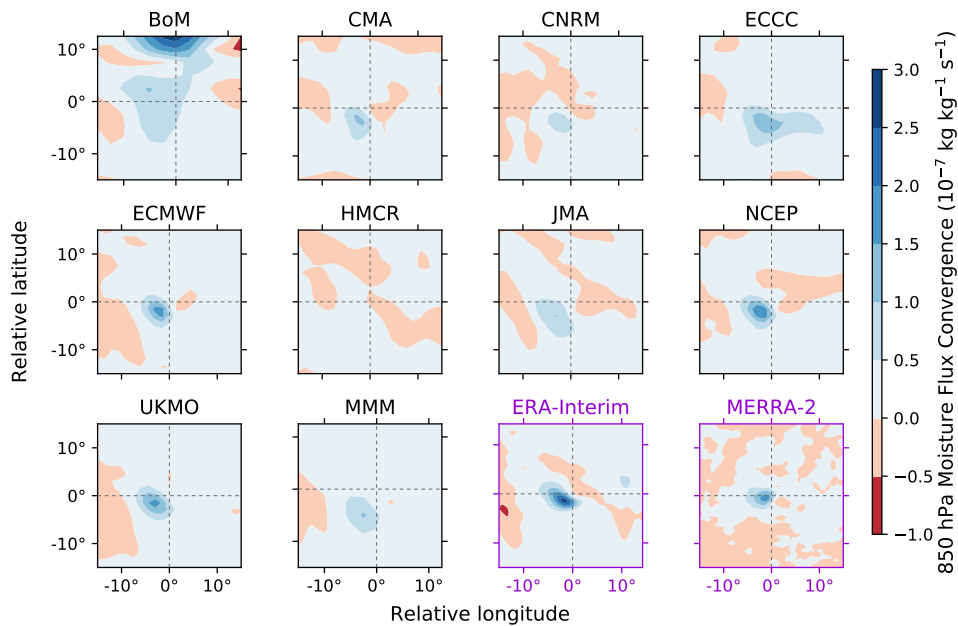


Figure 4.10: Moisture-flux convergence ($10^{-7} \text{ kg kg}^{-1} \text{ s}^{-1}$) at 850 hPa of storm-centred composites of strong Indian monsoon low-pressure systems in all ensemble members of nine S2S models, ERA-Interim (ERA-I) and MERRA-2 reanalysis datasets during June–September 2001–2010. Moisture-flux convergence is considered for forecast lead times of 0–15 days in S2S models. The multimodel mean (MMM) of nine S2S models is also shown. Note that the ISAC-CNR and KMA models are not shown in this figure since the specific humidity field is not available.

abatic quasigeostrophic ascent dominating in the lower troposphere over the maximum precipitation region (Rajamani and Rao, 1981; Murthy and Boos, 2020). We investigate moisture-flux convergence at 850 hPa (Figure 4.10) since other fields such as vertical velocity are not commonly available in S2S models. It should be noted that we have excluded the ISAC-CNR and KMA models since specific humidity is not available. Among all S2S models, the HMCR model features the weakest moisture-flux convergence, which explains the lowest precipitation in this model. There is a strong positive linear correlation (Figure 4.11a) between mean moisture-flux convergence and mean precipitation (both considered within 800 km of the composite centre) among S2S models—the Pearson correlation coefficient is 0.84 and it is statistically significant at the 95% confidence level. Since LPSs are

located closer to the Himalayas in BoM than in other models, there is a large moisture-flux convergence to the relative north. The magnitude of precipitation for SLPSs is smaller in MERRA-2 than in ERA-I (Figure 4.12d), which is attributed to a weaker moisture-flux convergence.

4.5.2 MSLP and relative vorticity

Here, we would like to understand the simulation of the structure of mean sea-level pressure anomaly and 850 hPa relative vorticity for SLPS composites. Figure 4.13 shows storm-centred 850 hPa relative vorticity (10^{-5} s^{-1}) in coloured contours and mean sea-level pressure (MSLP) anomaly in line contours. The difference between composites of MERRA-2 and ERA-I is shown in Figure 4.12c. The maximum relative vorticity and MSLP anomaly are located at the composite centre in all S2S models, the MMM, ERA-I and MERRA-2. The CMA, NCEP, ECMWF and ISAC-CNR models simulate the largest relative vorticity and MSLP anomaly, whereas the HMCR (BoM) model simulates the smallest relative vorticity (MSLP anomaly). There is a strong negative and statistically significant (at the 95% confidence level) intermodel linear correlation (Pearson correlation coefficient of -0.74) between maximum MSLP anomaly and maximum precipitation (Figure 4.11b). Weaker rainfall (Figure 4.9), therefore, is associated with weaker intensity of SLPSs. The intensity at the composite centre in reanalyses is similar; however, the intensity to the relative north and northeast of the composite centre in MERRA-2 is more than in ERA-I. This does not have any implications for the model result since the spread of errors among models is larger than the observational uncertainty. With respect to ERA-I, the root mean square error for MSLP anomaly (850 hPa relative vorticity) is the largest for the HMCR (BoM and CMA) models, whereas the BoM and HMCR models have the largest root mean square error for both fields with respect to MERRA-2 (see Table 4.1).

Model	850 hPa wind climatology (m s ⁻¹ , anomaly)	Precipitation (mm day ⁻¹)	850 hPa ζ (10 ⁻⁵ s ⁻¹)	MSLP anomaly (hPa)	925 hPa ΔT (K)	300 hPa ΔT (K)
BoM	7.94 (0.57)	3.85	1.46	0.55	0.40	0.22
CMA	5.82 (0.51)	4.94	1.05	0.60	0.38	0.41
CNRM	5.39 (0.56)	3.14	1.04	0.57	0.25	0.22
ECCC	4.99 (0.69)	4.77	1.04	0.56	0.31	0.52
ECMWF	5.29 (0.57)	2.93	1.01	0.49	0.20	0.18
HMCR	5.16 (0.76)	3.63	0.97	0.67	0.41	0.17
ISAC-CNR	5.57 (0.66)	4.38	1.04	0.42	0.31	0.18
JMA	5.46 (0.61)	2.36	0.98	0.49	0.25	0.12
KMA	5.20 (0.55)	2.98	1.05	0.43	0.29	0.24
NCEP	5.17 (0.54)	3.99	1.06	0.52	0.43	0.31
UKMO	5.10 (0.54)	2.68	1.07	0.64	0.29	0.18

Table 4.1: Root mean square error of different fields in S2S models with respect to MERRA-2. ζ and ΔT show relative vorticity and temperature anomaly, respectively.

In conclusion, stakeholders could benefit from the MMM, ECMWF, ISAC-CNR, NCEP and UKMO models given the best simulation of the horizontal structure of fields discussed in this section.

4.6 Vertical structure

In this section, we analyse the vertical structure of relative vorticity, temperature and moist static energy of composites of SLPSs in all S2S models, the MMM, ERA-I and MERRA-2. The vertical structures are drawn above the zero-latitude line, so relative west is to the left and relative east is to the right of 0° relative longitude. Similar to previous analyses, we consider forecast lead times of 0–15 days in all S2S models.

4.6.1 Relative vorticity

Figure 4.14 shows the vertical structure of relative vorticity anomaly of composites of SLPSs in all ensemble members of eleven S2S models, the MMM, ERA-I and MERRA-2, whereas Figure 4.15 shows the difference between MERRA-2 and ERA-I. The structure is zonally symmetric with a tilt towards the relative west, and it has a maximum intensity near the 850 hPa level, which agrees with past studies (e.g., Godbole 1977; Hunt et al.

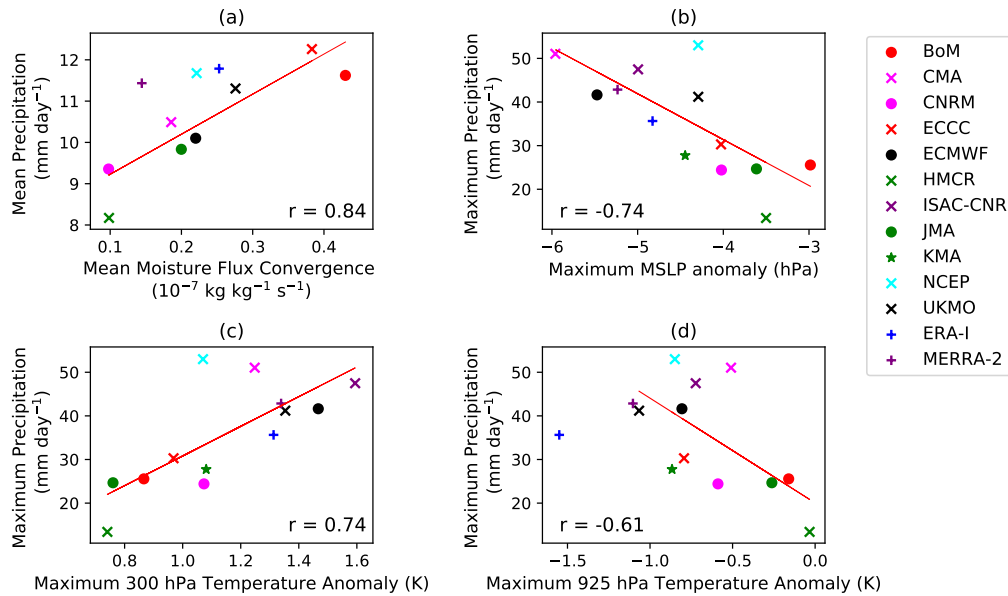


Figure 4.11: Scatter plots showing: (a) mean moisture-flux convergence (10^{-7} kg kg⁻¹ s⁻¹) vs mean precipitation (mm day⁻¹), (b) maximum mean sea-level pressure (MSLP) anomaly (hPa) vs maximum precipitation (mm day⁻¹), (c) maximum 300 hPa temperature anomaly (K) vs maximum precipitation (mm day⁻¹), and (d) maximum 925 hPa temperature anomaly (K) vs maximum precipitation (mm day⁻¹) for composites of SLPSs in S2S models, ERA-Interim (ERA-I) and MERRA-2 reanalysis datasets. These fields are considered within a distance of 800 km from the composite centre of SLPSs. The period in (a) is June–September 2001–2010, whereas that in (b), (c) and (d) is June–September 1999–2010. A solid red line in each subplot shows the best linear fit across S2S models. The number in each subplot indicates the intermodel Pearson correlation coefficient for S2S models, which is statistically significant at the 95% level in each case. Note that the ISAC-CNR and KMA models are not shown in (a) since the specific humidity field is not available.

2016a). The BoM and HMCR models simulate smallest anomalies, whereas ECMWF and ISAC-CNR simulate largest anomalies. Compared to ERA-I and MERRA-2, most S2S models and the MMM simulate shallower and weaker anomalies. The overall structure is shallower in MERRA-2 than in ERA-I. The vertical extent of the structure in the best performing models such as ECMWF and ISAC-CNR is similar to that in ERA-I; however, it is shallower in MERRA-2 than in these models and ERA-I. In the MMM, most S2S models, ERA-I and MERRA-2, there are negative anomalies in the upper-troposphere due

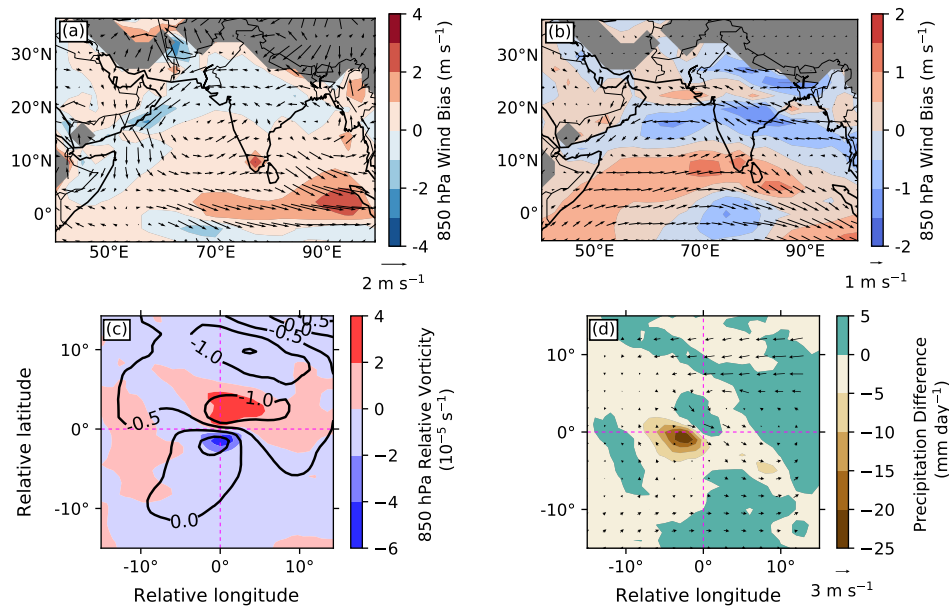


Figure 4.12: (a) Wind bias in the climatology of 850 hPa winds in MERRA-2 during June–September 1999–2010 compared to ERA-Interim (ERA-I) reanalysis. (b) 850 hPa wind bias in MERRA-2 on strong low-pressure system days during June–September 1999–2010. (c) Storm-centred difference in 850 hPa relative vorticity (coloured contours) and mean-sea level pressure anomaly (line contours) between MERRA-2 and ERA-I. (d) Storm-centred difference in daily precipitation (mm day^{-1}) and 850 hPa wind anomaly (m s^{-1}) between MERRA-2 and ERA-I during June–September 2001–2010. Note that GPM IMERG dataset is used to calculate precipitation difference, and the wind anomalies are computed against the respective summer mean climatology for the same period in ERA-I and MERRA-2.

to the divergent outflow of SLPSs. The root mean square error is largest for the HMCR and BoM models with respect to ERA-I and MERRA-2, whereas it is smallest for the ECMWF and CMA models with respect to ERA-I and MERRA-2, respectively. As seen in previous results, the spread in errors among S2S models is larger than the observational uncertainty.

4.6.2 Temperature

We would now like to understand the vertical structure of temperature anomaly (Figure 4.16). As discussed in Section 4.1, LPSs have a warm-over-cold structure; the cold core in

the lower troposphere is attributed to evaporative cooling due to precipitation and

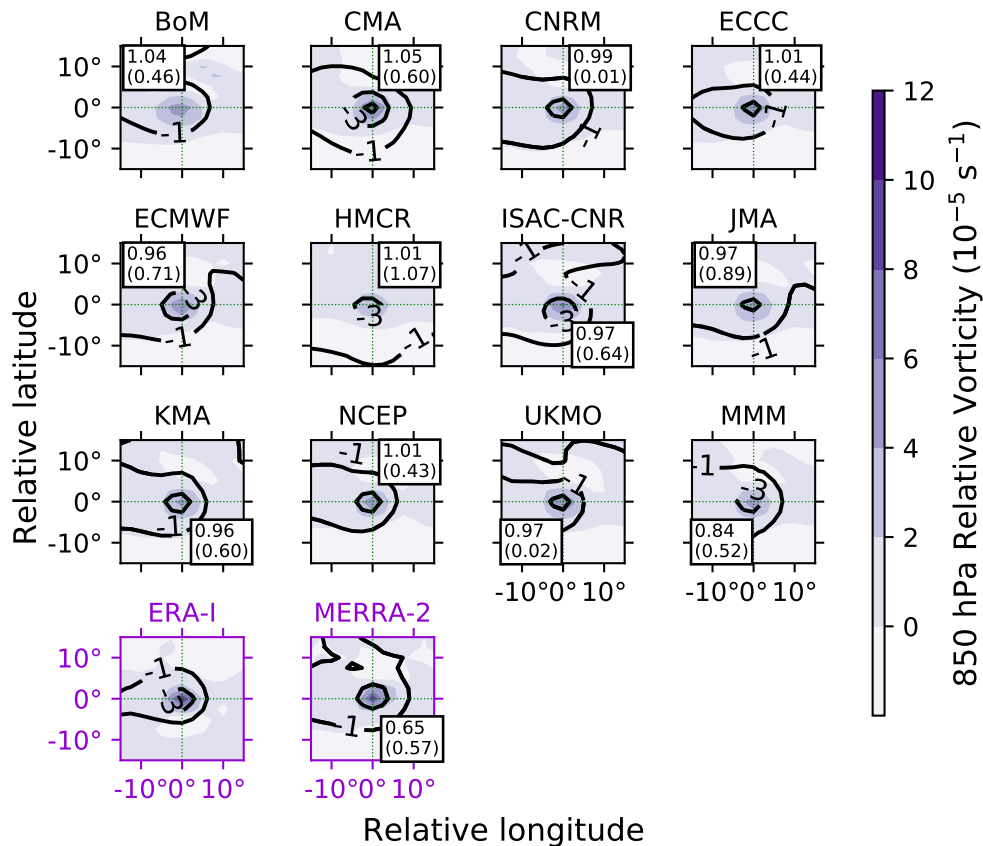


Figure 4.13: Storm-centred relative vorticity (10^{-5} s^{-1}) at 850 hPa in shaded contours and mean sea-level pressure anomaly (hPa) in line contours for composites of strong Indian monsoon low-pressure systems tracked in all ensemble members of eleven S2S models, ERA-Interim (ERA-I) and MERRA-2 reanalysis datasets during June–September 1999–2010. The anomaly is considered for forecast lead times of 0–15 days in all S2S models, and is computed against the summer mean climatology for S2S models and ERA-I. The multimodel mean (MMM) of S2S models is also shown. Numbers indicate the root mean square error in the 850 hPa relative vorticity (10^{-5} s^{-1}) and mean sea-level pressure anomaly (hPa, shown in brackets) between the respective S2S models and ERA-I. For MERRA-2, numbers represent root mean square error in the same fields, which is computed with respect to ERA-I.

reduced insolation due to significant cloud cover (Sarker and Chowdhury, 1988; Sørland and Sorteberg, 2015), whereas the warm-core is attributed to latent heating from deep convection (Ashok et al., 2000; Hunt et al., 2016b). All S2S models and the MMM simulate

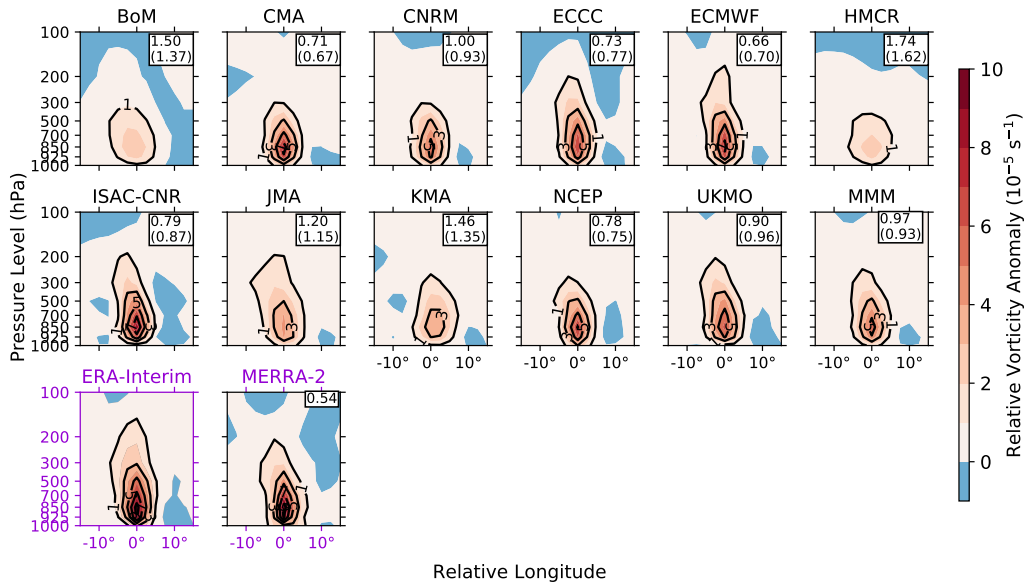


Figure 4.14: Vertical structure of relative vorticity anomaly (10^{-5} s^{-1}) of storm-centred composites of strong Indian monsoon low-pressure systems in all ensemble members of eleven S2S models, ERA-Interim and MERRA-2 reanalysis datasets during June–September 1999–2010. The anomaly is considered for forecast lead times of 0–15 days in all S2S models, and is computed against the summer mean climatology. The multimodel mean (MMM) of S2S models is also shown. The vertical structure is drawn above the zero-relative-latitude line in a horizontal composite. Numbers indicate the root mean square error in the relative vorticity anomaly (10^{-5} s^{-1}) between the respective S2S models and ERA-I, or against MERRA-2 in brackets. The number in MERRA-2 shows the root mean square error between MERRA-2 and ERA-I.

the upper-tropospheric warm core; however, there are biases in the simulation of its vertical extent. The composite warm core is shallower in the BoM, ECCC and JMA models than in other models. It is the weakest in the BoM, JMA and HMCR models, suggesting that either there is less convection or the convective scheme is producing less heating. The warm core is weaker in the MMM than in reanalyses. In contrast, models such as the ECMWF, ISAC-CNR, UKMO and NCEP simulate a strong warm core, whose magnitude is similar to that in ERA-I and MERRA-2. There is a strong positive and statistically significant (at the 95% confidence level) intermodel linear correlation (Pearson correlation coefficient of 0.74) between the maximum intensity of the warm core at 300 hPa and

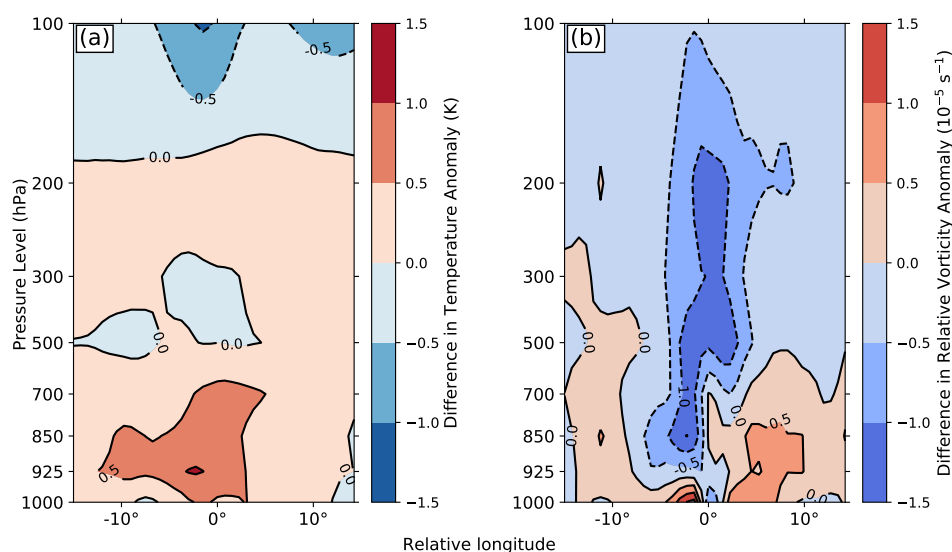


Figure 4.15: Vertical structures showing differences in: (a) temperature anomalies and (b) relative vorticity anomalies between MERRA-2 and ERA-Interim composites of strong Indian monsoon low-pressure systems during June–September 1999–2010. The vertical structures are drawn above the zero-relative-latitude line in a horizontal composite. The anomalies are computed against summer mean climatologies in the respective reanalysis dataset.

maximum precipitation within 800 km of the composite centre (Figure 4.11c).

Unlike for the warm core, there are larger biases in the simulation of the lower-tropospheric cold core. The HMCR model does not simulate the cold core. The most intense structure of the cold core in ERA-I, MERRA-2, ECCO, ECMWF and UKMO models is exactly above the composite centre; however, it is displaced in other S2S models and the MMM. Similar to the warm core, the cold core is shallower in the BoM and JMA models than in other models and reanalyses, which is due to the weak intensity of SLPSs. There is a moderate negative and statistically significant (at the 95% confidence level) intermodel linear correlation (Pearson correlation coefficient of -0.61) between the magnitude of the cold core (i.e., maximum 925 hPa temperature anomaly) and maximum precipitation within 800 km of the composite centre (Figure 4.11d), agreeing with findings of previous studies (Sarker and Chowdhury, 1988; Hunt et al., 2016a) that the develop-

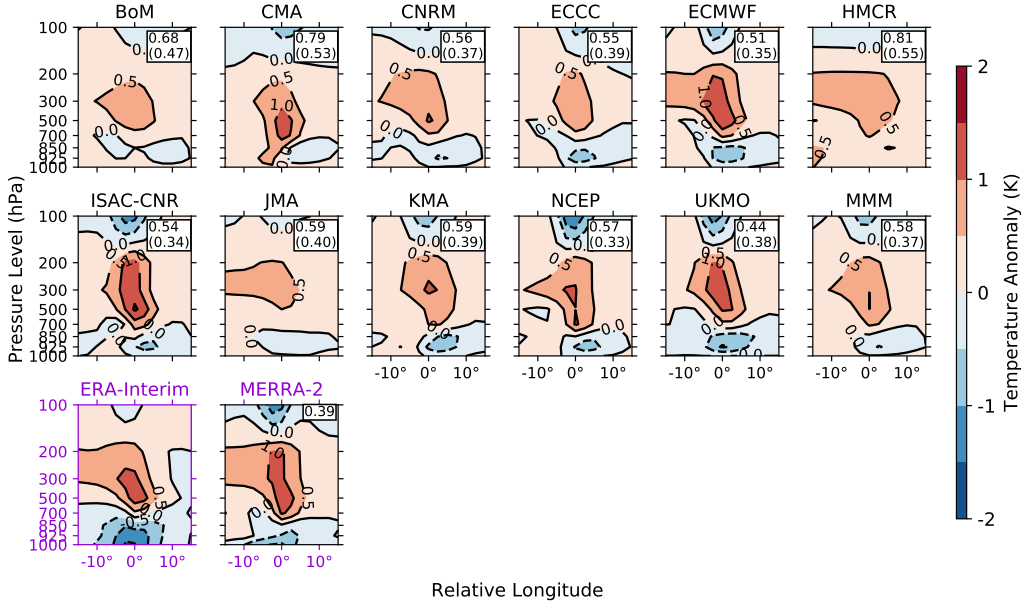


Figure 4.16: As Figure 4.14 but for temperature anomaly (K).

ment of the cold core is attributed to precipitation. This result also suggests that the general thermal structure is well captured in models featuring more accurate rainfall (e.g., NCEP). The UKMO and NCEP models feature the smallest root mean square error with respect to ERA-I and MERRA-2, respectively.

4.6.3 Moist static energy

We investigate the vertical structure of moist static energy (MSE) anomaly in this subsection. MSE is a useful thermodynamic parameter to understand moist convection since it is conserved under hydrostatic balance and moist adiabatic processes. It has been used to analyse LPSs in past studies (e.g., Karmakar et al. 2020). The MSE (h) is defined as:

$$h = c_{pd}T + q_vL + gz \quad (4.4)$$

where c_{pd} is the heat capacity of dry air at constant pressure, T is the temperature, q_v is the specific humidity, L is the latent heat of vaporization of liquid water, g is the

acceleration due to gravity and z is the altitude. We compute the gravitational contribution term gz from the geopotential height. The second term in this equation shows the importance of latent heating and its contribution to the first term that measures the dry-air enthalpy (Yano and Ambaum, 2017). Therefore, large values of MSE are related to more moisture content, which is associated with the intensity of LPSs. We could not compute MSE anomalies for the ISAC-CNR and KMA models since the specific humidity field is not available. The MSE anomaly in all models, the MMM, ERA-I and MERRA-2 (Figure 4.17) is maximum in the lower troposphere near the 850–700 hPa level. The MSE anomaly is the weakest in the HMCR, JMA and ECCC models, which does not exceed $3 \times 10^3 \text{ J kg}^{-1}$. The ECMWF and CNRM models feature anomalies of $6 \times 10^3 \text{ J kg}^{-1}$, which are similar to those in MERRA-2. However, the magnitude of the lower-tropospheric MSE anomaly is weaker in MERRA-2 than in ERA-I. Similar to the structure of relative vorticity anomaly (Figure 4.14) and temperature anomaly (Figure 4.16), the MSE anomaly structure shows a westward tilt with height in some models such as BoM and NCEP. The ECMWF and NCEP models feature the smallest RMSE error with respect to ERA-I and MERRA-2, whereas the BoM, HMCR and ECCC models feature large errors.

In conclusion, the ECMWF, NCEP and UKMO models have the best simulation of horizontal as well as vertical structures of SLPS composites, whereas the HMCR model has the worst.

4.7 Variability

In order to better represent various LPS processes in models, it is important to understand how the structure evolves with the LPS lifespan as well as forecast lead time of S2S models. Here, we focus on the evolution of 850 hPa relative vorticity, lower-tropospheric cold core and upper-tropospheric warm core since they have not been explored in previous studies. We consider these fields at the centre of LPSs. It should be noted that we consider LPSs

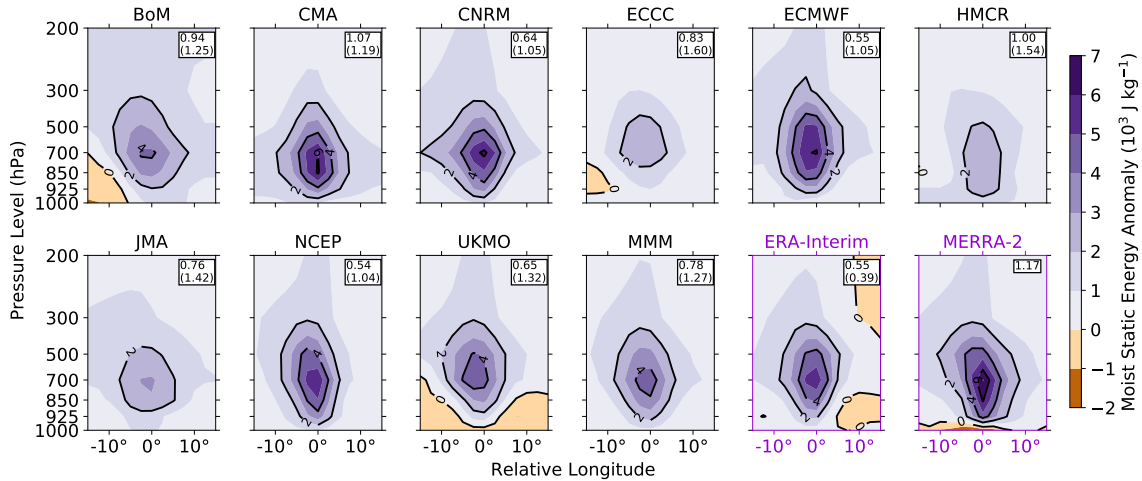


Figure 4.17: As Figure 4.14 but for moist static energy anomaly (10^3 J kg^{-1}). The results for the ISAC-CNR and KMA models are not shown due to the unavailability of the specific humidity field. Output for the 100 hPa level is not shown in ERA-I and MERRA-2 since it is not available in S2S models.

instead of SLPSs since we are interested in the lifetime evolution of these fields and we would not expect an SLPS to meet its vorticity threshold throughout its life.

4.7.1 Evolution over forecast lead time

Understanding how the structure of LPS varies with forecast lead time may provide insights into bias development and how modelled LPS could be better represented in the future. Figure 4.18 shows the evolution of 850 hPa relative vorticity anomaly, 925 hPa temperature anomaly (a measure of the cold core) and 300 hPa temperature anomaly (a measure of the warm core) for forecast lead times of 0–15 days. In the BoM (HMCR) model, the 850 hPa relative vorticity anomaly increases (decreases) with forecast time, and there is a prominent increase in the relative vorticity anomaly between forecast lead times of 3 and 10 days in the CMA model. The relative vorticity anomaly in the CMA model decreases after attaining the maximum magnitude at forecast lead times of ~ 5 days. We compute the estimated convective available potential energy (ECAPE; Ditchek et al. 2016) to understand the results. ECAPE is the difference between the surface moist static energy

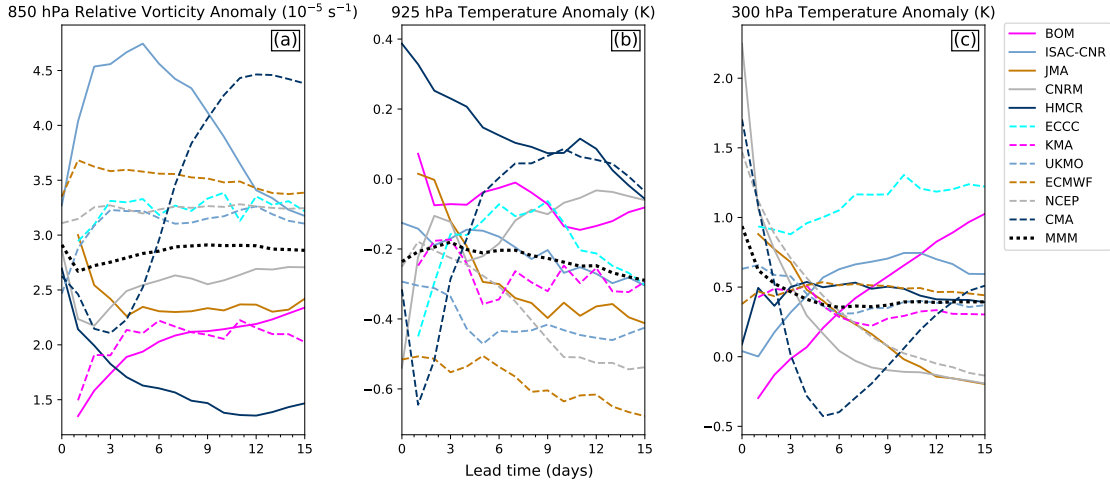


Figure 4.18: (a) Relative vorticity anomaly (10^{-5} s^{-1}) at the 850 hPa level, temperature anomalies (K) at (b) 925 hPa and (c) 300 hPa levels of composites of Indian monsoon low-pressure systems (LPSs) as a function of forecast lead time (days). These anomalies, which are computed against the summer mean climatology, are taken from the centre of LPSs tracked in all ensemble members of eleven S2S models during June–September 1999–2010. The anomalies are considered for forecast lead times of 0–15 days. The multimodel mean (MMM) is also shown. Step 0 is not available for the BoM, ECCC, JMA and KMA models.

and the upper-tropospheric vertically averaged saturation moist static energy. Ditchek et al. (2016) found that ECAPE has the largest anomalous contribution to the seasonal cycle of genesis of MDs. For illustration purposes, we will discuss the results for the CMA and HMCR models. Compared to forecast lead times of 0 to 5 days, the ECAPE in the CMA model increases by $6 \times 10^3 \text{ J kg}^{-1}$ over the monsoon core zone and head of the BoB during forecast lead times of 10 to 15 days (Figure 4.19a). This leads to an increase in the relative vorticity anomaly during forecast lead times of 10 to 15 days. In contrast, ECAPE difference between forecast lead times of 12 to 15 days and 0 to 3 days in the HMCR model is $-5 \times 10^3 \text{ J kg}^{-1}$ (Figure 4.19b), suggesting unfavourable conditions for LPSs during forecast lead times of 12 to 15 days.

Most models feature an intensification of the 925 hPa temperature anomaly with increasing forecast lead times. The intensification of the temperature anomaly in the HMCR model suggests that there is a tendency of more lysis of LPSs with increasing forecast lead

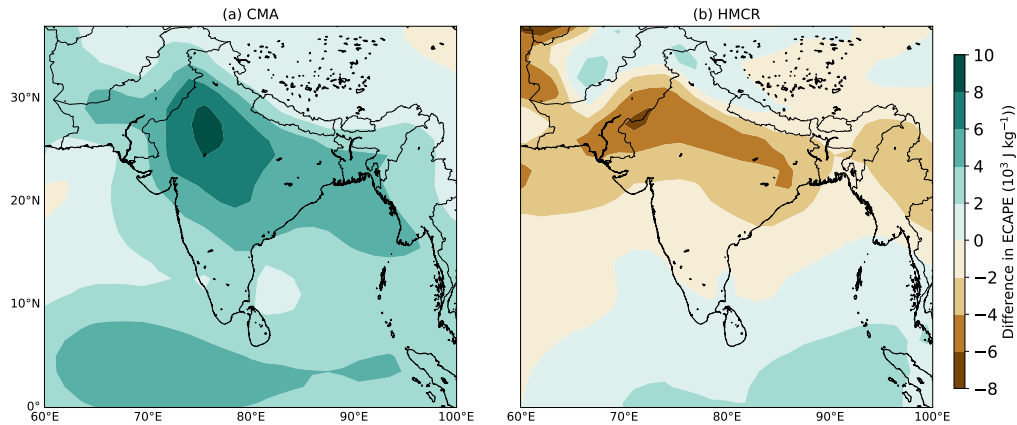


Figure 4.19: Difference in the estimated cape (ECAPE; 10^3 J kg^{-1}) for (a) CMA and (b) HMCR models during June–September 1999–2010. The difference in (a) is calculated for forecast lead times of 10 to 15 days minus 0 to 5 days, whereas that in (b) is calculated for forecast lead times of 12 to 15 days minus 0 to 3 days.

times—matured LPSs at longer lead times would have a cooler lower-troposphere than their younger counterparts. The CMA model shows anomalous warming in the lower troposphere after ~ 1 day forecast lead time, suggesting a significant proportion of young LPSs. This is also evident from the 300 hPa temperature anomaly that shows an increase from lead times of ~ 6 days onwards. Interestingly, the BoM model also shows anomalous warming at longer lead times at the 300 hPa level, suggesting a significant proportion of young LPSs.

In conclusion, the MMM is less sensitive to forecast lead time than individual S2S models.

4.7.2 Evolution over LPS lifespan

In order to fully compare various LPS processes in S2S models with observed behaviour, it is necessary to study the evolution of structure during LPS lifetime. We interpolate atmospheric fields of interest onto a common time axis since different LPSs can have a different lifespan. Here we construct a lifetime-percentage array, following Hunt et al.

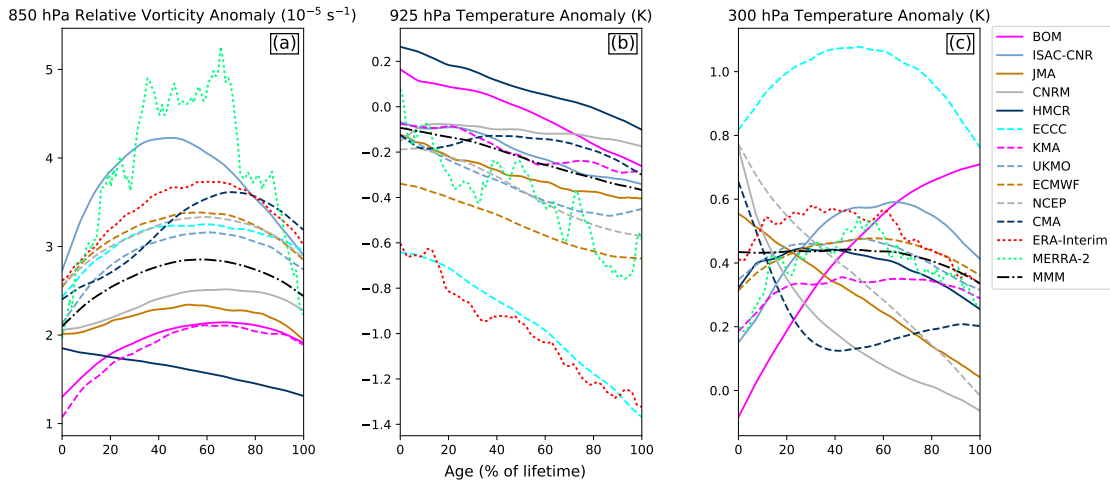


Figure 4.20: (a) Relative vorticity anomaly (10^{-5} s^{-1}) at the 850 hPa level, temperature anomalies (K) at (b) 925 hPa and (c) 300 hPa levels of composites of Indian monsoon low-pressure systems (LPSs) as a function of LPS lifespan (percentage) during June–September 1999–2010. These anomalies are computed against the summer mean climatology, and are considered for forecast lead times of 0–15 days. They are taken from the centre of LPSs tracked in all ensemble members of eleven S2S models, ERA-Interim and MERRA-2 reanalysis datasets. The multimodel mean (MMM) is also shown.

(2016a). We first calculate the percentage age of an LPS at each time step, with the first (final) time step denoting genesis (lysis) or 0% (100%) lifespan, and then interpolate fields for all such time steps on this array. We iterate this process for all LPSs, and finally compute a mean value for each S2S model, ERA-I and MERRA-2.

Most S2S models along with the MMM feature maximum 850 hPa relative vorticity anomalies around midlife (Figure 4.20), in agreement with ERA-I, MERRA-2 and previous findings (Hunt et al., 2016a). However, the CMA and HMCR models feature a different pattern. LPSs in the CMA model attain a maximum magnitude at $\sim 70\%$ lifespan, whereas those in the HMCR model do not feature a midlife maximum, suggesting that LPSs do not evolve in a realistic manner. As discussed in the previous subsection, ECAPE in the HMCR model is not favourable for the intensification or genesis of LPSs at longer lead times (Figure 4.19b), which seems to be preventing LPSs from attaining a midlife maximum. This is supported by findings of Chapter 3 (Deoras et al., 2021a), which suggest

that SLPSs in the HMCR model are not able to propagate inwards over the land (see lysis in Figure 3.5 of Chapter 3). The slightly delayed maximum anomaly in the CMA model is attributed to an increase in the relative vorticity during forecast lead times of 3 to 10 days, when LPSs having genesis in the early period of reforecasts would be in their mature phase. Similar to the findings for relative vorticity anomaly, many models, and ERA-I and MERRA-2 reanalyses feature a midlife maximum in the 300 hPa temperature anomaly. This is expected since latent heating due to convection would respond to the LPS intensity. However, BoM shows increasing temperature anomaly with increasing LPS lifespan, whereas CMA, JMA and NCEP show decreasing temperature anomaly. The influence of forecast lead time on these results is clear since the BoM model features increasing temperature anomalies, whereas the CMA, JMA and NCEP feature decreasing temperature anomalies with increasing forecast lead time (see Figure 4.18). The 925 hPa temperature anomalies intensify in all S2S models, ERA-I and MERRA-2 with increasing LPS lifespan. More mature LPSs are more likely to be found over land rather than sea. Since land has a lower heat capacity than sea, the effect of reduced insolation due to LPS-cloud cover becomes more prominent over land, resulting in greater cooling in the lower troposphere.

In conclusion, the BoM, CMA, HMCR and ISAC-CNR models have a high sensitivity to forecast lead time, whereas the MMM has a lower sensitivity than individual models. The evolution of fields with respect to LPS lifespan in the ECWMF, UKMO and NCEP models, which have the best simulation of horizontal as well as vertical structures, is most similar to ERA-I and MERRA-2. Therefore, these models and the MMM are useful for understanding LPS processes. The BoM, CMA, HMCR and ISAC-CNR models, most of which feature large biases in LPS tracks, may be of interest to the modelling community for further exploring the factors responsible for atypical evolution of fields.

4.8 Conclusions

Indian monsoon low-pressure systems (LPSs) are major rain-bearing cyclonic vortices that form during the summer monsoon season (June–September). Despite their important role for water supply and triggering floods, the simulation of their structure by numerical weather prediction models is not well understood. In this chapter, we analysed the simulation of the structure of strong LPSs (SLPSs) by eleven models of the Subseasonal-to-Seasonal (S2S) prediction project. Here, SLPSs are systems whose minimum intensity (central 850 hPa relative vorticity) reaches at least the 75th percentile of the population of all tracked LPSs in the respective S2S model or reanalysis dataset. These systems were analysed in all ensemble members of eleven S2S models during a common reforecast period of June–September 1999–2010 and for forecast lead times of 0–15 days. The results were verified against the European Centre for Medium-Range Weather Forecasts ERA-Interim (ERA-I) reanalysis and Modern-Era Retrospective Analysis for Research and Applications, version 2 (MERRA-2) datasets. The key results of this chapter can be summarised as follows:

The simulation of the circulation and summer mean precipitation

All S2S models and the multimodel mean (MMM) simulated the main features of the lower-tropospheric (850 hPa) monsoon circulation during the climatological period. They also simulated the intensification of the circulation when SLPSs were present. However, there were regional biases in some models such as BoM, NCEP and ECCC. We found dry precipitation biases over the monsoon core zone, northeastern India, head of the Bay of Bengal (BoB) and nearby coastal regions in the BoM and CMA models, which were associated with an easterly wind bias at the 850 hPa level. In contrast, the JMA and ECCC models simulated weak wet biases over the monsoon core zone, which were associated with a westerly wind bias. The precipitation contribution of LPSs to the summer monsoon

precipitation was smaller in all S2S models than in ERA-I. This was mainly due to biases in LPS precipitation in most S2S models. In summary, the CMA, ECMWF, HMCR, ISAC-CNR, JMA, KMA and UKMO models well simulated the monsoon circulation in general, and the MMM outperformed individual models for precipitation.

The simulation of the structure of SLPSs

We examined horizontal structures of precipitation, mean sea-level pressure (MSLP), wind and relative vorticity at 850 hPa for composites of SLPSs. There was a prominent underestimation of maximum precipitation and composite-mean precipitation in the HMCR model, which was associated with the weak intensity of SLPSs. Many models correctly simulated the location of maximum precipitation to the relative southwest of the centre, except for the CMA, ECCC, HMCR and ISAC-CNR models, which featured precipitation maximum to the relative south of the centre, coinciding with the maximum moisture-flux convergence at 850 hPa. The CMA, NCEP, ECMWF and ISAC-CNR (HMCR) models simulated the largest (smallest) relative vorticity as well as MSLP anomalies.

We found that the vertical structure of relative vorticity anomaly was shallower and weaker in all S2S models and the MMM than in ERA-I and MERRA-2. The upper-tropospheric warm core was shallow (i.e. eroded from the top) in the BoM, ECCC and JMA models. The HMCR model, which simulated a weak warm core, did not simulate the lower-tropospheric cold core. We also found that the moist static energy anomaly was the weakest in the HMCR, JMA and ECCC models, and the structure showed a westward tilt with height in some models such as BoM and NCEP. In summary, the ECMWF, NCEP and UKMO models had the best simulation of horizontal and vertical structures of SLPSs, whereas HMCR had the worst.

Evolution of fields

We examined the evolution of central 850 hPa relative vorticity and temperature anomalies at 925 hPa and 300 hPa as a function of both model lead time and LPS age. The BoM, CMA, HMCR and ISAC-CNR models were highly sensitive to forecast lead time due to variations in large-scale conditions such as the estimated convective available potential energy (Ditchek et al., 2016). There was an influence of the forecast lead time on the lifetime-evolution of fields in these models. However, other S2S models and the MMM featured midlife maxima in the 850 hPa relative vorticity anomaly and 300 hPa temperature anomaly, in agreement with Hunt et al. (2016a). The cold core in the lower-troposphere strengthened in all models and the MMM with increasing LPS age. This was likely due to the effect of reduced insolation due to cloud cover from older LPSs over land. This effect is more prominent over land than sea due to differences in heat capacities.

The results of this chapter demonstrate that S2S models simulate the structure of SLPSs, with the ECMWF, NCEP and UKMO models having the best simulation in general. These results, combined with the results of Chapter 3 (Deoras et al., 2021a), suggest that stakeholders could use S2S models for forecasting LPSs. The results of this study in particular would encourage the modelling community to carry out further investigations of factors such as biases in temperature anomalies in S2S models. In addition, the results would benefit meteorologists and hydrologists, who could use the S2S dataset for developing better products for forecasting SLPSs as well as their impacts. Since the tropical intraseasonal oscillation (ISO) strongly controls LPS frequency (Krishnamurthy and Ajayamohan, 2010), it is entirely plausible that LPS composites feature more intense structures during active phases of the ISO than during inactive phases. Vitart (2017) found that S2S models can skilfully predict the Madden-Julian Oscillation with a lead time of up to four weeks. The S2S models can also predict the Boreal Summer Intraseasonal Oscillation (BSISO) 1 and BSISO2 events with a lead time of up to 6–24.5 and 6.5–14 days,

respectively (Jie et al., 2017). However, an analysis of how this affects SLPS structure is beyond the scope of this study. Lastly, a role of the El Niño Southern Oscillation in modulating the frequency and LPS structure needs to be examined in the S2S dataset. In this study, we assumed that any bias in the results due to heterogeneity in the reforecast configuration was insignificant. This aspect could be investigated in a future study by determining the sensitivity of the results to the ensemble size and reforecast frequency. For example, SLPS structures could be intercompared in a range of ensemble members in each S2S model.

In this chapter, we have developed a framework that could be used to explore the structure of LPSs occurring over other regions. As previously discussed, BoB LPSs have been the main focus of LPS studies. As a result, LPSs occurring over other regions remain less explored. We would therefore like to use this framework to explore regional varieties of South Asian LPSs in the next chapter.

CHAPTER 5

THE FOUR REGIONAL VARIETIES OF SOUTH ASIAN MONSOON LOW-PRESSURE SYSTEMS

Opening remarks

This chapter is an expanded form of Deoras et al. (2021b). The published paper was constrained to a word limit of 4000 words. Hence, its sections were expanded to develop a full chapter for this thesis. Furthermore, an additional analysis on the modulation of Sri Lankan LPSs by ENSO and the IOD has been included in this chapter (Section 5.7).

5.1 Introduction

As discussed in previous chapters, LPS studies have extensively explored characteristics of Bay of Bengal (BoB) monsoon depressions. However, it is known that LPSs can form over other regions of South Asia such as the Arabian Sea (e.g., Seetaramayya and Master 1984). Krishnamurthy and Ajayamohan (2010) examined the climatology of LPSs that formed over the Arabian Sea during June–September 1888–2003, for which they used the LPS dataset compiled by Mooley and Shukla (1987) and Sikka (2006) from weather

reports published by the India Meteorological Department. They found that these systems formed off the western coast of India and moved generally northwestwards. Their frequency was largest in June and they were concentrated near Kutch and the Saurashtra coast of Gujarat in western India in July. They were responsible for producing intense rainfall over the western coast of India by strengthening the lower-tropospheric monsoon circulation. In addition to the Arabian Sea, LPSs can form near the southeastern coast of Sri Lanka during the boreal summer season (e.g., Fine et al. 2016), and these systems have triggered catastrophic floods in Sri Lanka in the past (e.g., Rodrigo et al. 2018; Koralegedara et al. 2019).

Hunt and Fletcher (2019) analysed the relationship between summer monsoon precipitation and Arabian Sea, BoB and Sri Lankan LPSs. BoB LPSs were named BoB-short or BoB-long depending on the track length. They defined short-lived BoB LPSs (BoB-short) as those that are confined to east India, in contrast to long-lived BoB LPSs (BoB-long) that propagate across the peninsula, reaching western and northwestern parts of India. Whilst BoB-short LPSs produced most climatological precipitation over India, BoB-long LPSs, Arabian and Sri Lankan were important for producing precipitation over north-west India, Pakistan and Sri Lanka respectively. Despite the important role of these four regional varieties of South Asian monsoon LPSs, we remain without a proper understanding of their track characteristics, structure and predictability, the results of which could benefit meteorologists, researchers, farmers and governments in the Indian subcontinent.

As discussed in Section 1.1.3, the BoB LPS activity is modulated by modes of tropical intraseasonal variability such as the Madden-Julian Oscillation (MJO). Haertel and Boos (2017) found that the climatology of LPSs is not sensitive to the amplitude of the MJO. However, their frequency is modulated by MJO phase, with phases 4–6 supporting genesis of LPSs in general. Since the MJO can be well predicted at long lead times of up to four weeks (e.g., Vitart 2017), meteorologists could consider the MJO-LPS relationship for predicting the occurrence of LPSs well in advance. For monitoring the northward-propagating

component of the tropical intraseasonal oscillation (ISO) over the Indian region, Suhas et al. (2013) proposed the Monsoon Intraseasonal Oscillation (MISO) index. Their main objective was to eliminate contaminations from the westward propagating 10–20 day mode of the ISO as well as synoptic-scale disturbances. Unlike for the MJO, formal relationships between LPS frequency and the BSISO and MISO indices have not been explored in the past. Moreover, the detailed behaviour of the four LPS varieties during all phases of the ISO has not been examined. Whilst previous studies have examined the modulation of BoB LPSs by ENSO and IOD (Singh et al., 2002; Hunt et al., 2016a), their impact on Sri Lankan LPSs remains unknown. In this chapter, our aim is to understand the following aspects:

- What are the differences between track statistics for the four LPS regional varieties?
- Are there important structural or thermodynamical differences between the different LPS varieties?
- How much precipitation is contributed by each LPS variety to the seasonal mean precipitation?
- How does the ISO, as measured by the BSISO, MISO and MJO indices, modulate LPS activity of each variety?
- How do ENSO and IOD modulate Sri Lankan LPSs?

We present an outline of the data and methodology in Section 5.2. We look at the track statistics in Section 5.3, vertical structures in Section 5.4, precipitation contribution in Section 5.5, and the modulation of LPSs by the ISO in Section 5.6. We then explore the modulation of Sri Lankan LPSs by ENSO and IOD in Section 5.7 and finally conclude in Section 5.8.

5.2 Data and methods

5.2.1 LPS catalogue

We use an LPS catalogue that was created by Hunt and Fletcher (2019); it is available at http://gws-access.jasmin.ac.uk/public/incompass/kieran/track_data/lps-tracks_v2.1.2_1979-2019.csv. In this catalogue, LPSs were identified in ERA-I using a feature-tracking algorithm discussed in Section 2.2.1. The LPS tracks were then partitioned into four clusters using a k -means clustering technique (MacQueen et al., 1967). The k -means clustering technique is an iterative process that groups points of a dataset into a fixed number of clusters (k). The algorithm first identifies the number of centroids (k) in a dataset, and then assigns each data point to its nearest centroid. New centroids of these k clusters are determined, following which data points are reassigned to their closest centroid. This process continues until the allocation of data points to k clusters is not changing anymore. We note that there are many methods to determine the optimal number of clusters, such as elbow and silhouette methods. However, Hunt and Fletcher (2019) determined the optimal number of clusters by plotting LPS tracks for an increasing number of clusters and determining if a further increase in them caused prominent differences in LPS tracks. We follow the same process for determining the optimal number of clusters in Section 6.2.2. We retain only those LPSs that had their genesis during June–September 1979–2018 since ERA-I data for September 2019 is not available. The processed LPS dataset is available at <https://zenodo.org/record/4572900#.YjHFjhDP2CQ>.

5.2.2 ERA-Interim and TRMM

For analysing vertical structures of the four LPS varieties, we use 27 output pressure levels of ERA-I from 1000 hPa to 100 hPa. A full description of ERA-I is already provided in Section 2.1.2 and will not be repeated here. For determining the precipitation contribution of each LPS variety, we consider the TRMM 3B42 version 7 dataset, which is already

discussed in Section 2.1.5.

5.2.3 BSISO, MISO and MJO indices

The MJO indices (Wheeler and Hendon, 2004) were obtained from the Bureau of Meteorology, Australia and can be accessed at <http://www.bom.gov.au/climate/mjo/graphics/rmm.74toRealtime.txt>. The MISO indices (Suhas et al., 2013) were downloaded from the Indian Institute of Tropical Meteorology, Pune and are available at https://www.tropmet.res.in/erpa/files/miso_data.php. The BSISO indices (Kikuchi and Wang, 2010; Kikuchi et al., 2012; Kikuchi, 2020) were obtained from http://iprc.soest.hawaii.edu/users/kazuyosh/Bimodal_ISO.html. Each index has daily frequency, and is separated into eight phases that represent different geographical locations (e.g., phases 2–3 of the MJO represent enhanced convection over the Indian Ocean, whereas phases 2–3 of the BSISO and MISO represent enhanced convection over the Indian Ocean-East Asia region and central India, respectively). The three indices are computed from different fields and over different regions—outgoing longwave radiation (OLR) and zonal wind anomalies (averaged over 15°S–15°N) at 850 hPa and 200 hPa are considered for the MJO; OLR and zonal wind at 850 hPa (over 10°S–40°N, 40°E–160°E) are considered for the BSISO; and daily rainfall data (over 12.5°S–30.5°N, 60.5°E–95.5°E) is considered for the MISO. The MJO index is computed for all months, whereas the BSISO (MISO) index is computed for May to October (June to September). From the common period of June–September 1998–2018, only those dates on which an index exceeds one standard deviation have been considered, in order to be able to cleanly identify the phase at a given instant. There are: 4, 5 and 7 Arabian LPSs; 47, 49 and 47 BoB-short LPSs; 22, 21 and 31 BoB-long LPSs; and 25, 26 and 23 Sri Lankan LPSs for which the amplitude of the BSISO, MISO and MJO respectively is less than one. Following convention, we refer to such LPSs as belonging to phase zero.

5.2.4 ENSO and IOD indices

We use the NOAA ERSSTv5 sea surface temperature (SST) dataset to compute ENSO and IOD indices. Details of this dataset and the computation of ENSO and IOD indices are already given in Sections 2.1.7 and 2.1.8 respectively.

5.2.5 Significance testing

We perform the independent t-test (e.g., Snedecor and Cochran 1989) to determine if the vertical composite of an LPS variety is significantly different from the all-LPS composite. Our null hypothesis, which is in relation to the second research question of this chapter, states that an LPS variety and the all-LPS composite have identical average values. Thus, areas where a 95% significance level is not satisfied are coloured grey in the corresponding figure.

5.3 Track statistics

In this section, we discuss the frequency, track characteristics and track density of the four LPS varieties. These results could benefit meteorologists in forecasting LPSs and encourage researchers to carry out further investigation.

5.3.1 Frequency and track characteristics

During June–September 1979–2018, there are 22 Arabian, 229 BoB-short, 135 BoB-long and 119 Sri Lankan LPSs. Table 5.1 shows the statistics for these four LPS varieties. BoB-short LPSs have the largest frequency of 5.7 (± 1.7) systems per season, whereas Arabian LPSs have the smallest frequency of 0.6 (± 0.8) systems per season. The figures in brackets indicate one standard deviation from the mean. BoB-long and BoB-short LPSs have mean durations of 7.6 and 7.3 days respectively, which are larger than those of Arabian and Sri Lankan LPSs. The mean track length and mean intensity (850 hPa relative vorticity at

Variety	Number per season	Mean track duration (days)	Mean track length (km)	Mean propagation speed (m s^{-1})	Mean 850 hPa relative vorticity (10^{-5} s^{-1})
Arabian	0.6 (0.8)	6.1	1105	2.5	5.3
BoB-long	3.4 (1.6)	7.6	1370	2.4	5.8
BoB-short	5.7 (1.7)	7.3	796	1.5	5.0
Sri Lankan	3.0 (1.4)	5.0	629	1.5	3.3

Table 5.1: Statistics for the four regional varieties of South Asian monsoon low-pressure systems during June–September 1979–2018. Figures in brackets indicate the population standard deviation from the mean. The mean 850 hPa relative vorticity is taken from the centre of systems.

the system centre) of BoB-long LPSs are the largest among all LPS varieties. Arabian LPSs have the fastest mean propagation speed of 2.5 m s^{-1} ; whereas BoB-short as well as Sri Lankan LPSs have the slowest mean propagation speed of 1.5 m s^{-1} .

All four LPS varieties can form throughout the summer monsoon season (Figure 5.1); the frequency of BoB-short as well as BoB-long LPSs is larger in July and August than in June and September, in agreement with Krishnamurthy and Ajayamohan (2010). The frequency of BoB-short LPSs is largest in July and smallest in September, whereas that of BoB-long LPSs is largest in August and smallest in June. The frequency of Arabian LPSs is largest in June, agreeing with the findings of Krishnamurthy and Ajayamohan (2010), and smallest in July. In our analysis period, 8 out of 13 Arabian LPSs formed during 1–7 June, which is the typical monsoon onset period over Kerala. This suggests that these LPSs are related to the monsoon onset vortex (e.g., Krishnamurti et al. 1981). The conditions over the Arabian Sea for LPS genesis are more favourable in June than in other months. The position of the Somali jet is further towards the equator in June than in other months of the summer monsoon season. Since there is positive (negative) low-level vorticity poleward (equatorward) of the axis of the jet, the positive low-level vorticity over the genesis region reaches a maximum value in June, supporting genesis of Arabian LPSs (Evan and Camargo, 2011). In contrast, Sri Lankan LPSs are least common in June, but

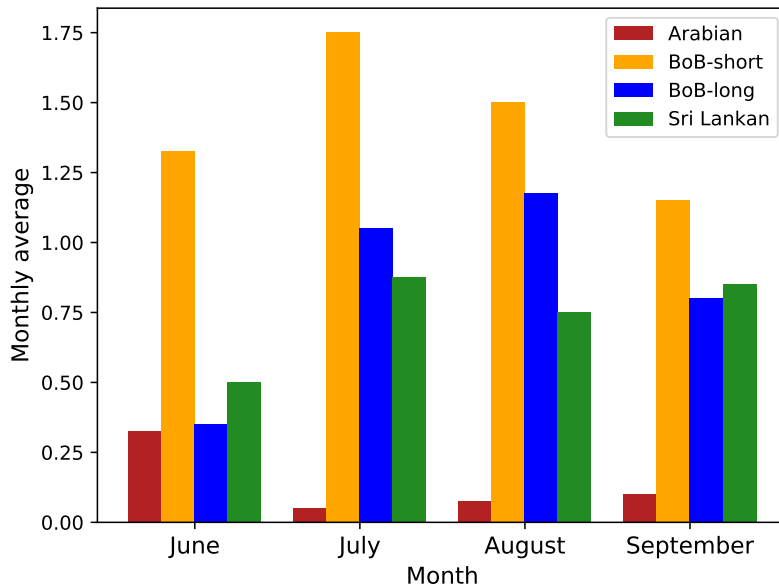


Figure 5.1: The monthly average genesis frequency of the four regional varieties of South Asian monsoon low-pressure systems during June–September 1979–2018.

most common in July.

We now investigate if there is any linear correlation between the interannual frequency of these LPS varieties (Figure 5.2). The interannual Pearson correlation coefficient between frequencies of BoB-short and BoB-long LPSs is -0.52 , which is significant at the 95% level, suggesting that large-scale conditions that benefit one might suppress the other. The correlation between interannual frequencies of Arabian and Sri Lankan LPSs is 0.25 , but it is not significant at the 95% level. The correlation for other cases is small in magnitude and not significant at the 95% level.

5.3.2 Track density

Figure 5.3 shows the track density of each LPS variety during June–September 1979–2018. Following Chapter 3, we calculate the track density by a kernel density estimation (KDE) technique. We first construct a smooth probability density estimate for the centre of an LPS track at each time step. This process is iterated for all LPSs of an LPS variety. We

BoB-long	1.00	-0.52	0.14	-0.11
BoB-short	-0.52	1.00	0.08	-0.06
Arabian	0.14	0.08	1.00	0.25
Sri Lankan	-0.11	-0.06	0.25	1.00
	BoB-long	BoB-short	Arabian	Sri Lankan

Figure 5.2: A matrix showing the interannual Pearson correlation coefficient between frequencies of the four regional varieties of South Asian monsoon low-pressure systems during June–September 1979–2018. The correlation strength is indicated by the colour scale, with dark blue colour showing a strong positive correlation and burnt orange colour showing a moderate negative correlation.

then multiply probability density estimates by the total number of LPSs to get a track density for an LPS variety.

The track density of BoB-short as well as BoB-long LPSs is at a maximum over eastern India, where there are about 8 LPSs per square degree for the 40-year period. These two LPS varieties share a common genesis location over the head of the BoB, but there is a clear difference in their lysis locations. Most Sri Lankan LPSs remain confined to the Sri Lankan region and their peak track density is similar in magnitude to that of BoB-long LPSs. However, some Sri Lankan LPSs reach southern parts of India. In contrast, Arabian LPSs have the smallest peak track density of 0.1–0.2 LPSs per square degree for the 40-year period. They feature a northwestward propagation in general, but some of them cross the western coast of India, agreeing with the findings of Krishnamurthy and Ajayamohan (2010).

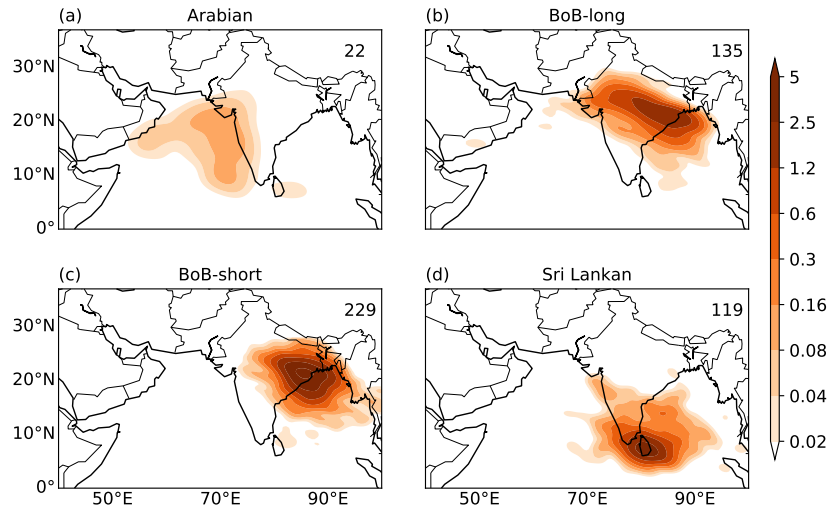


Figure 5.3: The track density of the four regional varieties of South Asian monsoon low-pressure systems (LPSs). The track density is calculated using a kernel density estimation technique. The total number of LPSs belonging to each variety is shown in each subplot. The unit of track density is LPS transits per square degree for June–September 1979–2018.

5.4 Vertical structure of temperature and moisture

In this section, we examine the composite vertical structure of temperature and moisture for each LPS variety. These results could benefit researchers in understanding the structural differences between different LPS varieties, encouraging them to carry out further investigation. We consider equivalent potential temperature (θ_e) instead of specific humidity or relative humidity since it provides an understanding of moist processes in LPSs from a thermodynamic perspective.

Figure 5.4 shows the vertical structure of temperature anomaly and equivalent potential temperature anomaly of composites of each LPS variety. Since LPS frequency shows a large variability on the monthly timescale, we consider a monthly climatology instead of a seasonal climatology. We first compute a climatology for each month during June–September 1979–2018, and then calculate anomalies against the climatology of the respective month. Following Chapter 4 (Deoras et al., 2022), LPSs of each variety are centred on 0° relative latitude and 0° relative longitude at each time step. The vertical

structure is then drawn above the zero-latitude line in a horizontal composite. Thus, relative west is to the left and relative east is to the right of 0° relative longitude.

The warm-over-cold core structure, which we discussed for composite LPSs in S2S models and reanalyses in Section 4.6.2, is seen in each LPS variety; the magnitude of the warm core is largest in Arabian LPSs (Figure 5.4a), implying greater latent heating and precipitation from deep convection than in other types of LPSs, whereas it is the smallest in Sri Lankan LPSs (Figure 5.4d). The warm core is located at the same pressure level in BoB-long and BoB-short LPSs. However, its peak magnitude at about 500 hPa is larger by 0.2 K in BoB-long LPSs than in BoB-short LPSs. In Sri Lankan LPSs, the warm core does not extend into the upper troposphere as evidenced by negative temperature anomalies above 300 hPa. BoB-long LPSs feature the strongest cold core, which sits right at the composite centre and extends up to the 700 hPa level. BoB-short LPSs feature a similar cold-core structure, but the magnitude is smaller than that of BoB-long LPSs. Arabian LPSs feature a weaker cold-core structure; their cold core is elevated, and there are maximum anomalies between 850 hPa and 700 hPa. Similar to the warm core, the magnitude of the cold core of Sri Lankan LPSs is the smallest among all LPS varieties, and the maximum anomaly is located below the 925 hPa level. The weak thermal structure of Sri Lankan LPSs is attributed to the weak intensity of these systems.

We now investigate the vertical structure of θ_e . Large values of θ_e anomaly for LPSs imply strong latent heating from deep convection, which is attributed to intense LPSs having a large moisture content. The maximum in θ_e is located at a lower altitude than that in temperature anomaly, suggesting that all four LPS varieties have a maximum moisture content in the lower troposphere. This agrees with the findings of Chapter 4 (Section 4.7.1) and previous studies (e.g., Hunt et al. 2016a). Arabian LPSs feature largest anomalies of 8 K, while Sri Lankan LPSs feature smallest anomalies of 2 K. Thus, these results are consistent with the observed intensity of the four LPS varieties.

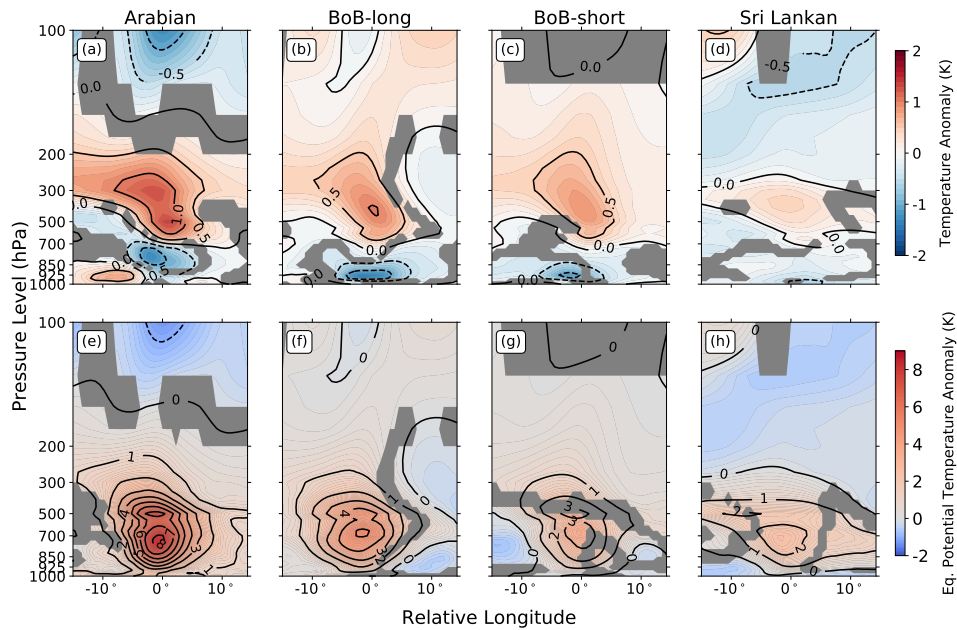


Figure 5.4: (a)–(d) Vertical structure of temperature anomaly (K), and (e)–(h) equivalent potential temperature anomaly (K) of storm-centred composites of the four regional varieties of South Asian monsoon low-pressure systems during June–September 1979–2018. Solid contour lines indicate positive anomalies, whereas dashed contour lines indicate negative anomalies. Coloured contours are greyed out where an LPS composite does not significantly differ from the all-LPS composite at the 95% level.

5.5 Precipitation contribution

In this section, we calculate the precipitation contribution of the four LPS varieties to the seasonal mean precipitation (June–September). This result could benefit meteorologists and flood forecasters in designing forecasting products for hydrological services. Following Hunt and Fletcher (2019), we attribute precipitation to an LPS if it falls within a distance of 800 km from the LPS centre at each time step.

Figure 5.5 shows the precipitation contribution and the mean track of each LPS variety. BoB-short and BoB-long LPSs produce up to 70% of the seasonal precipitation over eastern parts of India in total. BoB-short LPSs have the largest precipitation contribution over the western Bay of Bengal and adjoining east India. They cause more than 40% of the

seasonal precipitation over this region and 10–30% of the seasonal precipitation over parts of central India, Bhutan, southern Tibet, Nepal, Bangladesh and western Myanmar. BoB-long LPSs also cause rainfall over eastern India, but the attributed rainfall is smaller due to the faster propagation, longer tracks and smaller frequency than those of BoB-short LPSs. We note that 10–30% of the seasonal precipitation over parts of Pakistan and central, western and northwestern parts of India is attributed to BoB-long LPSs. Over southern parts of Afghanistan and adjoining eastern Iran, the attributed precipitation exceeds 40%.

Sri Lankan LPSs are responsible for 20–40% of the seasonal rainfall over Sri Lanka and adjoining parts of southeast India. In fact, the attributed precipitation exceeds 40% over northern Sri Lanka. In contrast, Arabian LPSs provide a very low precipitation contribution of up to 20% over the central Arabian Sea and less than 10% over the west coast of India and Pakistan. While our results agree with Hunt and Fletcher (2019) in general, we find a larger precipitation contribution from Sri Lankan and smaller precipitation contribution from Arabian LPSs than their results.

5.6 Modulation of LPS activity by the ISO

In this section, we investigate how the ISO modulates the frequency of the four LPS varieties. Since the ISO can be well predicted on the subseasonal time scale (e.g., Fu et al. 2007), a better understanding of the ISO-LPS relationship could help in providing useful LPS forecasts with lead times of several weeks, which will benefit weather-dependent socioeconomic sectors. Figure 5.6 shows the anomalous occurrence of the four LPS varieties in each phase of the BSISO, MISO and MJO during June–September 1998–2018. The anomalous occurrence is a ratio of the difference between the number of LPSs whose genesis occurs in each phase and the climatological expected value of LPSs in all phases to the climatological expected value of LPSs in all phases. Thus, a 0% value indicates that the

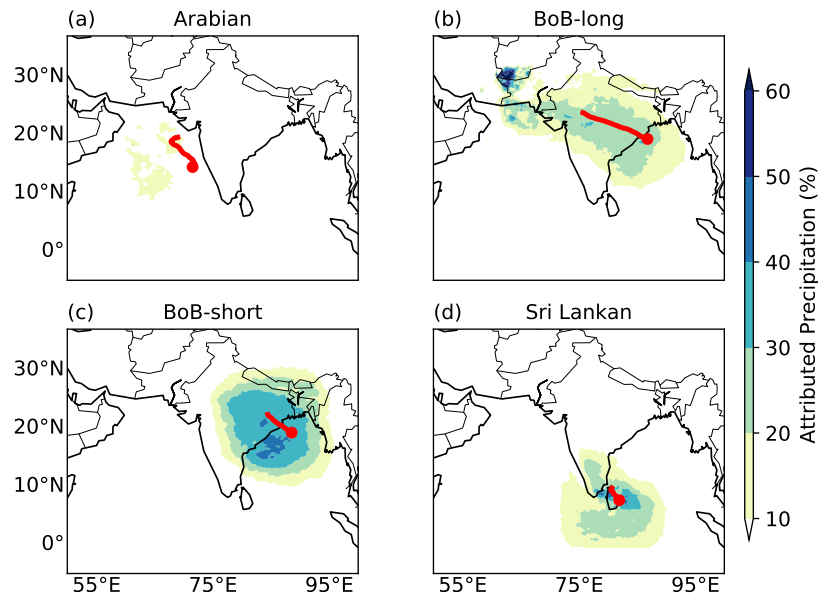


Figure 5.5: Percentage of seasonal (June–September 1998–2018) precipitation attributed to the four regional varieties of South Asian monsoon low-pressure systems. A solid red line shows the mean track of each variety, whereas a red dot shows the genesis location. Rainfall is attributed to a system if it falls within 800 km of its centre.

frequency of occurrence of LPSs equals the climatological expected value, 100% indicates twice that of the climatological expected value, and -100% indicates no occurrence of LPSs. The spatial pattern of convective anomalies in a given phase of the MISO is similar to that in the BSISO five phases earlier. Hence, MISO phases in Figure 5.6 have been offset by five phases to align them with the corresponding BSISO phases.

BoB-long and BoB-short LPSs form during all phases of the BSISO, MISO and MJO. However, Arabian LPSs are only found to form during BSISO phases 2–4, MISO phases 1, 3 and 8, and MJO phases 1–3. Sri Lankan LPSs form only during BSISO phases 1–4 and 7–8, MISO phases 1–2 and 4–8, and MJO phases 1–4 and 6–8. Their frequency peaks in BSISO phases 2–3 and MISO phases 7–8. The anomalous frequency of Arabian and Sri Lankan LPSs is maximum in MJO phases 1–2, when convection is over the Indian Ocean and adjoining east Africa. BoB systems follow a similar pattern, but their frequency peaks several phases later as the ISO propagates northward. Since the frequency of Arabian LPSs

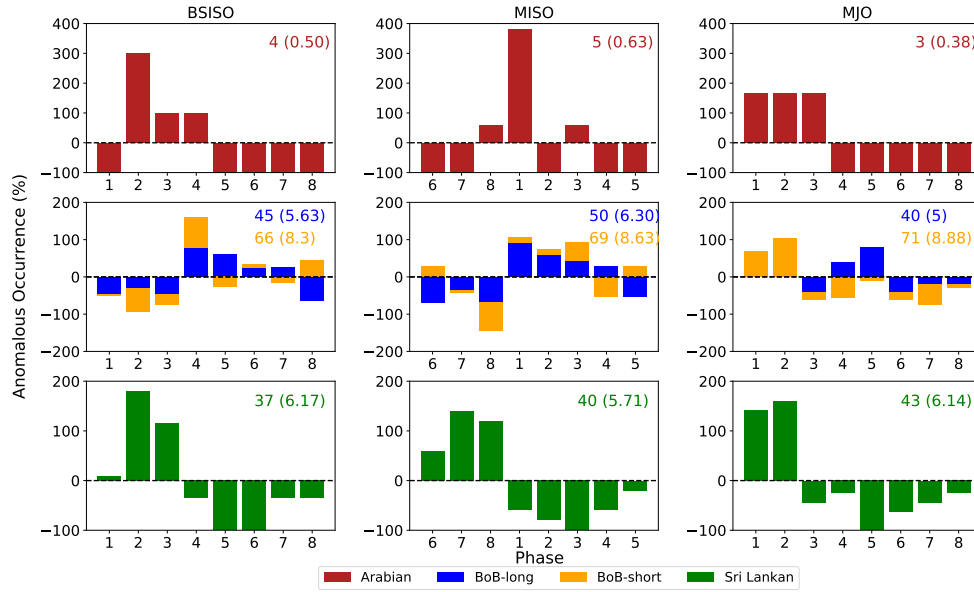


Figure 5.6: Anomalous occurrence (%) of the four regional varieties of South Asian monsoon low-pressure systems (LPSs) during phases of the Boreal Summer Intraseasonal Oscillation (BSISO), Monsoon Intraseasonal Oscillation (MISO), and Madden-Julian Oscillation (MJO) over June–September 1998–2018. Numbers in subfigures indicate the total number of LPSs. A 0% value indicates that the frequency of occurrence of LPSs equals the climatological expected value (shown in brackets in each subfigure), whereas 100% indicates twice that of the climatological mean value. A -100% value indicates no occurrence of LPSs. Only those LPS occurring during BSISO, MISO or the MJO in which the amplitude exceeds one standard deviation are retained. The MISO phases have been phase-shifted by 5 to align with the corresponding BSISO phases. See Sections 5.1 and 5.2.3 for definitions. Bars for BoB-long and BoB-short LPSs are not subdivided—they represent the sum of individual changes to these LPS varieties. Note the different y -axes in subfigures for Arabian, BoB and Sri Lankan LPSs.

is very small, the ISO controls them more strongly than BoB and Sri Lankan LPSs.

We perform a composite analysis of 500 hPa specific humidity, 850 hPa vector wind and 700 hPa vertical velocity for all phases of the BSISO, MISO and MJO to understand the results. These parameters are important for deep convection and genesis of LPSs (e.g., Sikka 1978). Figures 5.7, 5.8 and 5.9 show anomalies of 500 hPa specific humidity (coloured contours) and 700 hPa vertical velocity (line contours) for different phases of the BSISO, MISO and MJO, respectively, whereas Figures 5.10, 5.11 and 5.12 show 850

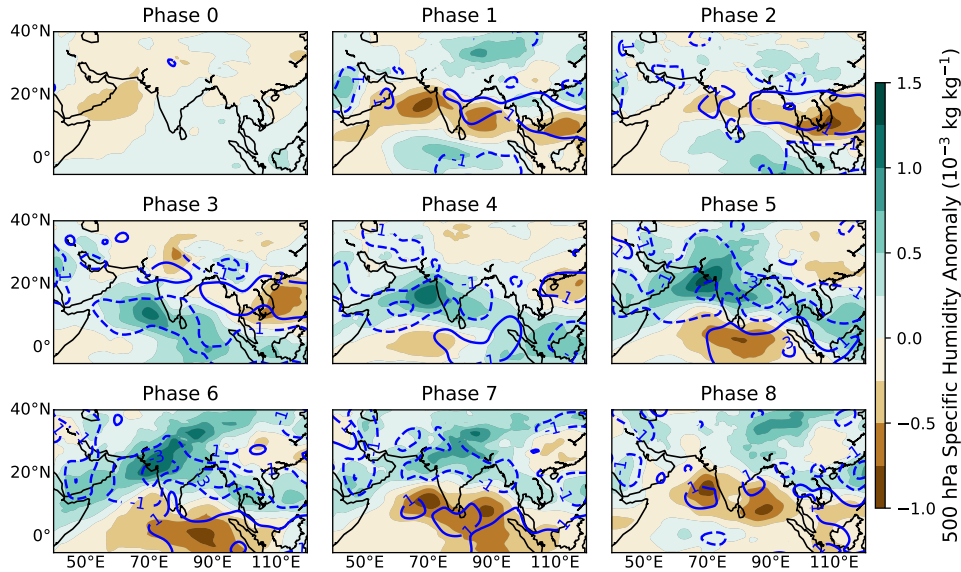


Figure 5.7: 500 hPa specific humidity anomaly ($10^{-3} \text{ kg kg}^{-1}$) in coloured contours and 700 hPa vertical velocity anomaly ($10^{-2} \text{ Pa s}^{-1}$) in line contours for all phases of the Boreal Summer Intraseasonal Oscillation (BSISO) during June–September 1998–2018. The anomalies are computed against the summer mean climatology (June–September 1979–2018). The vertical velocity anomalies are smoothed using a 2-D Gaussian filter with a standard deviation of $\sim 200 \text{ km}$. Solid (dashed) contour lines indicate anomalous descent (ascent). Coloured and line contours are not shown where the mean surface pressure is less than 500 hPa and 700 hPa respectively. Phase 0 represents BSISO events featuring an amplitude less than one.

hPa wind anomalies. All anomalies are computed against a summer mean climatology (June–September 1979–2018). In BSISO phase 1 and MISO phase 6, positive specific humidity anomaly and anomalous ascent first appear to the south of Sri Lanka and there is a cyclonic shear over Sri Lanka. In BSISO phases 2–4 and MISO phases 1 and 7–8, these anomalies are seen over Sri Lanka and adjoining parts of the Arabian Sea, which favour genesis of Sri Lankan and Arabian LPSs in general (Figure 5.6). In subsequent phases, these anomalies intensify and propagate northward/northeastward, favouring genesis of BoB systems. While convection is active over the BoB, negative specific humidity anomalies and anomalous descent develop over Sri Lanka and adjoining parts of the Arabian Sea, which suppress the frequency of these two LPS varieties. The negative anomalies

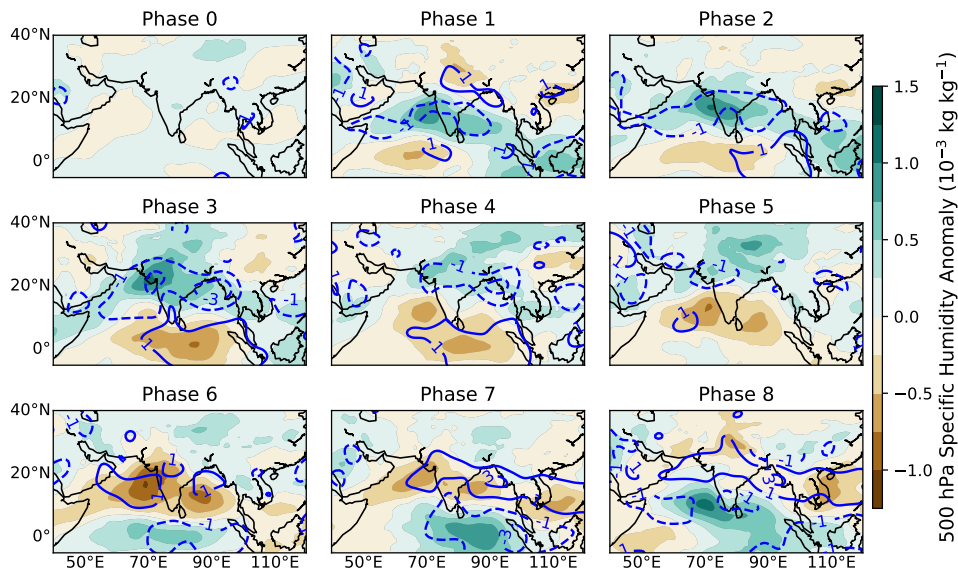


Figure 5.8: As in Figure 5.7, but for all phases of the Monsoon Intraseasonal Oscillation. Note the different contour interval for 500 hPa specific humidity anomaly than shown in Figure 5.7.

propagate in a similar manner, suppressing frequency of BoB systems several phases later. For the MJO, anomalous positive specific humidity anomalies, anomalous ascent and cyclonic shear over the western Indian Ocean (i.e., Arabian Sea and Sri Lanka) in phases 1 and 2 favour genesis of Arabian and Sri Lankan LPSs. These anomalies then propagate eastwards favouring BoB LPSs and suppressing Arabian as well as Sri Lankan LPSs.

Since BoB-short and BoB-long LPSs form over the same region and have similar features, the latter could be considered as an extension of the former. Therefore, we now try to understand if the ISO forcing has any role in evolving BoB-short LPSs into BoB-long LPSs. We focus on the BSISO and MJO in order to understand the impact of the two different components of the ISO. Krishnan et al. (2011) investigated long-lived BoB monsoon depressions during the 2006 positive Indian Ocean Dipole event. They found that lifespan of these systems was enhanced due to an increase in barotropic instability of the large-scale monsoon flow, moisture over the Bay of Bengal, and mid-level flows entering the stratiform rain region. They concluded that barotropic instability was enhanced due

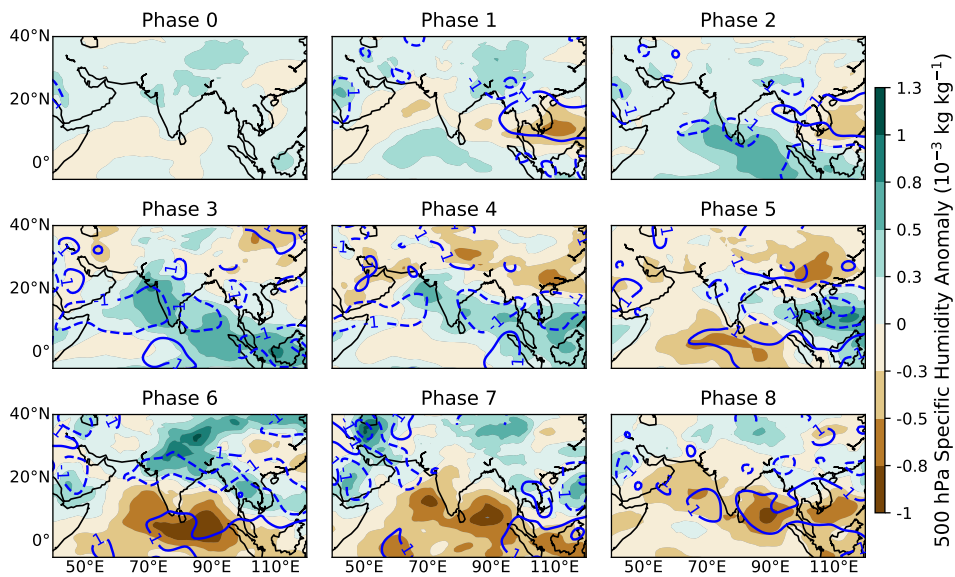


Figure 5.9: As in Figure 5.7, but for all phases of the Madden-Julian Oscillation. Note the different contour interval for 500 hPa specific humidity anomaly than shown in Figure 5.7.

to an increase in the meridional shear of the zonal wind around 21°N . Figures 5.13 and 5.14 show composite Hovmöller plots of 850 hPa zonal wind anomaly for all phases of the BSISO and MJO, respectively. The anomalies are averaged over 70°E – 100°E and considered for a period between two days before and two days after the genesis of BoB-long LPSs during June–September 1979–2018.¹ In BSISO phases 5–7 and MJO phases 4–5, which feature most BoB-long LPSs, there is an enhancement of barotropic instability, as evidenced by an increase in the meridional shear of the zonal wind anomalies around 21°N during the composite period. In contrast, the meridional shear is weak when the frequency of BoB-long LPSs is suppressed (e.g., BSISO phases 1–3 and MJO phases 6–8). Therefore, ISO forcing helps in the evolution of BoB-short LPSs into BoB-long LPSs. Further investigation is needed to examine the role of internal dynamics in this process.

¹We have considered 1979–2018 instead of 1998–2018 in order to have a larger sample size than that considered in Figure 5.6. For the June–September 1979–2018 period, the anomalous occurrence of BoB-long LPSs is negative in BSISO phases 1–3 and 7–8 and positive in BSISO phases 4–6. For the MJO, the anomalous occurrence is negative in phases 1–2 and 6–8 and positive in phases 3–5.

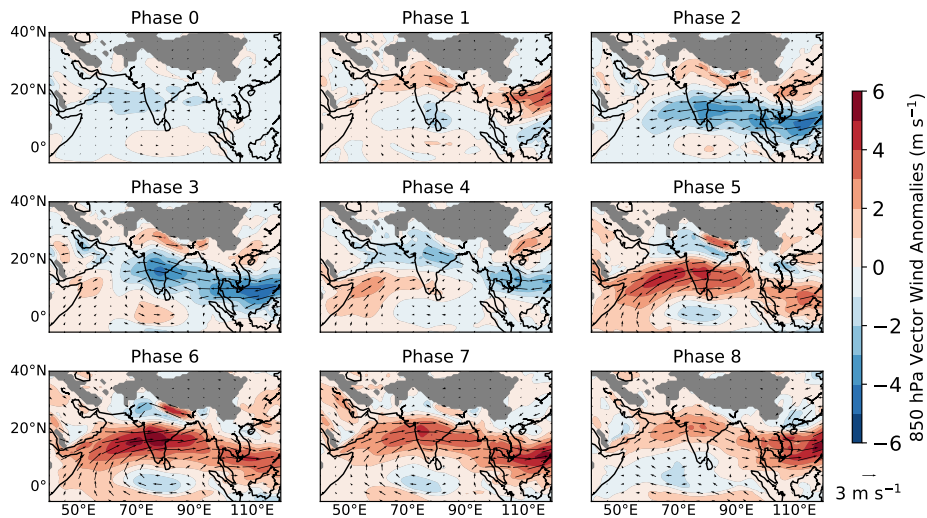


Figure 5.10: 850 hPa vector wind anomalies (m s^{-1}) for all phases of the Boreal Summer Intraseasonal Oscillation (BSISO) during June–September 1998–2018. The anomalies are computed against the summer mean climatology (June–September 1979–2018). Contours are greyed out where the mean surface pressure is less than 850 hPa.

5.7 Modulation of Sri Lankan LPSs by ENSO and IOD

Since Sri Lankan LPSs have an important role in producing summer monsoon precipitation and floods in Sri Lanka, it is important to understand their modulation by ENSO and IOD. Moreover, these relationships have not been explored in the past for these systems. We do not investigate the impact of ENSO and IOD on the frequency of other LPS varieties since previous studies have examined them (e.g., Singh et al. 2002; Hunt et al. 2016a; Vishnu et al. 2020a). These results could benefit meteorologists and researchers in designing forecasting products (e.g., seasonal outlooks of the occurrence of Sri Lankan LPSs), potentially benefiting stakeholders such as governments and farmers.

We group the years between 1980–2018 into terciles as per the SST anomaly in the Niño 3.4 region during June–September.² In addition to boosting the sample size, we get equal number of years in each tercile, which allows for an unbiased comparison. The highest

²We exclude 1979 in order to group the years between 1980 and 2018 into terciles.

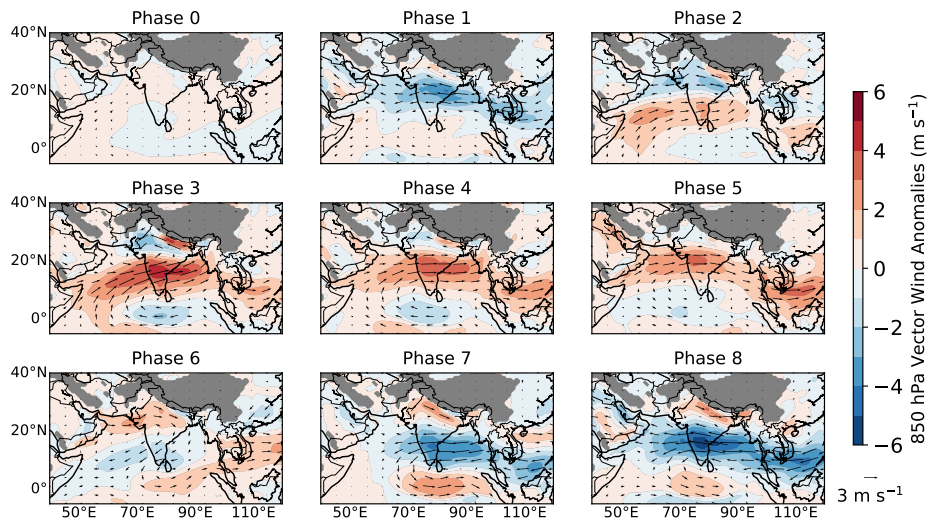


Figure 5.11: As in Figure 5.10, but for all phases of the Monsoon Intraseasonal Oscillation.

tercile comprises El Niño years, whereas the lowest tercile comprises La Niña years. We follow the same method for the Dipole Mode Index of Saji et al. (1999); the highest tercile comprises positive IOD (pIOD) events, whereas the lowest tercile comprises negative IOD (nIOD) events. We consider the long-term mean (June–September 1980–2018) frequency of Sri Lankan LPSs, and compute the anomalous occurrence of these systems for different categories (i.e., combined and separate influence) of ENSO and IOD, for which we follow Ummenhofer et al. (2009). Compared to the climatological occurrence, the frequency of Sri Lankan LPSs is suppressed during pure El Niño, pure pIOD, neutral ENSO and IOD, and a combination of El Niño and pIOD (Figure 5.15). Their frequency is enhanced during pure nIOD, La Niña, and a combination of La Niña and pIOD as well as La Niña and nIOD. However, there are only two seasons during which La Niña co-occurred with pIOD. Thus, this result suggests that large-scale conditions during nIOD and La Niña favour the genesis of these weather systems.

We now analyse the track density of these weather systems during El Niño, La Niña, pIOD and nIOD years. We consider terciles instead of pure events in order to have an

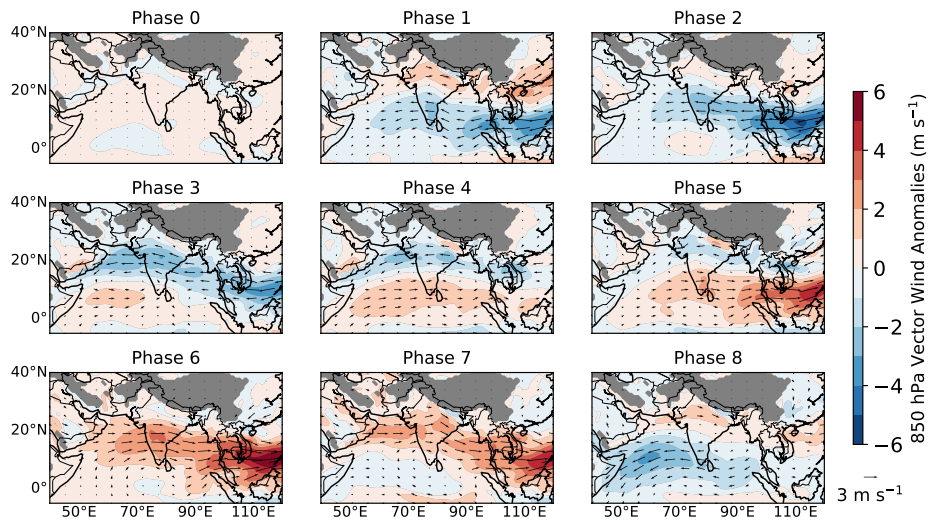


Figure 5.12: As in Figure 5.10, but for all phases of the Madden-Julian Oscillation.

equal sample size for our comparison. For example, there are 6 pure El Niño and 4 pure pIOD years, but we get 13 years in each case when using terciles. There are 42 Sri Lankan LPSs in total during La Niña years as opposed to 33 during El Niño years. Whilst they remain confined to Sri Lanka and nearby coastal regions of southern India during El Niño years, there is a spread in their tracks during La Niña years (Figure 5.16). For the IOD, more Sri Lankan LPSs form during nIOD events than during pIOD events (Figure 5.16). Furthermore, these systems are stronger during nIOD and La Niña years (mean central 850 hPa relative vorticity of $3.48 \times 10^{-5} \text{ s}^{-1}$ and $3.51 \times 10^{-5} \text{ s}^{-1}$) than during El Niño and pIOD ($3.01 \times 10^{-5} \text{ s}^{-1}$ and $3.04 \times 10^{-5} \text{ s}^{-1}$). We analyse anomalies of 850 hPa wind and relative vorticity in order to understand how these large-scale conditions modulate genesis of these weather systems. There is a positive relative vorticity anomaly to the southeast of Sri Lanka during nIOD, which favours the genesis of these systems. In contrast, there is a negative relative vorticity anomaly over the same region during pIOD that suppresses the genesis of these systems. Compared to the IOD, the anomalies are smaller in magnitude for ENSO (Figures 5.16e and 5.16f).

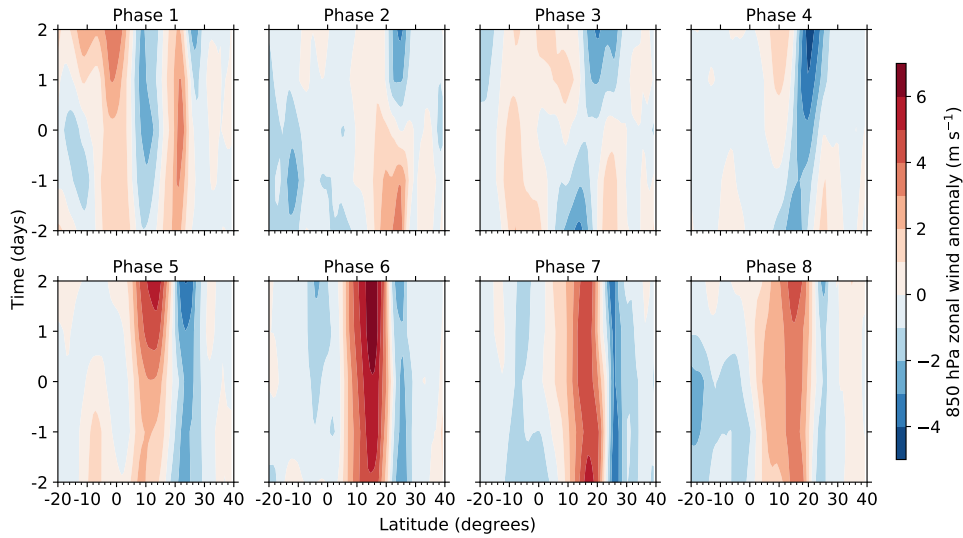


Figure 5.13: A Hovmöller plot (latitude-time section) of 850 hPa zonal wind anomaly (m s^{-1}) for the eight phases of the Boreal Summer Intraseasonal Oscillation (BSISO) during June–September 1979–2018. Day 0 represents the genesis of BoB-long LPSs. These anomalies are zonally averaged over 70°E – 100°E , and computed against a summer mean climatology (June–September 1979–2018). Only those LPS occurring when the BSISO amplitude exceeds one standard deviation, are considered.

5.8 Discussion and conclusions

Several studies have investigated various features of Bay of Bengal (BoB) monsoon depressions; however, South Asian monsoon low-pressure systems (LPSs) forming over the Arabian Sea and near Sri Lanka remain excluded. In this chapter, we investigated the four regional LPS varieties (Arabian, Sri Lankan, short-lived and long-lived BoB LPSs), which had their genesis during June–September 1979–2018. We used a catalogue of the four LPS varieties (Hunt and Fletcher, 2019) that was generated by applying a feature-tracking algorithm to 850 hPa relative vorticity in ERA-Interim. The LPS tracks were then partitioned into four clusters using a k -means clustering technique. We examined track statistics, thermal and moisture structure, and the precipitation contribution of each LPS variety. We investigated the modulation of each LPS variety by the tropical intraseasonal oscillation (ISO). We also investigated the modulation of Sri Lankan LPSs by ENSO

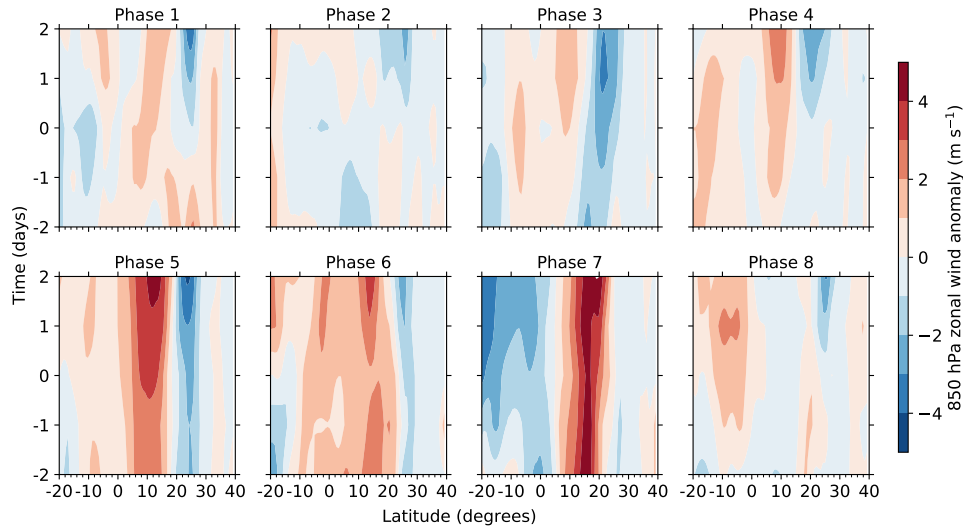


Figure 5.14: As in Figure 5.13, but for the MJO. Note the different contour interval in this figure than used in Figure 5.13.

and IOD. The results of this chapter can be summarised as follows:

The differences between track statistics

We identified 22 Arabian and 119 Sri Lankan LPSs. In addition, 364 LPSs were identified over the head of the BoB and nearby coastal regions, of which 229 LPSs were confined to east India (BoB-short) and 135 LPSs travelled to western and northwestern India (BoB-long). LPSs were most common in July or August, except for Arabian LPSs, which were most common in June due to the possible role of monsoon onset conditions. We found that BoB-long LPSs were the strongest and Arabian LPSs were the fastest among all varieties. In contrast, Sri Lankan LPSs were the weakest, and along with BoB-short LPSs, they were the slowest among all LPSs. We also found a moderate negative correlation between interannual frequencies of BoB-long and BoB-short LPSs, suggesting the possibility of a contrasting role of large-scale conditions in modulating their frequencies.

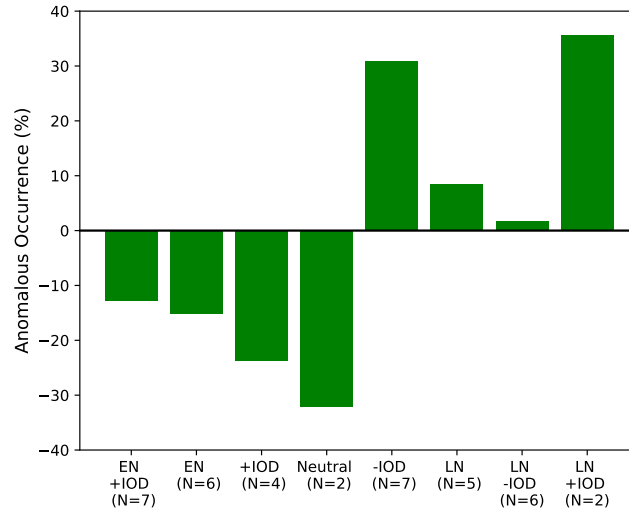


Figure 5.15: Anomalous frequency (%) of Sri Lankan LPSs (per season) during combined and separate events (categories) of ENSO and IOD, after Ummenhofer et al. (2009). The anomalous occurrence of these systems is computed with respect to their seasonal mean frequency during June–September 1980–2018. These categories are: El Niño and positive IOD (EN+IOD), pure El Niño (EN), pure positive IOD (+IOD), ENSO and IOD neutral (Neutral), negative IOD (-IOD), pure La Niña (LN), and La Niña and negative IOD (LN- IOD). An El Niño event has not co-occurred with a negative IOD event in this period. For each category, the number of years (N) is shown in each x -axis label.

Vertical structure

All the four LPS varieties featured a warm-over-cold thermal structure, which is commonly seen in BoB LPSs (e.g., Chapter 4; Hunt et al. 2016a). Arabian and BoB-long LPSs featured the strongest warm and cold core respectively. In contrast, Sri Lankan LPSs had the weakest warm core and cold core structure, which was attributed to their weak intensity. All four LPS varieties had their maximum anomaly in equivalent potential temperature in the lower troposphere; Arabian LPSs had largest anomalies, whereas Sri Lankan LPSs had smallest anomalies.

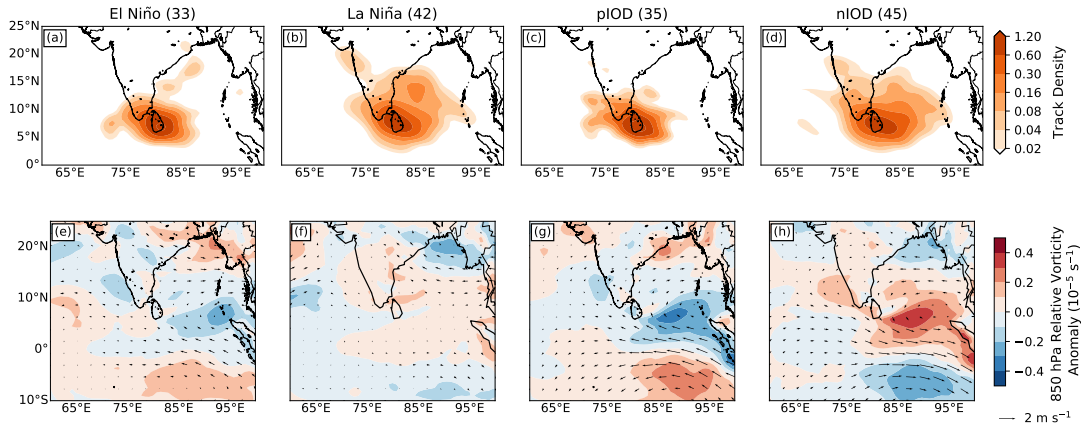


Figure 5.16: The track density of Sri Lankan low-pressure systems during (a) El Niño, (b) La Niña, (c) positive IOD (pIOD), and (d) negative IOD (nIOD) events. The number in each title indicates the frequency of these weather systems in each composite. The track density is calculated using a kernel density estimation technique, and its unit is LPS number per square degree for June–September 1980–2018. Coloured contours in (e)–(h) show 850 hPa relative vorticity anomaly (10^{-5} s^{-1}) for different composites, with vectors showing the 850 hPa wind anomaly. These anomalies are computed against a summer mean climatology (June–September 1979–2018).

Precipitation contribution

We calculated the precipitation contribution of each LPS variety to the summer mean precipitation. We found that BoB-short LPSs had the largest precipitation contribution over the western Bay of Bengal and nearby coastal regions, BoB-long LPSs were the major precipitation contributors to interior parts of India as well as parts of Pakistan, Iran and Afghanistan. In contrast, Arabian LPSs had the smallest precipitation contribution, whereas Sri Lankan LPSs had a moderate contribution to rainfall over Sri Lanka and adjoining parts of south India. We found a larger precipitation contribution from Sri Lankan LPSs and smaller from Arabian LPSs than the results of Hunt and Fletcher (2019).

Modulation of LPSs by the ISO

We investigated the anomalous occurrence of the four LPS varieties during June–September 1998–2018 and found that only BoB-short and BoB-long LPSs formed in all phases (am-

plitude greater than one standard deviation) of the Boreal Summer Intraseasonal Oscillation (BSISO), Monsoon Intraseasonal Oscillation (MISO) and Madden-Julian Oscillation (MJO), which are the three commonly used indices for monitoring the ISO. The propagation of the ISO modulated the anomalous occurrence of each variety; the anomalous occurrence of Arabian and Sri Lankan LPSs peaked when the ISO was active over Sri Lanka and adjoining parts of the Arabian Sea, whereas that of BoB systems peaked several phases later with the northward/northeastward prorogation of the ISO. We found that a cyclonic shear, positive specific humidity anomalies and anomalous ascent (negative specific humidity anomalies and anomalous descent) favoured (opposed) LPS genesis. We also found that enhanced barotropic instability of the large-scale monsoon circulation favoured the genesis of BoB-long LPSs, agreeing with the findings of Krishnan et al. (2011).

Modulation of Sri Lankan LPSs by ENSO and IOD

We investigated the modulation of Sri Lankan LPSs by ENSO and IOD. We found an increased frequency of these systems during La Niña and negative IOD years than during El Niño and positive IOD years. A positive relative vorticity anomaly at 850 hPa to the southeast of Sri Lanka favoured genesis of these weather systems during La Niña and nIOD years.

This study opens a new avenue for research on the four regional LPS varieties and the role of ISO forcing in modulating their frequency. Further investigation is needed to compare more dynamical properties of the four LPS varieties. The genesis mechanisms of Sri Lankan LPSs need to be understood. Here we speculate that the interaction between cross-equatorial winds of the monsoon and the high-central Sri Lankan terrain provides low-level cyclonic vorticity on the lee side for spin up of Sri Lankan LPSs. In addition, the role of equatorial waves in the formation of Sri Lankan LPSs needs to be explored.

In this chapter, we discussed how large-scale conditions related to the ISO modulate

LPSs. We have developed a framework, which we will use in the next chapter for examining large-scale controls on LPSs in the S2S dataset. Based on a moderate negative interannual correlation (-0.52) between frequencies of BoB-short and BoB-long LPSs, we hypothesise that large-scale conditions might have a contrasting role in modulating interannual frequencies of these two LPS varieties. We will test this hypothesis in the next chapter.

CHAPTER 6

LARGE-SCALE CONTROLS ON INDIAN MONSOON

LOW-PRESSURE SYSTEMS

6.1 Introduction

We have seen in the previous chapter that LPSs produce nearly half of the summer monsoon precipitation over India, with Bay of Bengal (BoB) LPSs producing up to 70% of the summer monsoon precipitation over the eastern coast of the country. This precipitation is important for the recharge of groundwater and agriculture in India. However, strong LPSs (SLPSs) such as monsoon depressions often trigger catastrophic floods, which cause adverse socio-economic impacts in the country. It is therefore important to understand the predictability of these weather systems, for which it is essential to understand the relationship between their genesis and the environment in which they occur.

From the results of Sikka (1978), it is known that high sea surface temperature (SST) over the head of the BoB, high lower-tropospheric cyclonic vorticity, high mid-tropospheric humidity, and weak vertical wind shear are necessary conditions for the formation of monsoon depressions. However, only a limited number of studies have explored this aspect,

resulting in a gap in our understanding of what large-scale conditions control LPSs. In contrast, many studies have investigated the relationship between large-scale conditions and the occurrence of TCs over different regions using various reforecasts, reanalysis datasets and climate models (e.g., Camargo et al. 2007; Song et al. 2015; Lee et al. 2020; Wang and Murakami 2020). Attempts to analyse the role of large-scale conditions in genesis of TCs can be traced back to the late 1940s (e.g., Palmén 1948; Riehl 1948). Gray (1979) developed an index to predict the seasonal frequency of TCs using six parameters: SST, mid-tropospheric relative humidity, vertical wind shear, Coriolis parameter, low-level relative vorticity, and atmospheric stability. Since then, many indices have been developed that estimate the potential for tropical cyclogenesis, including the Genesis Potential Parameter (Kotal and Bhattacharya, 2013) and the commonly used genesis potential index (GPI) by Emanuel and Nolan (2004). The GPI is defined only over ocean, preventing it from being suitable to estimate the genesis potential of LPSs that can form over land. Ditchek et al. (2016) developed the monsoon disturbance genesis index (MDGI) to analyse the geographical distribution and seasonal cycle of monsoon depressions. The MDGI is based on the estimated convective available potential energy (ECAPE), 850 hPa absolute vorticity, 600 hPa relative humidity, and total column water vapour. Since then, it has been used to understand future changes in LPSs (Sandeep et al., 2018) and the relationship between the Pacific Decadal Oscillation and monsoon depressions (Vishnu et al., 2018). However, it has not been used to understand the genesis potential of LPSs in seasonal forecasts, such as those of the models of the Subseasonal-to-Seasonal (S2S) prediction project (Vitart et al., 2017), which could provide insights into model biases and the skill of these models at predicting these weather systems.

Large-scale modes of climate variability such as the MJO and ENSO modulate the large-scale conditions responsible for TC genesis, serving as an important predictor for TCs at a long lead time (e.g., Camargo and Sobel 2005; Lee et al. 2020). In Chapter 5 (Deoras et al., 2021b), we investigated the modulation of LPSs by the MJO, and found that

BoB LPSs can form in all phases of the MJO; however, their frequency is enhanced when the MJO is active over the western Indian Ocean and the Maritime Continent. Previous studies (e.g., Singh et al. 2002; Hunt et al. 2016a; Vishnu et al. 2020a) examined the relationships between ENSO, IOD and monsoon depressions in different datasets. Whilst Vishnu et al. (2020a) did not find any impact of ENSO and IOD on the frequency of monsoon depressions, Singh et al. (2002) and Hunt et al. (2016a) found a larger frequency of monsoon depressions during El Niño years than during La Niña years. However, no study has investigated the modulation of SLPSs by the MJO, ENSO and IOD in the S2S dataset, the results of which could improve our understanding of the relationship between modes of intraseasonal and interannual monsoon variability and LPS activity. This could improve operational seasonal forecasts and ultimately benefit stakeholders such as farmers. This gains importance since Vitart (2017) found that all S2S models can predict the MJO with lead times of up to four weeks, and an evaluation of six S2S models by Lee et al. (2018b) and Lee et al. (2020) suggests that S2S models are able to represent the MJO-TC relationship. In Chapter 5, we also discussed characteristics of BoB-long and BoB-short LPSs, which produce most LPS-related precipitation over western and eastern parts of India, respectively. If we are able to understand what large-scale atmospheric conditions control the frequency of these two LPS varieties, it could help meteorologists in predicting the specific BoB LPS variety well in advance.

Whilst past LPS studies mainly focused on BoB LPSs, it is important to understand characteristics of LPSs that have their genesis over the South China Sea and adjoining western Pacific Ocean, following which they propagate towards India in the direction of the tropical easterly jet. Such systems are known as downstream LPSs (Krishnamurti et al., 1977). There is no consensus on the frequency of BoB LPSs forming as downstream LPSs: 32% and 95% in Chen and Weng (1999) and Meera et al. (2019), respectively. Given that their genesis location is far from India, these systems can provide a larger window of opportunity for preparedness in India than that provided by LPSs forming over the BoB.

In this chapter, our objective is to understand the following aspects:

- How well do S2S models simulate the genesis potential of SLPSs?
- How well do S2S models simulate the modulation of SLPSs by the MJO, ENSO and IOD?
- What is the relationship between large-scale atmospheric fields and interannual frequency of short-lived and long-lived BoB LPSs?
- How many LPSs originate over the South China Sea and western Pacific Ocean and what are their characteristics?

We present an outline of the data and methodology in Section 6.2, and analyse the relationship between the MDGI and SLPS frequency in Section 6.3. We then analyse the intraseasonal and interannual variability of SLPSs in Section 6.4. In Section 6.5, we investigate relationships between large-scale atmospheric fields and interannual frequency of BoB LPS varieties. We explore characteristics of downstream LPSs in Section 6.6, and finally conclude in Section 6.7.

6.2 Data and methods

6.2.1 The S2S, ERA-I, TRMM and LPS datasets

A full description of the S2S, ERA-I and TRMM datasets is already given in Sections 2.1.1, 2.1.2 and 2.1.5, respectively, and we will not repeat the description here. We use a catalogue of LPSs tracked in all ensemble members of the eleven S2S models, ERA-I and MERRA-2 reanalysis datasets during June–September 1999–2010 (Deoras et al., 2021c). Details about the identification of LPSs are already provided in Sections 2.2.1, 2.2.2 and 2.2.3 and will not be repeated here. We also use a catalogue of the four regional LPS varieties that were tracked in ERA-I during June–September 1979–2018 (Hunt et al.,

2021a). Details of this catalogue were provided in Section 5.2.1. Both catalogues contain monsoon depressions, deep depressions and low-pressure areas.

6.2.2 Identifying downstream LPSs in ERA-I

For identifying downstream LPSs in ERA-I, we apply the feature-tracking algorithm (Section 2.2.1; Hunt et al. 2016a, 2018b) on 700 hPa relative vorticity. We consider the 700 hPa pressure level instead of 850 hPa in order to be able to track LPSs that might disintegrate due to the high orography over the Southeast Asia region (see Figure 6.1). In the feature-tracking algorithm, we set the minimum 700 hPa relative vorticity threshold to $0.1 \times 10^{-5} \text{ s}^{-1}$ for identifying weaker vortices. For further analysis, only those LPSs that occurred during June–September 1979–2018 were retained, provided they lasted for more than two days. We did not apply any post-tracking intensity filters since we are not interested in examining a specific LPS category (e.g., monsoon depressions). A total of 1118 systems were identified in this period, following which we applied a k -means clustering technique (Chapter 5; MacQueen et al. 1967) to vectors containing longitudes and latitudes of LPSs, interpolated to a common length.

6.2.3 IMD Cyclone e-Atlas

We use the IMD Cyclone e-Atlas dataset¹ to investigate the influence of ENSO and IOD on the frequency of monsoon depressions over a time period longer than that of ERA-I. This dataset contains tracks of tropical depressions (including monsoon depressions) and tropical cyclones that occurred over the north Indian Ocean between 1891 and 2020. Whilst many previous studies have used this dataset (e.g., Mohanty et al. 2012; Prajeesh et al. 2013; Mahala et al. 2015), it suffers from many limitations. The dataset is affected by changes in the IMD’s observational network. The IMD started using satellites for weather surveillance from 1960, so tracking of tropical cyclones and tropical depressions

¹This dataset is available at: <http://14.139.191.203/Login.aspx>

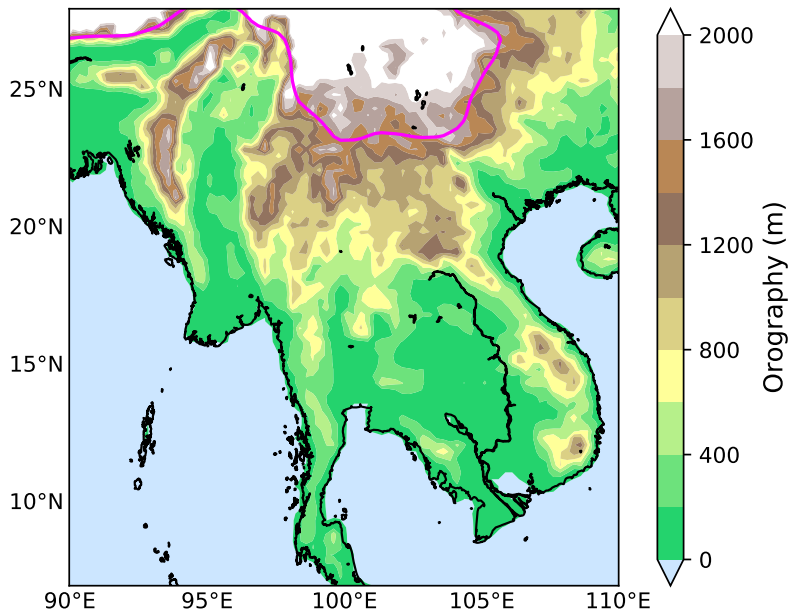


Figure 6.1: The orography of the Southeast Asia region (m) obtained from the National Center for Atmospheric Research’s TerrainBase dataset (National Geophysical Data Center, NESDIS, NOAA, U.S. Department of Commerce, 1995). The 850 hPa level, which is located using the mean surface pressure (June–September 1979–2018) in ERA-I, is shown by a magenta contour.

during the pre-satellite era was carried out using ship reports and the surface observational network in India (IMD, 2011). Mohapatra et al. (2012) compared the frequency of tropical depressions over data sparse regions during the pre-satellite era with that during the satellite era. They found an increase in the frequency of tropical depressions during the satellite era. They suggested that the frequency of monsoon depressions over the head of the BoB could have been over estimated during the pre-satellite era. They speculated that due to the late detection of monsoon depressions in synoptic charts, their lifetime over the BoB could have been shorter by a day in half of the total observations. The shortcomings of this dataset were also highlighted by Cohen and Boos (2014), who found that observed monsoon depressions were missing from this dataset during summer monsoon seasons of 2002, 2010 and 2012. Another limitation of this dataset is that it does not contain tracks of weaker LPSs such as low-pressure areas.

6.2.4 MJO index

For S2S models, we use the MJO index (Wheeler and Hendon, 2004) computed by Vitart (2017) in each ensemble member of the ten S2S models during the common reforecast period of 1999–2010 and forecast lead times of 1–32 days. From the common period of June–September 1999–2010, we consider only those dates on which the MJO index exceeds a standardised amplitude of one. The MJO index was downloaded from: <https://acquisition.ecmwf.int>, but is not available for the KMA model. The MJO index in reanalysis datasets was obtained from the Bureau of Meteorology, Australia, available at <http://www.bom.gov.au/climate/mjo/graphics/rmm.74toRealtime.txt>.

6.2.5 ENSO and IOD indices

We use the NOAA ERSSTv5 sea surface temperature (SST) dataset to compute ENSO and IOD indices. Details of this dataset and the computation of ENSO and IOD indices are already given in Sections 2.1.7 and 2.1.8, respectively.

6.2.6 Significance testing

We determine if the interannual Pearson correlation coefficient between various large-scale atmospheric fields and the observed frequency of SLPSs is significantly different from zero. Our null hypothesis states that the interannual Pearson correlation coefficient is equal to zero. Thus, areas where a 95% significance level is satisfied will be stippled in the corresponding figures. We use a Pearson’s correlation table to determine the 95% significance level for 21-year moving correlations.

6.3 Relationship between the MDGI and SLPS frequency

In this section, we investigate the genesis potential of SLPSs in S2S models for forecast lead times of 1–32 days during June–September 1999–2010. We first compute the MDGI

in S2S models, and then compare it with the simulated genesis density of SLPSs that were identified in these models. These results could encourage the modelling community to investigate biases related to the genesis potential of SLPSs in S2S models. We will then explore the time-varying relationship between the MDGI and observed frequency of SLPSs in ERA-I over a time period (June–September 1979–2018) longer than the common reforecast period of S2S models (June–September 1999–2010). This analysis would help in evaluating the accuracy of the MDGI on the interannual time scale.

6.3.1 Genesis potential of SLPSs in S2S models

As discussed in Section 6.1, the MDGI is based on the ECAPE, 850 hPa absolute vorticity, 600 hPa relative humidity and total column water vapour. The ECAPE, which measures the difference between the surface-air moist static energy and 200–400 hPa vertically averaged saturation moist static energy, is defined as:

$$\text{ECAPE} = h(2 \text{ m}) - \frac{1}{(p_2 - p_1)} \int_{p_1}^{p_2} h^*(p) dp, \quad (6.1)$$

where the moist static energy (h) is defined as $h = c_p T + L_v q + gz$; here, c_p is the heat capacity of air at constant pressure, L_v is the latent heat of vaporization, T is the temperature, q is the specific humidity, z is the altitude and g is the acceleration due to gravity. The variable h^* denotes the saturation moist static energy. Since 600 hPa and 400 hPa output pressure levels are not available in the S2S dataset, we consider 500 hPa relative humidity, and output pressure levels between 500 hPa and 200 hPa (i.e., 500 hPa, 300 hPa and 200 hPa) for computing the ECAPE. We consider the same output pressure levels in reanalysis datasets for verifying the results.² The MDGI is defined as:

$$\mu = \exp[\mathbf{b}^T \mathbf{x} + \log(\Delta x \Delta y T \cos \phi)], \quad (6.2)$$

²We note that the choice of these levels affects the MDGI, reducing its maximum value over the head of the BoB from ~ 4 to ~ 2.5 SLPSs per grid point over June–September 1979–2018.

where μ is the expected number of monsoon disturbances during the climatological period, \mathbf{b} is the vector of regression coefficients (0.14 for ECAPE, 0.34 for 850 hPa absolute vorticity, 0.025 for total column water vapour, and 0.074 for 500 hPa relative humidity), \mathbf{x} is the vector containing variables (ECAPE, 850 hPa absolute vorticity, total column water vapour, and 500 hPa relative humidity), Δx and Δy are the longitude and latitude grid spacings in degrees, respectively, ϕ is the latitude in radians, and T is the number of years in the climatology. For S2S models, both Δx and Δy are 1.5° , whereas for MERRA-2, Δx and Δy are 0.5° and 0.625° , respectively, and both variables are 0.7° for ERA-I. The climatological period T is 12 (i.e., 12 years covering the period 1999–2010).

Figure 6.2 shows the mean MDGI in eight S2S models, the MMM, and reanalysis datasets. The MDGI for reanalysis datasets is regridded to $1.5^\circ \times 1.5^\circ$ to match the spatial resolution of S2S models. We did not compute the MDGI for the BoM, ISAC-CNR and KMA models due to the unavailability of specific humidity at the selected output pressure levels and mean sea-level pressure; these variables are essential for computing the ECAPE and total column water vapour. A light green box in Figure 6.2a shows the main genesis region (15°N – 25°N , 80°E – 90°E) of LPSs (Prajeesh et al., 2013; Cohen and Boos, 2014) and numbers in each subfigure indicate the mean MDGI in this region. All S2S models correctly simulate the genesis potential of SLPSs over the main genesis region; however, HMCR and the MMM overestimate the MDGI compared to ERA-I, and most models underestimate the MDGI compared to MERRA-2. In addition, the CNRM, HMCR, ECMWF and NCEP models overestimate the MDGI over the eastern Arabian Sea (i.e., off the western coast of India) where Arabian LPSs occur (Chapter 5; Deoras et al. 2021b). The performance of the HMCR model is the worst since it simulates the genesis potential along the entire Indo-Gangetic Plain (IGP), and the MDGI over the main genesis region is approximately 5 times that of ERA-I. The MDGI over the main genesis region is larger in MERRA-2 than in ERA-I.

It is important to understand the source of the large bias in the MDGI over the main

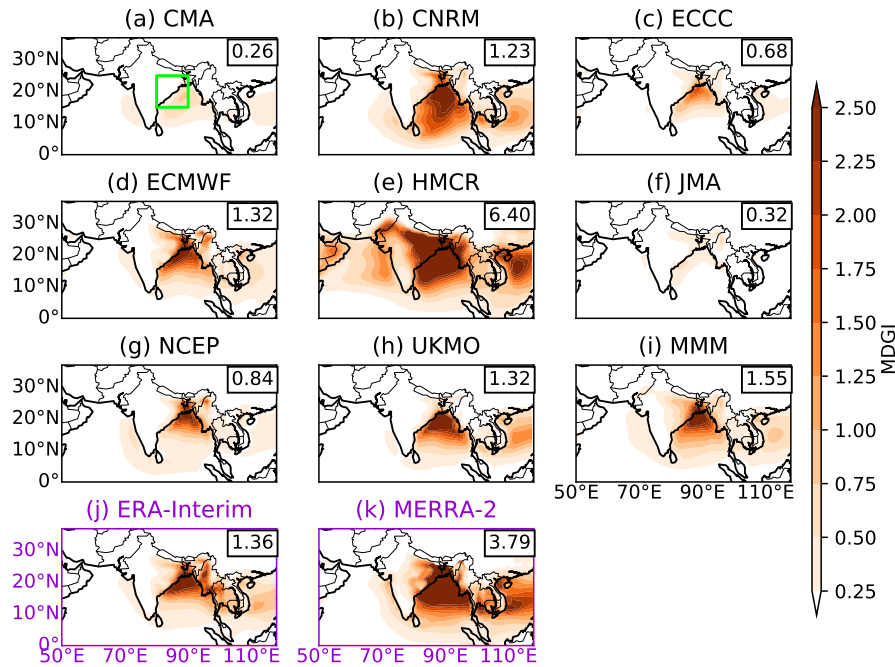


Figure 6.2: The monsoon disturbance genesis index (MDGI) for eight S2S models, ERA-Interim and MERRA-2 reanalysis datasets. The unit of the MDGI in this case is the number of monsoon disturbances per grid point during 12 years (1999–2010) in the given season (June–September). Forecast lead times of 1–32 days are considered for S2S models. The multimodel mean (MMM) of eight S2S models is also shown. The MDGI in ERA-I and MERRA-2 is regridded to match the spatial resolution of S2S models, which is $1.5^\circ \times 1.5^\circ$. Numbers in each subfigure show the mean MDGI over the main genesis region (15°N – 25°N , 80°E – 90°E), which is shown by a light green box in (a). The subfigures for ERA-Interim and MERRA-2 are highlighted in dark violet to distinguish them from S2S models.

genesis region in the HMCR model. We therefore compute biases in the four components of this index with respect to ERA-I (Figure 6.3). The overestimation of the MDGI is attributed to positive biases in the ECAPE and 500 hPa relative humidity. The total column water vapour has a negligible bias, whereas 850 hPa absolute vorticity has a small negative bias.

We now compute the genesis density of SLPSs in these S2S models for forecast lead times of 1–32 days during June–September 1999–2010 (Figure 6.4). Following Chapter 5, we use a non-parametric, Gaussian kernel density estimation (KDE) technique to construct

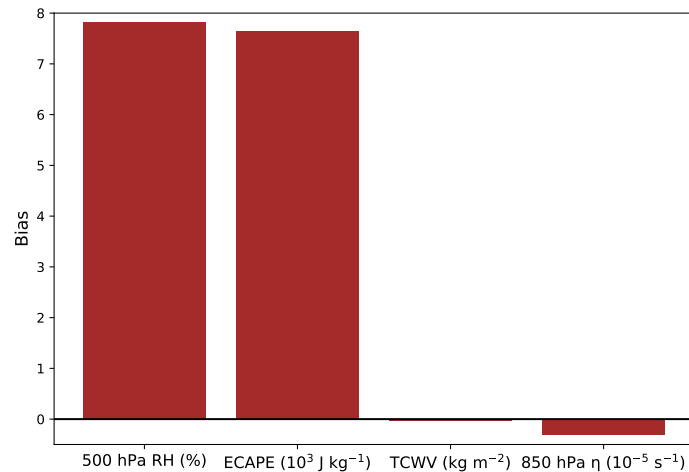


Figure 6.3: Biases in the four components of the monsoon disturbance genesis index over the main genesis region (15°N – 25°N , 80°E – 90°E) in the HMCR model during June–September 1999–2010. These four components are 500 hPa relative humidity (RH), estimated cape (ECAPE), total column water vapour (TCWV) and 850 hPa absolute vorticity (η). The biases are calculated with respect to ERA-I.

a smooth probability density estimate of the observed data. As seen in Figure 3.4 of Chapter 3, most SLPSs in the CMA model do not form over the main genesis region; however, this is not predicted by the MDGI. Compared to the simulated genesis density, the genesis potential of SLPSs over the main genesis region is overestimated in both reanalysis datasets and nearly all S2S models including the MMM, except for CMA and JMA.

6.3.2 Time-varying relationship between the MDGI and observed SLPS frequency

We now investigate the time-varying relationship between the MDGI and observed frequency of SLPSs in ERA-I. Figure 6.5 shows time series of the observed seasonal frequency of SLPSs and the MDGI over the main genesis region during June–September 1979–2018. There is a lack of statistically significant linear correlation between them—the interannual Pearson correlation coefficient is 0.22 and it is not significant at the 95% level. The MDGI

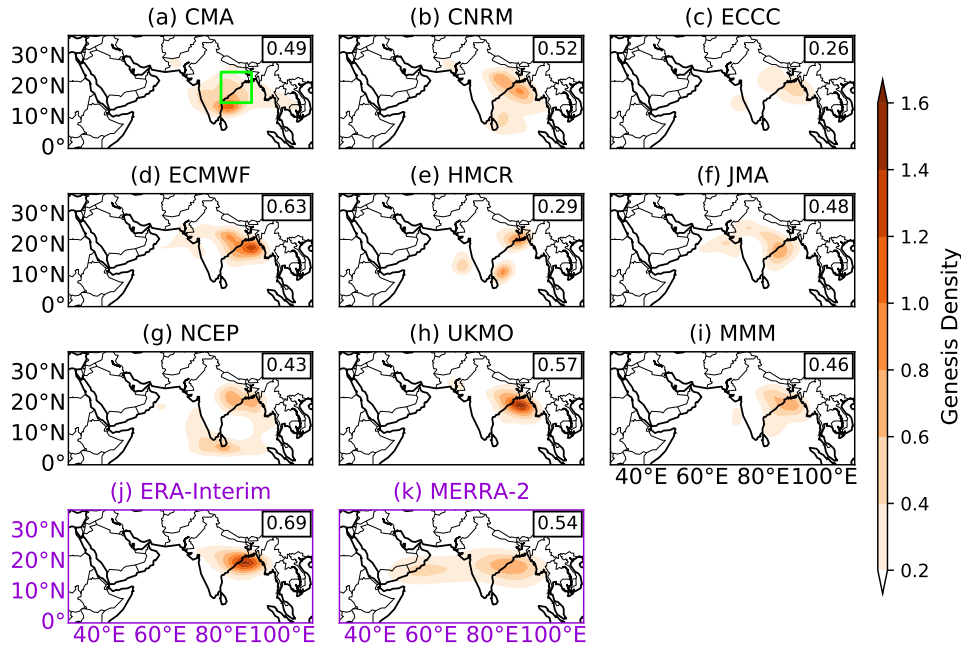


Figure 6.4: The genesis density of strong Indian monsoon low-pressure systems (SLPSs) identified in eight S2S models, the multimodel mean (MMM), ERA-Interim and MERRA-2 reanalysis datasets during June–September 1999–2010. Forecast lead times of 1–32 days are considered in S2S models. The genesis density is calculated using a kernel density estimation technique. The unit of genesis density is the number of SLPSs per $1.5^\circ \times 1.5^\circ$ for June–September 1999–2010. Following Chapter 3 (Deoras et al., 2021a), the genesis density in S2S models is normalised with respect to the ensemble size and reforecast frequency. The genesis density in ERA-I and MERRA-2 is regridded to match the spatial resolution of S2S models, which is $1.5^\circ \times 1.5^\circ$. The genesis density is not shown for the BoM, ISAC-CNR and KMA models since the MDGI for these models could not be computed in Figure 6.2. Numbers in each subfigure show the mean genesis density over the main genesis region (15°N – 25°N , 80°E – 90°E), which is shown by a light green box in (a). The subfigures for ERA-Interim and MERRA-2 are highlighted in dark violet to distinguish them from S2S models.

underestimates the seasonal frequency of SLPSs in general, with a prominent underestimation during years such as 1980, 1990 and 2000. The two time series are well correlated until 2005. In fact, the interannual Pearson correlation coefficient during 1979–1998 is 0.65, which is statistically significant at the 95% level. However, the strength of the correlation decreases to -0.34 during 1999–2018, and it is not significant at the 95% level. This leads to an obvious question: what factors are responsible for the decoupling of the two

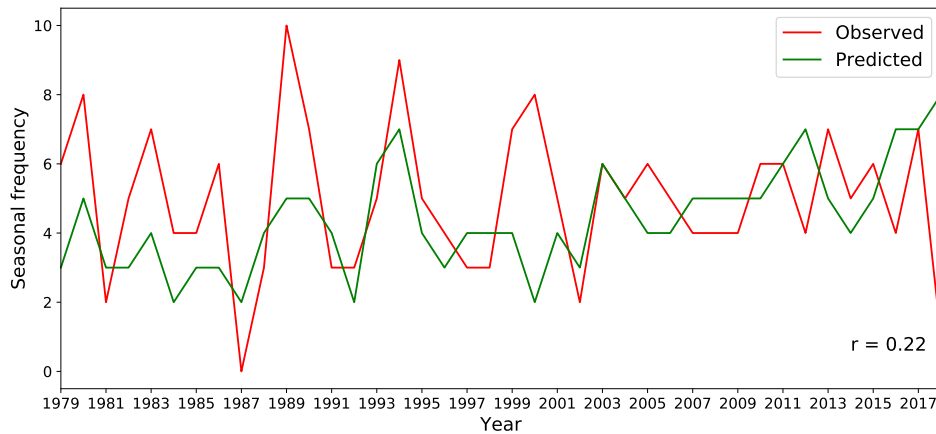


Figure 6.5: Time series showing the observed seasonal (June–September) frequency of strong Indian monsoon low-pressure systems (SLPSs; solid red) and that predicted by the monsoon disturbance genesis index (solid green) over the main genesis region (15° – 25° N, 80° – 90° E) during 1979–2018 in ERA-I. The interannual Pearson correlation coefficient between the observed and predicted seasonal frequencies is also shown.

time series over the last two decades?

We analyse 21-year running correlations between the four components of the MDGI and the observed SLPS frequency over the main genesis region during June–September 1979–2018. We first check trends in the four components of the MDGI over the main genesis region (Figure 6.6). There is an increasing linear trend in the ECAPE, 600 hPa relative humidity and total column water vapour, which is statistically significant at the 95% level. We first remove the linear trend from these three time series by subtracting the line of best fit, following which we compute 21-year running correlations (Figure 6.7). The critical value for a two-tailed test with a 95% significance level and 19 degrees of freedom is 0.43, which is shown as dashed lines in Figure 6.7. The correlations for all MDGI components weaken over the last two decades, which explains the decoupling between the MDGI and observed SLPS frequency. Among the four MDGI components, the correlation is strongest (~ 0.6) for 850 hPa absolute vorticity, which is statistically significant during 1990–2005. To investigate if the correlation is particularly affected by any specific year (e.g., a particularly large ENSO event), we replace each single year in turn with the cli-

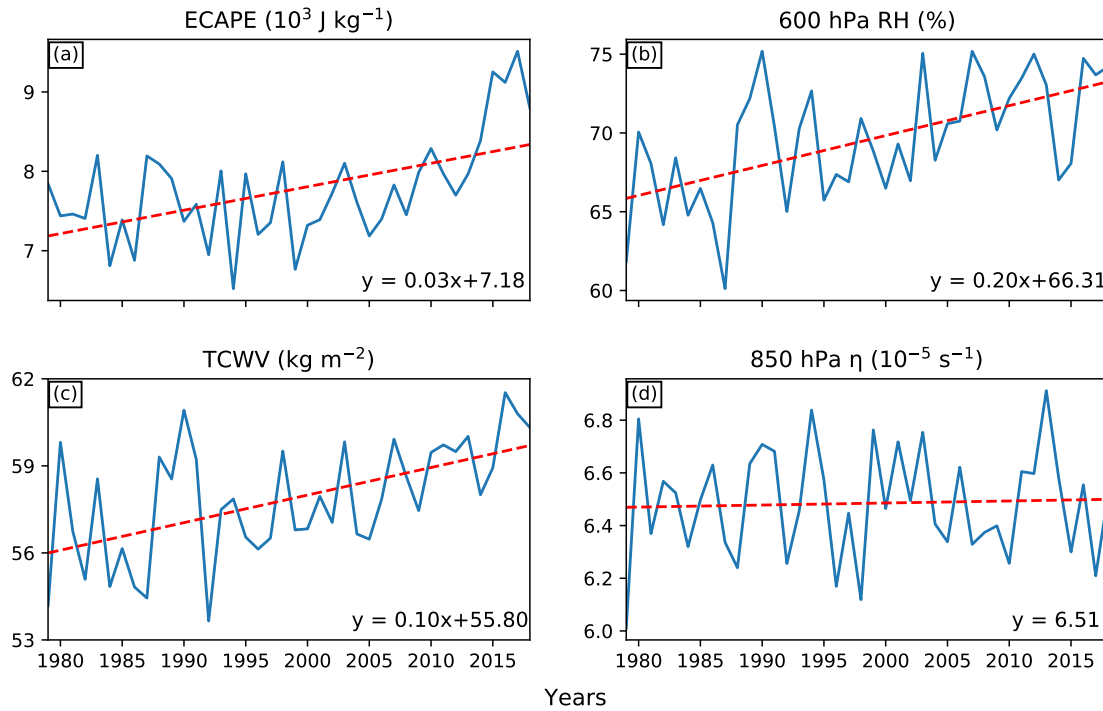


Figure 6.6: Time series of (a) estimated cape (ECAPE), (b) 600 hPa relative humidity (RH), (c) total column water vapour (TCWV), and (d) 850 hPa absolute vorticity (η) over the main genesis region (15°N – 25°N , 80°E – 90°E) in ERA-I during June–September 1979–2018. Red dashed lines show trend lines.

matological value (i.e., climatology during June–September 1979–2018). The strength of the correlation for all components decreases over the last two decades, suggesting that the weakening of the correlation between these components and the observed SLPS frequency is not affected by anomalies in any specific year (not shown). We hypothesise that nonlinear interactions between the four components of the MDGI could be weakening the relationship between the MDGI and observed SLPS frequency, which is not captured by the MDGI. However, this aspect needs further investigation, which is beyond the scope of this chapter.

In summary, HMCR overestimates the genesis potential of SLPSs over the main genesis region when compared to reanalysis datasets. A comparison between the MDGI and the

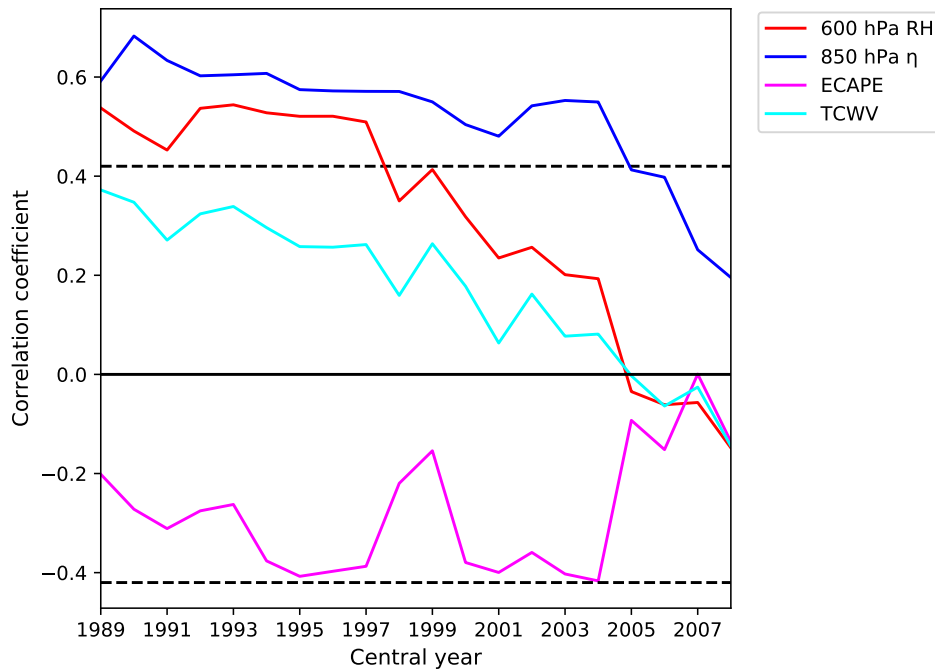


Figure 6.7: 21-year running correlations between 600 hPa relative humidity (RH), 850 hPa absolute vorticity (η), estimated cape (ECAPE), total column water vapour (TCWV) and the observed frequency of strong Indian monsoon low-pressure systems over the main genesis region (15°N – 25°N , 80°E – 90°E) in ERA-I during June–September 1979–2018. The central year is shown on the x -axis. Dashed black lines indicate the 95% significance level.

simulated genesis density of SLPSs suggests that nearly all S2S models and the MMM overestimate the genesis potential over the main genesis region. The HMCR model has the largest bias in the MDGI. ECMWF, UKMO and the MMM could be useful to stakeholders since they outperform individual models. The correlation between the MDGI and observed frequency of SLPSs over the main genesis region in ERA-I has weakened over the last two decades, which is attributed to a weakening of correlations between the components of the MDGI and observed frequency of SLPSs. Thus, the MDGI is not useful for analysing the interannual variability of SLPSs during June–September 1979–2018.

6.4 Intraseasonal and interannual variability of SLPSs

In this section, we investigate the intraseasonal and interannual variability of SLPSs. We first explore the modulation of SLPSs by large-scale modes such as the MJO and then by ENSO and the IOD. These results could help meteorologists and flood forecasters in developing subseasonal to seasonal outlooks for SLPS frequency, which could ultimately benefit agriculture and other socio-economic sectors.

6.4.1 Madden-Julian Oscillation

In this subsection, we investigate the modulation of SLPSs by the MJO in S2S models. Vitart (2017) found that all S2S models can predict the phase of the MJO with a lead time of up to four weeks. Following Cassou (2008) and Chapter 5 published as Deoras et al. (2021b), we calculate the anomalous occurrence of SLPSs in each phase of the MJO for forecast lead times of 1–32 days during June–September 1999–2010. The anomalous occurrence is a ratio of the difference between the number of SLPSs in each MJO phase and the climatological expected value of SLPSs in all phases to the climatological expected value of SLPSs in all phases. Thus, a 0% value indicates that the frequency of occurrence of SLPSs equals the climatological expected value, whereas a 100% value indicates twice the climatological expected value. We compute the anomalous occurrence in each ensemble member, following which an ensemble mean is calculated for an S2S model.

As discussed in Chapter 5 (Deoras et al., 2021b), BoB LPSs can form in all phases of the MJO. However, genesis of short-lived BoB LPSs is enhanced when the MJO is active over the western Indian Ocean (i.e., phases 1–2), whereas that of long-lived BoB LPSs is enhanced when the MJO is active over the Maritime Continent (i.e., phase 5). With the eastward propagation of the MJO towards the western Pacific (i.e., phases 7–8), LPS genesis is suppressed. Most S2S models, including the MMM, simulate the MJO response well in general (Figure 6.8), when compared with ERA-I and MERRA-2 (not

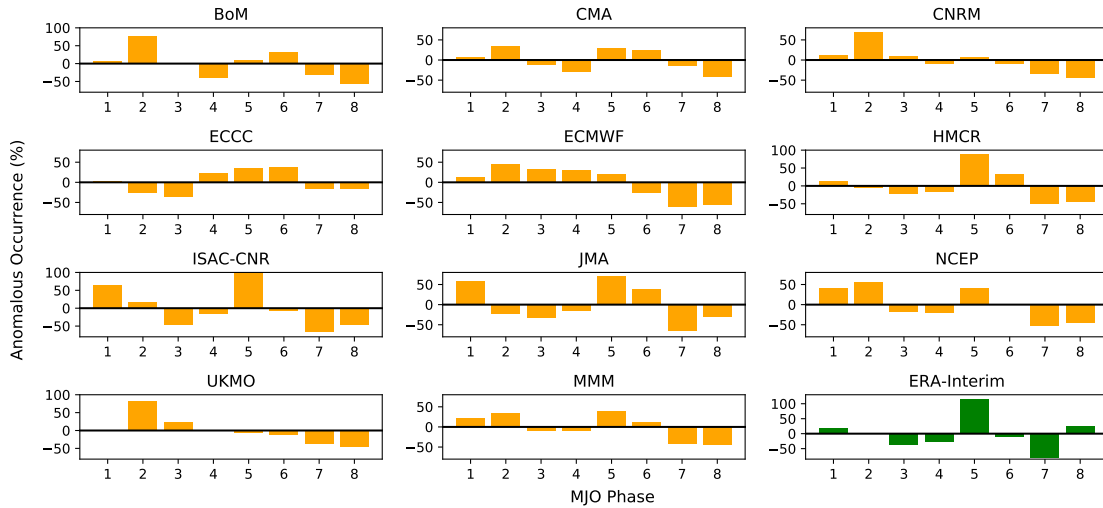


Figure 6.8: Anomalous occurrence (%) of strong Indian monsoon low-pressure systems (SLPSs) in ten S2S models during phases of the Madden-Julian Oscillation (MJO) after Cassou (2008) and Chapter 5 (Deoras et al., 2021b). Forecast lead times of 1–32 days are considered in each S2S model during June–September 1999–2010. Only those SLPSs occurring when the MJO index exceeds a standardised amplitude of one are retained. The multimodel mean (MMM) of ten S2S models is also shown. The result for the KMA model is not shown due to the unavailability of precomputed MJO indices. The MJO indices for SLPSs in ERA-I were obtained from the Bureau of Meteorology, Australia, and the bars are shown using a different colour to distinguish the result from S2S models. Note the different y -axes in subfigures for BoM, HMCR, ISAC-CNR, UKMO and ERA-Interim.

shown). However, the anomalous occurrence of SLPSs in phase 5 is smaller in models such as CNRM and UKMO than in others and ERA-I. Furthermore, SLPS genesis in the ECMWF model continues to remain enhanced (i.e., positive anomalous occurrence) throughout phases 1–5.

In Chapter 5 (Deoras et al., 2021b), we examined anomalies in 850 hPa wind, 700 hPa vertical velocity and 500 hPa specific humidity in each phase of the MJO since these fields are important for deep convection and genesis of LPSs (e.g., Sikka 1978). Here, we investigate anomalies in 850 hPa wind (not shown) and 500 hPa specific humidity (Figure 6.9) since the 700 hPa vertical velocity field is not available in the S2S dataset. The observed genesis biases in the CNRM, UKMO and ECMWF models are not attributable to 850 hPa wind anomalies since they are similar to those in reanalysis datasets (i.e., biases

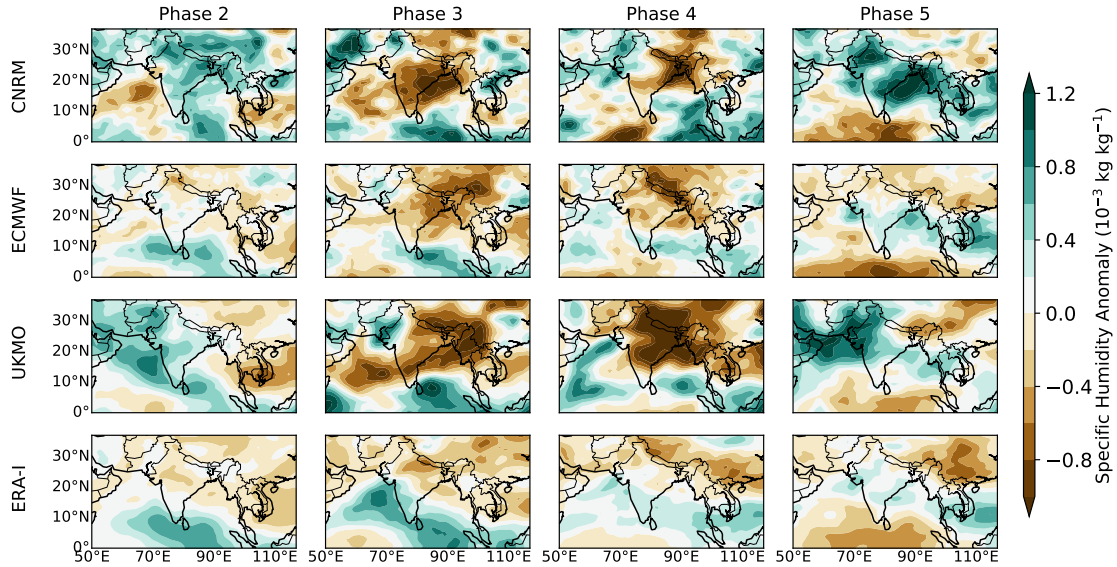


Figure 6.9: 500 hPa specific humidity anomaly ($10^{-3} \text{ kg kg}^{-1}$) in phases 2–5 of the Madden-Julian Oscillation in the CNRM, ECMWF and UKMO models and ERA-I. Forecast lead times of 1–32 days are considered in S2S models, and the result is shown for MJO events during June–September 1999–2010. Only those dates when the MJO index exceeds a standardised amplitude of one are retained. The anomalies are computed against the summer mean climatology (June–September 1999–2010).

are small). In the ECMWF model, negative specific humidity anomalies over the main genesis region in phases 2–4 are larger than those in ERA-I. In the CNRM and UKMO models, positive specific humidity anomalies over the main genesis region in phase 5 are larger than those in ERA-I. Thus, biases in SLPS genesis are not attributable to biases in either the mid-tropospheric moisture or 850 hPa winds that are caused by the MJO. This aspect needs further investigation, which could be possible when other fields (e.g., 700 hPa vertical velocity) are made available.

6.4.2 El Niño Southern Oscillation

In this subsection, we investigate the modulation of SLPSs by ENSO in all S2S models. We compute SST anomalies in each S2S model against the summer mean climatology (June–September 1999–2010), following which we group years into terciles as per the

concurrent seasonal SST anomaly in the Niño 3.4 region during June–September. We consider terciles in order to ensure reasonable sample sizes for each category. For the sake of simplicity, we refer to the upper tercile as El Niño years (2002, 2004, 2006 and 2009), the lowest tercile as La Niña years (1999, 2000, 2007 and 2010), and the middle tercile as neutral years (2001, 2003, 2005 and 2008).³

Figure 6.10a shows the anomalous occurrence (%) of SLPSs in all ensemble members of the eleven S2S models, the MMM, ERA-I and MERRA-2 in different phases of ENSO. Following Kohavi et al. (2009), we compute the 95% confidence interval for anomalous occurrence in each model and reanalysis datasets.⁴ In most S2S models, including the MMM, the anomalous occurrence of SLPSs is highest during La Niña years, which agrees with ERA-I and MERRA-2.⁵ This could be due to more favourable large-scale conditions for SLPS genesis over the head of the BoB (e.g., increased lower-tropospheric convergence) during La Niña years than during El Niño years. The HMCR model simulates a larger frequency of SLPSs during El Niño years than during La Niña years, whereas the CMA, ECMWF and KMA models simulate a larger frequency of SLPSs during neutral years than during La Niña years. However, the difference between them is small. For example, the ECMWF model simulates 9 SLPSs per El Niño year and 10 SLPSs per neutral as well as La Niña year. Vishnu et al. (2020a) compared the frequency of LPSs in six LPS datasets, including tracks derived from ERA-I (1979–2018) and MERRA-2 (1980–2019). They found that ERA-I has roughly the same number of monsoon depressions in El Niño and La Niña years, whereas the frequency of monsoon depressions in MERRA-2 is slightly larger during La Niña years than during El Niño years. These results disagree with Singh et al. (2002) and Hunt et al. (2016a) who found a larger frequency of monsoon depressions

³These terciles match with the published online ENSO databases (e.g., Climate Prediction Centre, which is available at: https://origin.cpc.ncep.noaa.gov/products/analysis_monitoring/ensostuff/ONI_v5.php).

⁴The confidence interval cannot be calculated using standard error since the data is not normally distributed.

⁵We also analysed the modulation of all LPSs by ENSO (not shown), and found that the anomalous occurrence of LPSs in most models and the MMM is highest during La Niña years.

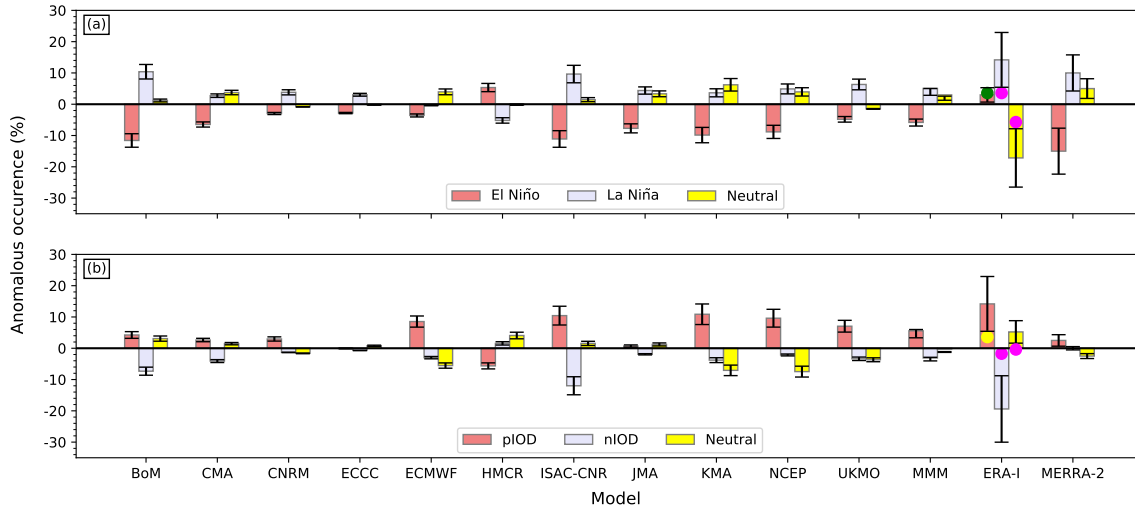


Figure 6.10: Anomalous occurrence (%) of strong Indian monsoon low-pressure systems (SLPSs) in all ensemble members of the eleven S2S models, ERA-Interim and MERRA-2 reanalysis datasets in: (a) different phases of the El Niño Southern Oscillation (ENSO), and (b) the Indian Ocean Dipole (IOD) during June–September 1999–2010. Forecast lead times of 1–32 days are considered for S2S models. The multimodel mean (MMM) of S2S models is also shown. Multicoloured circles show the anomalous occurrence of SLPSs over the main genesis region (15°N–25°N, 80°E–90°E) in respective phases of ENSO and IOD in ERA-I during June–September 1980–2018. The error bars show the 95% confidence intervals for the relative difference in SLPS frequency.

during El Niño years than during La Niña years. Such variations in the results could be due to differences in the LPS-tracking process and intensity thresholds used in these studies.

6.4.3 Indian Ocean Dipole

We compute the DMI for forecast lead times of 1–32 days in S2S models during June–September 1999–2010. Following the method discussed in the previous subsection, we group years into terciles to boost the sample size, which we refer to as positive IOD (pIOD) years (2003, 2006, 2007 and 2008), negative IOD (nIOD) years (2001, 2004, 2005 and 2009) and neutral IOD years (1999, 2000, 2002 and 2010).⁶ Figure 6.10b shows the

⁶During 1999–2010, only one event was classified as a pIOD and one as a nIOD in 2006 and 2010, respectively by the Bureau of Meteorology (BoM), Australia. Therefore, our classification of IOD events in this study differs from that of the BoM.

anomalous occurrence of SLPSs during phases of the IOD. The SLPS frequency is larger in all models and the MMM during pIOD years than during nIOD years, which agrees with ERA-I and MERRA-2.⁷ This could be due to more favourable large-scale conditions (e.g., lower-tropospheric convergence) over the head of the BoB during pIOD years than during nIOD years. However, the SLPS frequency is larger in HMCR during nIOD years than during pIOD years. Vishnu et al. (2020a) found that roughly the same number of monsoon depressions form during pIOD and nIOD years in all datasets, but there is a larger frequency of weak LPSs during nIOD years than during pIOD years.

6.4.4 Interannual variability of SLPSs over a long time period

Following the results discussed in the previous subsections, we use the ERA-I SLPS dataset to investigate the modulation of SLPSs by ENSO and IOD over a time period longer than the common reforecast period of S2S models. We consider SLPSs over the main genesis region during June–September 1980–2018.⁸ Multicoloured circles in Figure 6.10 show the anomalous occurrence of SLPSs during phases of ENSO and IOD. The frequency of SLPSs is exactly the same during El Niño and La Niña years, whereas it is larger during pIOD years than during nIOD years.

We now consider the IMD Cyclone e-Atlas dataset to investigate the modulation of BoB monsoon depressions by ENSO and IOD during 1891–2018.⁹ We can examine the impact of ENSO and IOD during their developing and mature phases. Figures 6.11a and 6.11b show the interannual standard deviation and normalised interannual standard deviation of SST anomaly in the Niño 3.4 region and the DMI, respectively. The standard deviation of the DMI has its maximum between September and November, whereas

⁷We also analysed the modulation of all LPSs by IOD (not shown), and found that the SLPS frequency is larger in all models and the MMM during pIOD years than during nIOD years.

⁸We exclude 1979 in order to group the years between 1980 and 2018 into terciles.

⁹We analysed the modulation of frequency of monsoon depressions (MDs) by ENSO and IOD during June–September 1980–2018, and found that more MDs form during El Niño and pIOD years than during La Niña and nIOD years.

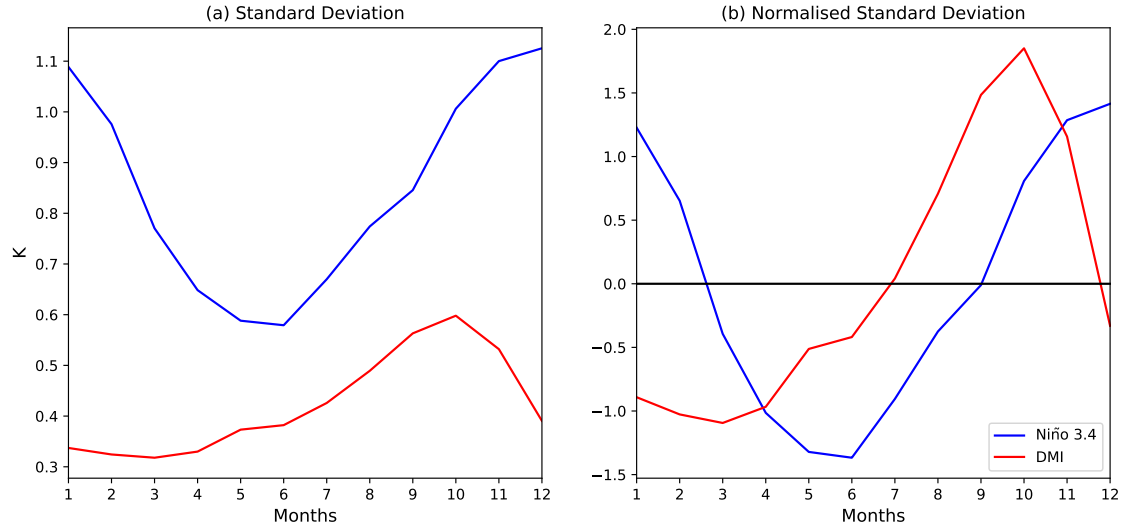


Figure 6.11: (a) Interannual standard deviation and (b) normalised interannual standard deviation of Niño 3.4 sea surface temperature (SST) anomaly and the Dipole Mode Index (DMI) during 1891–2018, which is computed using the ERSSTv5 dataset.

that of the Niño 3.4 SST anomaly occurs between November and January. We therefore consider September–November and November–January as the mature phase for IOD and ENSO, respectively. We consider the long-term mean (June–September 1891–2018) of monsoon depressions in this dataset, and compute the anomalous occurrence of monsoon depressions for different categories of ENSO and IOD (i.e., their combined and separate influences). Figures 6.12a and 6.12b show the anomalous occurrence of monsoon depressions during the developing and mature phases of ENSO and IOD, respectively. During the developing phase, the median anomalous frequency is negative for La Niña-negative IOD events, whereas during the mature phase, it is negative for El Niño and La Niña-negative IOD events. However, differences between the median anomalous occurrence of monsoon depressions in different categories are small. Furthermore, the anomalous occurrence of monsoon depressions during individual seasons is positive as well as negative in each category, suggesting no obvious impact of ENSO and IOD on their frequency.

In summary, most S2S models and the MMM well simulate the modulation of SLPSs

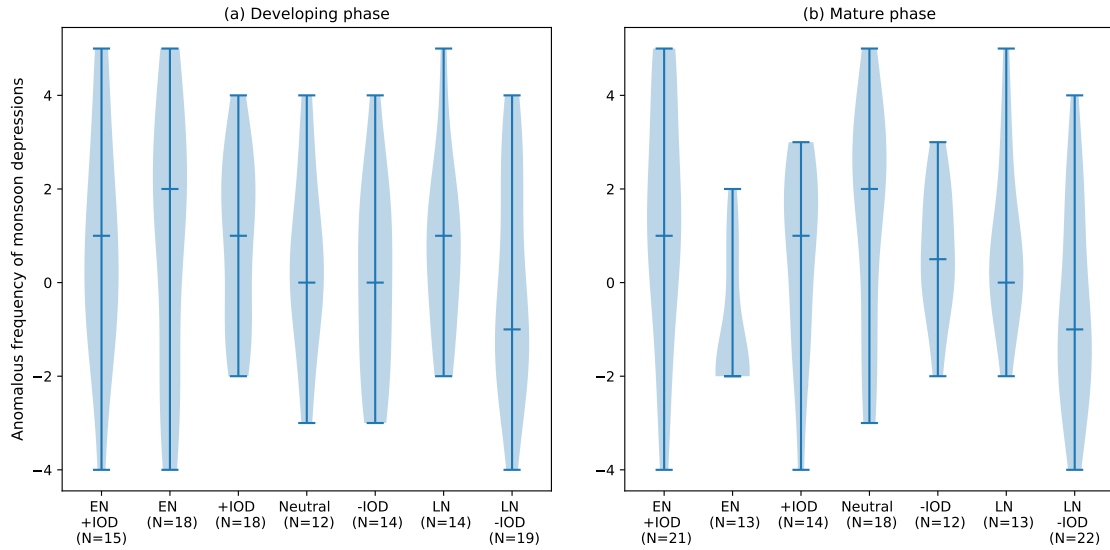


Figure 6.12: Anomalous frequency of monsoon depressions (per June–September season) in the IMD Cyclone e-Atlas dataset for (a) developing phase and (b) mature phase of ENSO and IOD during 1891–2018. For the developing phases of ENSO and IOD, June–September period is considered. For the mature phase of the IOD, concurrent September–November period is considered, whereas November–January period is considered for ENSO. The anomalous occurrence of monsoon depressions is computed with respect to their mean frequency during June–September 1891–2018. ENSO and IOD events are separated into different categories after Ummenhofer et al. (2009). These categories are: El Niño and positive IOD (EN + IOD), pure El Niño (EN), pure positive IOD (+IOD), ENSO and IOD neutral (Neutral), negative IOD (-IOD), pure La Niña (LN), and La Niña and negative IOD (LN-IOD). The widths of individual violins are Gaussian kernel estimates for the probability density functions of the respective distributions. For each category, the number of years (N) is shown in each x -axis label.

by the MJO. The frequency of SLPSs in most models during La Niña and pIOD years is larger than during El Niño and nIOD years. For the 1980–2018 period, their frequency over the main genesis region in ERA-I during La Niña and El Niño years is equal, whereas that during pIOD years is larger than during nIOD years. There is no obvious impact of ENSO and IOD on the frequency of monsoon depressions in the IMD Cyclone e-Atlas dataset during 1891–2018. As a result, we do not carry out a similar analysis using S2S models.

6.5 Relationship between large-scale atmospheric fields and frequency of BoB LPS varieties

In this section, we attempt to understand the mechanisms by which large-scale modes might exert controls on the frequency of BoB LPSs. As discussed in Chapter 5 (Deoras et al., 2021b), there is a moderate negative correlation between interannual frequencies of short-lived and long-lived BoB LPSs, suggesting that large-scale conditions might play a role in determining whether LPSs continue their propagation across north-central India. We therefore analyse correlations between large-scale atmospheric fields and interannual frequencies of these weather systems. Stakeholders (e.g., meteorologists) could use these large-scale fields as predictors of LPSs, which could ultimately help in developing subseasonal to seasonal outlooks of LPSs.

6.5.1 MDGI components

Figure 6.13 shows the correlation between the three components of the MDGI and interannual frequencies of BoB LPSs. The 600 hPa relative humidity field over the head of the BoB and Indo-Gangetic Plain (IGP) is positively correlated with the frequency of total BoB LPSs (i.e., the sum of short-lived and long-lived BoB LPSs), and this correlation is statistically significant over western and northwestern parts of India (Figure 6.13a). In addition, there is a moderate positive linear correlation between 600 hPa relative humidity over the western North Pacific Ocean and the frequency of total BoB LPSs, suggesting that there could be a relationship between low-pressure systems over this region and BoB LPSs; we shall explore this relationship in Section 6.6. A comparison between correlations for BoB-short and BoB-long LPSs (Figures 6.13b and 6.13c) suggests that enhanced mid-tropospheric moisture benefits the formation of BoB-long LPSs. We do not show the result for total column water vapour due to its similarity with 600 hPa relative humidity. The ECAPE and frequency of BoB-total LPSs over the main genesis region are not

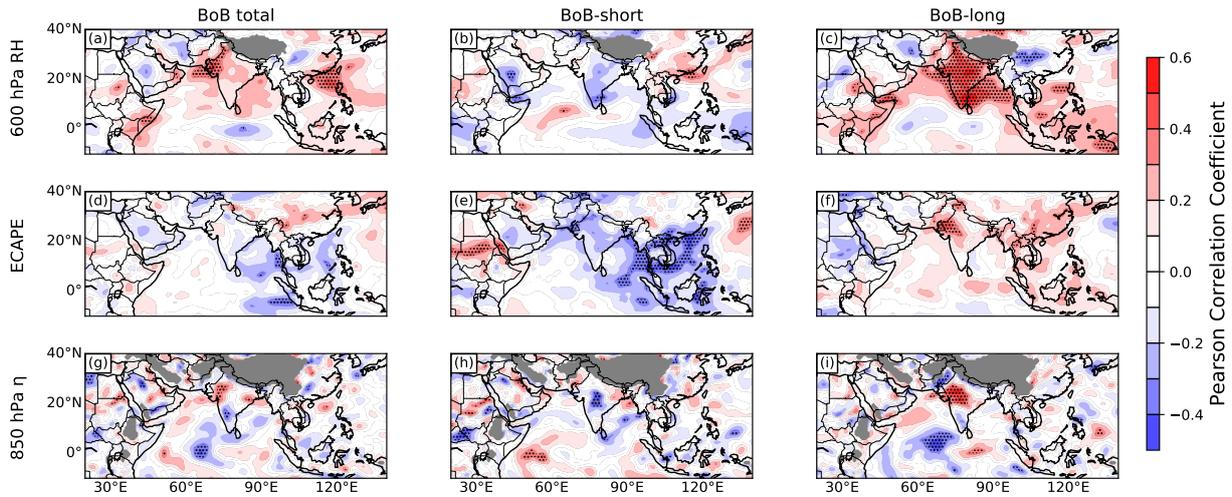


Figure 6.13: Interannual Pearson correlation coefficient between the three components of the monsoon disturbance genesis index (MDGI) and observed frequency of Bay of Bengal (BoB) monsoon low-pressure systems (LPSs) in ERA-I that had genesis during June–September 1979–2018. The three components of the MDGI are 600 hPa relative humidity (RH), estimated convective available potential energy (ECAPE) and 850 hPa absolute vorticity (η). The BoB systems (BoB total) are partitioned into short-lived (BoB-short) and long-lived (BoB-long) LPSs as per their track length after Chapter 5 (Deoras et al., 2021b). Stippling indicates where the Pearson correlation coefficient is significantly different from zero at the 95% level. Grey areas are indicative of major orography, where the mean surface pressure is less than 850 hPa and 600 hPa levels in respective subfigures.

significantly correlated; however, there is a negative correlation between the frequency of BoB-short LPSs and the ECAPE over the South China Sea and adjoining parts of the western North Pacific Ocean (Figure 6.13e). Over western and central parts of India, there is a moderate positive correlation between 850 hPa absolute vorticity and frequency of BoB-long LPSs (Figure 6.13i), whereas there is a moderate negative correlation between the two for BoB-short LPSs (Figure 6.13h). We hypothesise that variations in the strength of the monsoon trough can affect LPS frequency—a strong monsoon trough can enhance the lifespan and propagation of LPSs towards interior parts of India, resulting in a larger frequency of BoB-long LPSs compared to that of BoB-short LPSs. We will investigate the relationship between the monsoon trough and SLPSs in the next subsection. Thus,

the MDGI components correlate well with the frequency of BoB-long LPSs, but not with BoB-short LPSs. This suggests that if conditions are favourable for the genesis of LPSs over the BoB as per the MDGI, they are also favourable for deeper inland penetration of these systems (i.e., the formation of BoB-long LPSs).

6.5.2 Monsoon trough

In this subsection, we investigate the relationship between the strength of the monsoon trough and frequency of BoB-total LPSs in ERA-I. We group the years between 1980 and 2018 into terciles as in the seasonal frequency analysis. The lowest tercile (i.e., suppressed LPS frequency) has a mean of 7 LPSs per season, whereas the highest tercile (i.e., enhanced LPS frequency) has a mean of 11 LPSs per season. We compare the strength of the monsoon trough (i.e., 850 hPa relative vorticity) on non-LPS days (i.e., when LPSs are absent) in a composite of suppressed (Figure 6.14a) and enhanced (Figure 6.14b) LPS frequency years. We also compare the composites for LPS days (Figures 6.14c and 6.14d). The monsoon trough on non-LPS days is weaker than during LPS days, and its strength is not affected by the frequency of LPSs on non-LPS days. On LPS days, the intensity of the monsoon trough is similar for suppressed and enhanced frequency of LPSs. This suggests the role of LPSs in intensifying the monsoon trough. Thus, correlations between the 850 hPa absolute vorticity and LPS frequency (Figures 6.13g and Figure 6.13i) are attributed to the relative vorticity of LPSs instead of our hypothesis about the variations in the strength of the monsoon trough. These results also suggest that large-scale modes (e.g., ENSO) might not be modulating LPSs through the monsoon trough, and 850 hPa absolute vorticity might not be a useful predictor of LPS frequency on the seasonal time scale.

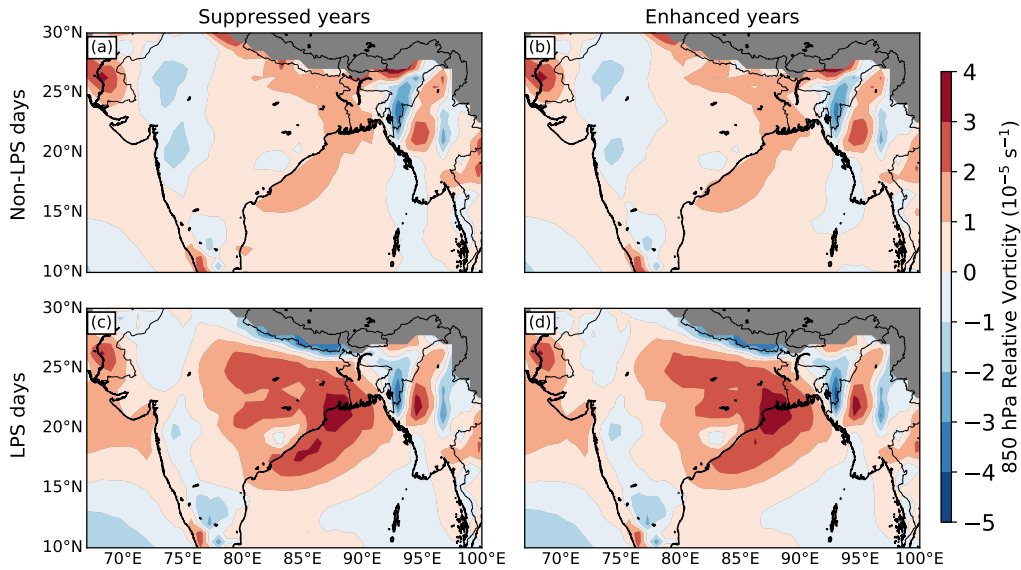


Figure 6.14: 850 hPa relative vorticity (10^{-5} s^{-1}) on days when Indian monsoon low-pressure systems (LPSs) are absent (a and b) and present (c and d) in ERA-I. The results are shown for seasons when LPS frequency is suppressed (a and c) and enhanced (b and d) during June–September 1979–2018. Grey areas are indicative of major orography, where the mean surface pressure is less than 850 hPa.

6.5.3 Zonal vertical shear and winds

LPSs occur in a background state of strong easterly vertical wind shear (e.g., Raman et al. 1978) created by the low-level monsoon westerlies and the upper-level tropical easterly jet. It is well known that the vertical shear is detrimental to the growth of tropical cyclones (e.g., Gray 1968). However, its exact role in the growth of LPSs remains less explored since the focus of previous studies has been on understanding if they grow due to barotropic or baroclinic instability in the large-scale monsoon flow. Some have suggested that they grow due to baroclinic instability (e.g., Mishra and Salvekar 1980). However, this requires LPSs to tilt upshear with height (Cohen and Boos, 2016) instead of the observed downshear tilt (e.g., Hunt et al. 2016a). Diaz and Boos (2019) concluded that barotropic instability in the monsoon flow due to meridional shear in the low-level winds favours the growth of monsoon depressions. Previous studies have found an inverse relationship between

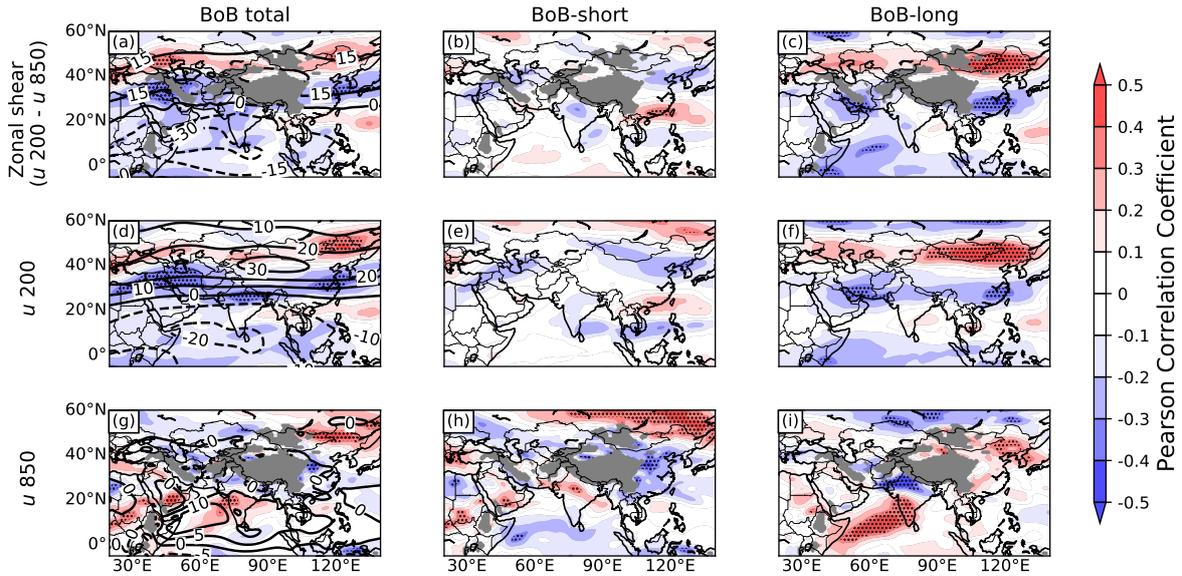


Figure 6.15: Interannual Pearson correlation coefficient between the zonal vertical shear (200–850 hPa; a–c), zonal winds at 200 hPa (d–f) and 850 hPa (g–i), and the observed frequency of Bay of Bengal (BoB) monsoon low-pressure systems (LPSs) that had genesis during June–September 1979–2018 in ERA-I. The BoB systems (BoB total) are partitioned into short-lived (BoB-short) and long-lived (BoB-long) LPSs as per their track length after Chapter 5 (Deoras et al., 2021b). Line contours show the climatological (June–September 1979–2019) zonal shear and zonal winds at 200 hPa and 850 hPa in respective subfigures. Grey areas are indicative of major orography, where the mean surface pressure is less than 850 hPa.

the seasonal frequency of monsoon depressions and seasonal vertical wind shear over the genesis region (e.g., Sikka 1978; Raman et al. 1978; Xavier and Joseph 2000; Ditchek et al. 2016). We therefore focus on analysing the correlation between the LPS frequency and the zonal vertical shear. We compute the zonal vertical shear as the difference between zonal winds at 200 hPa and 850 hPa (i.e., 200 minus 850 hPa). For all cases (Figures 6.15a–c), there is an absence of statistically significant linear correlation between the interannual frequency of BoB LPSs and the zonal vertical shear over the main genesis region. However, frequencies of BoB-total and BoB-short LPSs (Figures 6.15a and 6.15b) are negatively correlated with the zonal vertical shear over central India. For BoB-long LPSs (Figure 6.15c), there is a statistically significant positive and negative correlation

over northeastern and southeastern parts of China, respectively. Interestingly, the sign of the correlation reverses for BoB-short LPSs.

For both LPS varieties and BoB-total LPSs, there is no significant correlation between the LPS frequency and 200 hPa zonal wind over the main genesis region, and the pattern of correlation in BoB total is similar to that in BoB-long. The BoB-total and BoB-long LPS frequencies are negatively correlated with the zonal wind over the IGP and regions such as Iran and the eastern coast of China. For BoB-short LPSs, there is a weak negative correlation over the IGP, but it is not significant. The pattern of correlation for 200 hPa zonal wind and zonal vertical shear to the north of approximately 20°N is similar, which is due to weak zonal winds at 850 hPa over this region. Figures 6.15c and 6.15f suggest that LPS frequency is sensitive to the latitude of the jet; we therefore investigate how shifts in the latitudinal position of the subtropical westerly jet and tropical easterly jet can influence the frequency of BoB LPS varieties. Following Hunt et al. (2018a) and Schiemann et al. (2009), we consider a region where the 200 hPa zonal wind is positive and the absolute wind magnitude exceeds 30 m s^{-1} as a jet streak within the subtropical westerly jet. On similar lines, we consider a region where the 200 hPa zonal wind is negative and the absolute wind magnitude is greater than or equal to 20 m s^{-1} as a jet streak in the tropical easterly jet. Figure 6.16 shows the mean location of the jet streak during June–September 1979–2018. We group seasons into terciles as per the seasonal frequency of BoB LPS varieties. There is a small northward shift in the subtropical westerly jet over northern China when the frequency of BoB-long LPSs is enhanced; this is evident from a broader jet streak (Figure 6.16c). Interestingly, this pattern is opposite for BoB-short LPSs. The jet streak within the tropical easterly jet is broader during enhanced LPS years than during suppressed LPS years. We hypothesise that the LPS frequency is enhanced due to a better access to the upper-air divergent region over the BoB, which is associated with the right-entrance region of the jet streak within the tropical easterly jet. Further investigation is needed to understand this aspect, which is beyond the scope of this chapter. For the zonal wind

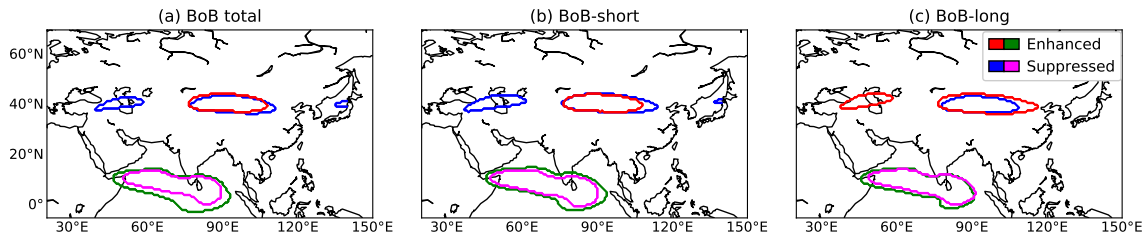


Figure 6.16: Mean location of the jet streak of the subtropical westerly jet and tropical easterly jet during June–September 1979–2018. The mean location is shown for enhanced (red and green) and suppressed (blue and magenta) frequency of (a) BoB-total, (b) BoB-short and (c) BoB-long LPSs.

at 850 hPa, there is a major difference in the sign of the correlation over the IGP and Arabian Sea. Strong westerly zonal wind over the IGP is unfavourable for the genesis of BoB-long LPSs. Moreover, strong zonal westerly wind over the Arabian Sea, which can result in an enhanced moisture transport towards India, favours the genesis of BoB-long LPSs instead of BoB-short LPSs.

In summary, large-scale atmospheric fields related to the four components of the MDGI, zonal vertical shear and winds have a contrasting role in modulating the frequency of BoB-short and BoB-long LPSs. The monsoon trough remains weak in the absence of LPSs, which suggests that the trough might not be playing an important role in the modulation of LPSs by large-scale modes such as ENSO.

6.6 Characteristics of downstream LPSs

In this section, we explore characteristics of downstream LPSs, which originate over the South China Sea and western Pacific Ocean, and propagate towards India in the direction of the tropical easterly jet. As discussed in Section 6.2.2, these systems are identified by applying a feature-tracking algorithm to 700 hPa relative vorticity in ERA-I during June–September 1979–2018, following which they are partitioned into clusters using a k -means clustering technique. These systems can provide a larger window of opportunity

for preparedness in India than that provided by LPSs forming over the BoB. Thus, these results could benefit stakeholders such as disaster management organisations in improving flood preparedness.

6.6.1 Frequency and track characteristics

Figure 6.17 shows tracks of individual low-pressure systems, their mean tracks and mean track durations in each cluster, which are named as per genesis locations and characteristics of mean tracks. There are 57 systems in the downstream cluster that form over the South China Sea, nearby coastal regions of Vietnam and the Philippines, and western Pacific Ocean. They have a mean lifetime of 8.2 days. Only one out of 346 systems in the South China Sea cluster reaches the eastern coast of India as against 32 out of 57 systems in the downstream cluster. This result motivates us to analyse the large-scale steering environment in all clusters, which we will discuss in the next subsection. Two clusters have tropical cyclones (TCs), which we name TC-short and TC-long as per the mean track length.

The downstream LPSs are most frequent in August (20 LPSs), which is followed by September (17 LPSs), June (11 LPSs) and July (9 LPSs). This result agrees with the findings of Meera et al. (2019) and Srujan et al. (2021). Systems in the TC-short cluster are most frequent in August, whereas those in the TC-long cluster are most frequent in September. Thus, the increased frequency of downstream LPSs during August and September coincides with the peak of the western North Pacific tropical cyclone season. Systems in the recurving and Central Pacific clusters are most frequent in August, whereas those in the non-recurving cluster are most frequent in July. In contrast, systems in the South China Sea cluster are most frequent during June and July and least frequent during September.

We now examine the sensitivity of the frequency of downstream LPSs to the choice of the pressure level for tracking. We repeat the tracking and clustering processes and

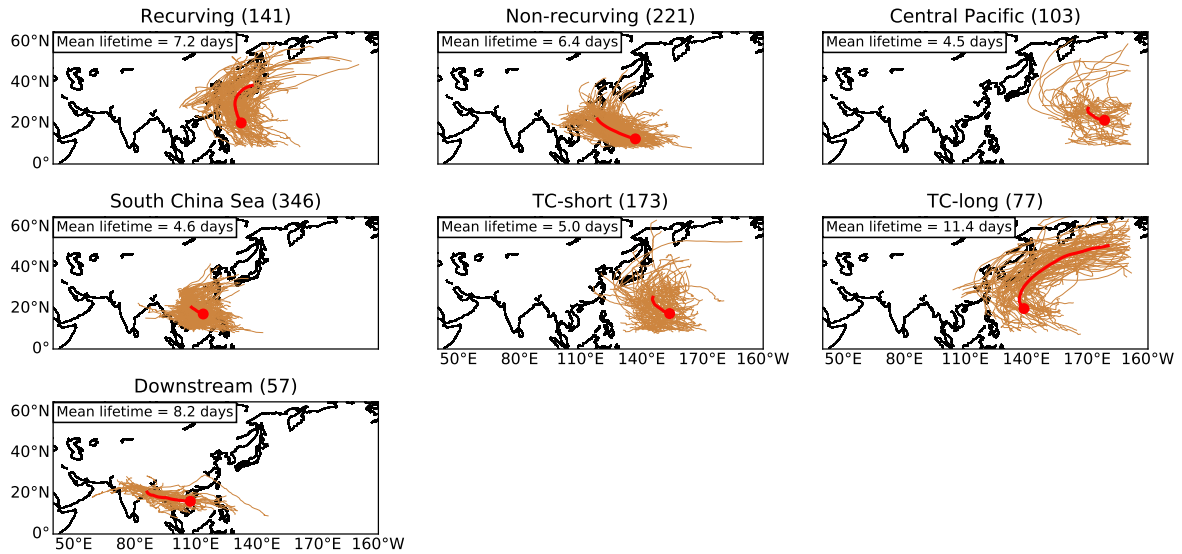


Figure 6.17: Tracks of low-pressure systems that had their genesis over the South China Sea, western and central Pacific Ocean, and nearby coastal regions during June–September 1979–2018. These systems are identified by applying a feature-tracking algorithm on 700 hPa relative vorticity in ERA-I, following which they are partitioned into seven clusters using a k -means clustering technique. A red line in each subplot shows the mean track, whereas a red circle shows the mean genesis location. The clusters are named as per the genesis location and characteristics of the mean tracks. Two clusters have tropical cyclones (TCs), which are named TC-short and TC-long as per the mean track length. The number of systems in each cluster is shown in the title. The mean lifetime of systems in each cluster is also shown. Track points to the east of 160°W are not shown in this figure.

identify 36 downstream LPSs at 850 hPa in ERA-I during June–September 1979–2018. We use a spatiotemporal matching technique to match these LPSs with those identified at 700 hPa. We consider a track at 850 hPa to match with a track at 700 hPa if the mean spatial separation between the two for the overlapping time period is less than or equal to a threshold value. We determine this spatial separation threshold by conducting a sensitivity test, which is similar to the one discussed in Section 2.2.3 of Chapter 2. For a range of spatial separation, we calculate a ratio of the number of matched LPSs to the total number of LPSs identified at 850 hPa. We select 100 km as the spatial separation threshold since the gradient of fraction is maximum for this value (Figure 6.18b). 13

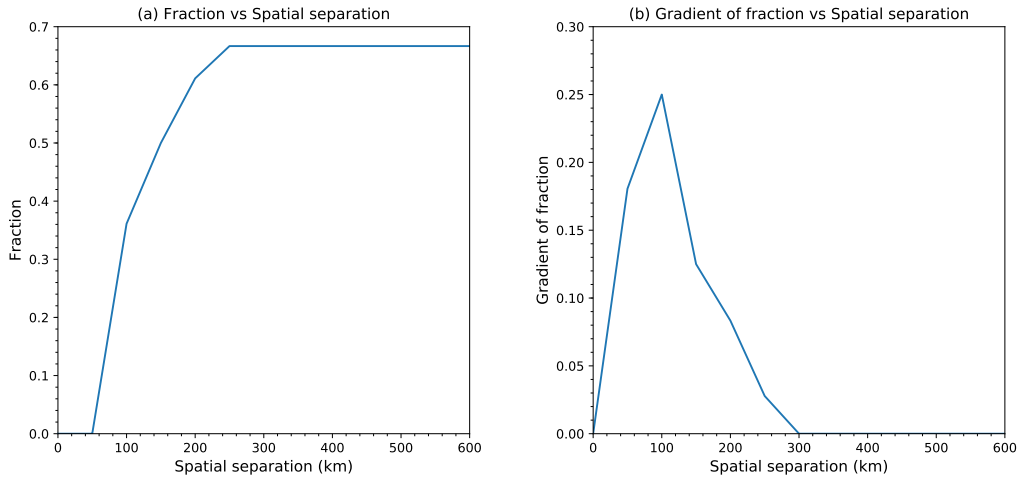


Figure 6.18: Result of the sensitivity test for determining the spatial threshold for the matching of downstream low-pressure systems (LPS) at 850 hPa in ERA-I with those at 700 hPa. The fraction represents a ratio of the number of matched systems to the total number of systems at 850 hPa (36). (a) shows the fraction vs spatial separation (km), whereas (b) shows the gradient of fraction vs spatial separation. For each LPS pair, the mean spatial separation during the overlapping time period is considered. These results are shown for LPSs that occurred during June–September 1979–2018.

downstream LPSs at 850 hPa match with those at 700 hPa, and most of them have genesis over the South China Sea and adjoining western Pacific Ocean (Figure 6.19a). In contrast, most unmatched downstream LPSs have genesis over the Indochina region (Figure 6.19b) and they could be orographically generated mid-tropospheric cyclones. Most unmatched systems have lysis over the eastern part of India, whereas most matched systems have lysis over central and west-central parts of India, resembling BoB-short and BoB-long LPSs, respectively (Chapter 5; Deoras et al. 2021b).

6.6.2 Steering of low-pressure systems in different clusters

In this subsection, we investigate the mechanisms responsible for steering low-pressure systems in the seven clusters. These results could be useful for the extended-range forecasting of BoB LPSs that begin as downstream LPSs. Several studies have analysed the effect of the western Pacific subtropical high (WPSH) on the propagation of tropical cy-

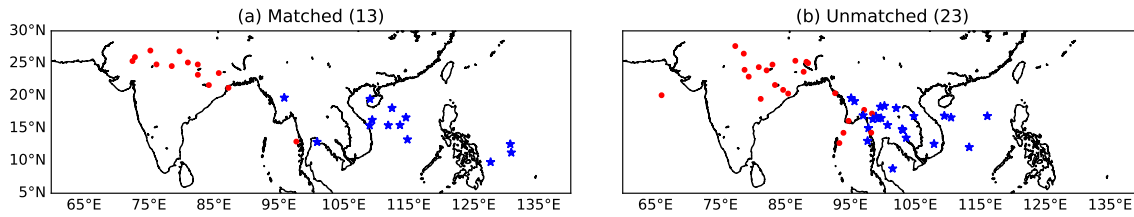


Figure 6.19: Genesis (blue stars) and lysis (red dots) points of downstream low-pressure systems at 850 hPa in ERA-I that: (a) match with systems identified at 700 hPa and (b) do not match with systems identified at 700 hPa. A track at 850 hPa is considered to match with a track at 700 hPa if the mean spatial separation between these two tracks for the overlapping time period is less than or equal to 100 km. The total number of systems in each case is shown in the title. Both results are for systems that occurred between June–September 1979–2018.

clones (e.g., Wu and Wang 2015; Camp et al. 2019; Feng et al. 2019). Wang et al. (2013) and Camp et al. (2019) found that a weakened WPSH favours landfall of tropical cyclones in eastern China, Korea and Japan. Following Camp et al. (2019), we consider 850 hPa geopotential height for analysing the effect of the WPSH on systems in the seven clusters. LPSs in most clusters have a mean lifespan of approximately 5 days; we therefore consider the position of the WPSH three days after genesis of systems in order to investigate the large-scale conditions during their midlife. There is a prominent westward extension of the WPSH in the non-recurving cluster (Figure 6.20b) that prevents a majority of LPSs from turning northwards and reaching Korea and Japan. In contrast, the WPSH in the recurving and TC-long clusters is weaker and does not feature a prominent westward extension, which allows systems in these clusters to propagate towards Japan. The WPSH does not influence the propagation of systems in the South China Sea and downstream clusters given the large distance between them.

As discussed in the previous subsection, systems in the South China Sea and downstream clusters form over the South China Sea and adjoining coast of Vietnam, but there is a considerable difference in their propagation. We therefore analyse composites of 500 hPa wind anomalies on the genesis day and up to 3 days after genesis (Figure 6.21). In the

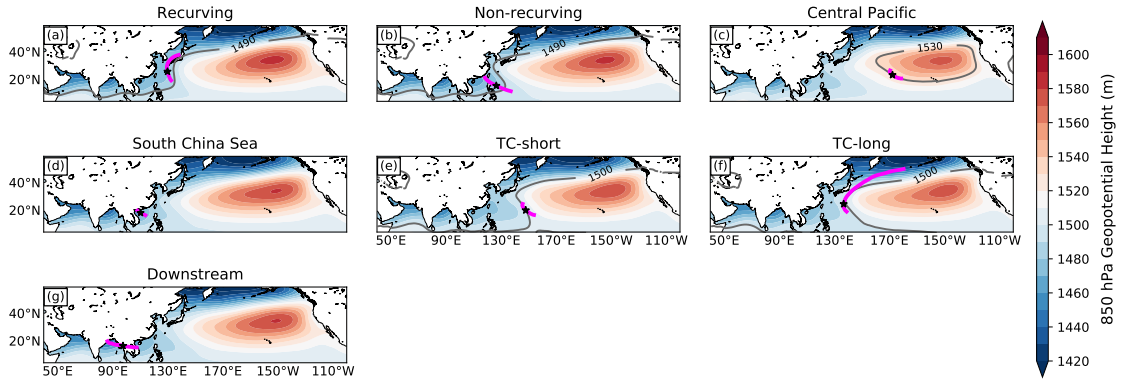


Figure 6.20: Mean 850 hPa geopotential height three days after genesis of low-pressure systems (LPSs) in each LPS cluster during June–September 1979–2018. Only those contours are labelled in some clusters that are closest to the mean LPS track. They are not labelled in the South China Sea and downstream clusters since the western Pacific subtropical high does not influence the propagation of LPSs. A dark violet line in each subplot shows the mean LPS track, whereas a black star shows the mean LPS location three days after the composite LPS genesis. Contours are not shown where the mean surface pressure is less than 850 hPa.

South China Sea cluster, there is an anticyclonic anomaly to the east of Taiwan throughout the investigation period (Figures 6.21a–d), which is responsible for the landfall of these systems in the northern coast of Vietnam and adjoining parts of China (Figure 6.21d). This anticyclonic anomaly is absent in composites of the downstream cluster. In fact, there are anomalous easterly winds over Vietnam and the Indochina region, which favour the west-northwestward movement of these systems towards the BoB and nearby coastal regions of India (Figure 6.21h).

6.6.3 Evolution over lifespan

In this section, we analyse the evolution of LPSs in all clusters over their lifespan. We interpolate central 700 hPa relative vorticity and central temperature anomalies at 925 hPa and 300 hPa onto a common time axis since different systems can have a different lifespan. We construct a lifetime-percentage array as in Hunt et al. (2016a) and Chapter 4 (Deoras et al., 2022). We first calculate the percentage age of an LPS at each time

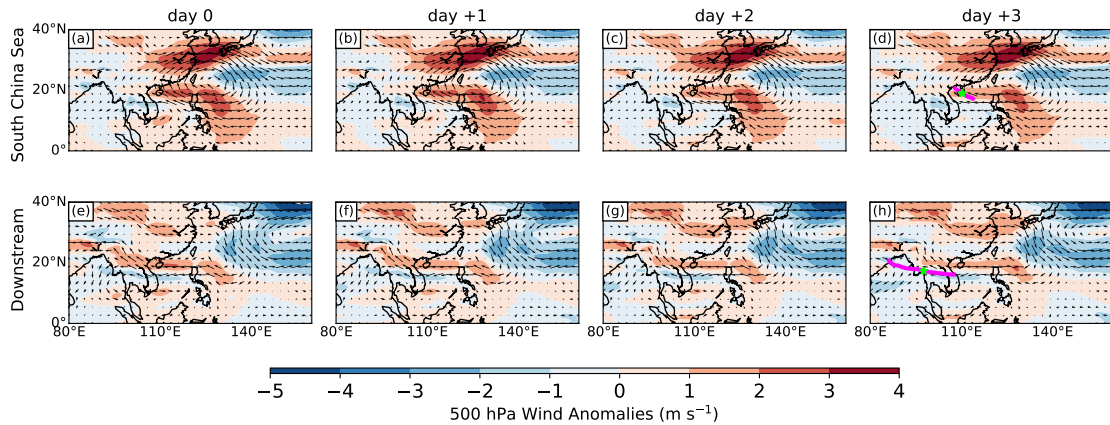


Figure 6.21: A composite of 500 hPa wind anomalies for low-pressure systems in the South China Sea and downstream clusters in ERA-I. Day 0 represents the genesis day of these systems, and composites are shown for a period of 3 days after genesis of low-pressure systems. These anomalies are computed against the summer mean climatology (June–September 1979–2018). A solid magenta line in (d) and (h) shows the mean track of systems in the respective two clusters, whereas a light green star shows the mean location of these systems three days after their genesis.

step, with the first (final) time step denoting genesis (lysis) or 0% (100%) lifespan, and then interpolate fields for all such time steps on this array. We iterate this process for all LPSs and compute a mean value. The temperature anomalies at 925 hPa and 300 hPa are useful in analysing the evolution of the lower-tropospheric cold core and upper-tropospheric warm core, respectively, and have implications in the understanding of moist thermodynamic processes therein.

Systems in the TC-long cluster are most intense, whereas those in the Central Pacific, South China Sea and downstream clusters are least intense (Figure 6.22a). The downstream LPSs attain their maximum intensity at approximately 20% lifespan, which is much earlier than systems in other clusters and SLPSs (Chapter 4; Deoras et al. 2022). These systems weaken over the Indochina region, but the rate of their weakening decreases at $\sim 50\%$ lifespan due to favourable conditions over the BoB. The systems in the non-recurring and TC-short clusters attain their maximum intensity at $\sim 70\%$ lifespan, which is much later than systems in other clusters. These systems are present over the

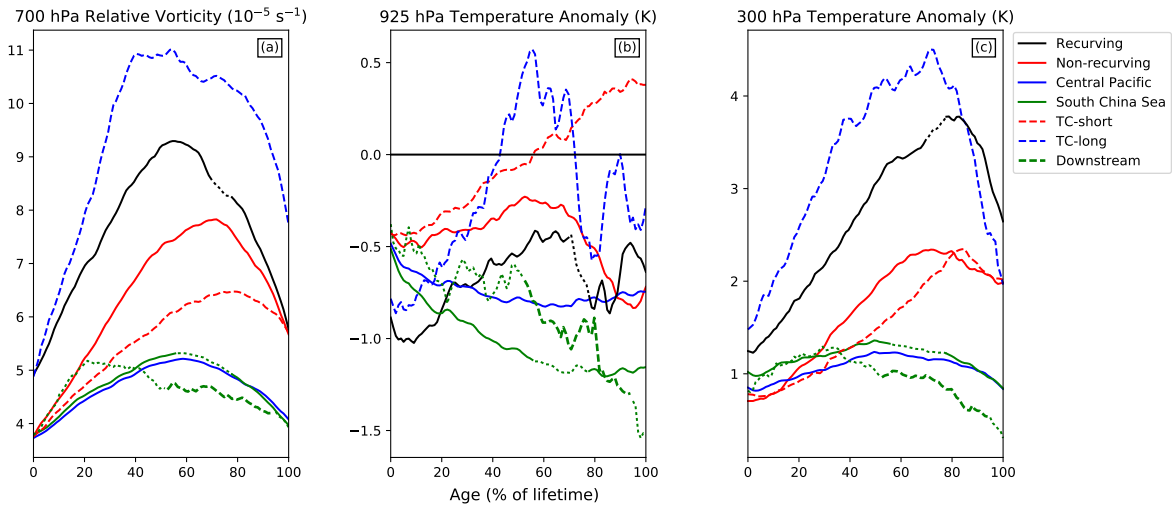


Figure 6.22: (a) 700 hPa relative vorticity anomaly (10^{-5} s^{-1}), (b) temperature anomaly (K) at 925 hPa, and (c) temperature anomaly (K) at 300 hPa as a function of the lifespan of composites of low-pressure systems in the seven clusters. Only those systems, which had genesis during June–September 1979–2018, are considered. The anomalies are computed against the summer mean climatology (June–September 1979–2018). Dotted lines in the recurring, South China Sea and downstream clusters show the stage when the mean track is over land.

tropical western Pacific Ocean for most of their lifespan, where favourable conditions for convection allow them to gradually intensify over a longer duration compared to systems in other clusters such as the downstream cluster. Interestingly, systems in the recurring and TC-long clusters also spend most of their lifespan over the western Pacific Ocean; however, they encounter cooler SSTs after crossing approximately 30°N . As a result, they attain their maximum strength around their midlife. The downstream LPSs and systems in most clusters feature a cold core in the lower troposphere (Figure 6.22b), which suggests that they are tropical depressions. In most clusters, the evolution of the upper-tropospheric warm core is similar to 700 hPa relative vorticity (Figure 6.22c). This is expected since the warm core is attributed to latent heating from deep convection, which is particularly observed in monsoon depressions (Hunt et al., 2016b). However, systems in the recurring and TC-long clusters attain their respective maximum magnitude of the warm core much

later than 700 hPa relative vorticity.

6.6.4 Precipitation contribution

We determine the precipitation contribution of downstream LPSs by attributing precipitation to an LPS if it falls within 800 km of its centre (Hunt and Fletcher 2019). Their precipitation contribution is largest over the coast of Vietnam and southern BoB, where they produce up to 14% of seasonal precipitation (Figure 6.23). Over eastern and central parts of India, they produce up to 8% of seasonal precipitation. This is substantially smaller than precipitation contributions of BoB-short and BoB-long LPSs that exceed 30% (Chapter 5; Deoras et al. 2021b). This difference is attributed to the smaller frequency of downstream LPSs compared to those of BoB-short and BoB-long LPSs.

In summary, there are 57 downstream LPSs at 700 hPa in ERA-I that have a mean lifetime of 8.2 days and highest frequency in August. Their west-northwestward propagation towards India is attributed to the anomalous mid-tropospheric easterlies over the Vietnam coast and the Indochina region. They feature a warm-over-cold core structure that is similar to SLPSs, and are responsible for up to 8% of the seasonal precipitation over central and eastern parts of India.

6.7 Conclusions

In this chapter, we investigated the large-scale drivers of Indian monsoon low-pressure systems (LPSs), which have been less explored than for other phenomena such as tropical cyclones. We considered strong LPSs (SLPSs) in all ensemble members of the eleven models of the Subseasonal-to-Seasonal (S2S) prediction project during a common reforecast period of June–September 1999–2010 and forecast lead times of 1–32 days. The results were verified against the European Centre for Medium-Range Weather Forecasts ERA-Interim (ERA-I) reanalysis and Modern-Era Retrospective Analysis for Research and

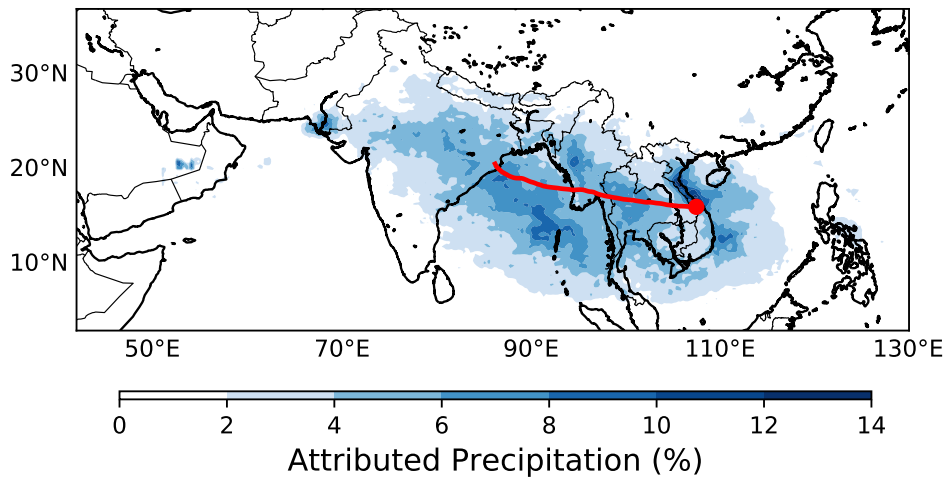


Figure 6.23: Percentage of seasonal (June–September 1998–2018) precipitation attributed to low-pressure systems (LPSs) in the downstream LPS cluster. Rainfall is attributed to a system if it falls within 800 km of its centre after Hunt and Fletcher (2019). A solid red line shows the mean LPS track, whereas a red dot shows the mean genesis location.

Applications, version 2 (MERRA-2) datasets. We then used ERA-I for further analysis since this dataset is available for a time period longer than the common reforecast period of S2S models. We also used ERA-I to explore characteristics of downstream LPSs, which originate over the South China Sea and adjoining western Pacific Ocean, and then propagate towards India in the direction of the tropical easterly jet. Given that their genesis location is far from India, these systems can provide a larger window of opportunity for preparedness in India than that provided by LPSs forming over the BoB. The key results of this chapter can be summarised as follows:

The simulation of the genesis potential of SLPSs

We computed the monsoon disturbance genesis index (MDGI; Ditchek et al. 2016) in eight S2S models for forecast lead times of 1–32 days, the multimodel mean (MMM), ERA-I and MERRA-2. We found that all models including the MMM correctly simulated the maximum genesis potential over the main genesis region (15° – 25° N, 80° – 90° E) compared

to other regions. However, a comparison with the simulated genesis density of SLPSs in these models suggested that nearly all of them and the MMM overestimated the genesis potential, with the HMCR model having the worst performance due to positive biases in the estimated CAPE and 500 hPa relative humidity. Thus, unlike for the SLPS structure (Chapter 4; Deoras et al. 2022), the MMM is not useful to stakeholders in predicting the genesis potential of SLPSs in S2S models. However, they could use ECMWF, UKMO and MMM due to their superior performance among the eight S2S models. We also found that the MDGI could not accurately predict the interannual variability of SLPSs over the main genesis region in ERA-I over the last two decades. This was due to a weakening of the correlation between the four components of this index and observed SLPS frequency.

Modulation of SLPSs by the MJO, ENSO and IOD

We investigated the modulation of SLPSs by the MJO, ENSO and IOD in S2S models, and found that most models and the MMM well simulated the enhanced frequency of SLPSs in phases 1–2 of the MJO and its suppression in phases 3–4 and 7–8, which agreed with previous studies (e.g., Chapter 5; Deoras et al. 2021b). The SLPS frequency was enhanced during La Niña and positive Indian Ocean Dipole (pIOD) years, whereas it was suppressed during El Niño and negative Indian Ocean Dipole (nIOD) years in most models as well as the MMM. These results agreed with ERA-I, MERRA-2 and previous studies (Vishnu et al., 2020a), but disagreed with the findings of Hunt et al. (2016a) and Singh et al. (2002). This could be due to differences in the LPS-tracking process and intensity thresholds used in these studies. We then analysed these relationships over a longer time span of 39 years (1980–2018) in ERA-I, and found that the frequency of SLPSs was the same during El Niño and La Niña years, whereas it was larger during pIOD years than during nIOD years. This did not support the findings of Vishnu et al. (2020a). We also analysed these relationships for monsoon depressions in the IMD Cyclone e-Atlas during June–September 1891–2018. We did not find any obvious impact of ENSO and IOD

on the frequency of monsoon depressions since there were small differences between the anomalous occurrence of monsoon depressions for different ENSO and IOD categories. It must be noted that this dataset suffers from shortcomings, which could have introduced a bias in our results. Nevertheless, we can conclude that the results for the modulation of SLPSs by ENSO and IOD are sensitive to the choice of the LPS dataset and time period.

Relationships between large-scale atmospheric fields and interannual frequency of BoB LPS varieties

We analysed correlations between the four components of the MDGI, zonal vertical shear and winds, and interannual frequency of BoB-short and BoB-long LPSs, which are the two regional varieties of BoB LPSs with a moderate negative interannual correlation (Chapter 5; Deoras et al. 2021b). We found that these large-scale atmospheric fields had a contrasting role in modulating the frequency of these two BoB LPS varieties.

Frequency and characteristics of downstream LPSs

We identified 57 downstream LPSs in ERA-I that had genesis during June–September 1979–2018. They mainly formed over the coast of Vietnam, had a mean lifespan of 8.2 days, and produced up to 8% of seasonal precipitation over central and eastern parts of India. They were most frequent in August, which agreed with previous studies (e.g., Meera et al. 2019; Srujan et al. 2021). This was related to the peak of the western North Pacific TC season. Anomalous easterly winds at 500 hPa over the South China Sea and Indo-Pacific region were responsible for their propagation towards the BoB. They featured a warm-over-cold core structure, and attained maximum intensity at approximately 20% lifespan, unlike for other low-pressure systems over the western Pacific Ocean and South China Sea that featured a midlife maximum.

The results of this chapter could potentially benefit meteorologists, flood forecasters

and researchers in developing products for forecasting LPSs using S2S models, benefiting stakeholders such as farmers and disaster management organisations in India. The results could therefore motivate researchers to identify large-scale conditions that are controlling the frequency of SLPSs over the main genesis region in the last two decades. As discussed in Chapter 4 (Deoras et al., 2022), the S2S models can predict the Boreal Summer Intraseasonal Oscillation (BSISO) 1 and BSISO2 events with a lead time of up to 6–24.5 and 6.5–14 days, respectively (Jie et al., 2017). Therefore, the modulation of SLPSs by the BSISO needs to be analysed in S2S models. Further work is required to investigate the mechanisms through which latitudinal shifts in the subtropical westerly jet and tropical easterly jet modulate the frequency of BoB LPS varieties. More characteristics of downstream LPSs need to be explored using ERA-I. More importantly, the skill of S2S models at predicting downstream LPSs needs to be analysed and compared with that of BoB LPSs.

Opening remarks

In this chapter, the main conclusions of the thesis will be briefly summarised since they were already presented in detail at the end of each chapter. In Section 7.1, we will address the four key questions of this thesis that were raised in the introduction chapter (Chapter 1). In Section 7.2, we will discuss limitations of the work, which will be followed by a discussion of the future work in Section 7.3. We will then discuss applications of the thesis in Section 7.4.

7.1 Summary of major results

Monsoon low-pressure systems (LPSs) are west-northwestward moving cyclonic vortices that produce around half of the summer monsoon rainfall over India and are known to trigger catastrophic floods (e.g., Hunt and Fletcher 2019; Hunt and Menon 2020). Despite their important role during the summer monsoon season, there has been insufficient evaluation of their predictability and prediction skill at long lead times such as the

subseasonal-to-seasonal (S2S) time scale (i.e., forecast lead times between 2 weeks and 2 months; Robertson et al. 2020). Furthermore, there is a gap in our understanding of what large-scale conditions control LPS frequency. In this thesis, we used a feature-tracking algorithm (Chapter 2; Hunt et al. 2016a, 2018b) to track LPSs in all ensemble members of eleven models of the S2S prediction project (Vitart et al., 2017) during the common reforecast period of June–September 1999–2010. The results were verified against ERA-Interim (ERA-I) and MERRA-2 reanalysis datasets, and further investigation of LPSs, including a comparison of the four regional varieties of South Asian LPSs, was carried out using ERA-I. The main outcomes of this thesis and how they answer the four key questions can be summarised as follows:

How skilful are S2S models at predicting LPSs?

In Chapter 3, we evaluated deterministic predictions of LPSs in all ensemble members of the eleven S2S models for forecast lead times of 0–15 days.

Compared to ERA-I and MERRA-2, all S2S models undersimulated the seasonal frequency of LPSs. These weather systems were more intense (central 850 hPa relative vorticity) than those in ERA-I, but less intense than those in MERRA-2.

We defined strong LPSs (SLPSs) as LPSs featuring minimum intensity greater than or equal to the third quartile intensity of all LPSs in an S2S model or reanalysis datasets. We examined the track density of SLPSs since they play a major role in triggering high-impact flood events in the Indian subcontinent (e.g., Hunt and Menon 2020). The NCEP, UKMO, CNRM, ECMWF and KMA models had the best simulation of the track density over the head of the BoB and eastern India, whereas BoM, JMA and CMA had prominent biases. Due to easterly mid-tropospheric steering winds, SLPSs simulated by the CMA model propagated westwards over peninsular India, resulting in the largest position error among all S2S models when verified against ERA-I. In contrast, models such as UKMO and KMA simulated tracks of these weather systems well, and had a smaller position error

than others. The intensity (central 850 hPa relative vorticity) bias was smallest for the JMA and CNRM models, but largest for the BoM and HMCR models.

We analysed the ensemble spread-error relationship, which ascertains if an ensemble prediction system is able to represent all possible forecast outcomes, and thus accurately predict the forecast error. Most S2S models were underdispersive (i.e., the ensemble spread was smaller than the ensemble mean error); the ECMWF and UKMO models had the best performance, whereas HMCR had the worst, possibly due to the perturbation method used to generate ensembles.

We used the Brier score and Brier skill score to analyse subseasonal probabilistic predictions of SLPS genesis frequency over the common forecast lead time of up to 32 days. Predictions of SLPS genesis by BoM, CMA, CNRM and ECMWF were more skilful and accurate than others, whereas the HMCR model had the worst performance, and the forecast skill was not dependent on the ensemble size.

In summary, S2S models in general featured good skill at predicting LPS tracks and genesis frequency in general. Models such as ECMWF and NCEP had the best performance in general, whereas HMCR had the worst.

How well do S2S models simulate the structure of LPSs?

The analysis of LPS predictions in Chapter 3 partly motivated us to explore the simulation of the structure of LPSs and precipitation biases in S2S models at forecast lead times of 0–15 days in Chapter 4. We particularly focused on SLPSs due to their impacts on the Indian subcontinent.

There were strong dry biases over the monsoon core zone, northeastern India, head of the Bay of Bengal (BoB) and nearby coastal regions in the BoM and CMA models, which were attributed to a weak bias in the lower-tropospheric monsoon circulation. These dry biases were similar to those in the current general circulation models, including the

multimodel mean of CMIP5 and CMIP3 models (Sperber et al., 2013; Praveen et al., 2015). In contrast, models such as JMA, ECCO and ISAC-CNR simulated wet biases over these regions due to strong wind biases in the lower-tropospheric monsoon circulation.

For composites of SLPSs, we analysed horizontal structures of precipitation, relative vorticity at 850 hPa, and mean sea-level pressure (MSLP) anomaly. Several S2S models correctly simulated the presence of a precipitation maximum to the relative southwest of the composite centre, which is well known from previous studies (e.g., Hunt et al. 2016a). However, the CMA, ECCO, HMCR and ISAC-CNR models featured a precipitation maximum to the relative south of the centre, which coincided with the maximum moisture-flux convergence at 850 hPa. The CMA, NCEP, ECMWF and ISAC-CNR models had the best simulation of the 850 hPa relative vorticity and MSLP anomaly, whereas HMCR had the worst.

We then analysed vertical structures of anomalies of relative vorticity, temperature and moist static energy. These anomalies were computed against the summer mean climatology. The vertical structure of relative vorticity anomaly was shallower and weaker in all S2S models than in ERA-I and MERRA-2. The HMCR model did not simulate the cold core in the lower-troposphere, and the structure of moist static energy anomaly was weakest in the ECCO, HMCR and JMA models.

In summary, the ECMWF, NCEP and UKMO models had the best simulation of the structure, whereas HMCR had the worst. Overall, S2S models that had the best (worst) simulation of LPS tracks also had the best (worst) simulation of the structure of these weather systems.

What are the differences between the four regional varieties of South Asian LPSs?

In Chapter 5, we partly used the framework developed in Chapter 4 to explore characteristics of the four regional varieties of South Asian LPSs using ERA-I. LPSs of these four varieties, which had their genesis during June–September 1979–2018, were first identified by Hunt and Fletcher (2019).

Among the four varieties, long-lived LPSs over the BoB (BoB-long LPSs) were strongest, whereas those near Sri Lanka (Sri Lankan LPSs) were weakest. Whilst BoB and Sri Lankan LPSs were most common in July or August, those over the Arabian Sea (Arabian LPSs) were most common in June, which were related to monsoon onset vortices over the southern Arabian Sea. Whilst Arabian LPSs were fastest among all varieties, short-lived BoB LPSs (BoB-short) and Sri Lankan LPSs were slowest. There was a statistically significant moderate negative correlation between interannual frequencies of BoB-short and BoB-long LPSs, suggesting a contrasting role of large-scale conditions in modulating their genesis.

All four varieties featured a warm-over-cold core thermal structure and a maximum anomaly in equivalent potential temperature in the lower troposphere. The vertical structures of Arabian and BoB-long LPSs had the largest anomalies, whereas those of Sri Lankan LPSs had the smallest anomalies.

Whilst BoB-short LPSs had the largest precipitation contribution to the summer monsoon rainfall over India, BoB-long LPSs were the major precipitation contributors to interior parts of India. In contrast, the precipitation contribution of Sri Lankan and Arabian LPSs to the summer monsoon rainfall was smaller than that of BoB LPSs. Nevertheless, Sri Lankan LPSs were important for producing LPS precipitation over Sri Lanka and adjoining parts of southern India.

The tropical intraseasonal oscillation (ISO) modulated the occurrence of each LPS variety by modifying large-scale conditions such as vertical velocity and mid-tropospheric

moisture. When the ISO was active over the Arabian Sea and Sri Lanka, it enhanced the genesis of Arabian and Sri Lankan LPSs. The northward/northeastward propagation of the ISO in subsequent phases then enhanced the genesis of BoB-short and BoB-long LPSs.

At interannual time scales, a cyclonic wind anomaly at 850 hPa to the southeast of Sri Lanka during La Niña and negative Indian Ocean Dipole (IOD) years enhanced the genesis of Sri Lankan LPSs.

What large-scale conditions control the frequency of LPSs on the S2S time scale?

The modulation of LPSs by the ISO (Chapter 5) partly motivated us to investigate large-scale controls on LPS frequency using the S2S dataset and ERA-I in Chapter 6. We considered a common forecast lead time of up to 32 days in the S2S dataset.

Most S2S models and the multimodel mean correctly simulated the modulation of SLPSs by the Madden-Julian Oscillation (MJO)—SLPS frequency was enhanced in phases 1–2 of the MJO and suppressed in phases 3–4 and 7–8, which agreed with the results discussed in Chapter 5.

In most S2S models, SLPS frequency was enhanced during concurrent (i.e., June–September) La Niña and positive IOD events, whereas it was suppressed during El Niño and negative IOD events. This agreed with previous studies (e.g., Vishnu et al. 2020a). However, there was no obvious impact of ENSO and the IOD when monsoon depressions in the IMD Cyclone e-Atlas dataset were analysed during June–September 1891–2018, suggesting that the results were sensitive to the choice of the LPS dataset and time period.

We used ERA-I to analyse linear correlations between the four components of the monsoon disturbance genesis index (Ditchek et al., 2016), zonal component of vertical wind shear (200–850 hPa), zonal winds at 200 hPa and 850 hPa, and interannual frequencies of BoB-short and BoB-long LPSs. The correlations had an opposite sign for BoB-short and BoB-long LPSs, which further supported our hypothesis that large-scale conditions play

a role in deciding whether the propagation of BoB LPSs is confined near to the coastline (short) or penetrates inland (long).

We then explored characteristics of 57 downstream LPSs, which propagated towards India in the direction of the tropical easterly jet after their genesis over the South China Sea and surrounding regions. Given the high orography over the Southeast Asia region, we identified them by first applying a feature-tracking algorithm to 700 hPa relative vorticity in ERA-I, and then partitioning LPS tracks into seven clusters using a k -means clustering technique. They produced up to 8% of seasonal precipitation over central and eastern India, and were most frequent in August, which agreed with previous studies (e.g., Meera et al. 2019). Anomalous easterly winds at 500 hPa over the South China Sea and Indo-Pacific region were responsible for their propagation towards the BoB.

7.2 Limitations

As outlined in Section 2.1.1, at the time of writing, S2S models have a common reforecast period of only 12 years (i.e., 1999–2010), which prevents model intercomparison over a long period of time. As a result, we had to consider a small number of ENSO, IOD and MJO events for our analysis of large-scale controls on LPS frequency in Chapter 6. A larger sample is necessary to ensure the robustness of the results, especially to account for the multidecadal variability in the ENSO-monsoon relationship (e.g., Srivastava et al. 2020).

The S2S reforecasts differ considerably in terms of the number of ensemble members and reforecast frequency. For example, the reforecast frequency of the UKMO model is four per month, whereas that of NCEP is daily. The BoM model has 33 ensemble members, whereas the KMA model has only 3 ensemble members. Whilst we assumed that any bias in the results due to differences in the reforecast configuration was insignificant, a sensitivity analysis would have been an important addition to this work.

Our analysis in Chapter 4 was constrained by the unavailability of many important fields in the S2S dataset such as vertical velocity. The unavailability of specific humidity in the ISAC-CNR and KMA model outputs prevented us from analysing the genesis potential of these models at simulating SLPSs in Chapter 6.

We computed the MDGI in S2S models in Chapter 6, for which we used regression coefficients computed by Ditchek et al. (2016) for ERA-I. Whilst the sensitivity of the MDGI to output pressure levels of S2S models was analysed in Section 6.3.1, the recomputation of these regression coefficients for S2S models would have been helpful in improving the accuracy of the results.

7.3 Future work

The sensitivity of the results of this chapter to the reforecast frequency of S2S models could be determined in a future study by considering models having a daily reforecast frequency (e.g., NCEP). The reforecast frequency of NCEP could be downsampled to that of the JMA model that has the smallest reforecast frequency. For downsampling, NCEP reforecasts that share the same reforecast start dates with JMA reforecasts could be considered. The sensitivity of the results could then be determined by repeating analyses presented in the thesis (e.g., vertical structures of SLPSs) in downsampled NCEP reforecasts.

Since the KMA model has the smallest ensemble size, the sensitivity of the results of this thesis to the ensemble size could be determined by considering only three ensemble members in other S2S models (e.g., BoM). The results for these three ensemble members in an S2S model could then be compared with the mean of all ensemble members of the same model to determine the sensitivity.

There is much scope for further analysis of LPSs to explain some findings of the thesis in further detail, including an investigation of the sources of SLPS structural biases in S2S models. Besides, case studies of LPSs using S2S models could be conducted in which

the predictability, prediction skill, and structure of prominent LPSs, such as those that triggered well-known catastrophic floods in India (e.g., the 2013 Uttarakhand flood), could be examined. We used the ERA5 LPS dataset (Vishnu et al., 2020a,b) in Chapter 3 for comparing some results; detailed intercomparisons between various LPS datasets could be done in a future study to better quantify the uncertainty between them. The following is a synthesis of the four most important research questions that might be of interest for future studies:

How does the ISO modulate LPS structure?

In Chapter 5, we discussed how the ISO modulates LPS genesis by modifying large-scale conditions. Thus, it is possible that composites of LPSs feature a stronger structure during active phases of the ISO than during inactive phases. In fact, Hunt et al. (2016a) found that monsoon depressions during the active phase of the monsoon are stronger than those during the inactive phase. The active-break phases of the monsoon are closely tied to the location of the ISO (e.g., Sikka and Gadgil 1980). However, there has not been any study analysing the structure of LPSs during different phases of the BSISO and MJO, which are the two distinct modes of the ISO. Karmakar et al. (2020) found that LPSs forming in the presence of active ISO over the north Indian Ocean have a higher probability of intensifying into monsoon depressions than those forming when the ISO is inactive. Thus, an examination of LPS structure during different phases of the ISO could help researchers in better understanding the role of large-scale conditions in the evolution of LPSs. For this analysis, they could use precomputed MJO and BSISO indices (Wheeler and Hendon, 2004; Kikuchi and Wang, 2010; Kikuchi et al., 2012; Kikuchi, 2020), LPS datasets and reanalysis datasets such as ERA-I or ERA5.

What physical mechanisms govern the genesis of Sri Lankan LPSs?

We discussed some characteristics of Sri Lankan LPSs in Chapter 5; however, the physical mechanisms governing their genesis remain unknown. It is possible that an interaction between cross-equatorial winds of the monsoon and the high-central Sri Lankan terrain provides low-level cyclonic vorticity on the lee side of these mountains for spin up of these weather systems. This hypothesis could be analysed in a future study by computing the Froude number in a reanalysis dataset, which will help in determining if lee vortices develop due to flow blocking and subsequently evolve into Sri Lankan LPSs.

Given that Sri Lankan LPSs form close to the equator, the role of convectively coupled equatorial waves in their genesis cannot be ruled out. This could be investigated by using the algorithm of Roundy (2012), which projects the NOAA interpolated outgoing longwave radiation data onto equatorial wave patterns, producing a time series of structures of different tropical wave modes (including the MJO).

A related aspect that could be investigated in a future study is the role of westerly wind bursts (WWBs) over the western Indian Ocean in triggering Sri Lankan LPSs. Here we think that strong WWBs off the west coast of Sri Lanka might lead to vortex-shedding off the east coast of Sri Lanka where Sri Lankan LPSs generally form. This analysis will also help in better understanding floods in Sri Lanka since WWBs have been implicated in triggering catastrophic floods in the country (Jayawardena et al., 2017).

What large-scale conditions are controlling LPS frequency in recent decades?

The results of Chapter 6 suggested that the linear correlation between the four components of the MDGI and observed interannual frequency of SLPSs has weakened over the last two decades. It is therefore important to determine the role of other large-scale conditions in controlling LPS frequency in recent decades. This aspect could be investigated by explor-

ing the linear correlation between various large-scale fields (e.g., upper-air divergence) and observed SLPS frequency.

As discussed in Chapter 6, latitudinal shifts in positions of the subtropical westerly jet and tropical easterly jet modulate interannual frequencies of BoB-short and BoB-long LPSs. Our hypothesis is that a broader jet streak within the tropical easterly jet enhances the frequency of BoB-long LPSs by providing a better access to the upper-air divergent region over the BoB. This hypothesis could be tested in a future study by analysing the large-scale dynamics.

How skilful are predictions of downstream LPSs?

As seen in Chapter 6, downstream LPSs require around 8 days to reach the eastern coast of India from the coast of Vietnam. Thus, they can provide a larger window of opportunity for preparedness in India than that provided by LPSs having their genesis over the BoB. The prediction skill and predictability of downstream LPSs could be explored by identifying them in S2S models and verifying the results against reanalysis datasets.

7.4 Applications

The results of this thesis could benefit meteorologists and flood forecasters in designing LPS forecasting products for hydrological services, ultimately benefiting stakeholders such as disaster management organisations, governments and farmers of the Indian subcontinent. Thus, it is important to identify the most useful and least useful S2S models as per different field of interests; we identify such models in all chapters of this thesis and present them in Table 7.1.

An important outcome of this thesis is the creation of a dataset (<https://doi.org/10.5281/zenodo.4659797>) containing track details of LPSs identified in the eleven S2S models. This dataset could benefit researchers and motivate the modelling community to

carry out further investigation of LPSs. In fact, there have been over 100 downloads of this dataset at the time of the submission of this thesis.

Field of interest	Most useful	Least useful	Reference
Seasonal frequency	NCEP	BoM	Section 3.3.1
Intensity	CMA ECCC ISAC-CNR	HMCR	Section 3.3.2
Track density	NCEP MMM	CMA HMCR	Section 3.3.3
Position bias	ECCC	CMA	Section 3.4.1
Intensity bias	ECCC JMA KMA UKMO	BoM HMCR	Section 3.4.1
Reliability of forecasts	NCEP ECMWF UKMO	HMCR	Section 3.4.4
Accuracy of probabilistic forecasts	BoM CMA CNRM ECMWF	HMCR	Section 3.5.1
Precipitation bias	ECMWF NCEP UKMO	BoM CMA ISAC-CNR	Section 4.4.1
LPS-centred precipitation	BoM NCEP	CMA HMCR	Section 4.5.1
Horizontal & vertical structures	ECMWF NCEP UKMO	HMCR	Sections 4.5 & 4.6
Genesis potential	ECMWF UKMO MMM	HMCR	Section 6.3.1
Modulation by the MJO	NCEP MMM	CNRM ECMWF UKMO	Section 6.4.1
Modulation by ENSO & IOD	BoM ISAC-CNR	HMCR	Sections 6.4.2 & 6.4.3

Table 7.1: Most useful and least useful S2S models for various field of interests and verification against ERA-I. MMM refers to the multimodel mean of the eleven S2S models.

BIBLIOGRAPHY

- Adames, Á. F. and Ming, Y. (2018) Interactions between water vapor and potential vorticity in synoptic-scale monsoonal disturbances: Moisture vortex instability. *Journal of the Atmospheric Sciences*, **75**, 2083–2106. <https://doi.org/10.1175/JAS-D-17-0310.1>.
- Ardilouze, C., Batté, L. and Déqué, M. (2017) Subseasonal-to-seasonal (S2S) forecasts with CNRM-CM: a case study on the July 2015 West-European heat wave. *Advances in Science and Research*, **14**, 115–121. <https://doi.org/10.5194/asr-14-115-2017>.
- Ashok, K., Soman, M. and Satyan, V. (2000) Simulation of monsoon disturbances in a GCM. *Pure and Applied Geophysics*, **157**, 1509–1539. <https://doi.org/10.1007/PL00001131>.
- Blanford, H. F. (1884) On the connection of the Himalaya snowfall with dry winds and seasons of drought in India. *Proceedings of the Royal Society of London*, **37**, 3–22. <https://doi.org/10.1098/rspl.1884.0003>.
- (1886) The Rainfall of India. *Mem. India Met. Dept*, **2**, 217–448.
- Boos, W. R., Hurley, J. V. and Murthy, V. S. (2015) Adiabatic westward drift of Indian

- monsoon depressions. *Quarterly Journal of the Royal Meteorological Society*, **141**, 1035–1048. <https://doi.org/10.1002/qj.2454>.
- Boos, W. R. and Kuang, Z. (2010) Dominant control of the South Asian monsoon by orographic insulation versus plateau heating. *Nature*, **463**, 218–222. <https://doi.org/10.1038/nature08707>.
- Bowman, A. W. and Azzalini, A. (1999) Applied smoothing techniques for data analysis: the kernel approach with S-plus illustrations. *Journal of the American Statistical Association*, **94**, 982.
- Brier, G. W. (1950) Verification of forecasts expressed in terms of probability. *Monthly Weather Review*, **78**, 1–3. [https://doi.org/10.1175/1520-0493\(1950\)078%3C0001:VOFEIT%3E2.0.CO;2](https://doi.org/10.1175/1520-0493(1950)078%3C0001:VOFEIT%3E2.0.CO;2).
- Buizza, R., Houtekamer, P. L., Pellerin, G., Toth, Z., Zhu, Y. and Wei, M. (2005) A comparison of the ECMWF, MSC, and NCEP global ensemble prediction systems. *Monthly Weather Review*, **133**, 1076–1097. <https://doi.org/10.1175/MWR2905.1>.
- Buizza, R. and Leutbecher, M. (2015) The forecast skill horizon. *Quarterly Journal of the Royal Meteorological Society*, **141**, 3366–3382. <https://doi.org/10.1002/qj.2619>.
- Camargo, S. J. (2013) Global and regional aspects of tropical cyclone activity in the CMIP5 models. *Journal of Climate*, **26**, 9880–9902. <https://doi.org/10.1175/JCLI-D-12-00549.1>.
- Camargo, S. J., Emanuel, K. A. and Sobel, A. H. (2007) Use of a genesis potential index to diagnose ENSO effects on tropical cyclone genesis. *Journal of Climate*, **20**, 4819–4834. <https://doi.org/10.1175/JCLI4282.1>.
- Camargo, S. J. and Sobel, A. H. (2005) Western North Pacific tropical cyclone intensity and ENSO. *Journal of Climate*, **18**, 2996–3006. <https://doi.org/10.1175/JCLI3457.1>.

- Camargo, S. J. and Zebiak, S. E. (2002) Improving the detection and tracking of tropical cyclones in atmospheric general circulation models. *Weather and Forecasting*, **17**, 1152–1162.
- Camp, J., Roberts, M., MacLachlan, C., Wallace, E., Hermanson, L., Brookshaw, A., Arribas, A. and Scaife, A. (2015) Seasonal forecasting of tropical storms using the Met Office GloSea5 seasonal forecast system. *Quarterly Journal of the Royal Meteorological Society*, **141**, 2206–2219. <https://doi.org/10.1002/qj.2516>.
- Camp, J., Roberts, M. J., Comer, R. E., Wu, P., MacLachlan, C., Bett, P. E., Golding, N., Toumi, R. and Chan, J. C. (2019) The western Pacific subtropical high and tropical cyclone landfall: Seasonal forecasts using the Met Office GloSea5 system. *Quarterly Journal of the Royal Meteorological Society*, **145**, 105–116. <https://doi.org/10.1175/JCLI-D-14-00618.1>.
- Camp, J., Wheeler, M. C., Hendon, H. H., Gregory, P. A., Marshall, A. G., Tory, K. J., Watkins, A. B., MacLachlan, C. and Kuleshov, Y. (2018) Skilful multiweek tropical cyclone prediction in ACCESS-S1 and the role of the MJO. *Quarterly Journal of the Royal Meteorological Society*, **144**, 1337–1351. <https://doi.org/10.1002/qj.3260>.
- Cassou, C. (2008) Intraseasonal interaction between the Madden–Julian oscillation and the North Atlantic Oscillation. *Nature*, **455**, 523–527. <https://doi.org/10.1038/nature07286>.
- Charney, J. G. (1969) The intertropical convergence zone and the Hadley circulation of the atmosphere. In *Proc. WMO/IUGG Symp. on Numerical Weather Prediction in Tokyo*, vol. 3, 73–79. Japan Meteorological Agency.
- Charney, J. G. and Shukla, J. (1981) Predictability of monsoons. *Monsoon dynamics*, **99**, 109.
- Chen, T. C. and Weng, S. P. (1999) Interannual and intraseasonal variations in monsoon depressions and their westward-propagating predecessors.

- Monthly Weather Review*, **127**, 1005–1020. [https://doi.org/10.1175/1520-0493\(1999\)127%3C1005:IAIVIM%3E2.0.CO;2](https://doi.org/10.1175/1520-0493(1999)127%3C1005:IAIVIM%3E2.0.CO;2).
- Cohen, N. Y. and Boos, W. R. (2014) Has the number of Indian summer monsoon depressions decreased over the last 30 years? *Geophysical Research Letters*, **41**, 7846–7853. <https://doi.org/10.1002/2014GL061895>.
- (2016) Perspectives on moist baroclinic instability: Implications for the growth of monsoon depressions. *Journal of the Atmospheric Sciences*, **73**, 1767–1788. <https://doi.org/10.1175/JAS-D-15-0254.1>.
- Daggupati, S. M. and Sikka, D. R. (1977) On the vorticity budget and vertical velocity distribution associated with the life cycle of a monsoon depression. *Journal of the Atmospheric Sciences*, **34**, 773–792. [https://doi.org/10.1175/1520-0469\(1977\)034%3C0773:OTVBAV%3E2.0.CO;2](https://doi.org/10.1175/1520-0469(1977)034%3C0773:OTVBAV%3E2.0.CO;2).
- Dee, D. P., Uppala, S. M., Simmons, A. J., Berrisford, P., Poli, P., Kobayashi, S., Andrae, U., Balmaseda, M., Balsamo, G., Bauer, D. et al. (2011) The ERA-Interim reanalysis: Configuration and performance of the data assimilation system. *Quarterly Journal of the Royal Meteorological Society*, **137**, 553–597. <https://doi.org/10.1002/qj.828>.
- DeMaria, M. (1996) The effect of vertical shear on tropical cyclone intensity change. *Journal of Atmospheric Sciences*, **53**, 2076–2088. [https://doi.org/10.1175/1520-0469\(1996\)053%3C2076:TEOVSO%3E2.0.CO;2](https://doi.org/10.1175/1520-0469(1996)053%3C2076:TEOVSO%3E2.0.CO;2).
- Deoras, A., Hunt, K. M. R. and Turner, A. G. (2021a) Comparison of the prediction of Indian monsoon low-pressure systems by Subseasonal-to-Seasonal prediction models. *Weather and Forecasting*. <https://doi.org/10.1175/WAF-D-20-0081.1>.
- (2021b) The four regional varieties of South Asian monsoon low-pressure systems and their modulation by tropical intraseasonal variability. *Weather*, **76**, 194–200. <http://dx.doi.org/10.1002/wea.3997>.

- (2021c) Track dataset of Indian monsoon low-pressure systems in Subseasonal-to-Seasonal prediction models, ERA-Interim and MERRA-2 reanalysis datasets. <https://doi.org/10.5281/zenodo.4659797>.
- (2022) The structure of strong Indian monsoon low-pressure systems in Subseasonal-to-Seasonal prediction models. *Quarterly Journal of the Royal Meteorological Society*, **148**, 2147–2166. <https://doi.org/10.1002/qj.4296>.
- Diaz, M. and Boos, W. R. (2019) Monsoon depression amplification by moist barotropic instability in a vertically sheared environment. *Quarterly Journal of the Royal Meteorological Society*, **145**, 2666–2684. <https://doi.org/10.1002/qj.3585>.
- Ditchek, S. D., Boos, W. R., Camargo, S. J. and Tippett, M. K. (2016) A genesis index for monsoon disturbances. *Journal of Climate*, **29**, 5189–5203. <https://doi.org/10.1175/JCLI-D-15-0704.1>.
- Eliot, J. (1884) Account of southwest monsoon storms generated in the Bay of Bengal during 1877–1881. *Mem. India Met. Dept*, **2**, 217–448.
- Emanuel, K. and Nolan, D. S. (2004) Tropical cyclone activity and the global climate system. In *26th Conference on Hurricanes and Tropical Meteorology*.
- Evan, A. T. and Camargo, S. J. (2011) A climatology of Arabian Sea cyclonic storms. *Journal of Climate*, **24**, 140–158. <https://doi.org/10.1175/2010JCLI3611.1>.
- Feng, X., Klingaman, N. P. and Hodges, K. I. (2019) The effect of atmosphere–ocean coupling on the prediction of 2016 western North Pacific tropical cyclones. *Quarterly Journal of the Royal Meteorological Society*, **145**, 2425–2444. <https://doi.org/10.1002/qj.3571>.
- Fine, C. M., Johnson, R. H., Ciesielski, P. E. and Taft, R. K. (2016) The role of topograph-

- ically induced vortices in tropical cyclone formation over the Indian Ocean. *Monthly Weather Review*, **144**, 4827–4847. <https://doi.org/10.1175/MWR-D-16-0102.1>.
- Flohn, H. (1957) Large-scale aspects of the “summer monsoon” in South and East Asia. *Journal of the Meteorological Society of Japan. Ser. II*, **35**, 180–186. https://doi.org/10.2151/jmsj1923.35A.0_180.
- Francis, P. and Gadgil, S. (2006) Intense rainfall events over the west coast of India. *Meteorology and Atmospheric Physics*, **94**, 27–42. <https://doi.org/10.1007/s00703-005-0167-2>.
- Froude, L. S. (2010) TIGGE: Comparison of the prediction of Northern Hemisphere extratropical cyclones by different ensemble prediction systems. *Weather and Forecasting*, **25**, 819–836. <https://doi.org/10.1175/2010WAF2222326.1>.
- (2011) TIGGE: Comparison of the prediction of Southern Hemisphere extratropical cyclones by different ensemble prediction systems. *Weather and Forecasting*, **26**, 388–398. <https://doi.org/10.1175/2010WAF2222457.1>.
- Froude, L. S., Bengtsson, L. and Hodges, K. I. (2007a) The predictability of extratropical storm tracks and the sensitivity of their prediction to the observing system. *Monthly Weather Review*, **135**, 315–333. <https://doi.org/10.1175/MWR3274.1>.
- (2007b) The prediction of extratropical storm tracks by the ECMWF and NCEP ensemble prediction systems. *Monthly Weather Review*, **135**, 2545–2567. <https://doi.org/10.1175/MWR3422.1>.
- Fu, X., Wang, B., Waliser, D. E. and Tao, L. (2007) Impact of atmosphere–ocean coupling on the predictability of monsoon intraseasonal oscillations. *Journal of the Atmospheric Sciences*, **64**, 157–174. <https://doi.org/10.1175/JAS3830.1>.

- Gadgil, S. (2003) The Indian monsoon and its variability. *Annual Review of Earth and Planetary Sciences*, **31**, 429–467. <https://doi.org/10.1146/annurev.earth.31.100901.14125>.
- (2018) The monsoon system: Land–sea breeze or the ITCZ? *Journal of Earth System Science*, **127**, 1–29. <https://doi.org/10.1007/s12040-017-0916-x>.
- Gelaro, R., McCarty, W., Suárez, M. J., Todling, R., Molod, A., Takacs, L., Randles, C. A., Darmenov, A., Bosilovich, M. G., Reichle, R. et al. (2017) The Modern-Era Retrospective Analysis for Research and Applications, Version 2 (MERRA-2). *Journal of Climate*, **30**, 5419–5454. <https://10.1175/JCLI-D-16-0758.1>.
- Godbole, R. V. (1977) The composite structure of the monsoon depression. *Tellus*, **29**, 25–40. <https://doi.org/10.1111/j.2153-3490.1977.tb00706.x>.
- Gray, W. M. (1968) Global view of the origin of tropical disturbances and storms. *Monthly Weather Review*, **96**, 669–700. [https://doi.org/10.1175/1520-0493\(1968\)096%3C0669:GVOTOO%3E2.0.CO;2](https://doi.org/10.1175/1520-0493(1968)096%3C0669:GVOTOO%3E2.0.CO;2).
- (1979) Hurricanes: Their formation, structure and likely role in the tropical circulation. *Meteorology over the tropical oceans*, **155**, 218.
- Hadley, G. (1735) Concerning the cause of the general trade-winds. *Philosophical Transactions of the Royal Society of London*, **39**, 58–62. <https://doi.org/10.1098/rstl.1735.0014>.
- Haertel, P. and Boos, W. R. (2017) Global association of the Madden-Julian Oscillation with monsoon lows and depressions. *Geophysical Research Letters*, **44**, 8065–8074. <https://doi.org/10.1002/2017GL073625>.
- Halley, E. (1686) An historical account of the trade winds, and monsoons, observable in the seas between and near the tropicks, with an attempt to assign the physical cause of

- the said winds. *Philosophical Transactions of the Royal Society of London*, **16**, 153–168. <https://doi.org/10.1098/rstl.1686.0026>.
- Hamill, T. M., Bates, G. T., Whitaker, J. S., Murray, D. R., Fiorino, M., Galarneau, T. J., Zhu, Y. and Lapenta, W. (2013) NOAA's second-generation global medium-range ensemble reforecast dataset. *Bulletin of the American Meteorological Society*, **94**, 1553–1565. <https://doi.org/10.1175/BAMS-D-12-00014.1>.
- Hamill, T. M., Whitaker, J. S. and Mullen, S. L. (2006) Reforecasts: An important dataset for improving weather predictions. *Bulletin of the American Meteorological Society*, **87**, 33–46. <https://doi.org/10.1175/BAMS-87-1-33>.
- Hersbach, H., Bell, B., Berrisford, P., Hirahara, S., Horányi, A., Muñoz-Sabater, J., Nicolas, J., Peubey, C., Radu, R., Schepers, D. et al. (2020) The ERA5 global reanalysis. *Quarterly Journal of the Royal Meteorological Society*, **146**, 1999–2049. <https://doi.org/10.1002/qj.3803>.
- Hodges, K. I., Cobb, A. and Vidale, P. L. (2017) How well are tropical cyclones represented in reanalysis datasets? *Journal of Climate*, **30**, 5243–5264. <https://doi.org/10.1175/JCLI-D-16-0557.1>.
- Hodges, K. I. and Emerton, R. (2015) The prediction of Northern Hemisphere tropical cyclone extended life cycles by the ECMWF ensemble and deterministic prediction systems. Part I: Tropical cyclone stage. *Monthly Weather Review*, **143**, 5091–5114. <https://doi.org/10.1175/MWR-D-13-00385.1>.
- Hodges, K. I., Hoskins, B. J., Boyle, J. and Thorncroft, C. (2003) A comparison of recent reanalysis datasets using objective feature tracking: Storm tracks and tropical easterly waves. *Monthly Weather Review*, **131**, 2012–2037. [https://doi.org/10.1175/1520-0493\(2003\)131%3C2012:ACORRD%3E2.0.CO;2](https://doi.org/10.1175/1520-0493(2003)131%3C2012:ACORRD%3E2.0.CO;2).

- Hopson, T. (2014) Assessing the ensemble spread–error relationship. *Monthly Weather Review*, **142**, 1125–1142. <https://doi.org/10.1175/MWR-D-12-00111.1>.
- Hoskins, B. J. and Hodges, K. I. (2002) New perspectives on the Northern Hemisphere winter storm tracks. *Journal of the Atmospheric Sciences*, **59**, 1041–1061.
- Huang, B., L’Heureux, M., Hu, Z.-Z. and Zhang, H.-M. (2016) Ranking the strongest ENSO events while incorporating SST uncertainty. *Geophysical Research Letters*, **43**, 9165–9172. <https://doi.org/10.1002/2016GL070888>.
- Huang, B., Thorne, P. W., Banzon, V. F., Boyer, T., Chepurin, G., Lawrimore, J. H., Menne, M. J., Smith, T. M., Vose, R. S. and Zhang, H.-M. (2017) Extended reconstructed sea surface temperature, version 5 (ERSSTv5): upgrades, validations, and intercomparisons. *Journal of Climate*, **30**, 8179–8205. <https://doi.org/10.1175/JCLI-D-16-0836.1>.
- Huffman, G. J., Bolvin, D. T., Braithwaite, D., Hsu, K., Joyce, R., Xie, P. and Yoo, S.-H. (2015) NASA global precipitation measurement (GPM) integrated multi-satellite retrievals for GPM (IMERG). *Algorithm Theoretical Basis Document (ATBD) Version*, **4**, 26.
- Hunt, K. M. R. (2017) *On the behaviour of tropical depressions and their interaction with the Indian monsoon trough region*. Ph.D. thesis, University of Reading.
- (2021) Monsoon low-pressure-system tracks over South Asia (1979-2019). <https://doi.org/10.5281/zenodo.5575336>.
- Hunt, K. M. R., Curio, J., Turner, A. G. and Schiemann, R. (2018a) Subtropical westerly jet influence on occurrence of western disturbances and Tibetan Plateau vortices. *Geophysical Research Letters*, **45**, 8629–8636. <https://doi.org/10.1029/2018GL077734>.

- Hunt, K. M. R., Deoras, A. and Turner, A. G. (2021a) Track dataset of four regional varieties of South Asian monsoon low-pressure systems. <https://doi.org/10.5281/zenodo.4572900>.
- Hunt, K. M. R. and Fletcher, J. K. (2019) The relationship between Indian monsoon rainfall and low-pressure systems. *Climate Dynamics*, **53**, 1859–1871. <https://doi.org/10.1007/s00382-019-04744-x>.
- Hunt, K. M. R. and Menon, A. (2020) The 2018 Kerala floods: a climate change perspective. *Climate Dynamics*, **54**, 2433–2446. <https://doi.org/10.1007/s00382-020-05123-7>.
- Hunt, K. M. R., Turner, A. G., Inness, P. M., Parker, D. E. and Levine, R. C. (2016a) On the structure and dynamics of Indian monsoon depressions. *Monthly Weather Review*, **144**, 3391–3416. <https://doi.org/10.1175/MWR-D-15-0138.1>.
- Hunt, K. M. R., Turner, A. G. and Parker, D. E. (2016b) The spatiotemporal structure of precipitation in Indian monsoon depressions. *Quarterly Journal of the Royal Meteorological Society*, **142**, 3195–3210. <https://doi.org/10.1002/qj.2901>.
- Hunt, K. M. R., Turner, A. G. and Schiemann, R. K. (2021b) How interactions between tropical depressions and western disturbances affect heavy precipitation in South Asia. *Monthly Weather Review*, **149**, 1801–1825. <https://doi.org/10.1175/MWR-D-20-0373.1>.
- Hunt, K. M. R., Turner, A. G. and Shaffrey, L. C. (2018b) The evolution, seasonality and impacts of western disturbances. *Quarterly Journal of the Royal Meteorological Society*, **144**, 278–290. <https://doi.org/10.1002/qj.3200>.
- Hurley, J. V. and Boos, W. R. (2015) A global climatology of monsoon low-pressure systems. *Quarterly Journal of the Royal Meteorological Society*, **141**, 1049–1064. <https://doi.org/10.1002/qj.2447>.

- Ihara, C., Kushnir, Y. and Cane, M. A. (2008) Warming trend of the Indian Ocean SST and Indian Ocean Dipole from 1880 to 2004. *Journal of Climate*, **21**, 2035–2046. <https://doi.org/10.1175/2007JCLI1945.1>.
- IMD (2011) Technical Note: Tracks of Cyclones and Depressions over North Indian Ocean. <http://14.139.191.203/Document.aspx?doctype=Notes>.
- Jayawardena, I., Sumathipala, W. and Basnayake, B. (2017) Impact of Madden Julian oscillation (MJO) and other meteorological phenomena on the heavy rainfall event from 19th-28th December, 2014 over Sri Lanka. *Journal of the National Science Foundation of Sri Lanka*, **45**.
- Jie, W., Vitart, F., Wu, T. and Liu, X. (2017) Simulations of the Asian summer monsoon in the sub-seasonal to seasonal prediction project (S2S) database. *Quarterly Journal of the Royal Meteorological Society*, **143**, 2282–2295. <https://doi.org/10.1002/qj.3085>.
- Joseph, S., Sahai, A., Sharmila, S., Abhilash, S., Borah, N., Chattopadhyay, R., Pillai, P., Rajeevan, M. and Kumar, A. (2015) North Indian heavy rainfall event during June 2013: diagnostics and extended range prediction. *Climate Dynamics*, **44**, 2049–2065. <https://doi.org/10.1007/s00382-014-2291-5>.
- Karmakar, N., Boos, W. R. and Misra, V. (2020) Influence of intraseasonal variability on the development of monsoon depressions. *Geophysical Research Letters*, **48**. <https://doi.org/10.1029/2020GL090425>.
- Kikuchi, K. (2020) Extension of the bimodal intraseasonal oscillation index using JRA-55 reanalysis. *Climate Dynamics*, **54**, 919–933. <https://doi.org/10.1007/s00382-019-05037-z>.
- Kikuchi, K. and Wang, B. (2010) Formation of tropical cyclones in the northern Indian Ocean associated with two types of tropical intraseasonal oscillation

- modes. *Journal of the Meteorological Society of Japan. Ser. II*, **88**, 475–496.
<https://doi.org/10.2151/jmsj.2010-313>.
- Kikuchi, K., Wang, B. and Kajikawa, Y. (2012) Bimodal representation of the tropical intraseasonal oscillation. *Climate Dynamics*, **38**, 1989–2000.
<https://doi.org/10.1007/s00382-011-1159-1>.
- Kohavi, R., Longbotham, R., Sommerfield, D. and Henne, R. M. (2009) Controlled experiments on the web: survey and practical guide. *Data Mining and Knowledge Discovery*, **18**, 140–181. <https://doi.org/10.1007/s10618-008-0114-1>.
- Koralegedara, S. B., Lin, C.-Y. and Sheng, Y.-F. (2019) Numerical analysis of the mesoscale dynamics of an extreme rainfall and flood event in Sri Lanka in May 2016. *Journal of the Meteorological Society of Japan. Ser. II*.
<https://doi.org/10.2151/jmsj.2019-046>.
- Korfe, N. G. and Colle, B. A. (2018) Evaluation of cool-season extratropical cyclones in a multimodel ensemble for eastern North America and the western Atlantic Ocean. *Weather and Forecasting*, **33**, 109–127. <https://doi.org/10.1175/WAF-D-17-0036.1>.
- Kotal, S. and Bhattacharya, S. (2013) Tropical cyclone Genesis Potential Parameter (GPP) and its application over the north Indian Sea. *Mausam*, **64**, 149–170.
<https://doi.org/10.54302/mausam.v64i1.663>.
- Kotal, S., Roy, S. S. and Bhowmik, S. R. (2014) Catastrophic heavy rainfall episode over Uttarakhand during 16–18 June 2013—observational aspects. *Current Science*, 234–245.
- Kothawale, D. and Kumar, K. R. (2002) Tropospheric temperature variation over India and links with the Indian summer monsoon: 1971-2000. *Mausam*, **53**, 289–308.
<https://doi.org/10.54302/mausam.v53i3.1646>.

- Krishnamurthy, V. and Ajayamohan, R. (2010) Composite structure of monsoon low pressure systems and its relation to Indian rainfall. *Journal of Climate*, **23**, 4285–4305. <https://doi.org/10.1175/2010JCLI2953.1>.
- Krishnamurthy, V. and Shukla, J. (2007) Intraseasonal and seasonally persisting patterns of Indian monsoon rainfall. *Journal of Climate*, **20**, 3–20. <https://doi.org/10.1175/JCLI3981.1>.
- (2008) Seasonal persistence and propagation of intraseasonal patterns over the Indian monsoon region. *Climate Dynamics*, **30**, 353–369. <https://doi.org/10.1007/s00382-007-0300-7>.
- Krishnamurti, T., Kanamitsu, M., Godbole, R., Chang, C.-B. et al. (1975) Study of a Monsoon Depression (I). *Journal of the Meteorological Society of Japan. Ser. II*, **53**, 227–240. <https://doi.org/10.2151/jmsj1965.53.4.227>.
- (1976) Study of a Monsoon Depression (II), Dynamical Structure. *Journal of the Meteorological Society of Japan. Ser. II*, **54**, 208–225. <https://doi.org/10.2151/jmsj1965.54.4.208>.
- Krishnamurti, T., Molinari, J., Pan, H.-l. and Wong, V. (1977) Downstream amplification and formation of monsoon disturbances. *Monthly Weather Review*, **105**, 1281–1297. [https://doi.org/10.1175/1520-0493\(1977\)105%3C1281:DAAFOM%3E2.0.CO;2](https://doi.org/10.1175/1520-0493(1977)105%3C1281:DAAFOM%3E2.0.CO;2).
- Krishnamurti, T. N., Ardanuy, P., Ramanathan, Y. and Pasch, R. (1981) On the onset vortex of the summer monsoon. *Monthly Weather Review*, **109**, 344–363. [https://doi.org/10.1175/1520-0493\(1981\)109%3C0344:OTOVOT%3E2.0.CO;2](https://doi.org/10.1175/1520-0493(1981)109%3C0344:OTOVOT%3E2.0.CO;2).
- Krishnan, R., Ayantika, D., Kumar, V. and Pokhrel, S. (2011) The long-lived monsoon depressions of 2006 and their linkage with the Indian Ocean Dipole. *International Journal of Climatology*, **31**, 1334–1352. <https://doi.org/10.1002/joc.2156>.

- Lal, P., Prakash, A., Kumar, A., Srivastava, P. K., Saikia, P., Pandey, A., Srivastava, P. and Khan, M. (2020) Evaluating the 2018 extreme flood hazard events in Kerala, India. *Remote Sensing Letters*, **11**, 436–445. <https://doi.org/10.1080/2150704X.2020.1730468>.
- Lee, C.-Y., Camargo, S. J., Vitart, F., Sobel, A. H., Camp, J., Wang, S., Tippett, M. K. and Yang, Q. (2020) Subseasonal predictions of tropical cyclone occurrence and ACE in the S2S dataset. *Weather and Forecasting*, **35**, 921–938. <https://doi.org/10.1175/WAF-D-19-0217.1>.
- Lee, C.-Y., Camargo, S. J., Vitart, F., Sobel, A. H. and Tippett, M. K. (2018a) Subseasonal tropical cyclone genesis prediction and MJO in the S2S dataset. *Weather and Forecasting*, **33**, 967–988. <https://doi.org/10.1175/WAF-D-17-0165.1>.
- (2018b) Subseasonal tropical cyclone genesis prediction and MJO in the S2S dataset. *Weather and Forecasting*, **33**, 967–988. <https://doi.org/10.1175/WAF-D-17-0165.1>.
- Leith, C. (1974) Theoretical skill of Monte Carlo forecasts. *Monthly Weather Review*, **102**, 409–418.
- Leutbecher, M. and Palmer, T. N. (2008) Ensemble forecasting. *Journal of Computational Physics*, **227**, 3515–3539. <https://doi.org/10.1016/j.jcp.2007.02.014>.
- Liu, Z. (2016) Comparison of Integrated Multisatellite Retrievals for GPM (IMERG) and TRMM Multisatellite Precipitation Analysis (TMPA) Monthly Precipitation Products: Initial Results. *Journal of Hydrometeorology*, **17**, 777–790. <https://doi.org/10.1175/JHM-D-15-0068.1>.
- L’Heureux, M. L., Collins, D. C. and Hu, Z.-Z. (2013) Linear trends in sea surface temperature of the tropical Pacific Ocean and implications for the El Niño-Southern Oscillation. *Climate Dynamics*, **40**, 1223–1236. <https://doi.org/10.1007/s00382-012-1331-2>.

- MacQueen, J. et al. (1967) Some methods for classification and analysis of multivariate observations. In *Proceedings of the fifth Berkeley symposium on mathematical statistics and probability*, vol. 1, 281–297.
- Mahala, B. K., Nayak, B. K. and Mohanty, P. K. (2015) Impacts of ENSO and IOD on tropical cyclone activity in the Bay of Bengal. *Natural Hazards*, **75**, 1105–1125. <https://doi.org/10.1007/s11069-014-1360-8>.
- Meera, M., Suhas, E. and Sandeep, S. (2019) Downstream and in situ: Two perspectives on the initiation of monsoon low-pressure systems over the Bay of Bengal. *Geophysical Research Letters*, **46**, 12303–12310. <https://doi.org/10.1029/2019GL084555>.
- Mishra, K., Sharma, M. and Mohapatra, M. (2021) Performance of numerical weather prediction models in predicting track of recurving cyclone Vayu over Arabian Sea during June 2019. *Journal of Earth System Science*, **130**, 1–18.
- Mishra, S. and Salvekar, P. (1980) Role of baroclinic instability in the development of monsoon disturbances. *Journal of Atmospheric Sciences*, **37**, 383–394. [https://doi.org/10.1175/1520-0469\(1980\)037%3C0383:ROBIIT%3E2.0.CO;2](https://doi.org/10.1175/1520-0469(1980)037%3C0383:ROBIIT%3E2.0.CO;2).
- Mohanty, U., Osuri, K. K., Pattanayak, S. and Sinha, P. (2012) An observational perspective on tropical cyclone activity over Indian seas in a warming environment. *Natural Hazards*, **63**, 1319–1335. <https://doi.org/10.1007/s11069-011-9810-z>.
- Mohapatra, M., Bandyopadhyay, B. and Tyagi, A. (2012) Best track parameters of tropical cyclones over the North Indian Ocean: A review. *Natural Hazards*, **63**, 1285–1317. <https://doi.org/10.1007/s11069-011-9935-0>.
- Molod, A., Takacs, L., Suarez, M. and Bacmeister, J. (2015) Development of the GEOS-5 atmospheric general circulation model: Evolution from MERRA to MERRA2. *Geoscientific Model Development*, **8**, 1339–1356.

- Mooley, D. A. (1973) Some Aspects of Indian Monsoon Depressions and the Associated Rainfall. *Monthly Weather Review*, **101**, 271–280.
- Mooley, D. A. and Shukla, J. (1987) *Characteristics of the westward-moving summer monsoon low pressure systems over the Indian region and their relationship with the monsoon rainfall*. Center for Ocean-Land-Atmosphere Interactions, University of Maryland.
- Mulky, G. R. and Banerji, A. K. (1960) THE MEAN UPPER-WIND CIRCULATION AROUND MONSOON DEPRESSIONS IN INDIA. *Journal of Atmospheric Sciences*, **17**, 8–14.
- Murakami, H. (2014) Tropical cyclones in reanalysis data sets. *Geophysical Research Letters*, **41**, 2133–2141. <https://doi.org/10.1002/2014GL059519>.
- Murakami, M. (1984) Analysis of the deep convective activity over the Western Pacific and Southeast Asia part II: seasonal and intraseasonal variations during Northern Summer. *Journal of the Meteorological Society of Japan. Ser. II*, **62**, 88–108. <https://doi.org/10.2151/jmsj1965.62.1.88>.
- Murthy, V. S. and Boos, W. R. (2020) Quasigeostrophic controls on precipitating ascent in monsoon depressions. *Journal of the Atmospheric Sciences*, **77**, 1213–1232. <https://doi.org/10.1175/JAS-D-19-0202.1>.
- National Geophysical Data Center, NESDIS, NOAA, U.S. Department of Commerce (1995) TerrainBase, Global 5 Arc-minute Ocean Depth and Land Elevation from the US National Geophysical Data Center (NGDC). <https://doi.org/10.5065/E08M-4482>.
- Onogi, K., Koide, H., Sakamoto, M., Kobayashi, S., Tsutsui, J., Hatsushika, H., Matsumoto, T., Yamazaki, N., Kamahori, H., Takahashi, K. et al. (2005) JRA-25: Japanese 25-year re-analysis project—Progress and status. *Quarterly Journal of the Royal Meteorological Society*, **131**, 3259–3268. <https://doi.org/10.1256/qj.05.88>.

- Onogi, K., Tsutsui, J., Koide, H., Sakamoto, M., Kobayashi, S., Hatsushika, H., Matsumoto, T., Yamazaki, N., Kamahori, H., Takahashi, K. et al. (2007) The JRA-25 reanalysis. *Journal of the Meteorological Society of Japan. Ser. II*, **85**, 369–432. <https://doi.org/10.2151/jmsj.85.369>.
- Palmen, E. (1948) On the formation and structure of tropical hurricanes. *Geophysica*, **3**, 26–38.
- Parthasarathy, B. and Mooley, D. (1978) Some features of a long homogeneous series of Indian summer monsoon rainfall. *Monthly Weather Review*, **106**, 771–781. [https://doi.org/10.1175/1520-0493\(1978\)106%3C0771:SFOALH%3E2.0.CO;2](https://doi.org/10.1175/1520-0493(1978)106%3C0771:SFOALH%3E2.0.CO;2).
- Pisharoty, P. R. and Asnani, G. C. (1957) Rainfall around monsoon depressions over India. *Indian J. Met. Geophys*, **8**, 15–20.
- Prajeesh, A., Ashok, K. and Rao, D. B. (2013) Falling monsoon depression frequency: A Gray-Sikka conditions perspective. *Scientific Reports*, **3**, 1–8. <https://doi.org/10.1038/srep02989>.
- Prakash, S., Mitra, A. K., AghaKouchak, A., Liu, Z., Norouzi, H. and Pai, D. (2018) A preliminary assessment of GPM-based multi-satellite precipitation estimates over a monsoon dominated region. *Journal of Hydrology*, **556**, 865–876. <https://doi.org/10.1016/j.jhydrol.2016.01.029>.
- Prakash, S., Mitra, A. K., AghaKouchak, A. and Pai, D. (2015) Error characterization of TRMM Multisatellite Precipitation Analysis (TMPA-3B42) products over India for different seasons. *Journal of Hydrology*, **529**, 1302–1312. <https://doi.org/10.1016/j.jhydrol.2015.08.062>.
- Prakash, S., Mitra, A. K., Pai, D. and AghaKouchak, A. (2016) From TRMM to GPM: How well can heavy rainfall be detected from space? *Advances in Water Resources*, **88**, 1–7. <https://doi.org/10.1016/j.advwatres.2015.11.008>.

- Praveen, V., Sandeep, S. and Ajayamohan, R. S. (2015) On the relationship between mean monsoon precipitation and low pressure systems in climate model simulations. *Journal of Climate*, **28**, 5305–5324. <https://doi.org/10.1175/JCLI-D-14-00415.1>.
- Rajagopalan, B. and Molnar, P. (2013) Signatures of Tibetan Plateau heating on Indian summer monsoon rainfall variability. *Journal of Geophysical Research: Atmospheres*, **118**, 1170–1178. <https://doi.org/10.1002/jgrd.50124>.
- Rajamani, S. and Rao, K. V. (1981) On the occurrence of rainfall over southwest sector of monsoon depression. *Mausam*, **32**, 215–220.
- Rajeevan, M., Gadgil, S. and Bhate, J. (2010) Active and break spells of the Indian summer monsoon. *Journal of Earth System Science*, **119**, 229–247. <https://doi.org/10.1007/s12040-010-0019-4>.
- Raman, C., Rao, Y., Subramanian, S. and Sheikh, Z. (1978) Wind shear in a monsoon depression. *Nature*, **276**, 51–53. <https://doi.org/10.1038/276051a0>.
- Ray, K., Pandey, P., Pandey, C., Dimri, A. and Kishore, K. (2019) On the recent floods in India. *Current Science*, **117**, 204–218. <https://doi.org/10.18520/cs/v117/i2/204-218>.
- Rayner, N., Parker, D. E., Horton, E., Folland, C. K., Alexander, L. V., Rowell, D., Kent, E. C. and Kaplan, A. (2003) Global analyses of sea surface temperature, sea ice, and night marine air temperature since the late nineteenth century. *Journal of Geophysical Research: Atmospheres*, **108**. <https://doi.org/10.1029/2002JD002670>.
- Richardson, D. (2005) The THORPEX interactive grand global ensemble (TIGGE). In *Geophys. Res. Abstr*, vol. 7, 02815.
- Riehl, H. (1948) On the formation of typhoons. *Journal of the Atmospheric Sciences*, **5**, 247–265. [https://doi.org/10.1175/1520-0469\(1948\)005%3C0247:OTFOT%3E2.0.CO;2](https://doi.org/10.1175/1520-0469(1948)005%3C0247:OTFOT%3E2.0.CO;2).
- (1954) Tropical meteorology. *Tech. rep.*, McGraw-Hill.

- Riehl, H. and Shafer, R. J. (1944) The recurvature of tropical storms. *Journal of Atmospheric Sciences*, **1**, 42–54. [https://doi.org/10.1175/1520-0469\(1944\)001%3C0001:TROTS%3E2.0.CO;2](https://doi.org/10.1175/1520-0469(1944)001%3C0001:TROTS%3E2.0.CO;2).
- Rienecker, M. M., Suarez, M., Todling, R., Bacmeister, J., Takacs, L., Liu, H., Gu, W., Sienkiewicz, M., Koster, R., Gelaro, R. et al. (2008) The GEOS-5 Data Assimilation System: Documentation of Versions 5.0. 1, 5.1. 0, and 5.2. 0. .
- Robertson, A. W., Vitart, F. and Camargo, S. J. (2020) Subseasonal to seasonal prediction of weather to climate with application to tropical cyclones. *Journal of Geophysical Research: Atmospheres*, **125**, e2018JD029375. <https://doi.org/10.1029/2018JD029375>.
- Rodrigo, C., Kim, S. and Jung, I. H. (2018) Sensitivity study of WRF numerical modeling for forecasting heavy rainfall in Sri Lanka. *Atmosphere*, **9**, 378. <https://doi.org/10.3390/atmos9100378>.
- Roundy, P. E. (2012) Tracking and prediction of large-scale organized tropical convection by spectrally focused two-step space–time EOF analysis. *Quarterly Journal of the Royal Meteorological Society*, **138**, 919–931. <https://doi.org/10.1002/qj.962>.
- Roxy, M. K., Ritika, K., Terray, P. and Masson, S. (2014) The curious case of Indian Ocean warming. *Journal of Climate*, **27**, 8501–8509. <https://doi.org/10.1175/JCLI-D-14-00471.1>.
- Saha, K., Sanders, F. and Shukla, J. (1981) Westward propagating predecessors of monsoon depressions. *Monthly Weather Review*, **109**, 330–343. [https://doi.org/10.1175/1520-0493\(1981\)109%3C0330:WPPOMD%3E2.0.CO;2](https://doi.org/10.1175/1520-0493(1981)109%3C0330:WPPOMD%3E2.0.CO;2).
- Saha, S., Moorthi, S., Pan, H.-L., Wu, X., Wang, J., Nadiga, S., Tripp, P., Kistler, R., Woollen, J., Behringer, D. et al. (2010) The NCEP climate forecast system reanalysis. *Bulletin of the American Meteorological Society*, **91**, 1015–1058. <https://doi.org/10.1175/2010BAMS3001.1>.

- Saji, N., Goswami, B. N., Vinayachandran, P. and Yamagata, T. (1999) A dipole mode in the tropical Indian Ocean. *Nature*, **401**, 360–363. <https://doi.org/10.1038/43854>.
- Sandeep, S., Ajayamohan, R., Boos, W. R., Sabin, T. and Praveen, V. (2018) Decline and poleward shift in Indian summer monsoon synoptic activity in a warming climate. *Proceedings of the National Academy of Sciences*, **115**, 2681–2686. <https://doi.org/10.1073/pnas.1709031115>.
- Sanders, F. (1984) Quasi-geostrophic diagnosis of the monsoon depression of 5–8 July 1979. *Journal of Atmospheric Sciences*, **41**, 538–552. [https://doi.org/10.1175/1520-0469\(1984\)041%3C0538:QGDOTM%3E2.0.CO;2](https://doi.org/10.1175/1520-0469(1984)041%3C0538:QGDOTM%3E2.0.CO;2).
- Sarker, R. P. and Chowdhury, A. (1988) A diagnostic structure of monsoon depressions. *Mausam*, **39**, 9–18.
- Schiemann, R., Lüthi, D. and Schär, C. (2009) Seasonality and interannual variability of the westerly jet in the Tibetan Plateau region. *Journal of Climate*, **22**, 2940–2957. <https://doi.org/10.1175/2008JCLI2625.1>.
- Schneider, T., Bischoff, T. and Haug, G. H. (2014) Migrations and dynamics of the intertropical convergence zone. *Nature*, **513**, 45–53. <https://doi.org/10.1038/nature13636>.
- Scott, D. W. (2015) *Multivariate density estimation: theory, practice, and visualization*. John Wiley & Sons.
- Seetaramayya, P. and Master, A. (1984) Observed air-sea interface conditions and a monsoon depression during MONEX-79. *Archives for Meteorology, Geophysics, and Bioclimatology, Series A*, **33**, 61–67. <https://doi.org/10.1007/BF02265431>.
- Sikka, D. R. (1978) Some Aspects of the Life History, Structure and Movement of Monsoon Depressions. In *Monsoon Dynamics*, 1501–1529. Springer. https://doi.org/10.1007/978-3-0348-5759-8_21.

- (2006) A Study on the Monsoon Low Pressure Systems over the Indian Region and their Relationship with Drought and Excess Monsoon Seasonal Rainfall. *Tech. Rep. 217*, Center for Ocean-Land-Atmosphere Studies.
- Sikka, D. R. and Gadgil, S. (1980) On the maximum cloud zone and the ITCZ over Indian longitudes during the southwest monsoon. *Monthly Weather Review*, **108**, 1840–1853. [https://doi.org/10.1175/1520-0493\(1980\)108%3C1840:OTMCZA%3E2.0.CO;2](https://doi.org/10.1175/1520-0493(1980)108%3C1840:OTMCZA%3E2.0.CO;2).
- Singh, O., Khan, T. M. A. and Rahman, M. S. (2002) Impact of southern oscillation on the frequency of monsoon depressions in the Bay of Bengal. *Natural Hazards*, **25**, 101–115. <https://doi.org/10.1023/A:1013736923929>.
- Snedecor, G. W. and Cochran, W. G. (1989) Statistical Methods, eight edition. *Iowa State University Press*.
- Song, Y., Wang, L., Lei, X. and Wang, X. (2015) Tropical cyclone genesis potential index over the western North Pacific simulated by CMIP5 models. *Advances in Atmospheric Sciences*, **32**, 1539–1550. <https://doi.org/10.1007/s00376-015-4162-3>.
- Sørland, S. L. and Sorteberg, A. (2015) The dynamic and thermodynamic structure of monsoon low-pressure systems during extreme rainfall events. *Tellus A: Dynamic Meteorology and Oceanography*, **67**, 27039. <https://doi.org/10.3402/tellusa.v67.27039>.
- Sperber, K. R., Annamalai, H., Kang, I.-S., Kitoh, A., Moise, A., Turner, A., Wang, B. and Zhou, T. (2013) The Asian summer monsoon: an intercomparison of CMIP5 vs. CMIP3 simulations of the late 20th century. *Climate Dynamics*, **41**, 2711–2744. <https://doi.org/10.1007/s00382-012-1607-6>.
- Srivastava, G., Chakraborty, A. and Nanjundiah, R. S. (2020) Multidecadal variations in ENSO-Indian summer monsoon relationship at sub-seasonal timescales. *Theoretical and Applied Climatology*, **140**, 1299–1314. <https://doi.org/10.1007/s00704-020-03122-6>.

- Srujan, K. S., Sandeep, S. and Suhas, E. (2021) Downstream and In Situ Genesis of Monsoon Low-Pressure Systems in Climate Models. *Earth and Space Science*, **8**, e2021EA001741. <https://doi.org/10.1029/2021EA001741>.
- Stano, G., Krishnamurti, T., Vijaya Kumar, T. and Chakraborty, A. (2002) Hydrometeor structure of a composite monsoon depression using the TRMM radar. *Tellus A: Dynamic Meteorology and Oceanography*, **54**, 370–381. <https://doi.org/10.3402/tellusa.v54i4.12154>.
- Suhas, E., Neena, J. and Goswami, B. (2013) An Indian monsoon intraseasonal oscillations (MISO) index for real time monitoring and forecast verification. *Climate Dynamics*, **40**, 2605–2616. <https://doi.org/10.1007/s00382-012-1462-5>.
- Tan, J., Huffman, G. J., Bolvin, D. T. and Nelkin, E. J. (2019) IMERG V06: Changes to the Morphing Algorithm. *Journal of Atmospheric and Oceanic Technology*, **36**, 2471–2482. <https://doi.org/10.1175/JTECH-D-19-0114.1>.
- Thomas, T. M., Bala, G. and Srinivas, V. V. (2021) Characteristics of the monsoon low pressure systems in the Indian subcontinent and the associated extreme precipitation events. *Climate Dynamics*, **56**, 1859–1878. <https://doi.org/10.1007/s00382-020-05562-2>.
- Toth, Z. and Kalnay, E. (1993) Ensemble forecasting at NMC: The generation of perturbations. *Bulletin of the American Meteorological Society*, **74**, 2317–2330.
- (1997) Ensemble forecasting at NCEP and the breeding method. *Monthly Weather Review*, **125**, 3297–3319.
- Ullrich, P. A. and Zarzycki, C. M. (2017) TempestExtremes: A framework for scale-insensitive pointwise feature tracking on unstructured grids. *Geoscientific Model Development*, **10**, 1069–1090. <https://doi.org/10.5194/gmd-10-1069-2017>.

- Ummenhofer, C. C., England, M. H., McIntosh, P. C., Meyers, G. A., Pook, M. J., Risbey, J. S., Gupta, A. S. and Taschetto, A. S. (2009) What causes southeast Australia's worst droughts? *Geophysical Research Letters*, **36**. <https://doi.org/10.1029/2008GL036801>.
- Vishnu, S., Boos, W., Ullrich, P. and O'Brien, T. (2020a) Assessing historical variability of South Asian monsoon lows and depressions with an optimized tracking algorithm. *Journal of Geophysical Research: Atmospheres*, **125**, e2020JD032977. <https://doi.org/10.1029/2020JD032977>.
- (2020b) Global track dataset of monsoon low pressure systems. <https://doi.org/10.5281/zenodo.3890646>.
- Vishnu, S., Francis, P. A., Sheno, S. C. and Ramakrishna, S. S. V. S. (2018) On the relationship between the Pacific Decadal Oscillation and monsoon depressions over the Bay of Bengal. *Atmospheric Science Letters*, **19**, e825. <https://doi.org/10.1002/asl.825>.
- Vitart, F. (2017) Madden—Julian Oscillation prediction and teleconnections in the S2S database. *Quarterly Journal of the Royal Meteorological Society*, **143**, 2210–2220. <https://doi.org/10.1002/qj.3079>.
- Vitart, F., Ardilouze, C., Bonet, A., Brookshaw, A., Chen, M., Codorean, C., Déqué, M., Ferranti, L., Fucile, E., Fuentes, M. et al. (2017) The subseasonal to seasonal (S2S) prediction project database. *Bulletin of the American Meteorological Society*, **98**, 163–173. <https://doi.org/10.1175/BAMS-D-16-0017.1>.
- Vitart, F., Robertson, A., Group, S. S. et al. (2015) Sub-seasonal to seasonal prediction: linking weather and climate. *Seamless prediction of the earth system: From minutes to months*, 385–401.
- Vitart, F. and Robertson, A. W. (2018) The sub-seasonal to seasonal prediction project (s2s) and the prediction of extreme events. *npj Climate and Atmospheric Science*, **1**, 1–7. <https://doi.org/10.1038/s41612-018-0013-0>.

- Vitart, F., Robertson, A. W. and Anderson, D. L. (2012) Subseasonal to seasonal prediction project: Bridging the gap between weather and climate. *Bulletin of the World Meteorological Organization*, **61**, 23.
- Wahiduzzaman, M. and Yeasmin, A. (2020) A kernel density estimation approach of North Indian Ocean tropical cyclone formation and the association with convective available potential energy and equivalent potential temperature. *Meteorology and Atmospheric Physics*, **132**, 603–612. <https://doi.org/10.1007/s00703-019-00711-7>.
- Wang, B. and Murakami, H. (2020) Dynamic genesis potential index for diagnosing present-day and future global tropical cyclone genesis. *Environmental Research Letters*, **15**, 114008. <https://doi.org/10.1088/1748-9326/abbb01>.
- Wang, B., Xiang, B. and Lee, J.-Y. (2013) Subtropical high predictability establishes a promising way for monsoon and tropical storm predictions. *Proceedings of the National Academy of Sciences*, **110**, 2718–2722. <https://doi.org/10.1073/pnas.1214626110>.
- Wang, B. and Xie, X. (1997) A model for the boreal summer intraseasonal oscillation. *Journal of the Atmospheric Sciences*, **54**, 72–86. [https://doi.org/10.1175/1520-0469\(1997\)054%3C0072:AMFTBS%3E2.0.CO;2](https://doi.org/10.1175/1520-0469(1997)054%3C0072:AMFTBS%3E2.0.CO;2).
- Wang, C., Tang, G., Han, Z., Guo, X. and Hong, Y. (2018) Global intercomparison and regional evaluation of GPM IMERG Version-03, Version-04 and its latest Version-05 precipitation products: Similarity, difference and improvements. *Journal of Hydrology*, **564**, 342–356. <https://doi.org/10.1016/j.jhydrol.2018.06.064>.
- Wheeler, M. C. and Hendon, H. H. (2004) An All-Season Real-Time Multi-variate MJO index: Development of an Index for Monitoring and Prediction. *Monthly Weather Review*, **132**, 1917–1932. [https://doi.org/10.1175/1520-0493\(2004\)132%3C1917:AARMMI%3E2.0.CO;2](https://doi.org/10.1175/1520-0493(2004)132%3C1917:AARMMI%3E2.0.CO;2).

- White, C. J., Carlsen, H., Robertson, A. W., Klein, R. J., Lazo, J. K., Kumar, A., Vitart, F., Coughlan de Perez, E., Ray, A. J., Murray, V. et al. (2017) Potential applications of subseasonal-to-seasonal (S2S) predictions. *Meteorological Applications*, **24**, 315–325. <https://doi.org/10.1002/met.1654>.
- Wu, L. and Wang, C. (2015) Has the western Pacific subtropical high extended westward since the late 1970s? *Journal of Climate*, **28**, 5406–5413. <https://doi.org/10.1175/JCLI-D-14-00618.1>.
- Xavier, P. K. and Joseph, P. (2000) Vertical wind shear in relation to frequency of monsoon depressions and tropical cyclones of Indian Seas. In *Proceedings of TROPMET-2000, National Symposium on Ocean and Atmosphere*, 232–245. Citeseer.
- Yanai, M., Li, C. and Song, Z. (1992) Seasonal heating of the Tibetan Plateau and its effects on the evolution of the Asian summer monsoon. *Journal of the Meteorological Society of Japan. Ser. II*, **70**, 319–351. <https://doi.org/10.2151/jmsj1965.70.1B.319>.
- Yano, J.-I. and Ambaum, M. H. (2017) Moist static energy: Definition, reference constants, a conservation law and effects on buoyancy. *Quarterly Journal of the Royal Meteorological Society*, **143**, 2727–2734. <https://doi.org/10.1002/qj.3121>.
- Yasunari, T. (1979) Cloudiness fluctuations associated with the Northern Hemisphere summer monsoon. *Journal of the Meteorological Society of Japan. Ser. II*, **57**, 227–242. <https://doi.org/10.2151/jmsj1965.57.3.227>.
- Yianilos, P. N. (1993) Data structures and algorithms for nearest neighbor search in general metric spaces. In *Soda*, vol. 93, 311–21.
- Yoon, J. H. and Chen, T. C. (2005) Water vapor budget of the Indian monsoon depression. *Tellus A: Dynamic Meteorology and Oceanography*, **57**, 770–782. <https://doi.org/10.3402/tellusa.v57i5.14737>.

Zhang, C. (2005) Madden-Julian Oscillation. *Reviews of Geophysics*, **43**.
<https://doi.org/10.1029/2004RG000158>.

Zheng, C., Chang, E. K.-M., Kim, H., Zhang, M. and Wang, W. (2019) Subseasonal to seasonal prediction of wintertime Northern Hemisphere extratropical cyclone activity by S2S and NMME models. *Journal of Geophysical Research: Atmospheres*, **124**, 12057–12077. <https://doi.org/10.1029/2019JD031252>.